The Properties and Environments of Superluminous Supernovae

The Properties and Environments of Superluminous Supernovae

A dissertation presented

by

Ragnhild Lunnan

to

The Department of Astronomy

in partial fulfillment of the requirements

for the degree of

Doctor of Philosophy

in the subject of

Astronomy and Astrophysics

Harvard University

Cambridge, Massachusetts

April 2015

Dissertation Advisor: Professor Edo Berger Ragnhild Lunnan

The Properties and Environments of Superluminous Supernovae

Abstract

Superluminous supernovae (SLSNe) are a rare class of stellar explosions discovered by wide-field optical transient surveys in the past decade. They are characterized by peak luminosities $10 - 100$ times that of ordinary core-collapse and Type Ia SNe, and radiated energies of order 10^{51} erg, comparable to the entire kinetic energy of a canonical supernova explosion. Proposed sources of these tremendous energies include interaction between the supernova ejecta and dense circumstellar material (CSM), energy injection from the spin-down of a rapidly rotating and highly magnetized neutron star, or the pair-instability explosion of a very massive star producing several solar masses of radioactive nickel. In this thesis, I present results from the Pan-STARRS1 Medium Deep Survey (PS1/MDS), which discovered 15 hydrogen-poor SLSNe out to redshift 1.6 over the four years of its operation. I address the nature of SLSNe from two different angles. First, I characterize the SNe themselves, and compare their observed properties to model predictions. The PS1/MDS SLSN sample exhibits a diversity of light curve properties, and a wider range of peak luminosities than previously reported, particularly when accounting for the flux-limited nature of the survey. The light curves can generally be fit with magnetar spin-down models, though our sample also contains one very slowly evolving event that could plausibly be powered by radioactive decay. Second, I present the first comprehensive study of SLSN host galaxy environments and the sub-galactic environments, demonstrating that H-poor SLSNe preferentially occur in low-luminosity, low-mass, low-metallicity galaxies with high specific star formation

rates. Their host galaxies are statistically distinct from the hosts of core-collapse SNe, but share many similarities with the galaxies that host long gamma-ray bursts (LGRBs). This suggests that the environmental factors leading to a massive star forming either a SLSN or a LGRB are similar, with a possible common ingredient being a preference for low-metallicity environments through the need of a progenitor with high core angular momentum. In terms of their local environments, resolved *Hubble Space Telescope* imaging reveals that SLSN locations are correlated with the UV light, though not as strongly as LGRBs are. Although a larger sample size is needed to distinguish them statistically, this trend is also consistent with the interpretation that SLSN progenitors are lower-mass than those of LGRBs, collapsing to form a rapidly spinning neutron star rather than a black hole launching a relativistic jet.

Contents

Acknowledgments

First, I thank my thesis adviser, Edo Berger, who happily took on a wandering graduate student wanting to do an observational thesis, even as I was completely new to the field of transients and supernovae. Edo has been an incredibly supporting adviser, and I thank him for always managing to make me feel better after leaving his office, for encouraging me to be independent and venture out of my comfort zone, for his endless enthusiasm and optimism, and for showing by example how to be a great adviser.

Most people growing up in small villages in the mountains of Norway do not end up doing PhDs in Astrophysics at Harvard, and I am incredibly grateful of the opportunities I have had that have led me here. I thank the United World College movement for two fantastic high school years at Waterford Kamhlaba United World College of Southern Africa, leaving me with lifelong friends, transformative experiences, and a solid foundation in and love of physics and mathematics thanks in particular to the excellent instruction and encouragement of Ms Sansom and Mr Shields. I went from WK to Princeton University as a Davis UWC Scholar, made possible by the generosity and philanthropy of Shelby Davis. I thank the department of Astrophysical Sciences at Princeton for being such a welcoming environment to undergraduates – my experiences there, particularly doing research, was the main reason I decided to major in astrophysics and go on to graduate school. Special thanks to director of undergraduate studies Neta Bachall, and to my junior paper and senior thesis advisers, who also wrote me letters for graduate school: Michael Strauss, Jim Stone, and J. Richard Gott, III. Coming to Harvard, I initially wanted to do computational work, and I thank my research exam advisers Lars Hernquist and Anna Frebel for guiding me through the first two years of

graduate school. I particularly thank Anna for accidentally contributing to making me an observer, taking me on my first trip to the Magellan Telescopes.

Embarking on a new field can be daunting, and this thesis could not have been written without the guidance and input of my group members and collaborators. I thank Ryan Chornock for all his help and support over the years, including taking me observing, teaching me data reduction, helping with the Pan-STARRS data and pipeline, providing sage advice, and patiently answering all my random day-to-day questions. Even though certain group members decided to award me a Certificate of Achievement after my defense for surviving his unique brand of mentorship, I really have had a blast. I thank postdocs Ashley Zauderer, Raffaella Margutti, Peter Williams, Dan Milisavljevic and Ryan Foley for teaching me astronomy skills as well as providing advice and mentorship. Thanks to Armin Rest, Dan Scolnic and David Jones at STScI/JHU for their help with processing Pan-STARRS data and for helping me hack their pipeline in order to do the PS1-HST astrometry. Thanks to past and present students in the Berger Time-Domain Research Group, Wen-fai Fong, Tanmoy Laskar, Maria Drout, Camille Leibler, Ian Czekala, Peter Blanchard, Phil Cowperthwaite, Ashley Villar, George Miller and Kate Alexander for company on observing trips and conferences, and for being such and awesome and supportive group of people to work with.

I thank my thesis committee, Robert Kirshner, Ramesh Narayan, Rosanne Di Stefano and Robert Quimby, for their guidance and support through the writing of this thesis. Thanks to the OIR division at the CfA for all of the tea and cookies, and for everything they have taught me about telescopes. Heartfelt thanks to the department administrators, Peg Herlihy, Robb Scholten, Lisa Catella, Donna Adams and Jean Collins – none of us could do our jobs without them.

I am very grateful to have been part of the CfA community of graduate students. Special thanks to my fantastic office mates, Elisabeth Newton and Rebekah Dawson, for being such wonderfully supportive friends, for enabling my tea addiction, sending me post cards from all over the world, and being generally awesome people, role models, and scientists. I thank Sarah Rugheimer for introducing me to the Pomodoro method, and for taking on the role of public speaking coach when needed. I miss now-graduated students Gurtina Besla, Laura Blecha, Sarah Ballard, Wen-fai Fong, Greg Snyder, Zach Berta-Thompson, Robert Harris, Diego Munoz, Lauranne Lanz, Joey Neilsen, and Jack Steiner, but thank them for their help in navigating graduate school as well as the postdoc application process. Thanks to Nick Stone, Lauren Woolsey, and Sukrit Ranjan for helping me start the tradition of CfA Board Game Nights. I thank my incoming class, Rebekah Dawson, Tanmoy Laskar, Dylan Nelson, Max Moe, Yucong Zhu, and Li Zeng for their camaraderie through the years. I have enjoyed many a beer, coffee or frozen yogurt with Katherine Rosenfeld, Anjali Tripathi, Sarah Wellons, Luke Kelley, Meredith MacGregor, Doug Ferrer, Laura Schaefer, Jason Dittman, Nathan Sanders, Bence Beky, Courtney Dressing, Chris Faesi, Katie Auchettl, Ruth Angus, Dawn Graninger, and Ryan Loomis.

Occasionally I do interact with non-astronomers. Thanks to Jess, Carman, Bora, Joanna, Minh, Neil, George, Eden & Gcinisiswe, Depapa & Bethany, and Marianna & Peter for many fabulous brunches, fun dinners, and board game nights. I thank the Dudley Chorus and the Summer Seasonals for providing a wonderful musical outlet the past three years, and I especially thank Tanmoy Laskar for recruiting me back into singing. I am grateful to Bow Street Yoga and the physical therapists at Harvard University Health Services for making graduate school and thesis writing a slightly less

back-breaking experience.

Finally, I thank my family. I can trace my love of the natural world back to hikes in the mountains where I grew up and dinnertime conversations about logic puzzles. I am incredibly grateful that my parents have always let me and my siblings pursue our interests, including being perfectly ok with me moving to Swaziland at age 17 to do an international high school program.

And last but not least, I thank my partner, Jareth Holt, for all of his love and support.

Chapter 1

Introduction

1.1 A New Era of Time-Domain Astronomy

There are historical records of "new stars" that appear and then fade away, in the case of Chinese astronomers going back as far as 185 AD, as well as the more recent examples studied by Tycho and Kepler in 1572 and 1604 (Green 2015). With the realization that "nebulae" were other galaxies outside our own in the early 20th century, Baade & Zwicky (1934) were the first to point out that there must be a tremendous difference in intrinsic brightness between the "novae" observed in the Milky Way and those seen occasionally in distant galaxies, and coined the term "super-nova" (SN) for the latter phenomenon. In the following years and decades, numerous SNe were discovered in galaxies of increasing distances.

With the technological advancements of large CCD cameras (enabling wide-field imaging surveys), as well as increasing computational power making large-scale image

processing and transient detection possible, the field of time-domain astronomy has made significant advances in the past decade. Surveys like the Robotic Optical Transient Search Experiment (ROTSE; Akerlof et al. 2003), the Catalina Real-Time Transient Survey (CRTS; Drake et al. 2009), the Palomar Transient Factory (PTF; Law et al. 2009) and the Panoramic Survey Telescope and Rapid Response System (Pan-STARRS; Kaiser et al. 2010) have led to the discovery of several new transient phenomena, due to at least two key advantages. First, simply by virtue of the volume of space they cover, these new surveys are well equipped to find intrinsically rare types of transients. Second, they are "blind" or galaxy-untargeted searches, thus able to find transient sources in all kinds of environments, without preselecting a set of galaxies to monitor. Both of these factors apply to the class of transients that are the subject of this dissertation: "superluminous" supernovae (SLSNe).

1.2 Defining Superluminous Supernovae

Traditionally, SNe are classified based on their spectroscopic properties (see e.g. Filippenko 1997 for a review). The basic subdivision of SNe into Type I (without hydrogen lines) and Type II (with hydrogen lines) goes back to Minkowski (1941). Each class has since been further divided into subtypes, with the Type Ia SNe showing strong absorption near 6150 Å due to Si II, Type Ib SNe lacking the Si II feature but showing strong He I features, and Type Ic SNe showing neither of these characteristics. Type II SNe exhibit a range of light curve and spectral properties, with subclasses IIP and IIL depending on the shape of the light curve, and Type IIn SNe which show narrow hydrogen emission features indicating circumstellar interaction.

Superluminous supernovae fall outside of this traditional classification scheme, with their defining characteristic being their extreme luminosites. Typically, the designation "superluminous" is given to SNe with peak luminosities brighter than -21 mag (Gal-Yam 2012; although as demonstrated in this thesis, the exact cutoff value is somewhat arbitrary), making them $10-100$ times more luminous than ordinary Type Ia and core-collapse SNe. From the point of view of the spectroscopic classification scheme, almost all SLSNe discovered to date are either of Type IIn (showing narrow hydrogen lines) or Type Ic (showing neither hydrogen or helium). However, the spectra of "Type Ic" SLSNe do not necessarily resemble those of ordinary Type Ic SNe, particularly near peak light when they are considerably bluer (e.g., Quimby et al. 2011b).

Gal-Yam (2012) has proposed that SLSNe without hydrogen features be subdivided into two subclasses: SLSN-R, which show a light curve decay rate consistent with ^{56}Co (the "R" stands for radioactivity), and SLSN-I which decay too fast to be powered by radioactivity. However, as I discuss in Section 1.4 and explore further in Chapter 5, whether the slowly-decaying SLSNe constitute a separate subclass is controversial. Throughout this thesis, I will just refer to either H-poor or H-rich SLSNe for the sake of simplicity.

1.3 Early SLSN discoveries

The first discoveries of SLSNe came from ROTSE, including the hydrogen-poor transient SN 2005ap (Quimby et al. 2007) and the hydrogen-rich SN 2006gy, SN 2008am and SN 2008es (Ofek et al. 2007; Smith et al. 2007; Chatzopoulos et al. 2011; Miller et al. 2009; Gezari et al. 2009). Other surveys soon followed suit, with the hydrogen-poor

and slowly evolving SN 2007bi discovered by the Nearby Supernova Factory (Gal-Yam et al. 2009), and CRTS adding SN 2008fz to the growing list of hydrogen-rich examples (Drake et al. 2010). Around the same time, the transient SCP06F6 was discovered serendipitously in the *Hubble Space Telescope* (*HST*) Cluster Supernova Survey (Barbary et al. 2009), although its nature was initially a mystery: the features in the spectrum were unknown, and no host galaxy was visible in the *HST* pre-explosion imaging. Quimby et al. (2011b) were able to show that SCP06F6 was an example of the same type of transient as SN 2005ap, but at a much higher redshift of $z = 1.189$, by comparing to four newly found SLSNe from PTF. SN 2005ap and SCP06F6 are now considered prototypes of the subclass of hydrogen-poor SLSNe, which is the focus of this dissertation.

Since these early discoveries, the number of known SLSNe has grown considerably, with about 50 events reported as of early 2015. A substantial contribution, particularly at the high-redshift end ($z \gtrsim 0.5$), has been made by the Pan-STARRS1 Medium Deep Survey (PS1/MDS), including work presented in this dissertation in Chapters 2 and 5.

1.4 Proposed Mechanisms For Powering SLSNe

To understand how spectacular and puzzling SLSNe are, it is useful to consider the energy budget and basic physics governing supernova explosions. The energy available in a core-collapse SN is of order 10^{53} erg (the binding energy of a neutron star), but the bulk of this energy is carried away by neutrinos. Typically, $\sim 1\%$ of the total energy, about 10^{51} erg is imparted to the kinetic energy of the ejecta. Finally, the energy radiated in the optical band is $\sim 1\%$ of the kinetic energy budget. The reason for the low fraction of radiated energy can be understood from that the fact that stars are opaque – the

SN explosion needs to expand before it can radiate efficiently, and in doing so, most of the internal energy is converted into kinetic energy (KE) via adiabatic expansion. As a result, the bulk of the radiated energy generally comes from processes that release energy at late times, such as recombination radiation from hydrogen that was ionized by the SN shock being released as the ejecta expand and cool (in Type IIp SNe), and the heating from radioactive ^{56}Ni produced in the explosion (half-life of 6.1 days) and its daughter product ^{56}Co (half-life 77.3 days).

By contrast, the energy radiated in the optical band in SLSNe can exceed 10^{51} erg, comparable to the entire kinetic energy of ordinary SN explosions. To explain such a tremendous output, they require either an additional energy source, or otherwise an efficient mechanism for converting the KE into radiation. Three main mechanisms have been proposed in the current literature: (i) radioactive heating by ^{56}Ni following the pair-instability explosion of a very massive star, (ii) energy injection by the spin-down of a newly born magnetar, or (iii) converting KE into radiation through interaction with dense circumstellar material (CSM). I review each briefly below.

1.4.1 Radioactive Decay

The optical light curves of ordinary Type I SNe are powered by radioactive decay of nickel (^{56}Ni $\rightarrow$ ^{56}Co $\rightarrow$ ^{56}Fe; e.g. Arnett 1982). A straightforward way of producing a more luminous supernova would therefore be to increase the amount of ^{56}Ni produced in the explosion. As it turns out, this cannot explain the majority of SLSNe, since the light curve widths are incompatible with the Ni masses required to reproduce the peak luminosities, leading to an unphysical solution with $M_{\rm Ni} > M_{\rm ej}$ (Quimby et al. 2011b;

Chomiuk et al. 2011). It has been proposed that ^{56}Ni decay is the energy source of the slowest-evolving SLSNe, however, and in particular of SN 2007bi (Gal-Yam et al. 2009; Gal-Yam 2012). SN 2007bi was discovered near peak (so the rise-time is not constrained), but showed a slow decay over > 500 rest frame days consistent with the slope of ^{56}Co decay. From this, and from modeling of the nebular-phase spectrum, it was argued that SN 2007bi produced $\approx 5\ M_\odot$ of Ni (and had a total ejecta mass $\approx 100\ M_\odot$).

The ejecta mass and Ni mass derived for SN 2007bi imply that if ^{56}Ni decay was indeed the power source, then it was likely a pair-instability supernova (PISN) rather than a core-collapse explosion. PISNe are the expected fates of stars with initial masses in the range $140 - 260\ M_\odot$, developing oxygen cores with masses $\gtrsim 50\ M_\odot$ (Barkat et al. 1967; Rakavy & Shaviv 1967). Electron-positron pair production due to the high core temperatures leads to loss of pressure support and explosive oxygen ignition, resulting in a powerful explosion that disrupts the entire star. PISNe are thought to have been particularly important in the early universe, as the predicted fates of massive Pop III stars (Heger & Woosley 2002); finding one at SN 2007bi's redshift of $z = 0.127$ in a galaxy with a metallicity $Z = 1/3\ \mathrm{Z}_\odot$ would be surprising since such massive stars are expected to lose most of their mass to metal-driven winds except at very low metallicity, and not develop cores massive enough to explode as PISNe.

The interpretation of SN 2007bi as a PISN (and by extension, the existence of Ni-powered SLSNe) is controversial. A key prediction of PISN models is a broad light curve with a slow rise to peak ($\gtrsim 100$ days; Kasen et al. 2011; Dessart et al. 2013) due to the large ejecta mass and correspondingly long diffusion time. Since SN 2007bi was discovered near peak, the existence of such a long rise could not be ascertained. In addition, SN 2007bi's light curve can also be fit with a magnetar spin-down or CSM

interaction model (Young et al. 2010; Chatzopoulos et al. 2013; Nicholl et al. 2013), so Ni-decay is not the only plausible energy source. Finally, similar SLSNe with slow decay times have since been discovered, that show moderate rise-times ($\sim$ 60 days) incompatible with the PISN predictions (Nicholl et al. 2013). I return to the question of Ni decay as an energy source for SLSNe in Chapter 5, where I discuss an intriguing new candidate found at the end of PS1/MDS.

1.4.2 Magnetar Spin-Down

Since Ni decay cannot be the energy source of the majority of SLSNe, alternatives have been proposed. Kasen & Bildsten (2010) and Woosley (2010) have argued that one potential energy source is the rotational energy of a neutron star born in the explosion, being extracted as it spins down through interaction with a strong magnetic field. In the regime where the magnetar is born with a fast initial spin period ($\sim 1 - 10$ ms) and a strong magnetic field (10^{14-15} G), the energy input of the magnetar is comparable to that of the SN explosion, significantly altering the observed light curve. Fundamentally, this model can be thought of as a delayed energy injection, as a key point is that the spin-down timescale in this parameter range is of order days to weeks, re-energizing the ejecta after it has already undergone substantial expansion.

The magnetar model can successfully reproduce most light curves of SLSNe, but this alone is not entirely satisfactory because of the many assumptions and large parameter space of this model. For example, current models do not address how the energy is deposited into the expanding supernova ejecta; it is simply assumed that it is thermalized spherically at the base of the ejecta. Free parameters include the initial spin of the

magnetar, the magnetic field, and the mass of the ejecta; sometimes a fourth parameter is added to describe the rate at which γ- and X-rays escape at late times (Wang et al. 2015). To establish whether a magnetar is indeed the energy source in hydrogen-poor SLSNe, it is necessary to test its other predictions, such as that the ejecta should be swept up in a shell that later expands at constant velocity (Kasen & Bildsten 2010), or searching for the X-ray breakout signature at late times (Metzger et al. 2014).

1.4.3 Interaction with Circumstellar Material

The third main scenario for powering SLSNe is CSM interaction. In this case, the energy source is the kinetic energy of the ejecta itself, being converted into radiation as it collides with and shock heats massive CSM that has been previously lost from the progenitor star (e.g., Chevalier & Irwin 2011; Ginzburg & Balberg 2012; Moriya & Maeda 2012). This mechanism is particularly relevant for the subclass of SLSNe with narrow Balmer lines in their spectra, a tell-tale sign of interaction with slower-moving material.

To obtain such high efficiencies in converting KE to radiation, the mass of the CSM shell needs to be comparable to the mass of the ejecta, meaning that the star must have lost a significant fraction of its mass immediately prior to explosion (e.g., 10 $M_{\odot}$ at a scale of 10^{15-16} cm to reproduce the observed luminosities and timescales; Rest et al. 2011; Smith et al. 2007). Proposed mechanisms to explain such mass loss include luminous blue variable (LBV)-like eruptions (Smith et al. 2007, 2008), wave-driven mass loss in late stages of nuclear burning (Quataert & Shiode 2012), or pulsational pair-instability (Woosley et al. 2007). The latter mechanism is related to PISN explosions but occurs in stars of lower initial masses ($95 - 130$ $M_{\odot}$), where pair production again

leads to explosive burning, but is insufficient to unbind the entire star. Instead several solar masses of surface material can be ejected; if the remaining core is sufficiently massive, it can encounter this instability again and eject several shells of material in a series of pulses. This mechanism provides a way to produce massive circumstellar shells composed of intermediate-mass elements, necessary for CSM interaction to be able to also explain H-poor SLSNe (Chatzopoulos & Wheeler 2012b). Still, it is unclear if the lack of narrow emission lines (of any element) seen in H-poor SLSNe can be explained with CSM interaction as the power source.

1.5 The Pan-STARRS1 Medium Deep Survey

The main focus of this thesis are the SLSNe discovered in the Pan-STARRS1 Medium Deep Survey, which operated from 2010 to 2014 on the 1.8 m PS1 telescope on Haleakala (Kaiser et al. 2010). A detailed description of the telescope and photometric system is given in the individual chapters, e.g. Section 2.2.1. The Medium Deep Survey consisted of 10 fields, each 7 square degrees, observed in four filters ($griz_{\rm P1}$) with a typical cadence of 3 days per filter, to a typical depth of 23.5 mag. Basic image processing was performed by the Pan-STARRS IPP system (Magnier 2006; Magnier et al. 2008), while the image subtraction and transient search (Rest et al. 2005) was run on the Harvard FAS Research computing cluster Odyssey. As part of the Harvard PS1 group, I have participated in running the transient pipeline, vetting transient candidates, and carrying out spectroscopic follow-up at the MMT, Magellan and Gemini observatories over the course of my thesis work.

Compared to other concurrent surveys like PTF and CRTS, PS1/MDS covers a

smaller area but is considerably deeper. For the purposes of finding SLSNe, this means our volume is primarily at high redshift; the final sample presented in Chapter 5 spans $0.5 < z < 1.6$.

1.6 Thesis Summary

This thesis aims to shed light on two fundamental questions: What are the explosion mechanisms of H-poor SLSNe, and what are their progenitors? I attack these questions with a two-fold approach: studying the properties of the explosions themselves, utilizing our PS1 light curves and follow-up data, and studying their host galaxy environments as a proxy for their progenitor properties.

Chapter 2 examines both these questions through a detailed study of a single event and its host galaxy: PS1-10bzj. PS1-10bzj was discovered in the first year of PS1/MDS, and stood out in exhibiting shorter time scales and less extreme energetics than previously discovered H-poor SLSNe. I compare the bolometric light curve to model predictions, and show that PS1-10bzj could still not be powered by radioactive Ni-decay, but that a magnetar model can explain the observed properties. PS1-10bzj happened to be located in the Extended Chandra Deep Field South, and as a result its host galaxy had imaging data from a number of surveys, including with the *Hubble Space Telescope*. I show that the host is a compact dwarf galaxy with a low metallicity, young stellar population and remarkably high specific star formation rate. This was only the second detailed study of a SLSN host galaxy at the time, providing important clues that their environments are unusual relative to ordinary core-collapse SNe.

The theme of host galaxy environments as a proxy for progenitor properties is continued in Chapter 3, where I present the first comprehensive study of the host galaxies of H-poor SLSNe. I target the galaxies of both PS1/MDS SLSNe and events reported in the literature, and obtain optical spectroscopy and optical/near-IR photometry, allowing me to determine the galaxy luminosities, stellar masses, star formation rates and metallicities. I show that H-poor SLSNe preferentially happen in low-mass, low-metallicity galaxies with high specific star formation rates. They are statistically incompatible with coming from the same environments as ordinary core-collapse supernovae in the same redshift range, but overall resemble the host galaxies of long gamma-ray bursts.

In Chapter 4, I use *Hubble Space Telescope* resolved galaxy imaging and precise astrometric matching to study the *local* environments of H-poor SLSNe. Their host galaxies are generally irregular and compact, with a median half-light-radius of only 0.9 kpc. By comparing the SLSN locations to the overall distribution of UV light, I find that they correlate with the underlying UV light distribution, though potentially not as strongly as do LGRBs, suggesting that their progenitors may be lower-mass stars. A larger sample size is still necessary to distinguish the populations statistically, however.

Chapter 5 returns to the question of the SLSN explosion properties, presenting light curves and spectra of the full sample of 15 H-poor SLSNe found in PS1/MDS. With a redshift range $0.5 < z < 1.6$, our multi-filter PS1 light curves probe the rest-frame UV emission, sensitive to the peak of the spectral energy distribution and allowing me to measure the temperature evolution and construct bolometric light curves. I discuss the ranges in peak luminosities and radiated energies, as well as model fits to the light curves. Interestingly, the one SLSN in our sample that is spectroscopically similar to SN 2007bi

shows a broad light curve with a $\gtrsim 100$ day rise and a decay rate consistent with ^{56}Co, demonstrating that some H-poor SLSNe can plausibly be powered by radioactivity.

Finally, in Chapter 6, I present concluding remarks and thoughts for future directions to make further progress in the context of existing and future facilities.

Chapter 2

PS1-10bzj: A Fast, Hydrogen-Poor Superluminous Supernova in a Metal-Poor Host Galaxy

R. Lunnan, R. Chornock, E. Berger, D. Milisavljevic, M. Drout, N. E. Sanders, P. M. Challis, I. Czekala, R. J. Foley, W. Fong, M. E. Huber, R. P. Kirshner, C. Leibler, G. H. Marion, M. McCrum, G. Narayan, A. Rest, K. C. Roth, D. Scolnic, S. J. Smartt, K. Smith, A. M. Soderberg, C. W. Stubbs, J. L. Tonry, W. S. Burgett, K. C. Chambers, R.-P. Kudritzki, E. A. Magnier, and P. A. Price

The Astrophysical Journal, Vol. 771, No. 97, 2013

Abstract

We present observations and analysis of PS1-10bzj, a superluminous supernova (SLSN) discovered in the Pan-STARRS Medium Deep Survey at a redshift $z = 0.650$. Spectroscopically, PS1-10bzj is similar to the hydrogen-poor SLSNe 2005ap and SCP 06F6, though with a steeper rise and lower peak luminosity ($M_{\rm bol} \simeq -21.4$ mag) than previous events. We construct a bolometric light curve, and show that while PS1-10bzj's energetics were less extreme than previous events, its luminosity still cannot be explained by radioactive nickel decay alone. We explore both a magnetar spin-down and circumstellar interaction scenario and find that either can fit the data. PS1-10bzj is located in the Extended Chandra Deep Field South and the host galaxy is imaged in a number of surveys, including with the *Hubble Space Telescope*. The host is a compact dwarf galaxy ($M_B \approx -18$ mag, diameter $\lesssim 800$ pc), with a low stellar mass ($M_* \approx 2.4 \times 10^7$ M$_\odot$), young stellar population ($\tau_* \approx 5$ Myr), and a star formation rate of $\sim 2 - 3$ M$_\odot$ yr^{-1}. The specific star formation rate is the highest seen in an SLSN host so far (~ 100 Gyr^{-1}). We detect the [O III] λ4363 line, and find a low metallicity: 12+(O/H) $= 7.8 \pm 0.2$ ($\simeq 0.1 Z_\odot$). Together, this indicates that at least some of the progenitors of SLSNe come from young, low-metallicity populations.

2.1 Introduction

The discovery of "superluminous" supernovae (SLSNe), with peak luminosities $30 - 100$ times brighter than normal supernovae and radiated energies $\gtrsim 10^{51}$ erg, is one of the most unexpected results from blank-field time-domain surveys like Pan-STARRS

(PS1), Palomar Transient Factory (PTF) and the Catalina Real-Time Transient Survey (CRTS). Several distinct subclasses has been identified, indicating different mechanisms to power the extreme luminosities. Some SLSNe can be classified as Type IIn, likely powered by interaction with a dense, H-rich circumstellar medium (e.g. Ofek et al. 2007; Smith et al. 2007, 2010; Rest et al. 2011; Moriya et al. 2013). The superluminous SN 2007bi was proposed to be a pair-instability explosion and so ultimately powered by radioactivity (Gal-Yam et al. 2009), though this claim is controversial (Dessart et al. 2012). The recently discovered SLSN PS1-10afx (Chornock et al. 2013) does not resemble any previous SLSNe and may define another class of objects.

A third subclass of hydrogen-poor SLSNe similar to the transients SN 2005ap (Quimby et al. 2007) and SCP 06F6 (Barbary et al. 2009) have also been identified, characterized by blue spectra with a few broad features not matching any standard supernova class (Quimby et al. 2007, 2011b; Barbary et al. 2009; Pastorello et al. 2010; Chomiuk et al. 2011; Leloudas et al. 2012; Berger et al. 2012). While the associated energetics, ejecta masses and host environments point toward the explosion of a young, massive star, the ultimate energy source remains unknown for these objects. Like the H-rich SLSNe, models based on circumstellar interaction has been proposed (Chevalier & Irwin 2011; Ginzburg & Balberg 2012; Moriya & Maeda 2012), but the lack of hydrogen seen in the spectrum requires such interaction to be dominated by intermediate-mass elements. Alternatively, the luminosity could be explained by energy injection from a central engine, such as the spin-down of a newborn magnetar (Woosley 2010; Kasen & Bildsten 2010; Dessart et al. 2012). This class has also been linked to Type Ic SNe through the late-time spectroscopic evolution of a few objects (Pastorello et al. 2010; Quimby et al. 2011b), but the relationship between the classes remains unclear.

Exploring the diversity of SLSNe and mapping the distribution of explosion properties will be important in further shedding light on the possible energy sources.

Another clue to the progenitor systems could come from studying the host environments. Of the 10 2005ap-like H-poor SLSNe published prior to this paper, only five have detected host galaxies (Neill et al. 2011; Leloudas et al. 2012; Berger et al. 2012; Chen et al. 2013). The host galaxy of SN 2010gx is the only one that has been studied in detail so far, and is a dwarf galaxy with a low metallicity ($Z = 0.06Z_{\odot}$), leading to speculation of whether metallicity plays a role in the progenitor channel (Chen et al. 2013). Increasing and characterizing the sample of SLSN host galaxies is essential for testing this hypothesis, and constraining the possible progenitors to these extreme explosions.

Here, we present the discovery and analysis of PS1-10bzj, a hydrogen-poor SLSN at $z = 0.650$ from the Pan-STARRS Medium-Deep Survey (PS1/MDS). We present a comprehensive study of the SN and its host environment. The discovery and observations of PS1-10bzj are described in Section 2.2. We analyze the properties of the supernova, including temperature evolution, bolometric light curve, possible models, and spectral modeling, in Section 2.3. Since PS1-10bzj is located in the Extended Chandra Deep Field South (ECDF-S), its host galaxy is detected in the GEMS, GaBoDs and MUSYC surveys (Rix et al. 2004; Taylor et al. 2009; Cardamone et al. 2010), as well as in the PS1 pre-explosion images. The host galaxy properties, including metallicity, star formation rate, stellar mass and population age, are analyzed in Section 2.4. We place this SN in a broader context, comparing it to previous events, and summarize our results in Sections 2.5 and 2.6. All calculations in this paper assume a ΛCDM cosmology with $H_0 = 70$ km s^{-1} Mpc^{-1}, $\Omega_{\rm M} = 0.27$ and $\Omega_{\Lambda} = 0.73$ (Komatsu et al. 2011).

2.2 Observations

2.2.1 PS1 Survey Summary

The PS1 telescope on Haleakala is a high-etendue wide-field survey instrument with a 1.8-m diameter primary mirror and a 3.3° diameter field of view imaged by an array of sixty 4800 × 4800 pixel detectors, with a pixel scale of 0.258″ (Kaiser et al. 2010; Tonry & Onaka 2009). The observations are obtained through five broad-band filters ($g_{\rm P1}r_{\rm P1}i_{\rm P1}z_{\rm P1}y_{\rm P1}$), with some differences relative to the Sloan Digital Sky Survey (SDSS); the $g_{\rm P1}$ filter extends 200 Å redward of $g_{\rm SDSS}$ to achieve greater sensitivity and lower systematics for photometric redshifts, and the $z_{\rm P1}$ filter terminates at 9300 Å, unlike $z_{\rm SDSS}$ which is defined by the detector response (Tonry et al. 2012). PS1 photometry is in the "natural" PS1 magnitude system, $m = -2.5\log(F_\nu) + m'$, with a single zero-point adjustment (m') in each band to conform to the AB magnitude scale, determined with PS1 observations of HST Calspec spectrophotometric standards (Bohlin et al. 2001). Magnitudes are interpreted as being at the top of the atmosphere, with 1.2 airmasses of atmospheric attenuation included in the system response function (Tonry et al. 2012).

The PS1 MDS consists of 10 fields (each with a single PS1 imager footprint) observed in $g_{\rm P1}r_{\rm P1}i_{\rm P1}z_{\rm P1}$with a typical cadence of 3 d in each filter, to a 5σ depth of $\sim$ 23.3 mag; $y_{\rm P1}$is observed near full moon with a typical depth of $\sim$ 21.7 mag. The standard reduction, astrometric solution, and stacking of the nightly images is done by the Pan-STARRS1 IPP system (Magnier 2006; Magnier et al. 2008) on a computer cluster at the Maui High Performance Computer Center. The nightly Medium Deep stacks are transferred to the Harvard FAS Research Computing cluster, where they are

processed through a frame subtraction analysis using the `photpipe` pipeline developed for the SuperMACHO and ESSENCE surveys (Rest et al. 2005; Garg et al. 2007; Miknaitis et al. 2007), which was further improved in order to increase the accuracy (A. Rest et al, in preparation, D. Scolnic et al., in preparation). The discovery and data presented here are from the `photpipe` analysis.

2.2.2 Photometry

PS1-10bzj was discovered in PS1 MD02 data on the rise on UT 2010 Dec 16, at coordinates RA=$03^{\rm h}31^{\rm m}39.826^{\rm s}$, Dec=$-27^\circ47'42.17''$ (J2000). Spectroscopic follow-up confirmed it to be at redshift $z = 0.650$ from host galaxy emission lines, placing the peak observed absolute magnitude at $\lesssim -21$ mag, thus classifying it as "superluminous". The transient was detected in $g_{\rm P1}r_{\rm P1}i_{\rm P1}z_{\rm P1}$ until PS1 stopped observing the field in early 2011 February. All photometry is listed in Table 2.1, and is corrected for foreground extinction with $E(B-V) = 0.008$ mag (Schlafly & Finkbeiner 2011). When PS1 resumed observing this field in late 2011 September, PS1-10bzj had faded below the detection limit of ~ 23.5 mag.

Table 2.1. PS1-10bzj Photometry

MJD	Phase[a]	Filter	AB Magnitude	Telescope/Instrument
55509.4	−32.9	$g_{\rm P1}$	> 23.74	PS1
55518.4	−27.4	$g_{\rm P1}$	> 22.72	PS1
55524.4	−23.8	$g_{\rm P1}$	> 22.21	PS1
55545.4	−11.1	$g_{\rm P1}$	21.30 ± 0.12	PS1
55548.4	−9.2	$g_{\rm P1}$	21.26 ± 0.15	PS1
55557.3	−3.8	$g_{\rm P1}$	21.33 ± 0.05	PS1
55574.6	+6.6	g	21.58 ± 0.10	Magellan/LDSS3
55586.1	+13.6	g	22.32 ± 0.06	Gemini-S/GMOS
55589.0	+15.4	g	22.83 ± 0.16	Gemini-S/GMOS
55596.2	+19.7	$g_{\rm P1}$	> 23.43	PS1
55627.5	+38.7	g	> 24.47	Magellan/IMACS
55648.9	+51.7	g	> 22.07	Gemini-S/GMOS
55509.4	−32.9	$r_{\rm P1}$	> 24.09	PS1
55518.5	−27.4	$r_{\rm P1}$	> 23.12	PS1
55524.4	−23.8	$r_{\rm P1}$	> 22.54	PS1
55545.4	−11.1	$r_{\rm P1}$	21.55 ± 0.06	PS1
55548.4	−9.2	$r_{\rm P1}$	21.32 ± 0.10	PS1
55557.4	−3.8	$r_{\rm P1}$	21.44 ± 0.06	PS1
55574.6	+6.6	r	21.33 ± 0.05	Magellan/LDSS3
55586.1	+13.6	r	21.49 ± 0.07	Gemini-S/GMOS
55589.0	+15.4	r	21.86 ± 0.08	Gemini-S/GMOS
55596.2	+19.7	$r_{\rm P1}$	22.25 ± 0.08	PS1
55627.5	+38.7	r	23.33 ± 0.13	Magellan/IMACS
55652.9	+54.1	r	> 22.5	Gemini-S/GMOS
55507.5	−34.0	$i_{\rm P1}$	> 23.89	PS1
55510.4	−32.3	$i_{\rm P1}$	> 23.74	PS1
55516.4	−28.6	$i_{\rm P1}$	> 23.53	PS1
55534.4	−17.7	$i_{\rm P1}$	22.92 ± 0.27	PS1
55546.4	−10.4	$i_{\rm P1}$	21.68 ± 0.08	PS1
55555.4	−5.0	$i_{\rm P1}$	21.51 ± 0.07	PS1

Table 2.1—Continued

MJD	Phase[a]	Filter	AB Magnitude	Telescope/Instrument
55574.6	+6.6	i	21.37 ± 0.07	Magellan/LDSS3
55576.3	+7.7	i_{P1}	21.49 ± 0.09	PS1
55586.1	+13.6	i	21.48 ± 0.03	Gemini-S/GMOS
55588.2	+14.9	i_{P1}	21.78 ± 0.08	PS1
55594.2	+18.5	i_{P1}	21.80 ± 0.07	PS1
55597.2	+20.3	i_{P1}	21.78 ± 0.07	PS1
55627.5	+38.7	i	22.68 ± 0.13	Magellan/IMACS
55648.9	+51.7	i	> 22.19	Gemini-S/GMOS
55508.4	−33.5	z_{P1}	> 23.56	PS1
55511.4	−31.7	z_{P1}	> 23.13	PS1
55517.4	−28.0	z_{P1}	> 23.28	PS1
55547.3	−9.9	z_{P1}	21.71 ± 0.07	PS1
55568.3	+2.8	z_{P1}	21.42 ± 0.08	PS1
55574.6	+6.6	z	21.28 ± 0.14	Magellan/LDSS3
55577.3	+8.3	z_{P1}	21.57 ± 0.11	PS1
55586.1	+13.6	z	21.59 ± 0.22	Gemini-S/GMOS
55586.3	+13.7	z_{P1}	21.55 ± 0.08	PS1
55589.2	+15.5	z_{P1}	21.57 ± 0.08	PS1
55595.2	+19.1	z_{P1}	21.84 ± 0.09	PS1
55627.5	+38.7	z	22.32 ± 0.12	Magellan/IMACS

[a]In rest-frame days, relative to maximum light on MJD 55563.65

In addition to the PS1 photometry, *griz* images were obtained along with spectroscopic observations with the Low Dispersion Survey Spectrograph (LDSS3) on the 6.5-m Magellan-Clay telescope, the Inamori-Magellan Areal Camera and Spectrograph (IMACS; Dressler et al. 2006) on the 6.5-m Magellan-Baade telescope, and the Gemini Multi-Object Spectrograph (GMOS; Hook et al. 2004) on the 8-m Gemini-South telescope, allowing us to extend the light curve until early 2011 April. These images were reduced using standard routines in IRAF[1], and transient flux was determined by subtracting the PS1 pre-explosion template images using ISIS (Alard & Lupton 1998) to correct for galaxy contamination, and measuring the flux in the difference image using aperture photometry. For the LDSS3 and IMACS images, calibrations were obtained either from observations of standard fields on the same night, or from the PS1 catalogs of stars in the field of PS1-10bzj corrected to the SDSS system by the relations in Tonry et al. (2012). In the case of Gemini, archival zeropoints were used for calibration, after verifying that they produce consistent results with the PS1 catalog.

In general the slight difference between the PS1 filter set and *griz* would not introduce any significant errors. At the particular redshift of PS1-10bzj, however, the [O III] λ5007 galaxy emission line is located at the edge between the i and z bands, contributing primarily to the $z_{\rm P1}$-filter in the PS1 photometric system, but to the i-band filter in the SDSS system used at Magellan and Gemini. This line contributes a substantial fraction of the galaxy flux (see Section 2.4). Therefore, non-PS1 i and z fluxes were either determined by subtracting the galaxy templates taken at Gemini

[1]IRAF is distributed by the National Optical Astronomy Observatory, which is operated by the Association of Universities for Research in Astronomy, Inc., under cooperative agreement with the National Science Foundation.

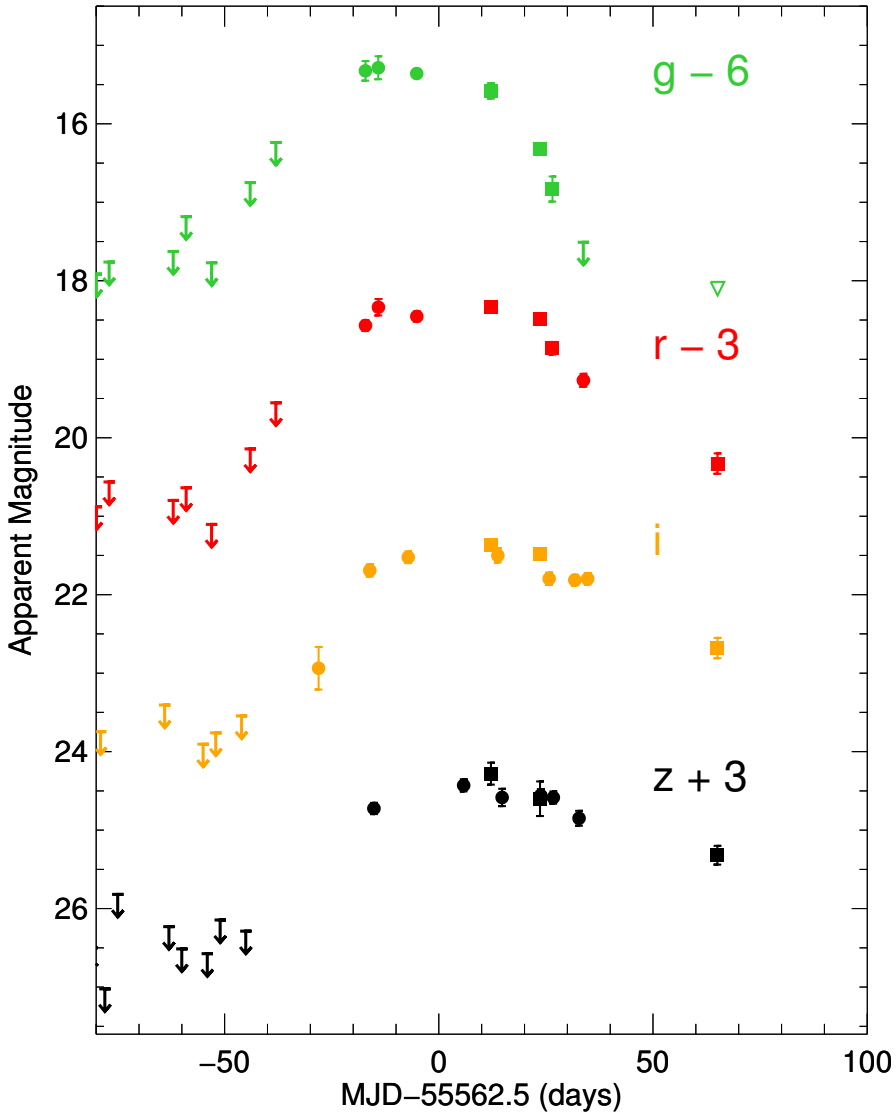

Figure 2.1.—: Observed light curve of PS1-10bzj. Time is shown in observer frame, relative to 2011 January 1 (MJD 55562.5). Circles show PS1 photometry, while the squares are photometry obtained with Magellan or Gemini. The arrows and triangles similarly show 3σ upper limits from PS1 and non-PS1 photometry, respectively. We note the rapid rise time and the faster fall-off in the bluer bands, which indicates temperature evolution.

and Magellan after the supernova had faded (Section 2.2.4), or corrected according to numerical subtraction.

Figure 2.1 shows the observed light curves. Since PS1 was observing this field prior to the detection, we are able to constrain the rise time, particularly in $i_{\rm P1}$-band, where PS1-10bzj brightened by > 1.2 mag in 12 days in the observed frame, corresponding to just 7 days in the rest frame. We also note that the later peak times in the redder bands indicate temperature evolution. Since the best-fit peak is different in different bands, we fit a low-order polynomial to our constructed bolometric light curve (Section 2.3.2) to determine the time of maximum light as UT 2011 January 02.65 (MJD 55563.65) ± 2 d. All phases listed are in rest-frame days with respect to this zeropoint.

2.2.3 Spectroscopy

We obtained four epochs of spectroscopy of PS1-10bzj. Details are given in Table 2.2. Our initial spectra were taken on 2011 January 18.2 using LDSS3 on the 6.5-m Magellan Clay telescope. Subsequent observations were obtained with GMOS on the 8-m Gemini-South telescope (Hook et al. 2004). Continuum and arc lamp exposures were obtained immediately after each object observation to provide a flat field and wavelength calibration. Basic two-dimensional image processing tasks were accomplished using standard tasks in IRAF. Observations of spectrophotometric standard stars were obtained on the same night as the LDSS3 data, while archival observations were used for the GMOS spectra. Our own IDL routines were used to apply a flux calibration and correct for telluric absorption bands.

The LDSS3 observations covered the range $3540 - 9450$ Å in a single setup using

the VPH-all grating and a 0.75″ slit oriented at the parallactic angle. Although no order-blocking filter was used for the object observations, this setup exhibits very little second-order light contamination, which we confirmed from observations of standard stars taken both with and without a filter, so we believe the spectral shape to be reliable.

The January 25 and 28 GMOS observations were taken with complementary blue and red setups, which we will sometimes present as a combined single spectrum. The January 25 blue spectra were taken with the slit oriented at a position angle of 175°, about 68° away from the parallactic angle, so differential light loss (Filippenko 1982) makes the blue continuum slope on that date unreliable. The other GMOS spectra were acquired in red setups either at low airmass (January 28) or near the parallactic angle (April 2 and 3), so their spectral slopes are reliable.

Our last GMOS observations on April 2 and 3 were obtained in nod-and-shuffle mode (Glazebrook & Bland-Hawthorn 2001). An error resulted in the object being nodded off the slit for half of the April 2 observations. The exposure time quoted in Table 2.2 reflects only the on-slit time. The April 2 and 3 data were combined into a single spectrum.

The spectra from January 18, 25 and 28 are shown in Figure 2.2. The April 2 spectrum is dominated by host galaxy light, and is shown in Section 2.4. All of our spectra show a number of narrow emission lines originating in the host galaxy, allowing us to determine a consistent redshift of $z = 0.650$ for PS1-10bzj.

Table 2.2. Log of Spectroscopic Observations

UT Date (YYYY-MM-DD.D)	Epoch[a] (days)	Instrument	Wavelength (Å)	Slit (″)	Grating	Filter	Exp. time (s)	Mean Airmass
2011-01-13.2	6.7	LDSS3	3540−9450	0.75	VPH-all	none	3900	1.3
2011-01-25.1	13.9	GMOS-S	3320−6140	1.0	B600	none	2400	1.4
2011-01-28.1	15.7	GMOS-S	5890−10100	1.0	R400	OG515	3000	1.1
2011-04-02.0	54.5	GMOS-S	5530−9830	1.0	R400	OG515	900	1.9
2011-04-03.0	55.1	GMOS-S	5530−9830	1.0	R400	OG515	1800	1.9

[a]In rest-frame days relative to maximum light on UT 2011-01-02.7.

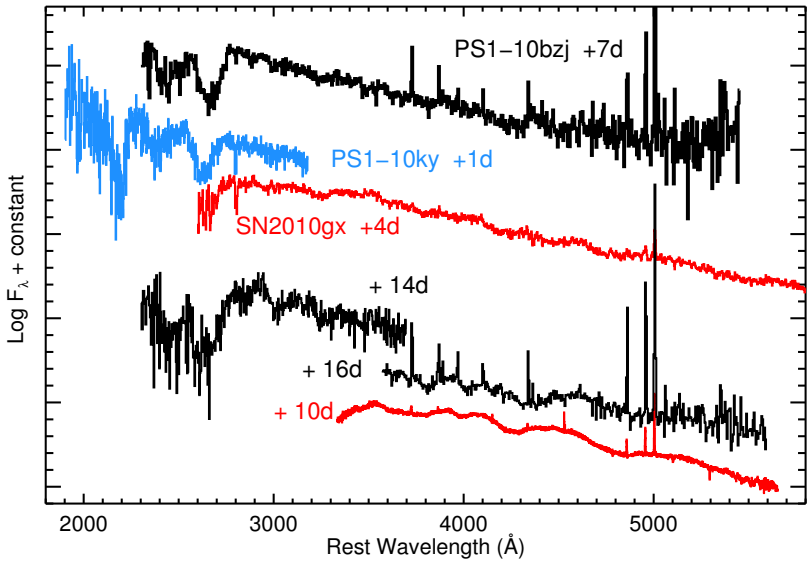

Figure 2.2.—: Spectra of PS1-10bzj (black), compared to spectra of other hydrogen-poor SLSNe PS1-10ky (blue; Chomiuk et al. 2011) and SN 2010gx (red; Pastorello et al. 2010). The blue continuum and broad UV features are common to hydrogen-poor SLSNe. By the Day 16 spectrum, PS1-10bzj had also developed a number of features in the optical, similar to those seen in SN 2010gx (Pastorello et al. 2010). See Section 2.3.3 for modeling and identification of the features.

2.2.4 Host Galaxy Photometry

The host galaxy of PS1-10bzj is detected in the PS1 pre-explosion stacked images in $g_{\rm P1}r_{\rm P1}i_{\rm P1}z_{\rm P1}$. In addition, we obtained deep host images with Gemini-S/GMOS, Magellan-Clay/LDSS3 and Magellan-Baade/IMACS in *griz* after the supernova had faded. Deep infrared imaging in J and K with the FourStar Infrared Camera on Magellan-Baade (Persson et al. 2008) yielded only upper limits. Table 2.3 lists all galaxy photometry.

PS1-10bzj is located in the ECDF-S and so photometry from a number of other surveys is also available. From the GEMS survey, there is *Hubble Space Telescope* (*HST*) imaging with the Advanced Camera for Surveys (ACS) in F606W and F850LP (Rix et al. 2004), and we retrieved the reduced images from the Mikulski Archive for Space Telescopes. From the GaBoDs survey (Taylor et al. 2009), there are detections in $U_{38}UBVRIz'$ (and non-detections in JHK). In addition, the MUSYC survey (Cardamone et al. 2010) provides imaging in 18 narrow-band filters. This field is also covered by the Spitzer Infrared Array Camera (IRAC) SIMPLE survey (Damen et al. 2011), but the galaxy is not detected in their catalog. Archival photometry of the host from the catalogs of these surveys is also included in Table 2.3.

Table 2.3. PS1-10bzj Host Galaxy Photometry

UT Date	Filter	AB Magnitude	Telescope/Instrument
	$g_{\rm P1}$	24.37 ± 0.13	PS1
	$r_{\rm P1}$	24.00 ± 0.12	PS1
	$i_{\rm P1}$	23.76 ± 0.10	PS1
	$z_{\rm P1}$	22.73 ± 0.05	PS1
	$y_{\rm P1}$	> 21.7	PS1
2011-11-29	g'	24.37 ± 0.08	Gemini-S/GMOS
2011-10-21	r'	23.86 ± 0.18	Magellan/LDSS3
2011-09-20	i'	23.12 ± 0.07	Gemini-S/GMOS
2012-07-19	z'	23.67 ± 0.15	Magellan/IMACS
2012-12-04	J	> 23.8	Magellan/FourStar
2011-12-07	K	> 22.7	Magellan/FourStar
	F606W	24.13 ± 0.05	HST/ACS[a]
	F850LP	23.63 ± 0.06	HST/ACS[a]
	$U38$	24.89 ± 0.08	ESO MPG 2.2m/WFI[b]
	U	24.86 ± 0.04	ESO MPG 2.2m/WFI[b]
	B	24.45 ± 0.02	ESO MPG 2.2m/WFI[b]
	V	24.44 ± 0.02	ESO MPG 2.2m/WFI[b]
	R	24.22 ± 0.02	ESO MPG 2.2m/WFI[b]
	I	23.23 ± 0.05	ESO MPG 2.2m/WFI[b]
	z'	23.39 ± 0.13	CTIO 4m/Mosaic-II[b]
	IA427	24.25 ± 0.07	Subaru/Suprime-Cam[c]
	IA445	24.49 ± 0.07	Subaru/Suprime-Cam[c]
	IA464	24.59 ± 0.14	Subaru/Suprime-Cam[c]
	IA484	24.45 ± 0.03	Subaru/Suprime-Cam[c]
	IA505	24.42 ± 0.06	Subaru/Suprime-Cam[c]
	IA527	24.53 ± 0.03	Subaru/Suprime-Cam[c]
	IA550	24.41 ± 0.05	Subaru/Suprime-Cam[c]
	IA574	24.42 ± 0.06	Subaru/Suprime-Cam[c]
	IA598	24.21 ± 0.02	Subaru/Suprime-Cam[c]
	IA624	23.84 ± 0.02	Subaru/Suprime-Cam[c]

Table 2.3—Continued

UT Date	Filter	AB Magnitude	Telescope/Instrument
	IA651	24.08 ± 0.02	Subaru/Suprime-Cam[c]
	IA679	24.59 ± 0.03	Subaru/Suprime-Cam[c]
	IA709	24.64 ± 0.12	Subaru/Suprime-Cam[c]
	IA738	24.58 ± 0.04	Subaru/Suprime-Cam[c]
	IA767	24.62 ± 0.10	Subaru/Suprime-Cam[c]
	IA797	23.78 ± 0.06	Subaru/Suprime-Cam[c]
	IA827	22.25 ± 0.03	Subaru/Suprime-Cam[c]
	IA856	24.68 ± 0.16	Subaru/Suprime-Cam[c]

[a]Data from GEMS survey catalog (Rix et al. 2004)

[b]Data from GaBoDs survey catalog (Taylor et al. 2009)

[c]Data from MUSYC survey catalog (Cardamone et al. 2010)

The various photometric measurements agree well in the bluer filters, but in the different i- and z-bands there is considerable discrepancy (e.g. the $i_{\rm P1}$measurement is ~ 0.6 mag fainter than the GMOS i-band, while the $z_{\rm P1}$measurement is ~ 0.9 mag brighter than the corresponding z filter). This is explained by the redshifted [O III] λ5007 emission line, located near the edge between i and z. The flux we measure in this line from the spectra (Section 2.4) is consistent with the differences in photometry. The effect of this line is also clearly seen in the narrow-band photometry in the IA827 filter.

2.3 Supernova Properties

2.3.1 Spectroscopic and Light Curve Comparisons

Given the redshift of $z = 0.650$, we find that PS1-10bzj reached a peak absolute magnitude of -21.17 ± 0.15 mag in $g_{\rm P1}$. This is luminous enough to be classified as "superluminous" according to the definition suggested in Gal-Yam (2012). Figure 2.2 shows our spectra of PS1-10bzj, compared to hydrogen-poor SLSNe PS1-10ky (Chomiuk et al. 2011) and SN 2010gx (Pastorello et al. 2010; Quimby et al. 2011b). Our first spectrum shows a blue continuum with broad UV features that are characteristic of the class of hydrogen-poor SLSNe (Quimby et al. 2011b; Chomiuk et al. 2011). These features are also visible in the blue GMOS spectrum taken 7 rest-frame days later. In the red GMOS spectrum on day 16, a number of broad, low amplitude features have also developed, similar to the features seen in SN 2010gx at late time. The combination of its luminosity and spectral features unambiguously establishes PS1-10bzj as another member of the class of 2005ap-like, hydrogen-poor SLSNe.

Figure 2.3 shows the light curve of PS1-10bzj in absolute magnitude versus rest frame phase compared to a few other hydrogen-poor SLSNe: PS1-10ky and PS1-10awh (Chomiuk et al. 2011), SN 2010gx (Pastorello et al. 2010; Quimby et al. 2011b) and PTF09cnd (Quimby et al. 2011b). We do not carry out detailed k-corrections due to the uncertainties in the spectral energy distributions (SEDs), but have picked bands at similar effective wavelengths as indicated on the plots to facilitate comparisons. With a fast rise time and slower decline, PS1-10bzj does not show the clearly symmetric light curve behavior seen in previous hydrogen-poor SLSNe (Quimby et al. 2011b), though we note that the rise time is less well constrained in the bluer bands due to shallower limits prior to detection. In general, the light curve of PS1-10bzj exhibits similar timescales to SN 2010gx and PS1-10ky, but has a flatter peak and is fainter overall.

2.3.2 Temperature Evolution and Bolometric Light Curve

We determine blackbody temperatures by fitting Planck functions to the broadband photometry, using a χ^2-minimization procedure. For the PS1 photometry, where different bands are observed on consecutive rather than the same night, we first interpolate the photometry to a common time by fitting a low-order polynomial to the nearby light curve points. The SED fits are shown in Figure 2.4, with the model temperatures and radii indicated. These numbers should be interpreted with some caution, as especially at later times the spectrum clearly deviates from that of a blackbody. In addition, by the time of the first spectrum the broad UV absorption features is clearly affecting the g-band flux, so that the temperature inferred from photometry is lower than that found by fitting to the spectrum.

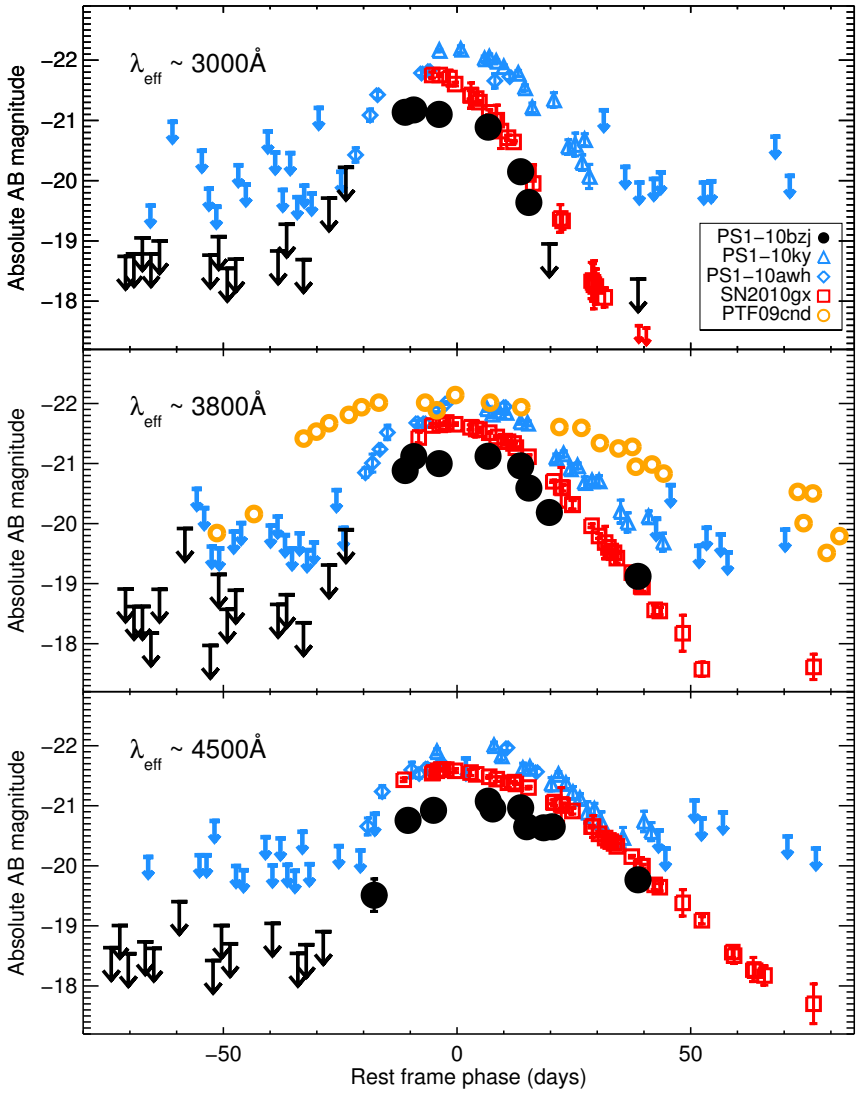

Figure 2.3.—: Absolute magnitude light curve of PS1-10bzj (solid black circles and black arrows) compared to other hydrogen-poor SLSNe at similar rest-frame wavelengths, showing $g_{\rm P1}$($\sim$ 3000 Å rest-frame, top), $r_{\rm P1}$($\sim$ 3800 Å rest-frame, middle), and $i_{\rm P1}$($\sim$ 4600 Å rest-frame, bottom). Blue diamonds and triangles show PS1-10awh and PS1-10ky $r_{\rm P1}$, $i_{\rm P1}$and $z_{\rm P1}$respectively (Chomiuk et al. 2011), red squares show SN 2010gx in u, g and r (Pastorello et al. 2010; Quimby et al. 2011b), and yellow open circles show PTF09cnd at $\sim$ 3600 Å (Quimby et al. 2011b).

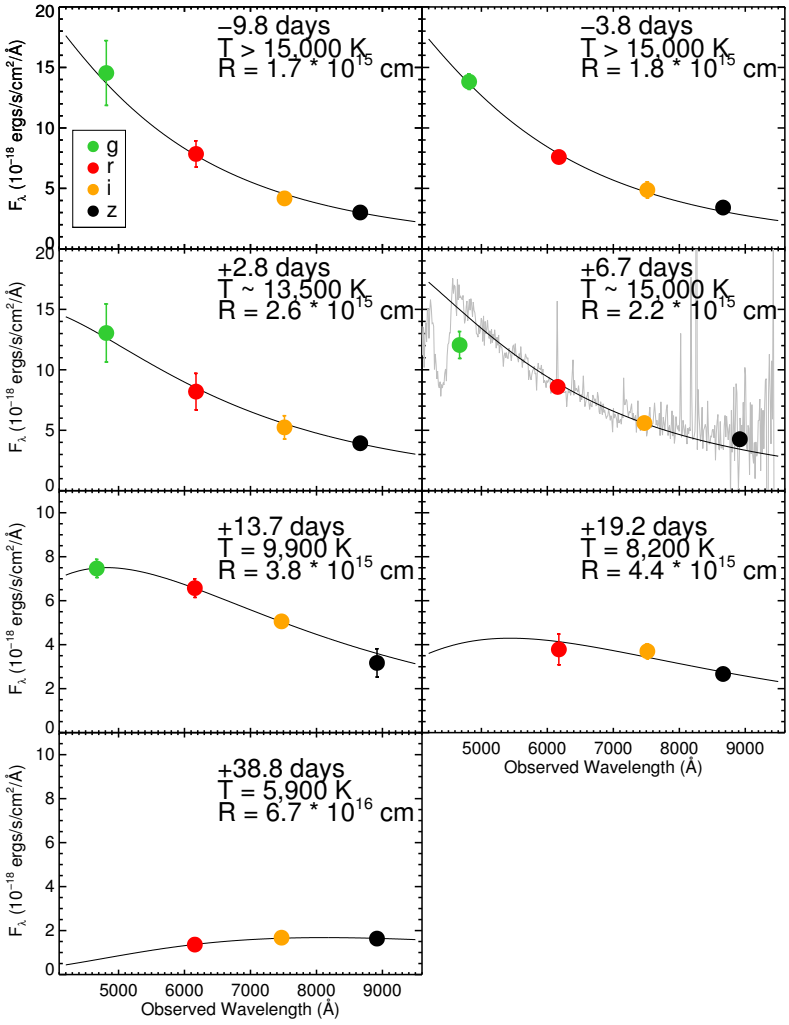

Figure 2.4.—: Spectral energy distribution fits to the photometry. The best-fit blackbody temperatures and radii are indicated in the individual panels. The concurrent spectrum is shown with the photometry in the fourth panel; we adopt the temperature derived from the spectrum rather than from the photometry for this date.

The resulting blackbody temperatures and radii from all the fits to the photometry is shown in the top two panels of Figure 2.5. Prior to peak, we can only place a lower limit on the temperature of $\sim 15,000$ K, since the peak of the blackbody curve is bluewards of the observed photometry and we are essentially fitting the Rayleigh-Jeans tail. After the peak, we find a clear decline in temperature and increase in radius. The best-fit straight line to the estimated blackbody radius (Figure 2.5) corresponds to an expansion velocity of $11,000 \pm 2000$ km s^{-1}, in good agreement with velocities derived from spectroscopic features (Section 2.3.3). We note that dividing the estimated radius at peak by the velocity gives a timescale of ~ 23 days, consistent with the observed photometric rise.

To construct a bolometric light curve, we first sum the observed flux by trapezoidal integration, interpolating to the edges of the observed bands. Since this only takes into account the flux in the observed wavelength range, it should be considered a strict lower limit of the total radiated power. Integrating this luminosity over the time period we observed the SN indicates a lower limit of the radiated energy $E_{\rm rad} \gtrsim (2.4 \pm 0.5) \times 10^{50}$ erg. The resulting light curve is shown as open red circles in the bottom panel of Figure 2.5.

To improve this estimate, following Chomiuk et al. (2011) we also include a blackbody tail redwards of the observed bands, using the temperatures determined by our blackbody fits. The resulting pseudo-bolometric light curve is shown as the black, filled circles the bottom panel of Figure 2.5. We also include the early $i_{\rm P1}$detection, assuming the same bolometric correction as the next light curve point. PS1-10bzj reached a peak bolometric magnitude $M_{\rm bol} = -21.4 \pm 0.2$ mag, and an estimated total radiated energy of $E_{\rm rad} \gtrsim (3.5 \pm 0.6) \times 10^{50}$ ergs. As expected from the light curve, this is significantly less luminous than previous events - for example, PS1-10awh and

PS1-10ky reached peak bolometric magnitudes of −22.2 mag and −22.5 mag respectively (Chomiuk et al. 2011). While the spectroscopic features clearly identify PS1-10bzj as a member of the same class of objects, it is one of the least luminous hydrogen-poor SLSNe discovered to date.

2.3.3 Line Identifications

We used the supernova spectrum synthesis code `SYNOW` to obtain line identifications and estimates of the expansion velocities, including manual and automated procedures employing the recently updated versions of the software `SYN++` in combination with `SYNAPPS`.[2] The basic assumptions of `SYNOW` include spherical symmetry, velocity proportional to radius, a sharp photosphere, line formation by resonant scattering treated in the Sobolev approximation, local thermodynamic equilibrium for the level populations, no continuum absorption, pure resonance scattering, and only thermal excitations. Fits are constrained by how we are able to best match absorption minimum profiles, as well as the relative strengths of all the features (see Branch et al. 2002 for more description of fitting parameters and Thomas et al. 2011 for software details).

The fit to the 2011 January 13 spectrum (phase +7 d) is shown in the left panel of Figure 2.6. The photospheric velocity is set at 13,000 km s^{-1}, and the temperature to 15,000 K. A maximum cut-off velocity of 40,000 km s^{-1} was used for all ions, with the minimum velocity set to 13,000 km s^{-1}. These parameters are comparable to the ions and associated velocities identified in other SLSNe (e.g., Quimby et al. 2011b; Chomiuk et al. 2011). Two strong features observed around 2440 and 2650 Å are fit reasonably

[2]Software was retrieved from https://c3.lbl.gov/es/

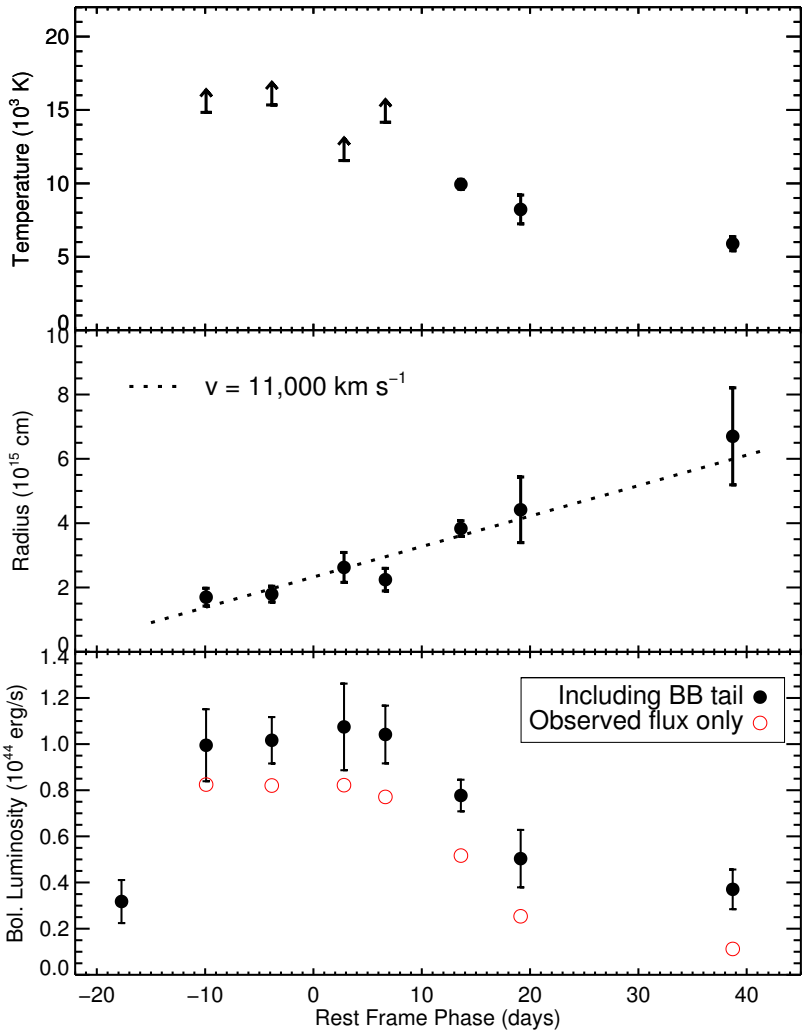

Figure 2.5.—: Top panel: temperature evolution of PS1-10bzj, as determined from fitting a blackbody curve to the observed photometry. The uncertainty at early times is largely due to the peak of the blackbody being blueward of our bluest bands; see Figure 2.4. Middle panel: radius of PS1-10bzj, as measured from the same blackbody fit to photometry as the temperature. The best-fit straight line (dashed) corresponds to an expansion velocity of $11,000 \pm 2000$ km s^{-1}. Bottom panel: estimated bolometric light curve of PS1-10bzj. The open red circles show observed flux only, while the black filled circles include the observed flux plus a blackbody tail in the red.

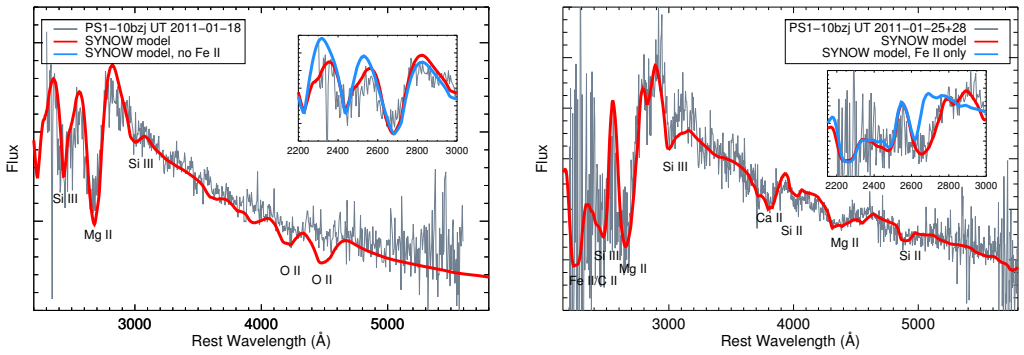

Figure 2.6.—: SYNOW fits to the spectra of PS1-10bzj. Left: the 2011 January 13 (phase +7 d) spectrum. The strong UV features are well fit with Si III and Mg II; minor features near 4500Å could be due to O II. The shape of the Si III feature is better fit when including Fe II, as illustrated in the inset, which shows the fit without including this ion. Right: fit to combined 2011 January 25+28 (phase +15 d) spectrum. Minor features in the optical are fit with Ca II, Mg II and Si II. The fit includes a substantial contribution from Fe II (shown in the inset), but the overlap of these features with the Mg and Si features and lack of features elsewhere prevent us from determining the relative strengths accurately.

well with Si III and Mg II, respectively. Introduction of Fe II improves the fit around the Si III line, as seen in the inset. Without Fe II, the red wing of the absorption could not be fit with Si III alone.

Additional weaker features with less certain identifications are also seen. A sharp cut-off around 3000 Å is likely attributable in part to Si III, and we fit absorption features around 4230 and 4490 with O II. We include in the synthetic spectrum C II, which is cut off to the blue of Si III, but is seen in the other SLSNe and in the later spectrum of this object.

The 2011 January 25 and 28 spectra were combined to fit a single phase +15 d spectrum, shown in the right panel of Figure 2.6. The photospheric velocity is set at 11,000 km s^{-1} and the temperature to 11,500 K. The maximum cut-off velocity was once again set to 40,000 km s^{-1} for all ions, which were fitted with minimum velocities

ranging between 11,000 and 15,000 km s^{-1}. We observe the same absorption features associated with Si III, Mg II, and C II. Again, including Fe II substantially improves the fit in this region; the contribution from Fe II only to the fit is shown in the inset. However, the lack of additional lines elsewhere in the spectrum at this temperature, as well as the noise at the bluest wavelengths, prevent determining the relative strengths accurately. Additional weaker features are fit with Ca II and Si II. The O II seen in the earlier spectrum no longer appears to be a conspicuous contributor to the spectrum.

Two other SLSNe have shown significant spectral evolution post-peak: in both SN 2010gx and PTF09cnd (Pastorello et al. 2010; Quimby et al. 2011b), the spectra evolved to look like normal Type Ic SNe at late times. The connection between H-poor SLSNe and SNe Ibc is also suggested by a transient "W"-shaped feature near 4200 AA seen in early spectra of the well-observed Type Ib SN 2008D, identified as the same feature as seen in SN 2005ap (Modjaz et al. 2009; Quimby et al. 2007). Following Quimby et al. (2007), Modjaz et al. (2009) modeled this feature with a blend of O III, N III and C III; later modeling by Quimby et al. (2011b) of SN 2005ap and other H-poor SLSNe updated the identification of the "W"-feature to O II. The presence of this transient feature in SN 2008D thus provides an additional link between Type Ibc SNe and SLSNe. A basic question is whether the SLSNe are truly distinct objects from normal Type Ic SNe, or whether there is a smooth continuum between the two. With its comparatively low peak luminosity, PS1-10bzj is closer in luminosity to luminous Type Ic SNe like SN 2010ay, which peaked at $M_r = -20.2$ (Sanders et al. 2012b), than to the prototype SLSNe 2005ap and SCP 06F6. From this perspective, it is interesting to note that at least over the time we were following it, the spectral features in PS1-10bzj do not look like SN Ic features, including objects like SN 2010ay.

2.3.4 Light Curve Model Fits

The optical luminosity of most canonical Type I SNe (i.e. type Ia, Ib and Ic) is powered by the radioactive decay of ^{56}Ni, with the shape of the light curve primarily dictated by three parameters: the nickel mass ($M_{\rm Ni}$) which sets the total luminosity, the total kinetic energy ($E_{\rm K}$), and ejecta mass $M_{\rm ej}$, which set the characteristic time of photon diffusion $\tau_c \propto M_{\rm ej}^{3/4} E_{\rm K}^{-1/4}$ and essentially determines the width of the light curve (Arnett 1982). Measurements of the photospheric velocity ($v_{\rm ph}$) from the spectra constrain $\sqrt{E_{\rm K}/M_{\rm ej}}$, so that all three parameters can be determined based on observable quantities. We fit our bolometric light curve of PS1-10bzj using the models of Valenti et al. (2008) and Drout et al. (2011); see Figure 2.7. The light curve can be reasonably fit with $M_{\rm Ni} \simeq 6 - 8$ M$_\odot$, with the best-fit model having $M_{\rm Ni} = 7.2$ M$_\odot$ and $\tau_c \simeq 19$ d. Using the photospheric velocity derived from the spectrum near peak, $v_{\rm ph} = 13,000$ km s^{-1}, yields $M_{\rm ej} \sim 5 - 11$ M$_\odot$, with 8.5 M$_\odot$ for the best-fit model. Therefore, if PS1-10bzj were powered by radioactive decay, it would require a ^{56}Ni mass of $\gtrsim 10$ times what is observed in typical Type Ibc or Ic-BL SNe ($0.2 - 0.5$ M$_\odot$; Drout et al. 2011). In addition, the ejecta would have to be $75 - 100\%$ ^{56}Ni by mass, a fraction seen in no observed SNe, including proposed pair-instability SNe like SN 2007bi where the inferred Ni mass was several M$_\odot$ (Gal-Yam et al. 2009). A composition of $> 75\%$ Ni would also result in a large amount of line-blanketing in the rest-frame UV, which is not seen. Radioactive decay, then, is unlikely to be the main contributor to the luminosity. This is consistent with what is found for other hydrogen-poor SLSNe (Chomiuk et al. 2011; Quimby et al. 2011b).

Since nickel decay is unlikely, other explanations have been proposed for the extreme

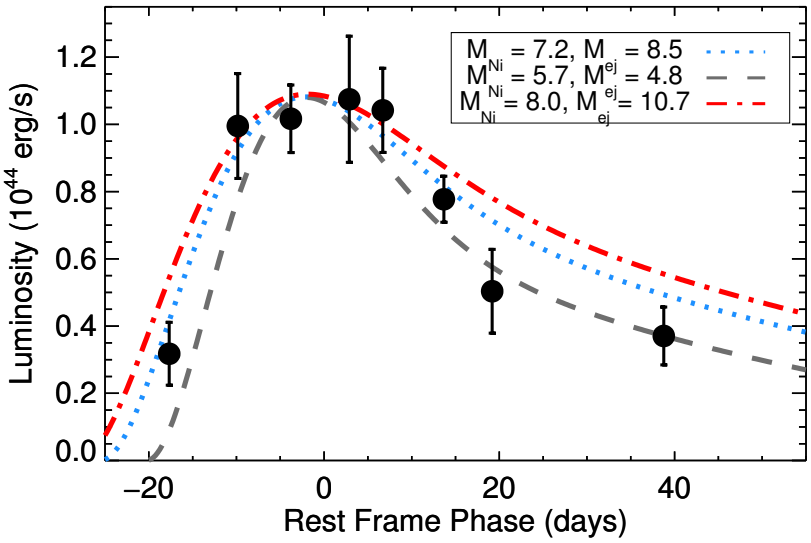

Figure 2.7.—: Model of radioactive Nickel decay, following Drout et al. (2011). The light curve can be reasonably fit with Ni masses in the range $6 - 8$ $M_\odot$, but require the ejecta composition to be $75 - 100\%$ Ni to simultaneously fit the peak luminosity and the light curve width.

luminosity of SLSNe. One possibility is energy injection by a central engine, such as the spin-down of a newborn magnetar (Kasen & Bildsten 2010; Woosley 2010). We fit our bolometric light curve with the model of Kasen & Bildsten (2010), following the procedure outlined in Chomiuk et al. (2011). Our assumptions include magnetic dipole spin-down, an opacity of $\kappa = 0.2$ cm^2 g^{-1}, and a supernova energy of 10^{51} erg; we vary the ejecta mass, the magnetar spin (p), and the magnetic field (B). With these assumptions, Figure 2.8 shows a best-fit model, with $M_{\rm ej} = 2$ M$_\odot$, $B = 3.5 \times 10^{14}$ G, and $p = 4$ ms; however we find that the light curve can be reasonably fit within the uncertainties with ejecta masses in the range $M_{\rm ej} \sim 1 - 6$ M$_\odot$. An ejecta mass lower than 1 M$_\odot$ predicts a light curve that is too narrow, while ejecta masses greater than ~ 6 M$_\odot$ require initial spins faster than the maximum (breakup) spin of ~ 1 ms to match the timescales. Within this range, however, parameters can be chosen to fit the light curve equally well within the uncertainties. We note that the inferred ejecta masses are similar to what is seen in normal Type Ibc SNe (Drout et al. 2011).

The magnetar model predicts that the ejecta will be swept up into a dense shell, which then expands at a constant velocity. For the range of models that fit the light curve, those with higher spin periods (and so a lower total energy, as the magnetar contribution scales as p^{-2}) generally have lower inferred velocities, in better agreement with the velocities inferred by the spectra. The 2 M$_\odot$ model shown in Figure 2.8 has the swept-up shell expanding at 11,000 km s^{-1}, in good agreement with the observed velocities. The predicted temperatures for this model also match the observed temperatures within the errors. A simple magnetar model thus provides a reasonable fit to the observed properties of PS1-10bzj. One caveat is that our modeling of the spectra support a slightly declining, rather than constant photospheric velocity. The rapid

evolution of the spectrum is also challenging to explain in the context of this model.

A third proposed mechanism for powering SLSNe is interaction with opaque, circumstellar material. This leads to efficient conversion of the kinetic energy to radiation, with the resulting lightcurve being due to shock breakout through this opaque wind. This class of models has been applied both to superluminous SNe IIn such as SN 2006gy, and to SN 2005ap-like objects (Smith & McCray 2007; Smith et al. 2010; Chevalier & Irwin 2011; Balberg & Loeb 2011; Ginzburg & Balberg 2012; Chatzopoulos et al. 2012). The light curve of the hydrogen-poor and superluminous SN 2006oz, in particular, showed a "dip" feature on the rise that has been interpreted as a signature of shock breakout (Leloudas et al. 2012; Moriya & Maeda 2012).

We can use the observed properties of PS1-10bzj and the analytical relations of Chevalier & Irwin (2011) to estimate the physical conditions required in the interaction scenario. Assuming a wind density profile $\rho_w = Dr^{-2}$, as expected from a steady wind, so that $D = \dot{M}/4\pi v_w \equiv 5 \times 10^{16} D_*$ in cgs units. The rise-time can be roughly equated to the diffusion time, $t_d = 6.6\kappa D_*$ d, where κ is the opacity in units of 0.34 cm^2 g^{-1}. We use $\kappa = 0.59$, as expected for an ionized He-rich wind. Taking the rise-time of PS1-10bzj to be $\sim$ 20 days, we find that $D_* \simeq 5.1$, which gives a total required wind mass of ~ 3.5 M$_\odot$, using the radius at peak to be $\sim 2.2 \times 10^{15}$ cm. Using $E_{\rm rad} \approx 3.5 \times 10^{50}$ erg, we find that the associated supernova energy is $2.2 \times 10^{51} (M_{\rm ej}/10{\rm M}_\odot)^{1/2}$ erg , and corresponding diffusion radius $R_d \approx 1 \times 10^{15}$ cm, assuming an ejecta mass of 10 M$_\odot$ and using Equations (5) and (3) in Chevalier & Irwin (2011) respectively. The predicted velocity of the photosphere, using Equation 3 in Chomiuk et al. (2011), is 11,800 km s^{-1}, in good agreement with the observed velocities. Thus, this model can also reproduce the basic observed properties, but require a wind mass of several M$_\odot$ of hydrogen-poor

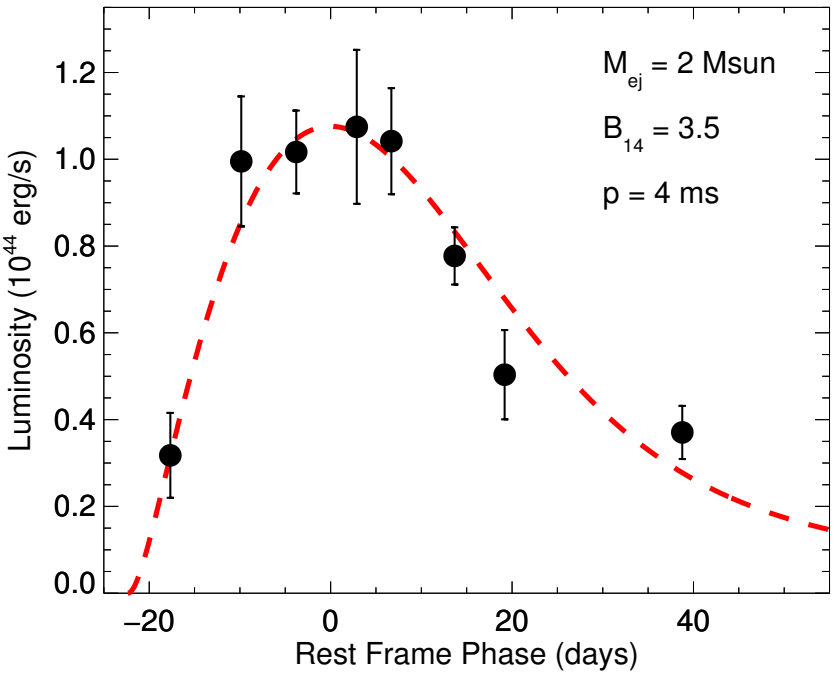

Figure 2.8.—: Magnetar model fit to the bolometric light curve, with $M_{\rm ej} = 2$ M$_\odot$, $B = 3.5 \times 10^{14}$ G, and $p = 4$ ms. While the observed light curve can be fit with a range of parameters within the uncertainties, the model shown also predicts a velocity and temperature evolution that agrees with the observed data.

material.

Recently, Ginzburg & Balberg (2012) have shown that the simple treatment in Chevalier & Irwin (2011) is not appropriate in regimes where the wind radius is comparable to the diffusion radius. Instead, they carried out hydrodynamical simulations of supernovae exploding into dense circumstellar material, successfully matching the light curves of SN 2005ap, SN 2006gy and SN 2010gx. Given the similarities between PS1-10bzj and SN 2010gx, it seems plausible that its light curve could also be fit by a more sophisticated shock breakout model, though calculating such a model is outside the scope of this paper. We note that the Ginzburg & Balberg (2012) model for SN 2010gx requires an even larger total wind mass ($M_w \simeq 16$ M$_\odot$) than our estimate for PS1-10bzj based on the simple Chevalier & Irwin (2011) relations, so an extreme mass loss episode would likely still be required.

A simple interaction model, then, can also explain the observed data, but requires a mass-loss rate of ~ 3 M$_\odot$ yr^{-1} in the last year before explosion, assuming a wind velocity of 1,000 km s^{-1}(as seen in Wolf-Rayet stars; e.g. Nugis & Lamers 2000). In addition, the lack of hydrogen and helium seen in the spectra would require this circumstellar material to be primarily composed of intermediate-mass elements. One might also expect to see intermediate-width lines in the spectra if the primary energy source is interaction, but this has not been seen in any of the H-poor SLSNe, including PS1-10bzj. A detailed radiative transfer model is necessary to see if this scenario can reproduce the spectra as well as the light curves.

2.4 Host Galaxy Properties

In addition to studying the SN explosion itself, additional clues to the nature of the progenitors come from studying the host environments of the SLSNe. In the case of PS1-10bzj there is a wealth of data on the host galaxy, allowing for a detailed study.

2.4.1 Luminosity and Size

The absolute magnitude of the host is $M_B = -18.0$ mag, corrected for cosmological expansion and foreground extinction. This is similar to what has been seen for other SLSN hosts, which seem to show a preference for low-luminosity galaxies (Neill et al. 2011; Chen et al. 2013). In terms of the luminosity function at $z \sim 0.7$ (Ilbert et al. 2005; Willmer et al. 2006), this corresponds to a $0.05L_*$ galaxy.

The host galaxy of PS1-10bzj is unresolved in all our ground-based images (with seeing down to $\sim 0.6''$). Since the field was covered by the GEMS survey, we also have available *HST*/ACS images in F606W and F850LP (Rix et al. 2004), shown in Figure 2.9. Even in these images, the host is not obviously resolved with a FWHM of $\sim 0.12''$ (whereas the mean FWHM of stars in the images is $\sim 0.10''$).At $z = 0.650$, this corresponds to an upper limit on the galaxy diameter of $\lesssim 800$ pc. We note that it is possible that what we see in the *HST* images is only one bright knot of star formation, and the galaxy itself could be more extended. Nevertheless, the combination of luminosity and size establishes the host as a compact dwarf galaxy.

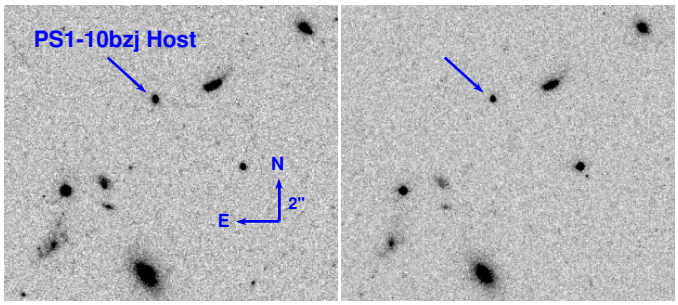

Figure 2.9.—: *HST*/ACS images of the field around PS1-10bzj, in filters F606W (left) and F850lp (right). The host, marked with the blue arrow, is remarkably compact.

2.4.2 Stellar Mass and Population Age

To determine the stellar mass (M_*) and population age (τ_*) of the host we fit the SED with the Maraston (2005) evolutionary stellar population synthesis models, using a Salpeter initial mass function and a red horizontal branch morphology. Since the model only accounts for the continuum emission, and the flux in the host emission lines is substantial, we restrict our fit to the MUSYC narrow-band filters without significant emission lines. The fit to the SED is shown in Figure 2.10. We find that the host SED is well fit with a stellar population age of $\tau_* \approx 5$ Myr, yielding a stellar mass of $M_* \approx 2.4 \times 10^7$ M$_\odot$. This assumes $A_V = 0$, measured from the Balmer decrement (Section 2.4.3).

Another estimate of the stellar population age comes from the Hβ equivalent width (EW). While we do not have a galaxy-only spectrum, the 2011 April 3 Gemini spectrum (Figure 2.11) does not show any broad supernova features and is dominated by galaxy light ($\gtrsim 50\%$; estimated from pre-explosion galaxy photometry). It can therefore be used to determine a lower limit on the Hβ EW, which we find to be $W_r \approx 61$ Å. This value yields a young stellar population age of $\lesssim 5$ Myr for a metallicity $Z = 0.2 - 0.4$ Z$_\odot$, using

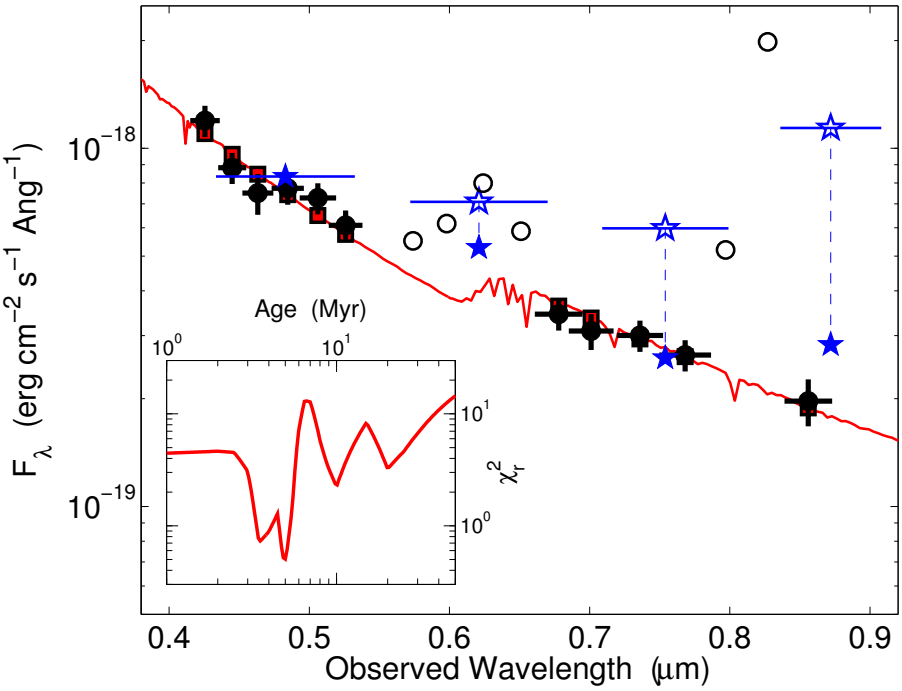

Figure 2.10.—: Best-fit spectral energy distribution models to the host galaxy photometry, using $A_V = 0$ mag. Only the narrow-band photometry is used in the fit (filled circles), due to the strong emission lines contaminating the broadband filters. Open circles show narrow-band filters which contain emission lines and are therefore not used for the fit. For comparison, the stars show PS1 broad-band photometry, both uncorrected (open) and corrected (filled) for the flux in the emission lines. Additional broad-band filters are largely redundant with the PS1 ones and are not shown. Our best-fit is a young ($\tau_* \approx 5$ Myr) and low-mass ($M_* \approx 2.4 \times 10^7$ M$_\odot$) stellar population; an acceptable fit also exist for a 3.5 Myr population, and slightly worse fits for a 10 or 20 Myr population, as shown in the inset.

the fits in Levesque et al. (2010a) to the models of Schaerer & Vacca (1998). This value is in excellent agreement with the stellar population age inferred from SED modeling.

2.4.3 Metallicity

While all of our spectra include contributions from both the galaxy and the SN, they clearly exhibit narrow emission lines originating in the host galaxy. Figure 2.11 shows the 2011 April 3 GMOS spectrum, which is dominated by galaxy light, with the strongest emission lines marked. We measure the line fluxes in all of our spectra by fitting Gaussian profiles (Table 2.4). With the exception of the [O III] λ4363 line, which was only robustly detected in the 2011 January 28 GMOS spectrum, we use the weighted average of the three measurements for line diagnostics. Absolute flux calibration is based on the 2011 January 13 LDSS3 spectrum, by scaling synthetic photometry from the spectrum to photometry obtained the same night. The GMOS spectra were then scaled according to the flux in the [O III] doublet.

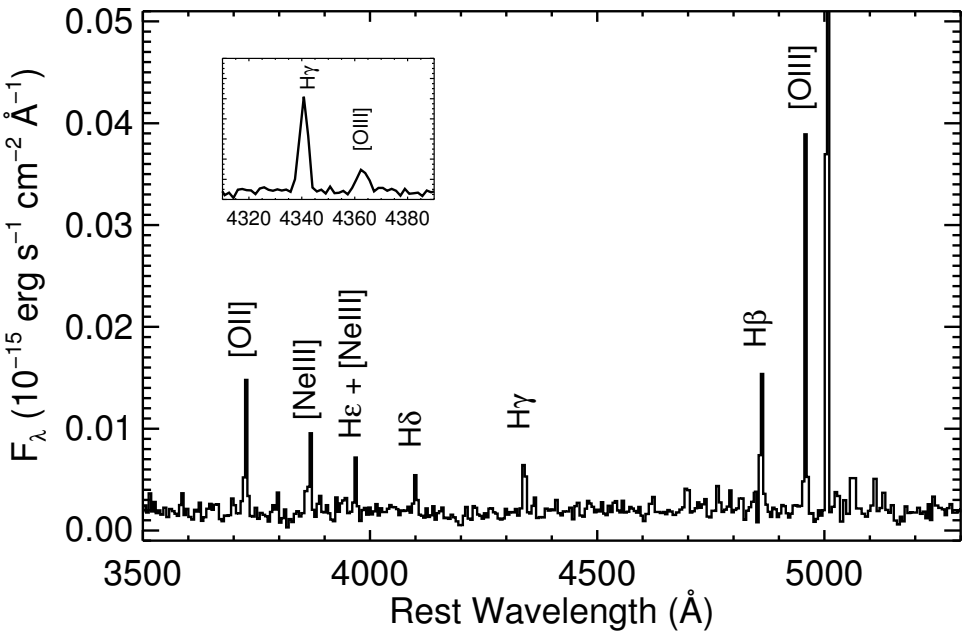

Figure 2.11.—: 2011 April 3 GMOS spectrum of PS1-10bzj, with strong host galaxy emission lines marked. While there is some supernova contribution to the flux in this spectrum, it is dominated by host galaxy light ($\gtrsim 50\%$). The inset shows the region around the auroral [O III] λ4363 line, from the 2011 Jan 28 spectrum, which has somewhat better signal-to-noise ratio.

Table 2.4. Host Galaxy Emission Line Fluxes

Line	Flux (10^{-16} erg s^{-1} cm^{-2})		
	Jan 13	Jan 28	Apr 3
[O III]λ5007	6.43 ± 0.18	6.36 ± 0.07	6.20 ± 0.08
[O III]λ4959	1.89 ± 0.14	2.04 ± 0.05	2.32 ± 0.06
Hβ	1.05 ± 0.16	1.04 ± 0.05	0.94 ± 0.08
[O III]λ4363	···	0.14 ± 0.04	···
Hγ	0.47 ± 0.07	0.53 ± 0.04	0.43 ± 0.05
Hδ	0.20 ± 0.06	0.22 ± 0.04	0.24 ± 0.04
Hϵ + [Ne III]λ3968	0.28 ± 0.08	0.27 ± 0.05	0.28 ± 0.06
Hζ	···	0.19 ± 0.05	···
[Ne III]λ3869	0.48 ± 0.08	0.37 ± 0.04	0.58 ± 0.06
[O II]λ3727	0.97 ± 0.09	0.83 ± 0.06	1.07 ± 0.08

None of our spectra cover Hα, which is located at 1.083 μm at this redshift. We therefore use the Balmer decrement as measured from Hγ/Hβ to estimate reddening, assuming a Case B recombination value of 0.469 (Osterbrock 1989). Since our measured value of 0.48 ± 0.03 is consistent with no reddening, we conclude that the host galaxy extinction is minimal.

We detect the auroral [O III] λ4363 line in the 2011 January 28 GMOS spectrum at 3.5σ significance, shown in the inset of Figure 2.11. Assuming an electron density $n_e = 100$ cm^{-3}, we calculate an electron temperature of $T_e(O^{++}) = 16,200^{+2,900}_{-1,700}$ K from the ratio of [O III] λ4363 to [O III] $\lambda\lambda 5007, 4959$, using the IRAF task `temden`. This result is not sensitive to the exact choice of density since T_e is insensitive to small changes in density (Kewley et al. 2007); for example, we find identical results when doubling the assumed electron density to 200 cm^{-3}. Using the relation $T_e(O^+) = 0.7 \times T_e(O^{++}) + 0.3$ from Stasińska (1982), we determine O^+/H and O^{++}/H using the relations in Shi et al. (2006). This gives an electron temperature metallicity of $12 + \log(\mathrm{O/H}) = 7.8 \pm 0.2$. This translates to $Z = 0.13 Z_\odot$, using the solar abundance of Asplund et al. (2009). This low abundance is consistent with the inferred young stellar population age and low stellar mass.

For comparison, we also estimate the oxygen abundance using the R_{23} diagnostic with the calibration of Kobulnicky & Kewley (2004). We measure $R_{23} \equiv ([\mathrm{O\ III}]\lambda\lambda 5007, 4959 + [\mathrm{O\ II}]\lambda 3727)/\mathrm{H}\beta = 9.25 \pm 0.36$, and an ionization parameter of $y \equiv \log([\mathrm{O\ III}]\lambda\lambda 5007, 4959/[\mathrm{O\ II}]\lambda 3727) = 0.95 \pm 0.03$. Using the iterative scheme in Kobulnicky & Kewley (2004), and assuming the lower metallicity branch based on the presence of the [O III] λ4363 line, this method gives a metallicity $12 + \log(\mathrm{O/H}) \approx 8.3$. This is 0.5 dex higher than the result from the direct method, but we note that this

discrepancy is not unusual; theoretical strong-line indicators are known to be offset from the direct method, with the difference being larger at the lower-metallicity end (Bresolin et al. 2009). A similar discrepancy is seen in the host galaxy of SN 2010gx, where Stoll et al. (2011) found $12 + \log(\mathrm{O/H}) = 8.36$ using the Kobulnicky & Kewley (2004) calibration, while the direct method yields $12 + \log(\mathrm{O/H}) = 7.46$ (Chen et al. 2013). Still, strong-line metallicity indicators provide a useful basis for comparison, since direct metallicity indicators are otherwise mostly only available for low-redshift samples.

2.4.4 Star Formation Rate

We estimate the SFR of the host galaxy from the [O II] λ3727 line flux, using the metallicity-dependent relation in Kewley et al. (2004). Using the metallicity and ionization parameter we determined from the R_{23} method, we find SFR ≈ 2 $\mathrm{M_\odot\ yr^{-1}}$. Alternatively, since the Hγ/Hβ ratio indicates no extinction, we can use the Hβ flux to predict the Hα flux, assuming a ratio Hα/H$\beta = 2.85$ according to case B recombination. Using SFR $= 7.9 \times 10^{-42} L_{\mathrm{H}\alpha}(\mathrm{erg\ s^{-1}})$ (Kennicutt 1998), we find SFR ≈ 4.2 $\mathrm{M_\odot\ yr^{-1}}$, in reasonable agreement with the [O II] λ3727 estimate.

A complementary method to calculating the SFR is to use the galaxy UV continuum flux. At this redshift, the UBg filters sample rest-frame $2300 - 2900$ Å, allowing us to use the relation from Kennicutt (1998): SFR $= 1.4 \times 10^{-28} L_\nu$. This yields SFR $\approx 2 - 3$ $\mathrm{M_\odot\ yr^{-1}}$, also in good agreement with the estimates from emission lines.

Combining the stellar mass with the SFR, we calculate a specific star formation rate (sSFR) of ~ 100 $\mathrm{Gyr^{-1}}$. This is significantly higher than the ~ 2.6 $\mathrm{Gyr^{-1}}$ measured in the host of SN 2010gx (Chen et al. 2013), and also higher than the ~ 10 $\mathrm{Gyr^{-1}}$ in the

host of PS1-10bam (Berger et al. 2012). The basic picture of a low metallicity, low mass and highly star-forming dwarf galaxy is similar to what has been seen for other SLSNe.

2.5 Discussion

2.5.1 The Diversity of SLSNe

As was shown by Quimby et al. (2011b), the hydrogen-poor SLSNe form a spectroscopic class, though with a range of light curve properties. Figure 2.12 shows the distribution of peak absolute magnitudes of all published 2005ap-like hydrogen-poor SLSNe, corrected for cosmological expansion by $M = m - 5\log\left(d_L(z)/10\mathrm{pc}\right) + 2.5\log(1+z)$. Due to the lack of SED information in several objects, we do not carry out full k-corrections, but note that where multiband photometry is available the observed peak is at a rest-frame wavelength of $\sim 3000 - 4000$Å. SN 2006oz is not included in this plot, as it was only observed on the rise and so the peak magnitude is not well constrained. Most of the hydrogen-poor SLSNe peak near $M \simeq -22$ mag, with a tail to higher luminosities. The apparent lack of lower-luminosity objects is likely due, at least in part, to the flux-limited surveys (and spectroscopic follow-up) so that there is a bias toward finding brighter objects. PS1-10bzj is both the lowest-luminosity and one of the lowest redshift SLSNe found in PS1/MDS, for example. Recently, Quimby et al. (2013a) found that the distribution of hydrogen-poor SLSNe seems to be narrowly peaked, also when taking the effects of flux-limited selection into account. If so, an event like PS1-10bzj would be intrinsically rarer than the -22 mag objects, at the low-luminosity tail of the distribution.

The timescales seen in SLSNe also vary by a factor of several, with rise times varying from ~ 20 d in the case of PS1-10bzj, to $\gtrsim 50$ d in PTF09cnd (Quimby et al. 2011b). If the faster timescales are typical for the lower-luminosity end of the distribution, it may present an additional selection bias against the fainter objects, as the timescales are approaching those of normal SNe and so the objects stand out less amongst the more common normal SNe.

Finding fainter hydrogen-poor SLSNe is particularly interesting because this class is linked to Type Ic SNe through the late time spectroscopic evolution of a few objects. A basic question is whether they are truly distinct populations, or whether there is a smooth transition between the two. There is a luminous tail to the Type Ic distribution: for example SN 2010ay reached a peak luminosity of -20.2 mag, though still had a light curve consistent with being powered by nickel decay and did not show the spectroscopic features typical of SLSNe (Sanders et al. 2012b). If the dearth of intermediate-luminosity objects represents a real cutoff rather than a selection effect, this places constraints on any proposed mechanism for powering the SLSNe. Such a low-luminosity cutoff is not predicted by theoretical models of SLSNe; for example the magnetar models presented in Kasen & Bildsten (2010) can reproduce a wide range of luminosities and timescales.

We also note that PS1-10bzj only has a few, early light curve points that are brighter than -21 mag, but is clearly a spectroscopic member of the class of 2005ap-like hydrogen-poor SLSNe. This suggests that a definition based on a luminosity cut, as was suggested in Gal-Yam (2012), is artificial and that this class of objects is better defined by spectroscopic features.

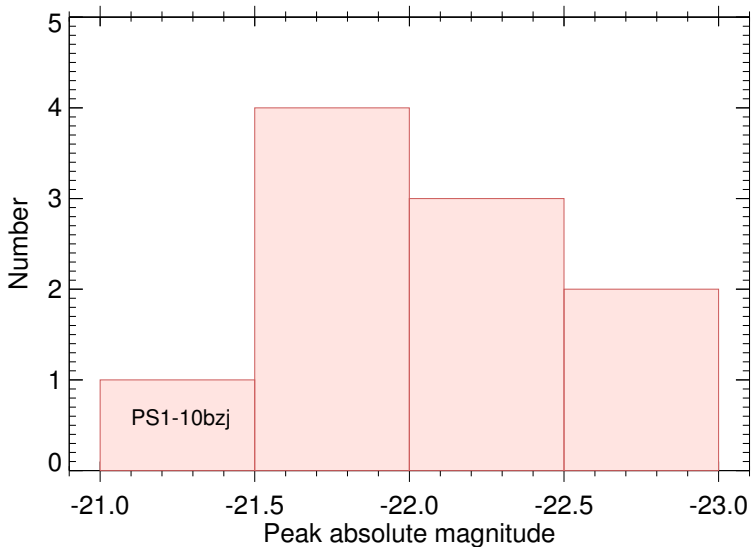

Figure 2.12.—: Distribution of peak observed absolute magnitudes for the hydrogen-poor SLSNe published to date. SN 2006oz is not included, as it was only observed on the rise and so only a lower limit < -21.5 mag is available.

2.5.2 The Host Galaxy Environments

Of the 10 2005ap-like hydrogen-poor SLSNe published prior to this work, only five have detected host galaxies and the upper limits on the undetected ones are $M_r \gtrsim -18$ mag (Neill et al. 2011). It has been speculated that this preference for low-luminosity environments is really a preference (and perhaps requirement) for low-metallicity environments (Neill et al. 2011; Stoll et al. 2011). This is supported by the host of SN 2010gx, the first SLSN host galaxy with a direct metallicity measurement, with $Z = 0.06 Z_{\odot}$ (Chen et al. 2013)). The low metallicity of 0.13 $Z_{\odot}$ for the host of PS1-10bzj follows the same trend.

To put these galaxy measurements in context, in Figure 2.13 we plot different properties of the two SLSN host galaxies, compared to other galaxy samples. The top

left panel shows a mass-metallicity ($M - Z$) plot, with metallicity measured by the R_{23} method from Kobulnicky & Kewley (2004) to facilitate comparison to different samples, including core-collapse SNe (Kelly & Kirshner 2012) and GRB host galaxies (Levesque et al. 2010b; Leibler & Berger 2010; Modjaz et al. 2008). We plot here also the host of the superluminous SN 2007bi, with R_{23} metallicity from Young et al. (2010), and mass we estimated from the SDSS photometry of this host. It is worth noting that all three SLSN hosts have very similar R_{23} metallicities. They are all less massive and more metal-poor than the core-collapse SN hosts, but occupy a similar region as the gamma-ray burst (GRB) host galaxies. One important caveat here is that the core-collapse SN hosts are generally at low redshift and contain a mix of hosts from targeted and untargeted surveys, so we would not necessarily expect them to follow the same $M - Z$ relation.

The remaining three panels plot metallicity as measured by the T_e method, against either luminosity, mass, or the combination of mass and SFR that minimizes scatter in metallicity (the so-called Fundamental Relation or FMR; Mannucci et al. 2010; Andrews & Martini 2013). The host of PS1-10bzj is consistent with each of the nearby relations within its uncertainties, indicating that it is not an unusually metal-poor galaxy given its mass, luminosity and SFR. The similarity to GRB hosts may indicate that the two phenomena happen in similar environments, but the sample sizes here are small. The host of SN 2010gx stands out as more extreme than the host of PS1-10bzj in terms of metallicity, and falls below the nearby/SDSS relations in each case. The two SLSN hosts are the most separated on the FMR plot, due to the larger sSFR of the PS1-10bzj host. As such, the most striking common factor between the two galaxies is their low metallicities.

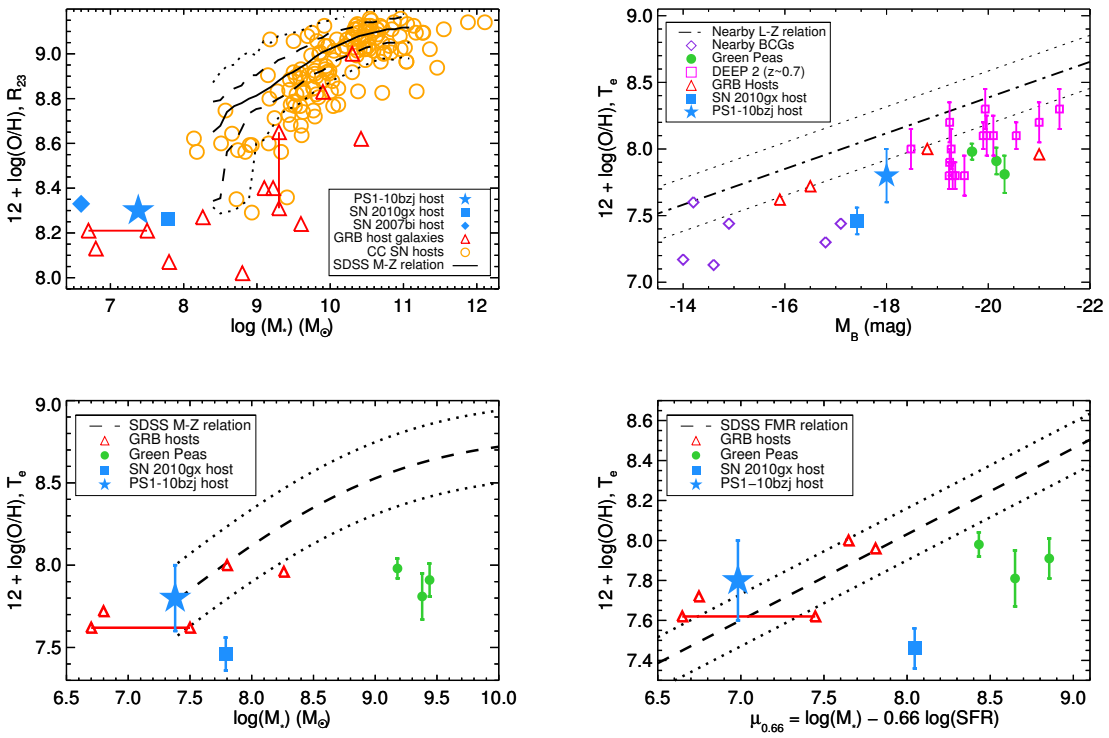

Figure 2.13.—: A comparison of the host of PS1-10bzj to other SLSNe and galaxy samples. The blue star and square show the hosts of PS1-10bzj and SN 2010gx, respectively. The top left panel is a mass-metallicity ($M - Z$) diagram, here plotting metallicity as calculated by the R_{23} method in Kobulnicky & Kewley (2004), to facilitate comparison to a broader sample. The black lines show the SDSS $M - Z$ relation Tremonti et al. (2004), where metallicity has been converted to the KK04 scale using the relations in Kewley & Ellison (2008). The orange circles show hosts of core-collapse supernova (any type), with metallicities similarly converted from the Tremonti et al. (2004) scale. Red triangles show GRB hosts; connected points indicate a dual solution for either the mass or the metallicity. The other three plots show metallicity measured by the direct method, comparing to either the nearby luminosity-metallicity relation (Guseva et al. 2009; top right) the SDSS $M - Z$ relation as measured by the direct method on spectra stacked by mass (Andrews & Martini 2013; bottom left), or the SDSS "fundamental relation", plotting metallicity against a combination of stellar mass and SFR that minimizes scatter (Andrews & Martini 2013; bottom right). Additional samples shown are DEEP2 star-forming galaxies (Hoyos et al. 2005), nearby blue compact galaxies (BCGs; Kewley et al. 2007) and "Green Pea" galaxies (Amorín et al. 2012). The host of PS1-10bzj is consistent with nearby relations in each case, and similar to the GRB host galaxies with direct metallicity measurements.

We note that if low metallicity is an important factor in producing this type of SLSN, this may present a challenge for models where the luminosity of the SN is powered by interaction with a dense wind. In particular, the mass loss would be unlikely to be driven by metal-line winds and so a different mass-loss mechanism would be required.

2.6 Conclusions

We show that PS1-10bzj is a hydrogen-poor superluminous supernova, spectroscopically similar to the objects described in Quimby et al. (2011b) and Chomiuk et al. (2011). Compared to previous events, it has the fastest rise time and lowest peak luminosity. From our reconstructed bolometric lightcurve, we estimate the total energy radiated over the time period observed to be $\sim 3.5 \times 10^{50}$erg, and the bolometric magnitude at peak to be about -21.4 mag. A magnetar model can fit the observed light curve, velocities and temperatures. Proposed interaction scenarios for SLSNe can also match the observed energetics but would require at least ~ 3 $M_\odot$ of hydrogen-poor circumstellar material. The lack of intermediate-width lines in the spectra, like with other SLSNe, also speaks against this model. A normal, Ni-decay Ic model would require $M_{\rm Ni} = 7$ $M_\odot$ and the ejecta composition to be $\gtrsim 80$ % Ni by mass, so although PS1-10bzj shows less extreme energetics than other hydrogen-poor SLSNe, radioactive decay is unlikely to be the primary energy source.

Like SN 2010gx and PTF09cnd, PS1-10bzj developed a number of spectral features after peak. Our model fits these features with intermediate-mass elements Mg, Ca and Si, and Fe is also likely. We do not have the spectroscopic coverage to determine whether these features at late times evolved into a more typical Type Ic SN spectrum, as was seen

in the other two objects. However, PS1-10bzj is interesting in the comparison to Type Ic SNe in the sense that it extends the distribution of SLSNe towards lower luminosities. Continuing to map out the low-luminosity tail of the SLSN population will be necessary to determine whether the two classes represent truly distinct phenomena, or whether there is a smooth continuum between them. If the timescales of PS1-10bzj are typical for the lower-luminosity objects, this may present a challenge for finding such events as they will not stand out photometrically as much as higher-luminosity events and will require spectroscopic confirmation.

The host galaxy of PS1-10bzj is detected both in our PS1 template images and in catalogs covering the ECDF-S. Combining this photometry with emission line measurements, we find that the host is a low luminosity ($M_B \simeq -18$ mag; $L \simeq 0.05L_*$), low metallicity ($Z = 0.13Z_\odot$), low stellar mass ($M_* \approx 2.4 \times 10^7$ $M_\odot$) galaxy. It is forming stars at a rate of $\sim 2 - 3$ $M_\odot yr^{-1}$, resulting in a high sSFR (100 Gyr^{-1}). Archival *HST* imaging further reveal the host to be compact, with a physical diameter $\lesssim 800$ pc. While the metallicity is not as low as the host galaxy of the superluminous SN 2010gx, the discovery of a second low metallicity host galaxy supports the hypothesis that metallicity may be important in the progenitor channel of SLSNe. Compared to the host of SN 2010gx, the host of PS1-10bzj has a higher SFR, and is generally consistent with the $M - Z$ relation for starforming galaxies at lower redshifts (Mannucci et al. 2010; Andrews & Martini 2013). Further increasing the sample of SLSNe with well-studied host galaxies will be necessary to assess whether this metallicity trend holds, and shed light on the nature of these extreme explosions.

Acknowledgements

We thank the staffs at PS1, Gemini and Magellan for their assistance with performing these observations. The Pan-STARRS1 Surveys (PS1) have been made possible through contributions of the Institute for Astronomy, the University of Hawaii, the Pan-STARRS Project Office, the Max-Planck Society and its participating institutes, the Max Planck Institute for Astronomy, Heidelberg and the Max Planck Institute for Extraterrestrial Physics, Garching, The Johns Hopkins University, Durham University, the University of Edinburgh, Queen's University Belfast, the Harvard-Smithsonian Center for Astrophysics, the Las Cumbres Observatory Global Telescope Network Incorporated, the National Central University of Taiwan, the Space Telescope Science Institute, and the National Aeronautics and Space Administration under grant No. NNX08AR22G issued through the Planetary Science Division of the NASA Science Mission Directorate. This work is based in part on observations obtained at the Gemini Observatory (under Programs GS-2010B-Q-4 and GS-2011A-Q-29 (PI: Berger) and GS-2011B-Q-44 (PI: Chornock)), which is operated by the Association of Universities for Research in Astronomy, Inc., under a cooperative agreement with the NSF on behalf of the Gemini partnership: the National Science Foundation (United States), the Science and Technology Facilities Council (United Kingdom), the National Research Council (Canada), CONICYT (Chile), the Australian Research Council (Australia), Ministério da Ciência, Tecnologia e Inovação (Brazil), and Ministerio de Ciencia, Tecnología e Innovación Productiva (Argentina). This paper includes data gathered with the 6.5 m Magellan Telescopes located at Las Campanas Observatory, Chile. This paper includes data based on observations made with the NASA/ESA *Hubble Space Telescope* and

obtained from the Hubble Legacy Archive, which is a collaboration between the Space Telescope Science Institute (STScI/NASA), the Space Telescope European Coordinating Facility (ST-ECF/ESA) and the Canadian Astronomy Data Centre (CADC/NRC/CSA). Some of the computations in this paper were run on the Odyssey cluster supported by the FAS Science Division Research Computing Group at Harvard University. The research leading to these results has received funding from the European Research Council under the European Union's Seventh Framework Programme (FP7/2007-2013)/ERC grant agreement No. [291222] (PI: S. J. Smartt). Partial support for this work was provided by National Science Foundation grants AST-1009749 and AST-1211196.

Chapter 3

Hydrogen-poor Superluminous Supernovae and Long-duration Gamma-ray Bursts Have Similar Host Galaxies

R. Lunnan, R. Chornock, E. Berger, T. Laskar, W. Fong, A. Rest, N. E. Sanders, P. M. Challis, M. R. Drout, R. J. Foley, M. E. Huber, R. P. Kirshner, C. Leibler, G. H. Marion, M. McCrum, D. Milisavljevic, G. Narayan, D. Scolnic, S. J. Smartt, K. W. Smith, A. M. Soderberg, J. L. Tonry, W. S. Burgett, K. C. Chambers, H. Flewelling, K. W. Hodapp, N. Kaiser, E. A. Magnier, P. A. Price, and R. J. Wainscoat

The Astrophysical Journal, Vol. 787, No. 138, 2014

Abstract

We present optical spectroscopy and optical/near-IR photometry of 31 host galaxies of hydrogen-poor superluminous supernovae (SLSNe), including 15 events from the Pan-STARRS1 Medium Deep Survey. Our sample spans the redshift range $0.1 \lesssim z \lesssim 1.6$ and is the first comprehensive host galaxy study of this specific subclass of cosmic explosions. Combining the multi-band photometry and emission-line measurements, we determine the luminosities, stellar masses, star formation rates and metallicities. We find that as a whole, the hosts of SLSNe are a low-luminosity ($\langle M_B \rangle \approx -17.3$ mag), low stellar mass ($\langle M_* \rangle \approx 2 \times 10^8$ M$_\odot$) population, with a high median specific star formation rate ($\langle \mathrm{sSFR} \rangle \approx 2$ Gyr^{-1}). The median metallicity of our spectroscopic sample is low, $12 + \log(\mathrm{O/H}) \approx 8.35 \approx 0.45 Z_\odot$, although at least one host galaxy has solar metallicity. The host galaxies of H-poor SLSNe are statistically distinct from the hosts of GOODS core-collapse SNe (which cover a similar redshift range), but resemble the host galaxies of long-duration gamma-ray bursts (LGRBs) in terms of stellar mass, SFR, sSFR and metallicity. This result indicates that the environmental causes leading to massive stars forming either SLSNe or LGRBs are similar, and in particular that SLSNe are more effectively formed in low metallicity environments. We speculate that the key ingredient is large core angular momentum, leading to a rapidly spinning magnetar in SLSNe and an accreting black hole in LGRBs.

3.1 Introduction

The advent of wide-field time-domain surveys like the Panoramic Survey Telescope and Rapid Response System (Pan-STARRS; PS1), the Palomar Transient Factory (PTF) and the Catalina Real-Time Transient Survey (CRTS) has led to the discovery of a growing number of "superluminous" supernovae (SLSNe), characterized by luminosities $\sim 10 - 100$ times larger than ordinary Type Ia and core-collapse SNe. Their spectra are diverse, though distinct subclasses are emerging (e.g., Gal-Yam 2012). For example, members of the subclass of the SLSNe that shows hydrogen in their spectra can be classified as Type IIn SNe, with the origin of the extreme luminosity being interaction with a dense circumstellar medium (e.g. Ofek et al. 2007; Smith et al. 2007, 2010; Rest et al. 2011; Moriya et al. 2013).

For the SLSNe without hydrogen, however, the energy source(s) remains a matter of debate. Many of these objects form a spectroscopic subclass characterized by a blue continuum with a few broad rest-frame UV absorption features from intermediate-mass elements; in some cases the spectra develop Ic features at late times (Pastorello et al. 2010; Quimby et al. 2011b; Chomiuk et al. 2011). An interaction scenario similar to the H-rich SLSNe has been proposed for these objects as well (Chevalier & Irwin 2011; Ginzburg & Balberg 2012; Moriya & Maeda 2012), but this requires extreme mass loss episodes (> 1 $M_{\odot}$/yr) shortly before the explosion and may be at odds with the lack of intermediate-width lines seen in the spectra (Chevalier & Irwin 2011; Chomiuk et al. 2011; Quimby et al. 2011b). Another proposed mechanism is energy injection by a newborn, rapidly spinning magnetar (Kasen & Bildsten 2010; Woosley 2010; Dessart et al. 2012), which can explain a wide range of luminosities and timescales (Chomiuk

et al. 2011; Lunnan et al. 2013; Inserra et al. 2013). Other H-poor SLSNe, most notably SN 2007bi, have been proposed to be examples of pair-instability SNe (Gal-Yam et al. 2009; Young et al. 2010), but this interpretation is controversial and the events can also be explained in an interaction or magnetar scenario (Dessart et al. 2012; Milisavljevic et al. 2013; Nicholl et al. 2013; McCrum et al. 2014). The superluminous SN PS1-10afx did not resemble any previously seen SLSNe, and may represent a new class of transients (Chornock et al. 2013); its unusual properties lead Quimby et al. (2013b) to conclude that it may have been a lensed Type Ia SN rather than a SLSN.

An important clue to the origin of the H-poor SLSNe may come from their host galaxy properties. An early study by Neill et al. (2011) utilized GALEX near-UV and Sloan Digital Sky Survey (SDSS) r'-band photometry of SLSN hosts, and used this to argue for a preference for low-luminosity (and by extension, possibly low-metallicity) galaxies. However, this study was limited in several ways. First, all SLSNe were analyzed as a group regardless of spectral properties. Second, it was based on limited data: of the seven H-poor SLSN hosts considered, only three were actually detected in either of the two photometric bands they considered. Third, it relied on the luminosities in only two bands to draw inferences about underlying properties of interest (e.g. metallicity), which were not measured directly. A possible trend of low-metallicity galaxies was also pointed out by Stoll et al. (2011), who determined the metallicities for two SLSN host galaxies, and found them to be low and comparable to the host galaxies of long-duration gamma-ray burst (LGRBs)(e.g. Savaglio et al. 2009; Levesque et al. 2010a,b). Recently, detailed studies of the host galaxies of two individual H-poor SLSNe (Chen et al. 2013; Lunnan et al. 2013) revealed low metallicities and high specific star formation rates, similar to LGRB host galaxies.

Despite these initial results it is clear that to fully examine the physical properties of SLSN host environments, make a meaningful comparison to other classes of transients and draw conclusions about the progenitors requires several key improvements on the existing data. First, high-quality spectroscopic data and optical/NIR photometric data are needed to accurately determine the host galaxy luminosities, stellar masses, metallicities, star formation rates (SFRs) and specific SFRs. Second, a comprehensive study, examining the SLSN host galaxies as a population rather than a few individual objects is essential. With the large number of SLSNe being discovered by Pan-STARRS and other surveys, this is now feasible.

Here, we present such observations and analysis of a sample of 31 SLSN hosts, spanning a redshift range of $0.1 \lesssim z \lesssim 1.6$. Our sample includes 15 objects from the Pan-STARRS1 Medium Deep Survey (PS1/MDS), and 16 targets from other surveys available in the literature. We only include hosts of H-poor SLSNe, as the energy source of Type IIn SLSNe is better understood and possibly distinct from the H-poor SLSNe. We do however include all types of H-poor SLSNe, so as not to make any initial assumptions about potentially different energy sources. This is the most comprehensive systematic study of SLSN hosts so far.

This paper is organized as follows. We describe our sample of SLSN hosts and follow-up photometric and spectroscopic observations in Section 3.2. We describe our comparison samples and statistical methods in Section 3.3. We detail how the various galaxy properties are derived from the data, and discuss them in Section 3.4. Implications for the progenitors and caveats are discussed in Section 3.5, and we summarize our conclusions in Section 3.6. All calculations in this paper assume a ΛCDM cosmology with $H_0 = 70$ km s^{-1} Mpc^{-1}, $\Omega_{\rm M} = 0.27$ and $\Omega_\Lambda = 0.73$ (Komatsu et al. 2011).

3.2 Observations

3.2.1 Targets

Our sample consists of 15 H-poor SLSNe discovered in the PS1/MDS transient search. To supplement the PS1 sample, which covers the redshift range $0.5 \lesssim z \lesssim 1.6$, we also include events from the literature, extending the redshift coverage down to $z \approx 0.1$ and bringing the total number of targets up to 31. Table 3.1 lists all targets, including references to the SN discoveries.

For the purposes of this paper, we define a H-poor SLSN as a SN with a peak absolute magnitude $M \lesssim -20.5$, and without evidence of hydrogen in the spectrum. The majority of objects belong to the subclass of SLSNe with spectra resembling SN 2005ap and SCP06F6 (Quimby et al. 2011b). However, we include other H-poor SLSNe such as SN 2007bi (Gal-Yam et al. 2009) and PS1-10afx (Chornock et al. 2013), to explore their environments and relation to the other events.

SLSNe from the PS1/MDS Transient Survey

The PS1 telescope on Haleakala is a high-etendue wide-field survey instrument with a 1.8-m diameter primary mirror and a 3.3° diameter field of view imaged by an array of sixty 4800×4800 pixel detectors, with a pixel scale of $0.258''$ (Kaiser et al. 2010; Tonry & Onaka 2009). The observations are obtained through five broad-band filters ($grizy_{\rm P1}$); details of the filters and photometric system are described in Tonry et al. (2012).

Table 3.1. H-Poor SLSN Sample

SN Name	Redshift	RA (J2000)	Dec (J2000)	E(B-V)[a] (mag)	Reference
PTF10hgi	0.098	$16^h37^m47.04^s$	$+06°12'32.3''$	0.074	1,2
SN 2010kd	0.101	$12^h08^m00.89^s$	$+49°13'32.88''$	0.021	3,4
PTF12dam	0.107	$14^h24^m46.20^s$	$+46°13'48.3''$	0.010	5,6
SN 2007bi	0.127	$13^h19^m20.14^s$	$+08°55'43.7''$	0.024	7
SN 2011ke	0.143	$13^h50^m57.77^s$	$+26°16'42.8''$	0.011	2,8
SN 2012il	0.175	$09^h46^m12.91^s$	$+19°50'28.7''$	0.019	2,9
PTF11rks	0.192	$01^h39^m45.64^s$	$+29°55'27.0''$	0.038	2,10
SN 2010gx	0.23	$11^h25^m46.71^s$	$-08°49'41.4''$	0.035	11,12
SN 2011kf	0.245	$14^h36^m57.34^s$	$+16°30'57.14''$	0.020	2,8,13
PTF09cnd	0.258	$16^h12^m08.94^s$	$+51°29'16.1''$	0.021	12
SN 2005ap	0.283	$13^h01^m14.83^s$	$+27°43'32.3''$	0.008	14
MLS121104:021643+204009[b]	0.303	$02^h16^m42.51^s$	$+20°40'08.47''$	0.150	15,16
PTF09cwl	0.349	$14^h49^m10.08^s$	$+29°25'11.4''$	0.014	12
SN 2006oz	0.396	$22^h08^m53.56^s$	$+00°53'50.4''$	0.041	17
PTF09atu	0.501	$16^h30^m24.55^s$	$+23°38'25.0''$	0.042	12
PS1-12bqf	0.522	$02^h24^m54.621^s$	$-04°50'22.72''$	0.025	18
PS1-11ap	0.524	$10^h48^m27.752^s$	$+57°09'09.32''$	0.007	19
PS1-10bzj	0.650	$03^h31^m39.826^s$	$-27°47'42.17''$	0.007	20
PS1-12zn	0.674	$09^h59^m49.615^s$	$+02°51'31.85''$	0.019	18
PS1-11bdn	0.738	$02^h25^m46.292^s$	$-05°03'56.57''$	0.025	18
PS1-13gt	0.884	$12^h18^m02.035^s$	$+47°34'45.95''$	0.015	18
PS1-10awh	0.909	$22^h14^m29.831^s$	$-00°04'03.62''$	0.070	21
PS1-10ky	0.956	$22^h13^m37.851^s$	$+01°14'23.57''$	0.031	21
PS1-11aib	0.997	$22^h18^m12.217^s$	$+01°33'32.01''$	0.044	18
SCP 06F6	1.189	$14^h32^m27.395^s$	$+33°32'24.83''$	0.009	22
PS1-10pm	1.206	$12^h12^m42.200^s$	$+46°59'29.48''$	0.016	23
PS1-11tt	1.283	$16^h12^m45.778^s$	$+54°04'16.96''$	0.008	18
PS1-10afx	1.388	$22^h11^m24.160^s$	$+00°09'43.49''$	0.048	24
PS1-11afv	1.407	$12^h15^m37.770^s$	$+48°10'48.62''$	0.014	18

Table 3.1—Continued

SN Name	Redshift	RA (J2000)	Dec (J2000)	E(B-V)[a] (mag)	Reference
PS1-11bam	1.565	$08^{h}41^{m}14.192^{s}$	$+44°01'56.95''$	0.024	25
PS1-12bmy	1.572	$03^{h}34^{m}13.123^{s}$	$-26°31'17.21''$	0.015	18

[a]Foreground extinction (Schlegel et al. 1998; Schlafly & Finkbeiner 2011).

[b]Referred to as MLS121104 throughout the paper.

Note. — References: (1) Quimby et al. (2010), (2) Inserra et al. (2013), (3) Vinko et al. (2010), (4) Quimby et al. (2013a), (5) Quimby et al. (2012), (6) Nicholl et al. (2013),(7) Gal-Yam et al. (2009), (8) Drake et al. (2011b), (9) Drake et al. (2012a), (10) Quimby et al. (2011a), (11) Pastorello et al. (2010), (12) Quimby et al. (2011b), (13) Prieto et al. (2012), (14) Quimby et al. (2007), (15) Drake et al. (2012b), (16) Fatkhullin & Gabdeev (2012), (17) Leloudas et al. (2012), (18) Lunnan et al., in prep., (19) McCrum et al. (2014), (20) Lunnan et al. (2013), (21) Chomiuk et al. (2011), (22) Barbary et al. (2009), (23) McCrum et al. (2015), (24) Chornock et al. (2013), (25) Berger et al. (2012).

The PS1/MDS consists of 10 fields (each with a single PS1 imager footprint) observed in $g_{\rm P1}r_{\rm P1}i_{\rm P1}z_{\rm P1}$with a typical cadence of 3 d in each filter, to a 5σ depth of ~ 23.3 mag; $y_{\rm P1}$is used near full moon with a typical depth of ~ 21.7 mag. The standard reduction, astrometric solution, and stacking of the nightly images are done by the Pan-STARRS1 Image Processing Pipeline (IPP) system (Magnier 2006; Magnier et al. 2008) on a computer cluster at the Maui High Performance Computer Center. The nightly MDS stacks are transferred to the Harvard FAS Research Computing cluster, where they are processed through a frame subtraction analysis using the `photpipe` pipeline developed for the SuperMACHO and ESSENCE surveys (Rest et al. 2005; Garg et al. 2007; Miknaitis et al. 2007; Rest et al. 2014).

A subset of targets is chosen for spectroscopic follow-up, using Blue Channel spectrograph on the 6.5m MMT telescope (Schmidt et al. 1989), the Gemini Multi-Object Spectrograph (GMOS; Hook et al. 2004) on the 8-m Gemini telescopes, and the Low Dispersion Survey Spectrograph (LDSS3) and Inamori-Magellan Areal Camera and Spectrograph (IMACS; Dressler et al. 2006) on the 6.5m Magellan telescopes. Since the beginning of the survey in 2010, we have discovered over 15 SLSNe in the PS1/MDS data (Chomiuk et al. 2011; Berger et al. 2012; Chornock et al. 2013; Lunnan et al. 2013; McCrum et al. 2015, 2014; Lunnan et al., in prep.). The combination of a relatively small survey area and deep photometry provides sensitivity primarily to SLSNe at higher redshifts; the current sample spans $0.5 \lesssim z \lesssim 1.6$. Thus, the PS1 sample is a great complement to the SLSNe from other surveys, which are generally found at $z \lesssim 0.5$ due to shallower photometry (Figure 3.3).

While PS1/MDS is an untargeted survey the spectroscopic follow-up is not complete. The SLSNe in our sample were targeted by some combination of light curve and host

properties, in particular for having long observed rise times, or standing out as being several magnitudes brighter than any apparent host. We discuss to what extent selection effects may affect our results in Section 3.5.1.

SLSNe from the Literature

In addition to the PS1/MDS SLSNe, we also include in our sample H-poor SLSNe reported by other surveys, most notably the Palomar Transient Factory (PTF; Law et al. 2009), the Catalina Real-Time Transient Survey (CRTS; Drake et al. 2009) and the Robotic Optical Transient Search Experiment (ROTSE-III; Akerlof et al. 2003). Table 3.1 lists these objects, with references. Since not all of the objects in this list have published spectra available, we include objects that are reported with a peak absolute magnitude $\lesssim -21$ mag, and classified as Type Ic or described as having a spectrum similar to known H-poor SLSNe.

3.2.2 Host Galaxy Photometry

Ground-Based Optical Photometry

For targets from the PS1/MDS SLSN sample, we stack the pre-explosion images and obtain deep $grizy_{\rm P1}$ photometry of the host galaxies. The results are listed in Table 3.2. In addition, a number of the literature hosts are detected in the Sloan Digital Sky Survey (SDSS), and we use available DR9 model magnitudes for these objects (Ahn et al. 2012).

Table 3.2. Host Galaxy Photometry & Limits from PS1/MDS Stacks

SN Name	$g_{\rm P1}$	$r_{\rm P1}$	$i_{\rm P1}$	$z_{\rm P1}$	$y_{\rm P1}$
PS1-10ky	> 24.7	> 24.6	> 24.5	> 24.0	> 22.1
PS1-10awh	> 25.0	> 25.1	> 25.3	> 24.7	> 22.7
PS1-11bam	23.63 ± 0.13	23.64 ± 0.12	23.78 ± 0.13	23.69 ± 0.14	> 23.4
PS1-10afx	23.84 ± 0.10	23.57 ± 0.10	23.34 ± 0.13	22.68 ± 0.10	22.29 ± 0.28
PS1-10bzj	24.35 ± 0.08	23.98 ± 0.12	23.75 ± 0.10	22.72 ± 0.05	> 21.7
PS1-10pm	> 25.2	> 25.1	> 25.0	> 24.0	> 23.0
PS1-11ap	24.20 ± 0.15	23.32 ± 0.10	22.86 ± 0.09	23.24 ± 0.13	> 22.5
PS1-11tt	> 24.6	> 24.7	> 24.8	> 24.1	> 23.0
PS1-11aib	> 24.2	> 24.4	> 24.7	> 23.9	> 22.2
PS1-11afv	> 24.9	> 24.8	> 25.1	> 24.9	> 22.8
PS1-11bdn	> 24.8	> 24.0	> 24.9	> 23.9	> 22.5
PS1-12bmy	> 24.2	> 24.2	> 24.1	> 23.6	> 22.3
PS1-12zn	24.64 ± 0.10	24.07 ± 0.07	23.77 ± 0.10	23.56 ± 0.14	> 22.5
PS1-12bqf	22.76 ± 0.12	21.89 ± 0.06	21.44 ± 0.03	21.40 ± 0.05	21.46 ± 0.14
PS1-13gt	> 24.5	> 24.5	> 24.7	> 24.4	> 22.7

Note. — Corrected for foreground extinction. Upper limits are 3σ.

To complement the survey photometry, we obtained deep imaging observations of a number of targets that were either not covered by or undetected in either PS1/MDS or SDSS. This was mainly done with LDSS and IMACS on Magellan, as well as with MMTCam[1], an f/5 imager on the 6.5m MMT telescope.

We processed and stacked all images using standard routines in IRAF[2]. We measured host galaxy magnitudes using aperture-matched photometry, with zeropoints determined either from observations of standard star fields taken at similar airmass on the same night, or from photometry of stars with listed SDSS and/or PS1/MDS magnitudes. In cases where the host galaxy was not detected, a 3σ upper limit was determined by measuring the mean magnitude of objects at the detection threshold (S/N of 3). Images of the hosts are shown in Figures 3.1 and 3.2 with the instrument and filter noted on each image. All non-PS1 and non-SDSS photometry is listed in Table 3.3, and the host galaxy apparent magnitude distribution is shown in Figure 3.3 as a function of redshift.

[1]http://www.cfa.harvard.edu/mmti/wfs.html

[2]IRAF is distributed by the National Optical Astronomy Observatory, which is operated by the Association of Universities for Research in Astronomy, Inc., under cooperative agreement with the National Science Foundation.

Table 3.3. Additional Host Galaxy Photometry

SN Name	Filter	AB mag	Instrument	UT date
PTF10hgi	g'	22.56 ± 0.06	IMACS	2013-05-07
PTF10hgi	i'	21.75 ± 0.06	IMACS	2013-05-07
PTF10hgi	z'	21.43 ± 0.12	IMACS	2013-04-11
PTF10hgi	J	21.48 ± 0.08	FourStar	2013-05-20
PTF10hgi	K_s	21.66 ± 0.13	FourStar	2013-05-20
SN 2011ke[a]	g'	22.44 ± 0.10	CFHT	...
SN 2011ke[a]	r'	22.01 ± 0.10	CFHT	...
SN 2011ke[a]	z'	23.00 ± 0.30	IMACS	2013-04-11
SN 2011ke[a]	J	22.86 ± 0.15	FourStar	2013-05-20
SN 2012il	J	21.78 ± 0.11	FourStar	2013-05-19
SN 2012il	K_s	21.90 ± 0.20	FourStar	2013-05-21
PTF11rks	z'	20.52 ± 0.10	LDSS3	2013-10-04
PTF11rks	K_S	20.75 ± 0.34	FourStar	2013-12-18
SN 2010gx	J	22.92 ± 0.11	FourStar	2012-12-04
SN 2011kf	g'	23.74 ± 0.07	IMACS	2013-05-07
SN 2011kf	r'	23.15 ± 0.12	IMACS	2013-05-10
SN 2011kf	i'	23.65 ± 0.33	MMTCam	2013-04-29
SN 2011kf	J	> 23.1	FourStar	2013-05-22
SN 2011kf	K_s	> 22.7	FourStar	2013-05-22
PTF09cnd	g'	23.75 ± 0.16	MMTCam	2013-05-02
PTF09cnd	r'	23.60 ± 0.25	MMTCam	2013-03-15
PTF09cnd	i'	23.70 ± 0.27	MMTCam	2013-05-02
SN 2005ap	i'	23.59 ± 0.07	MMTCam	2014-03-23
MLS121104	J	20.39 ± 0.10	FourStar	2013-12-18
MLS121104	K_S	19.63 ± 0.12	FourStar	2013-12-18
PTF09cwl	r'	> 24.4	MMTCam	2013-03-13
SN 2006oz	J	23.43 ± 0.26	FourStar	2012-12-04
PTF09atu	r'	> 25.2	IMACS	2013-05-07
PS1-12bqf	F475W	22.94 ± 0.02	*HST*/ACS	2013-11-18
PS1-12bqf	K_S	> 19.9	FourStar	2013-12-18

Table 3.3—Continued

SN Name	Filter	AB mag	Instrument	UT date
PS1-12bqf	3.6μm	20.82 ± 0.06	*Spitzer*/IRAC	...
PS1-12bqf	4.5μm	21.29 ± 0.06	*Spitzer*/IRAC	...
PS1-11ap	F475W	24.02 ± 0.02	*HST*/ACS	2013-10-09
PS1-11ap	3.6μm	23.33 ± 0.39	*Spitzer*/IRAC	...
PS1-11ap	4.5μm	23.38 ± 0.29	*Spitzer*/IRAC	...
PS1-10bzj	3.6μm	23.79 ± 0.16	*Spitzer*/IRAC	...
PS1-10bzj	4.5μm	24.00 ± 0.18	*Spitzer*/IRAC	...
PS1-12zn	J	23.09 ± 0.25	FourStar	2013-05-20
PS1-12zn	K_s	> 22.7	FourStar	2013-05-20
PS1-12zn	3.6μm	23.09 ± 0.12	*Spitzer*/IRAC	...
PS1-12zn	4.5μm	24.24 ± 0.57	*Spitzer*/IRAC	...
PS1-11bdn	F475W	26.09 ± 0.10	*HST*/ACS	2013-11-13
PS1-11bdn	r'	> 25.5	IMACS	2012-07-19
PS1-11bdn	i'	25.40 ± 0.25	LDSS3	2013-10-05
PS1-11bdn	z'	> 24.2	LDSS3	2013-01-12
PS1-11bdn	J	> 24.2	FourStar	2012-12-04
PS1-10awh	F606W	27.00 ± 0.20	*HST*/ACS	2013-09-04
PS1-10ky	F606W	> 27.4	*HST*/ACS	2012-12-13
PS1-10ky	F850LP	> 27.0	*HST*/ACS	2012-12-13
PS1-10pm	F606W	25.38 ± 0.05	*HST*/ACS	2012-12-10
PS1-10pm	F110W	24.40 ± 0.08	*HST*/WFC3	2013-01-15
PS1-11tt	F606W	25.78 ± 0.08	*HST*/ACS	2012-12-02
PS1-11tt	F110W	25.83 ± 0.05	*HST*/WFC3	2013-04-21
PS1-11afv	F606W	25.26 ± 0.08	*HST*/ACS	2013-04-09
PS1-11afv	F110W	24.65 ± 0.08	*HST*/WFC3	2012-11-24
PS1-11bam	F814W	23.82 ± 0.02	*HST*/ACS	2013-10-11
PS1-12bmy	g'	25.25 ± 0.10	LDSS3	2013-10-05
PS1-12bmy	r'	25.46 ± 0.10	LDSS3	2013-10-04
PS1-12bmy	i'	25.10 ± 0.16	LDSS3	2013-10-05
PS1-12bmy	z'	24.64 ± 0.40	LDSS3	2013-10-05

Table 3.3—Continued

SN Name	Filter	AB mag	Instrument	UT date
PS1-12bmy	F814W	25.01 ± 0.05	*HST*/ACS	2013-09-17
PS1-12bmy	J	24.02 ± 0.21	FourStar	2013-12-18
PS1-12bmy	K_s	> 22.2	FourStar	2013-12-18

[a]Flux from dwarf galaxy host only; see Section 3.7.1 for details.

Note. — Corrected for foreground extinction. Upper limits are 3σ.

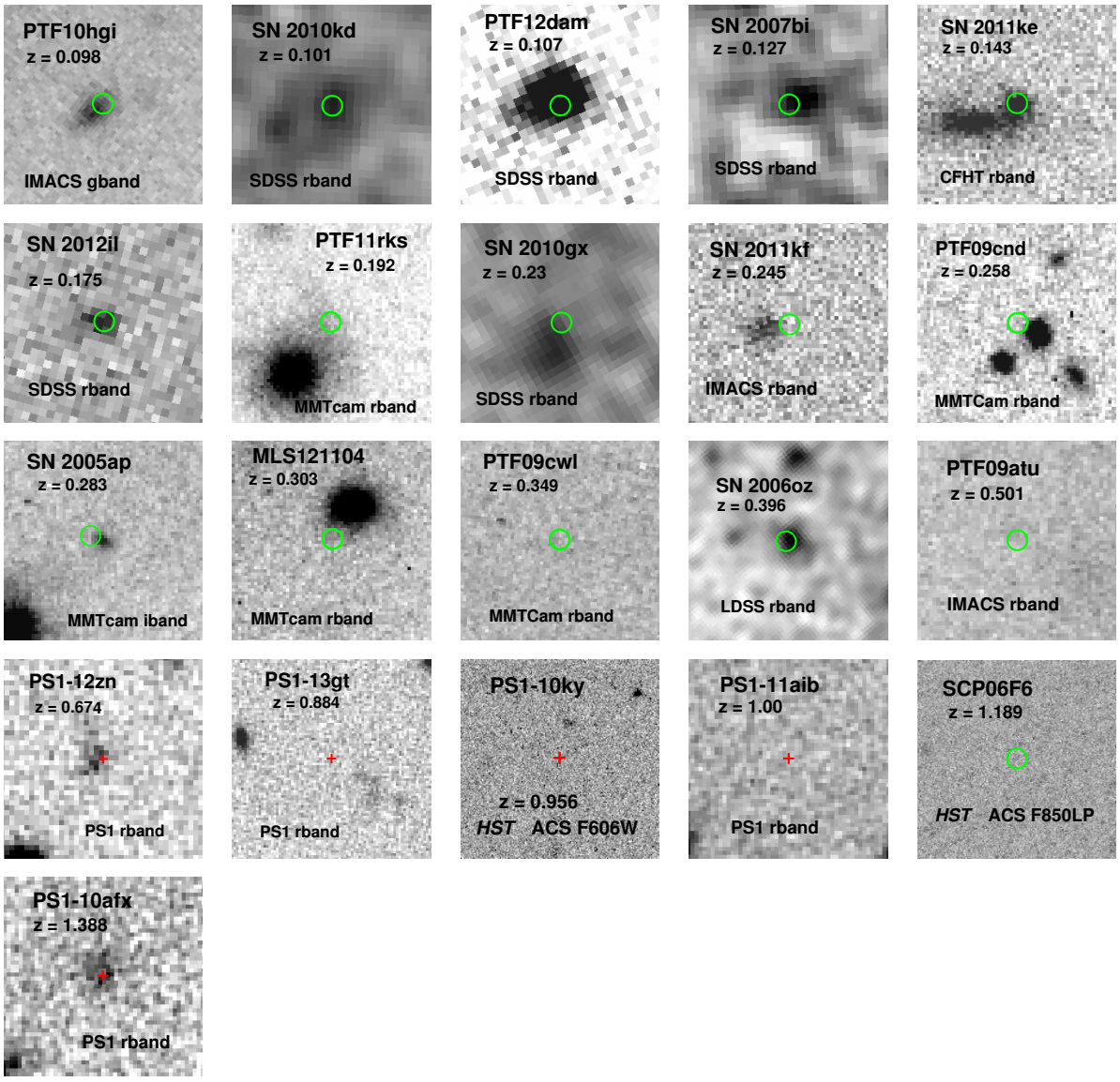

Figure 3.1.—: Images of 21 SLSN hosts considered in this paper ($10'' \times 10''$). All images are oriented with north corresponding to up and east to the left. The 10 remaining objects in our sample were detected in *HST* imaging, and are shown in Figure 3.2. The PS1 objects have the SN position marked by red crosses, as determined by relative astrometry. For the non-PS1 objects, we mark the absolute position reported in the literature with a green circle (radius $0.5''$). Six hosts remain undetected: PTF09cwl, PTF09atu, PS1-13gt, PS1-11aib, PS1-10ky and SCP06F6. The latter two remain undetected even in deep *HST* imaging.

Ground-Based NIR Photometry

We obtained J- and K_s-band photometry for a subset of our targets using the FourStar Infrared Camera on the 6.5m Magellan/Baade telescope (Persson et al. 2013). We used the IRAF/`FSRED` package (Andy Monson 2013, private communication) to calibrate, align, and co-add the Fourstar observations for each object and filter. We performed aperture photometry using standard packages in IRAF, using sources in common with 2MASS to determine the zeropoint. All NIR photometry is listed in Table 3.3.

HST Optical and NIR Photometry

We obtained *HST* imaging of ten SLSN hosts from PS1 (programs GO-13022 and GO-13326; PI: Berger and Lunnan). All hosts, with the exception of PS1-10ky were detected, and images corresponding to the rest-frame UV are shown in Figure 3.2. The host of PS1-10bzj (Lunnan et al. 2013) has serendipitous *HST* imaging from the GEMS survey (Rix et al. 2004), and is also shown in Figure 3.2.

In addition to a filter covering the rest-frame UV, we imaged the hosts of PS1-11tt, PS1-11afv, PS1-10pm, PS1-10awh and PS1-10ky with a second filter covering the rest-frame optical (F850LP or F110W, depending on redshift). We processed and stacked all *HST* images using the AstroDrizzle software (Fruchter & Hook 2002; Gonzaga et al. 2012). As with our other photometry, we determined host galaxy fluxes using aperture photometry (Table 3.3).

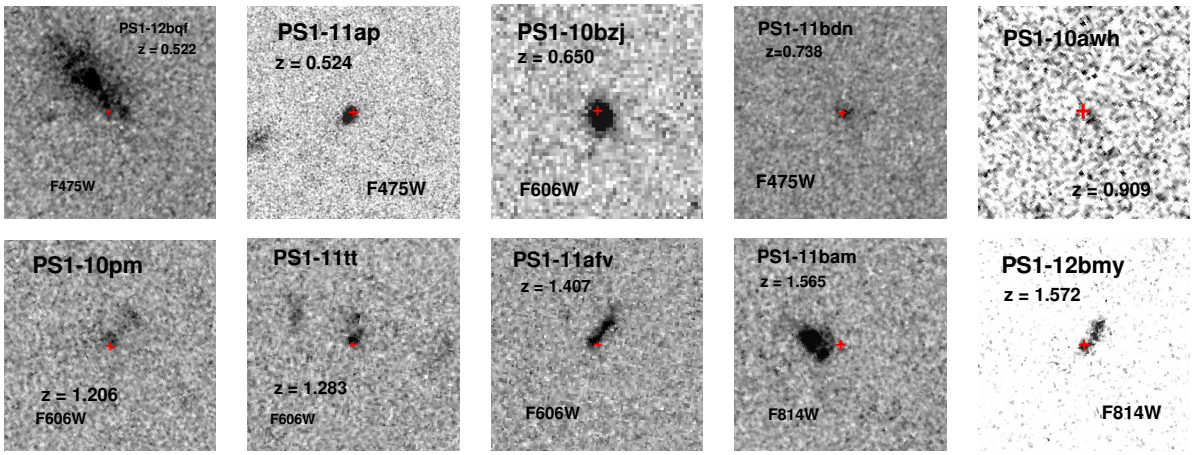

Figure 3.2.—: *HST* images of the remaining ten SLSN hosts in our sample ($3''\times$ $3''$). The SN positions relative to the host are determined by astrometrically aligning the *HST* images with PS1 SN images, and shown as red crosses.

Spitzer Photometry

Several PS1/MDS fields overlap with *Spitzer* survey coverage. Four of the lower-redshift PS1 host galaxies are detected in archival images from the *Spitzer* Extragalactic Representative Volume Survey (SERVS; Mauduit et al. 2012), the COSMOS *Spitzer* survey (S-COSMOS; Sanders et al. 2007), or the *Spitzer* Extended Deep Survey (SEDS; Ashby et al. 2013). We use the catalog photometry for PS1-10bzj and PS1-12bqf (Table 3.3). The other two hosts (PS1-11ap and PS1-12zn) lack reliable catalog photometry, and so we downloaded the survey images and performed the photometry ourselves.

At the depth of these observations, *Spitzer* images are confusion-limited for faint sources. As a result, in several cases the region around the host galaxy is contaminated by light from nearby stars or galaxies. Prior to performing photometry, we used the GALFIT software package (Peng et al. 2002) to model and subtract these neighboring

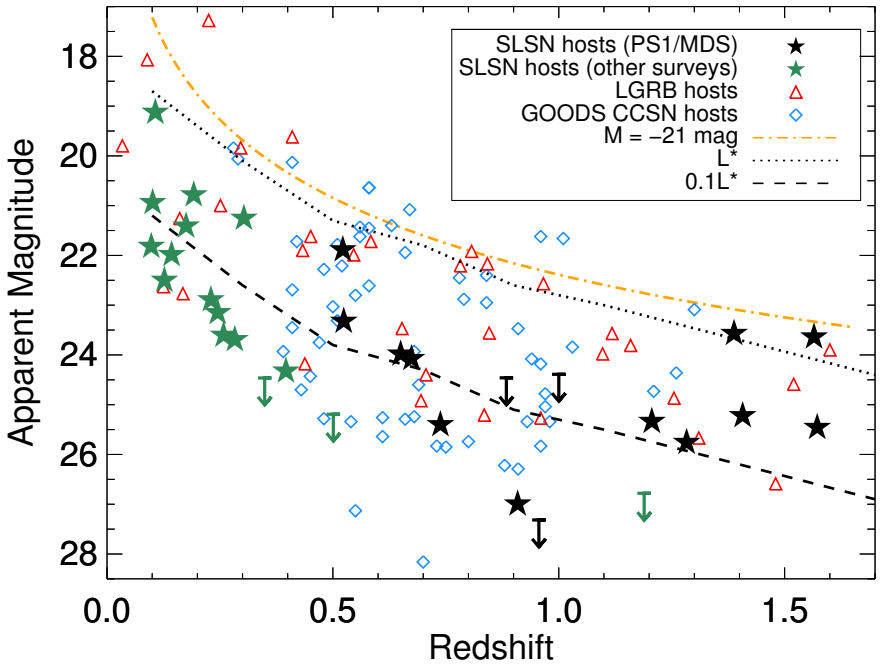

Figure 3.3.—: Host apparent magnitude versus redshift for the SLSN host galaxies in our sample, with targets from PS1/MDS shown in black and other SLSN targets shown in green. Also shown are LGRB host galaxies, and core-collapse SN host galaxies from the GOODS survey, which we use as comparison samples (Section 3.3). To guide the eye, the dotted and dashed black lines show tracks for L_* and $0.1L_*$. The SLSNe themselves generally peak above the dash-dotted orange line, which corresponds to an absolute magnitude $M = -21$ mag. r-band is plotted when available for the LGRB and SLSN host galaxies, though F606W is plotted instead for some SLSN hosts; V-band is plotted for the GOODS CCSN hosts.

sources using the procedure described in Laskar et al. (2011). We used a 3″ aperture and a 3–7″ background annulus and determined aperture corrections using the PSFs derived from the mosaics. We include the contribution of correlated noise from the mosaicking process in our estimate of the uncertainty on the derived fluxes following Laskar et al. (2011).

Other PS1/MDS hosts also lie within the survey footprints, but were not detected. We find that the upper limits are too shallow to constrain the host spectral energy distributions (SED), so we do not consider them here. We also searched the *Spitzer* archive for observations of non-PS1 host galaxies; SN 2005ap and SCP06F6 lie in areas of *Spitzer* coverage, but the limits are not constraining.

3.2.3 Astrometry

To establish an absolute astrometry scale on the MMTCam and Magellan images, we download catalog images of the field (SDSS, PS1 or DSS) and use the IRAF routine `ccmap` to align the images after identifying common point sources. For the non-PS1 objects, we do not have SN images available to precisely determine the location of the SN relative to its host galaxy, but we mark the absolute reported literature positions in Figure 3.1.

For the PS1/MDS objects we also have SN images that can be used to perform relative astrometry. We use these to determine the SN position relative to the host galaxies in the non-PS1 images, again by identifying common point sources in the two images and aligning them using the IRAF package `ccmap`. Depending on the source density and depth of the PS1 image, the number of overlap sources varies from

$\sim 10 - 100$, with a resulting uncertainty of the astrometric tie of $\approx 20 - 80$ mas. The positions of the PS1/MDS SLSNe relative to their hosts are marked in Figures 3.1 and 3.2.

3.2.4 Spectroscopy

We obtained spectra of 12 host galaxies at $z \lesssim 0.7$, using LDSS3, IMACS and BlueChannel. Beyond this redshift, our targets are generally too faint for spectroscopy, or at too high redshift to measure [O III]λ 5007, which is required for a metallicity determination (Figure 3.3). Table 3.4 summarizes the spectroscopic observations and observing setups. All spectra were taken at parallactic angle unless otherwise noted. Continuum and arc lamp exposures were obtained after each observation to provide a flatfield and wavelength calibration. Basic two-dimensional image processing tasks were performed using standard tasks in IRAF. Observations of spectrophotometric standard stars were obtained on the same night, and we used our own IDL routines to apply a flux calibration and correct for telluric absorption bands.

Table 3.4. Log of Host Galaxy Spectroscopic Observations

Object	UT Date (YYYY-MM-DD.D)	Instrument	Wavelength Range (Å)	Slit (″)	Grating	Filter	Exp. time (s)	Mean Airmass
PTF10hgi	2013-04-11.3	IMACS	4000-10270	0.9	300-17.5	none	3600	1.22
PTF10hgi	2013-05-07.4	IMACS	4000-10270	0.9	300-17.5	none	4200	1.75
SN 2010kd	2013-05-13.3	BlueChannel	3330-8550	1	300GPM	none	1800	1.23
PTF12dam	2013-07-13.3	BlueChannel	3300-8530	1	300GPM	none	1800	1.57
SN 2011ke[a]	2013-04-11.3	IMACS	4000-10270	0.9	300-17.5	none	2400	1.80
SN 2012il	2013-04-15.2	BlueChannel	3350-8570	1	300GPM	none	1800	1.15
SN 2011kf	2013-05-10.2	IMACS	4000-10270	0.9	300-17.5	none	1800	1.44
SN 2011kf	2013-06-03.1	IMACS	4000-10270	0.9	300-17.5	none	5400	1.43
PTF11rks	2013-10-05.3	LDSS3	3900-10000	1	VPH-All	none	1800	1.95
MLS121104	2013-07-12.4	LDSS3	4080-10720	1	VPH-All	none	3000	1.77
SN 2006oz	2013-07-12.3	LDSS3	4080-10720	1	VPH-All	none	5400	1.23
PS1-12zn	2013-01-10.3	LDSS3	5850-9970	1	VPH-Red	OG590	5000	1.18
PS1-12bqf	2013-10-05.2	LDSS3	5310-9970	1	VPH-Red	none	3600	1.19
PS1-11bdn	2013-01-13.1	LDSS3	5850-9970	1	VPH-Red	OG590	5400	1.39

[a]Taken with the slit oriented through a nearby galaxy; see Section 3.7.1 for details. Note that IMACS has an atmospheric dispersion corrector, so that observing away from parallactic angle does not affect relative line fluxes.

Absolute flux calibration (to account for slit losses and/or non-photometric conditions) was determined by performing synthetic photometry on the observed spectra and applying an overall scaling factor to match the galaxy broadband photometry. We find that generally factors derived from different filters agree well, indicating that the standard star calibration reliably recovers the shape of the spectrum. In spectra where the continuum is not well detected, we do not make this correction, and the overall calibration is derived from the spectrophotometric standard stars only. The relative line fluxes and quantities that are derived by ratios (i.e., extinction and metallicity) are reliable, but the overall scaling and in particular a line flux derived star formation rate may be marginally affected.

In cases where the galaxy continuum is well detected, we construct a stellar model spectrum using the FAST stellar population synthesis code (Kriek et al. 2009) by fitting the observed spectrum (with strong emission lines masked). We then subtract the model to correct for underlying stellar absorption in the Balmer lines before measuring line fluxes. In practice, we find that this correction only makes a significant difference ($\gtrsim 10\%$ correction in the Hβ flux) for a few objects in our sample. Since the objects with weak continuum emission also exhibits the highest equivalent width (EW) emission lines, the correction for these objects is marginal.

We measure emission line fluxes by fitting Gaussian profiles, and list the results in Table 3.5. In two objects, SN 2006oz and PTF10hgi, low-precision redshifts were previously only known from cross-correlating SN features, but we now detect galaxy emission lines from both hosts and adjust the redshifts to $z = 0.396$ for SN 2006oz, and $z = 0.098$ for PTF10hgi. These redshifts are consistent with the inferred SN redshifts (0.376 ± 0.014 and 0.100 ± 0.014, respectively; Leloudas et al. 2012; Inserra et al. 2013).

Table 3.5. Raw Measured Emission Line Fluxes (10^{-15} erg s^{-1} cm^{-2})

Object	[O II]λ3727	Hγ	[O III]λ4363	Hβ	[O III]λ4959	[O III]λ5007	Hα	[N II]λ6584
PTF10hgi	...	...	...	0.020 ± 0.006	...	0.024 ± 0.005	0.083 ± 0.008	< 0.01
SN 2010kd	0.068 ± 0.013	0.033 ± 0.025	...	0.065 ± 0.011	0.106 ± 0.016	0.293 ± 0.013	0.120 ± 0.010	< 0.012
PTF12dam	12.12 ± 0.11	3.47 ± 0.07	0.67 ± 0.05	8.07 ± 0.08	15.82 ± 0.13	47.19 ± 0.24	24.20 ± 0.18	0.82 ± 0.06
SN 2011ke	0.88 ± 0.07	0.30 ± 0.02	0.046 ± 0.015	0.71 ± 0.02	0.95 ± 0.02	2.83 ± 0.03	1.77 ± 0.02	< 0.04
SN 2012il	0.32 ± 0.01	0.10 ± 0.01	...	0.24 ± 0.01	0.44 ± 0.02	1.38 ±0.02	0.70 ± 0.04	< 0.035
PTF11rks	0.65 ± 0.08	...	...	0.12 ± 0.02	0.07 ± 0.02	0.22 ± 0.03	0.40 ± 0.03	0.07 ± 0.03
SN 2011kf	0.047 ± 0.016	...	...	0.046 ± 0.01	0.032 ± 0.01	0.099 ± 0.01	0.094 ± 0.01	< 0.019
MLS121104	0.53 ± 0.02	0.095 ± 0.009	...	0.198 ± 0.007	0.152 ± 0.007	0.419 ± 0.007	0.538 ± 0.009	0.059 ± 0.004
SN 2006oz	0.026 ± 0.032	...	...	0.018 ± 0.005	0.016 ± 0.003	0.047 ± 0.002	0.037 ± 0.01	< 0.006
PS1-12zn	0.236 ± 0.015	< 0.04	...	0.069 ± 0.01	0.076 ± 0.02	0.29 ± 0.01	...	...
PS1-12bqf	0.13 ± 0.01	...	...	0.050 ± 0.005	0.010 ± 0.004	0.046 ± 0.008	...	...
PS1-11bdn	0.043 ± 0.008	...	...	< 0.03	0.048 ± 0.01	0.13 ± 0.01	...	...

All spectra are shown in Figure 3.4. In addition to our spectra, 7 more objects have spectra with emission lines available in the literature: SN 2010gx (Chen et al. 2013), SN 2007bi (Young et al. 2010), PS1-11bam (Berger et al. 2012), PS1-10afx (Chornock et al. 2013), PS1-10bzj (Lunnan et al. 2013), PTF09cnd (Quimby et al. 2011b) and PS1-11ap (McCrum et al. 2014). Combining the spectra presented here with the literature data leads to line measurements for 19 hosts.

3.3 Comparison Samples

We compare the SLSN host galaxies to galaxies hosting two other types of transients: LGRBs and core-collapse supernovae (CCSNe). For LGRB host galaxies, we use the sample from Svensson et al. (2010), who provide luminosities, stellar masses and star formation rates of 34 hosts at $z \lesssim 1.2$ based on photometry reported in Savaglio et al. (2009) and Fruchter et al. (2006). We supplement these data with spectroscopy from Savaglio et al. (2009), Levesque et al. (2010a,b) and Graham & Fruchter (2013), and also include any LGRB host galaxies at $z \lesssim 1.7$ that are analyzed in these papers but which are not part of the sample in Svensson et al. (2010). This leads to a sample of 44 LGRB hosts in the same redshift range as the SLSNe, of which 17 hosts also have metallicity measurements.

For core-collapse SN hosts, we use the GOODS sample (Fruchter et al. 2006; Svensson et al. 2010). As GOODS was primarily searching for Type Ia SNe, only a subset of the SNe in this sample were spectroscopically typed, with the rest classified as core-collapse based on light curve properties (Strolger et al. 2004) and so subtypes are not available. Still, this sample has two key advantages over local supernova hosts

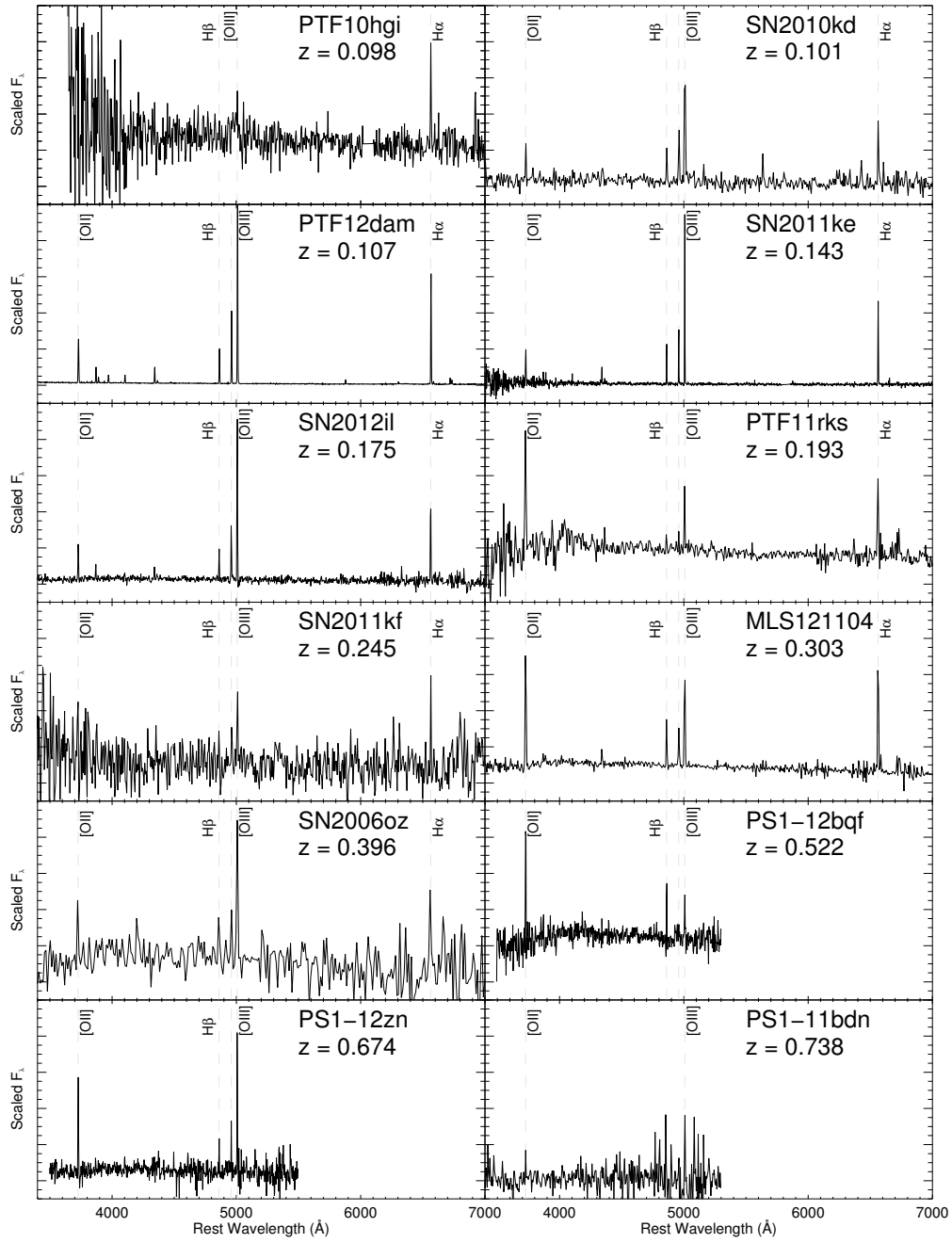

Figure 3.4.—: Spectra of SLSN host galaxies at $z \lesssim 0.75$ (Table 3.4). The main emission lines used for analyzing galaxy properties are marked. In addition to the 12 spectra shown here, an additional 7 hosts have emission line measurements available in the literature, providing spectroscopic information for more than half of our sample.

for our purposes: it is an untargeted sample, and it covers a similar redshift range as the SLSN hosts, thus minimizing effects due to galaxy redshift evolution. The GOODS sample includes luminosities, stellar masses and star formation rates derived from SED fits, but does not include metallicities.

In Figure 3.5 we show the redshift distributions of the three samples, including separately the subsamples for which we have metallicity measurements, as well as the SLSNe from PS1/MDS . The redshift distributions are similar both for the full samples and the spectroscopic subsamples, thereby minimizing any potential galaxy evolution effects.

The SLSN host galaxy data contain both detections and upper limits. To include the information from the non-detections, we use techniques from survival analysis, as implemented in the ASURV statistics package (Lavalley et al. 1992). To estimate and display the distribution function of each quantity, we use the Kaplan-Meier estimator. This is a non-parametric estimator of the cumulutive distribution function, where the weight of each upper limit is distributed uniformly among the detections at lower values. If there are no upper limits, the Kaplan-Meier estimator reduces to the usual empirical distribution function. For each detected value x_i in the sample, N_i is the number of objects (detected or undetected) with $\geq x_i$, and d_i is the number of objects at x_i. The Kaplan-Meier estimator is then given by

$$\widehat{S}_{KM}(x_i) = \prod_{x \geq x_i} \left(1 - \frac{d_i}{N_i}\right). \tag{3.1}$$

In addition, the presence of upper limits means that common statistical tests for two-sample comparisons (e.g., the Kolmogorov-Smirnov test) cannot be applied. To test

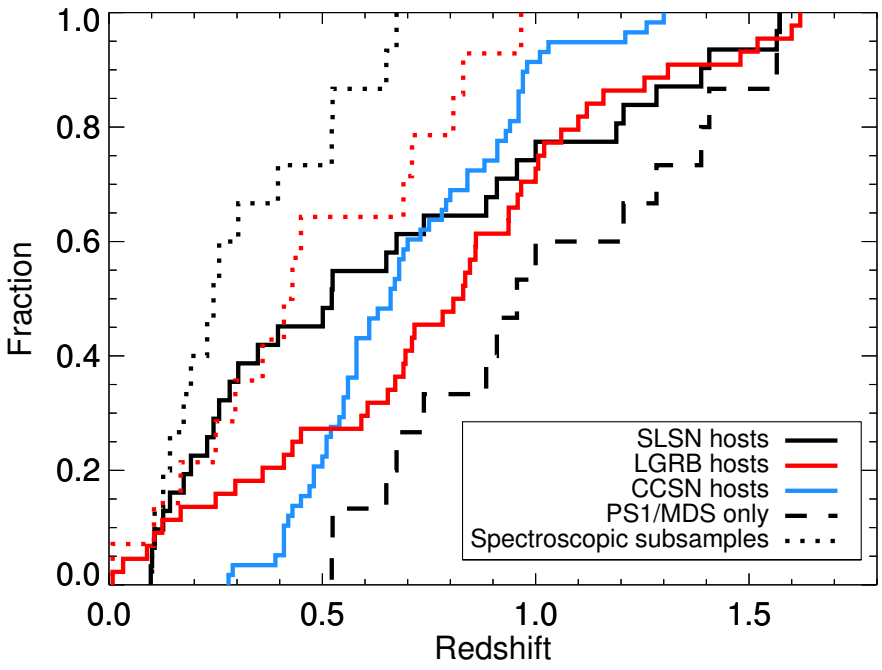

Figure 3.5.—: Redshift distribution of the SLSN host sample (black) and the comparison samples: LGRB host galaxies (red) and the GOODS core-collapse SNe (blue). The dotted lines indicate the subsamples with metallicity measurements for the SLSN and LGRB host galaxies. The dashed black line shows the SLSNe from PS1/MDS only.

the null hypothesis that two samples are drawn from the same underlying distribution, we instead use a generalized Wilcoxon rank-sum test (Peto-Prentice test), also available as part of the ASURV statistics package. The p-values we report are the probabilities for obtaining the calculated value of the test statistic, given the null hypothesis that the two samples are drawn from the same distribution. A 3σ significant difference thus corresponds to $p < 0.003$, whereas a 2σ significant difference corresponds to $p < 0.05$.

For two-sample comparisons where we do not have upper limits in the data, we use a Kolmogorov-Smirnov (K-S) test. The K-S test statistic D is defined as $D = \sup_x |F_1(x) - F_2(x)|$, where F_1 and F_2 are the empirical distribution functions of the two samples. By comparing D to the K-S distribution, we can calculate the probability (p-value) of obtaining a value D under the null hypothesis that the two samples are drawn from the same underlying distribution.

3.4 Physical Properties of SLSN Host Galaxies

For the SLSN hosts with multi-band photometry, we construct galaxy models with the FAST stellar population synthesis code (Kriek et al. 2009). FAST takes as inputs a choice of stellar population synthesis (SPS) models, IMF, reddening law, and a grid of stellar population properties (age, star formation timescale, dust content, metallicity and redshift), and computes model fluxes for each point in the grid. The best-fit parameters are determined by computing the χ^2 at each point in the grid and finding the minimum. The confidence intervals are calibrated using Monte Carlo simulations, taking into account the uncertainties both in the observed fluxes and in the models (Brammer et al. 2008).

We fit the SLSN host galaxies using the Maraston (2005) stellar library, and assuming an exponential star formation history and a Salpeter IMF. We assume a metallicity of $Z = 0.5Z_{\odot}$, unless the metallicity measured from spectroscopy (Section 3.4.6) requires a library with $Z = 0.05Z_{\odot}$ or $Z = 1Z_{\odot}$. If we have a measurement of the extinction from spectroscopy (Section 3.4.1), A_V is restricted to that range but is otherwise allowed to vary freely. In cases where our galaxy spectra show strong emission lines, the filter containing [O III]λ5007 is typically excluded from the fit. The resulting best-fit galaxy SEDs are shown in Figure 3.6.

3.4.1 Extinction

We estimate the reddening by measuring Balmer decrements, using the ratio of Hα to Hβ or Hγ to Hβ (if Hα is not available), assuming intrinsic ratios according to Case B recombination (Osterbrock 1989). The measured emission line fluxes are then corrected for reddening using the extinction curve of Cardelli et al. (1989). We estimate error bars on A_V using the 1σ uncertainties in our line flux measurements. For galaxies where we can measure extinction from Balmer lines, the SED fit for the galaxy is constrained to the 1σ uncertainty range from spectroscopy.

For hosts with no Balmer decrement measurements but with multi-band photometry, we do not restrict the range of allowed extinction in the SED fits. As with the stellar mass, the fitting procedure returns both a best-fit and a 1σ uncertainty range on the extinction. While the uncertainty from the SED fits is generally larger than from our Balmer decrements, we list the extinction estimates from SED modelling in Table 3.6 for the galaxies where no estimate from Balmer lines are available.

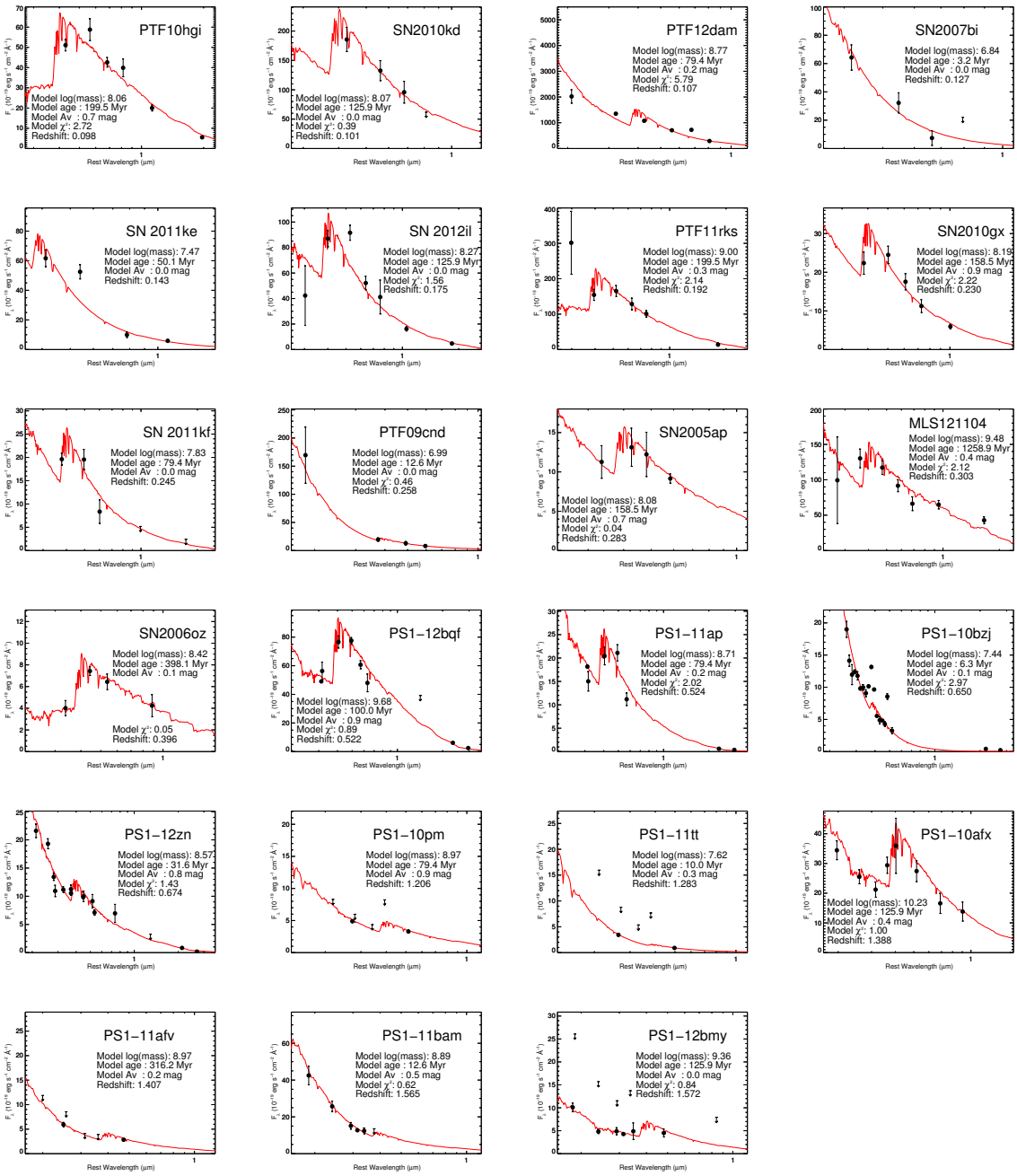

Figure 3.6.—: Model fits to the SEDs of 23 host galaxies with multi-band photometry. The red lines show the model SEDs (calculated using FAST; Kriek et al. 2009), while the black points with error bars show the photometry. The main parameters of the model and fit are listed in each panel, and summarized in Table 3.6.

Table 3.6. Derived Host Galaxy Properties

Object	M_B (mag)	A_V (mag)	$\log(M_*)$ ($M_\odot$)	$\log(M_*), A_V = 0$ ($M_\odot$)	$\log(\text{age}), A_V = 0$ (yr)	SFR ($M_\odot$ yr^{-1})	$12 + \log(\text{O/H})$ T_e method	$12 + \log(\text{O/H})$ R_{23} method
PTF10hgi	-15.78	$1.14^{+0.87}_{-1.14}$	$8.06^{+0.03}_{-0.57}$	$7.87\ ^{+0.58}_{-0.01}$	$8.50^{+1.40}_{-0.02}$	3.8×10^{-2}	...	...
SN 2010kd	-17.15	0.0	$8.07^{+0.15}_{-0.74}$	$8.07^{+0.14}_{-0.15}$	$8.10^{+0.66}_{-0.27}$	2.5×10^{-2}	...	8.16 / 8.71
PTF12dam	-19.25	$0.16^{+0.04}_{-0.04}$	$8.77^{+0.02}_{-0.04}$	...	...	6.4	8.02[a]	8.40
SN 2007bi[b]	-16.40	$0.0^{+1.09}_{-0.00}$	$6.84^{+0.22}_{-0.07}$	$6.84^{+0.17}_{-0.08}$	$6.50^{+0.30}_{-0.50}$	1.1×10^{-2}	...	8.33
SN 2011ke	-16.65	$0.30^{+0.36}_{-0.30}$	$7.47^{+0.14}_{-0.11}$	$7.47^{+0.14}_{-0.07}$	$7.70^{+0.71}_{-0.19}$	0.77	7.59	8.13
SN 2012il	-17.58	$0.0^{+0.23}_{-0.00}$	$8.27^{+0.06}_{-0.07}$	$8.27^{+0.06}_{-0.07}$	$8.10^{+0.16}_{-0.14}$	0.47	...	8.27
PTF11rks	-18.66	$0.30^{+0.47}_{-0.30}$	$9.00^{+0.09}_{-0.21}$	$8.92^{+0.01}_{-0.08}$	$8.40^{+0.17}_{-0.10}$	0.49	...	8.42 / 8.57
SN 2010gx[c]	-16.98	$0.96^{+0.08}_{-0.08}$	$8.19^{+0.06}_{-0.07}$	...	...	1.30	7.46	8.27
SN 2011kf	-16.87	0.0	$7.83^{+0.23}_{-0.11}$	$7.83^{+0.28}_{-0.15}$	$7.90^{+1.06}_{-0.14}$	0.14	...	8.05 / 8.84
PTF09cnd[d]	-16.75	$0.00^{+0.54}_{-0.00}$	$6.99^{+0.51}_{-0.12}$	$6.99^{+0.38}_{-0.12}$	$7.10^{+0.71}_{-0.22}$	0.22	...	8.33 / 8.64
SN 2005ap	-16.73	$0.70^{+2.45}_{-0.70}$	$8.08^{+0.56}_{-0.57}$	$8.17^{+0.22}_{-0.28}$	$9.00^{+0.41}_{-1.03}$	...	...	...
MLS121104	-19.39	0.0	$9.48^{+0.04}_{-0.06}$	$9.44^{+0.14}_{-0.07}$	$9.10^{+0.38}_{-0.28}$	1.27	...	8.80
PTF09cwl	> -16.5	...	< 7.9	...	...	...	...	...
SN 2006oz	-16.96	0.0	$8.42^{+0.64}_{-0.16}$	$8.43^{+0.55}_{-0.14}$	$8.70^{+1.17}_{-0.24}$	0.23	...	8.00 / 8.88

Table 3.6—Continued

Object	M_B (mag)	A_V (mag)	$\log(M_*)$ ($M_\odot$)	$\log(M_*), A_V = 0$ ($M_\odot$)	$\log(\text{age}), A_V = 0$ (yr)	SFR ($M_\odot$ yr^{-1})	$12 + \log(\text{O/H})$ T_e method	$12 + \log(\text{O/H})$ R_{23} method
PTF09atu	> -16.7	...	< 7.9	...	...	...	...	...
PS1-12bqf	-20.28	$0.90^{+0.39}_{-0.90}$	$9.68^{+0.13}_{-0.10}$	$9.60^{+0.15}_{-0.04}$	$8.40^{+0.59}_{-0.02}$	1.73	...	7.84 / 9.04
PS1-11ap[e]	-18.83	$0.20^{+0.32}_{-0.20}$	$8.71^{+0.15}_{-0.12}$	$8.69^{+0.06}_{-0.10}$	$8.00^{+0.28}_{-0.10}$	0.49	...	8.34 / 8.64
PS1-10bzj[f]	-17.90	$0.0^{+0.21}_{-0.00}$	$7.44^{+0.11}_{-0.05}$	$7.47^{+0.10}_{-0.11}$	$7.10^{+0.22}_{-0.30}$	4.2	7.80	8.30
PS1-12zn	-18.75	$0.0^{+2.60}_{-0.00}$	$8.57^{+0.24}_{-0.32}$	$8.85^{+0.03}_{-0.35}$	$8.90^{+0.07}_{-1.10}$	6.7	...	8.45
PS1-11bdn	-17.35	$1.0^{+1.88}_{-1.00}$	$8.11^{+0.77}_{-0.59}$	$8.23^{+0.45}_{-0.57}$	$8.80^{+0.56}_{-1.17}$	1.54	...	...
PS1-13gt	> -18.9	...	< 8.7	...	...	< 1.6	...	...
PS1-10awh	-16.47	...	$7.76^{+0.33}_{-0.65}$	...	...	0.18	...	...
PS1-10ky	> -16.3	...	< 7.6	...	...	0.4	...	...
PS1-11aib	> -19.3	...	< 8.9	...	...	< 2.8	...	...
SCP06F6[g]	> -16.9	...	< 8.0	...	...	...	...	...
PS1-10pm	-19.29	$0.90^{+0.10}_{-0.90}$	$8.97^{+0.32}_{-0.34}$	$8.95^{+0.34}_{-0.13}$	$8.30^{+0.95}_{-0.43}$	1.5	...	...
PS1-11tt	-18.15	$0.30^{+1.01}_{-0.30}$	$7.62^{+0.73}_{-0.16}$	$7.74^{+0.18}_{-0.28}$	$7.50^{+0.34}_{-0.52}$	1.1	...	...
PS1-10afx[h]	-22.03	$0.40^{+2.00}_{-0.40}$	$10.23^{+0.16}_{-0.12}$	$10.26^{+0.03}_{-0.07}$	$9.01^{+0.16}_{-0.31}$	13	...	...

Table 3.6—Continued

Object	M_B (mag)	A_V (mag)	$\log(M_*)$ ($M_\odot$)	$\log(M_*), A_V = 0$ ($M_\odot$)	$\log(\text{age}), A_V = 0$ (yr)	SFR ($M_\odot$ yr^{-1})	$12 + \log(\text{O/H})$ T_e method	$12 + \log(\text{O/H})$ R_{23} method
PS1-11afv	-19.50	$0.20^{+1.51}_{-0.20}$	$8.97^{+0.22}_{-0.56}$	$9.01^{+0.16}_{-0.31}$	$8.70^{+0.23}_{-0.98}$	2.2	...	...
PS1-11bam[i]	-20.89	$0.50^{+0.61}_{-0.50}$	$8.89^{+1.07}_{-0.25}$	$9.59^{+0.53}_{-0.73}$	$8.60^{+0.61}_{-1.20}$	6.0	...	...
PS1-12bmy	-20.36	$0.0^{+0.76}_{-0.00}$	$9.36^{+0.60}_{-0.11}$	$9.36^{+0.30}_{-0.11}$	$8.10^{+0.60}_{-0.11}$	2.6	...	...

[a]From Chen et al., in prep.

[b]Based on data in Young et al. (2010).

[c]Based on data in Chen et al. (2013).

[d]Metallicity and SFR derived from a spectrum published in Quimby et al. (2011b); see Section 3.7.2 for details.

[e]Based on data in McCrum et al. (2014).

[f]Based on data in Lunnan et al. (2013).

[g]Based on data in Barbary et al. (2009).

[h]Based on data in Chornock et al. (2013).

[i]Based on data in Berger et al. (2012).

While a wide range of A_V is allowed by the SED fits, we find that with a few exceptions the data are consistent with zero extinction. We therefore also compute a set of galaxy models that assume zero extinction. Table 3.6 also lists the stellar mass and population age for these fits.

3.4.2 Absolute Magnitudes

We calculate absolute B-band magnitudes by transforming the galaxy models to the rest frame and integrating over the B-band filter curve. We also use these models to calculate a mean k-correction as a function of redshift, and use this to determine absolute magnitudes or upper limits for the objects with only single-band photometry or non-detections.

In Figure 3.7 we show the resulting B-band absolute magnitudes, both as a function of redshift and the cumulative distribution using the Kaplan-Meier estimator. The overall range is -16 to -22 mag, but the population is strikingly low-luminosity with a median absolute magnitude of $\langle M_B \rangle \approx -17.6$ mag ($\approx 0.05 L_*$; Willmer et al. 2006). A large fraction of the lowest-luminosity hosts are found at the low-redshift end: when we consider the PS1 sample + SCP06F6 separately ($z \gtrsim 0.5$), we find a median magnitude of -18.8 mag ($\approx 0.1 L_*$), whereas the sample at lower redshifts (all the non-PS1 hosts, and excluding SCP06F6) has a median magnitude of -17.0 mag ($\approx 0.04 L_*$). This may indicate that the typical host of a SLSN shifts to fainter galaxies at lower redshift, an effect one might expect if, for example, low metallicity is a driving ingredient for producing SLSNe. As the data at high and low redshift come from different surveys, however, this could also reflect different survey or follow-up strategies.

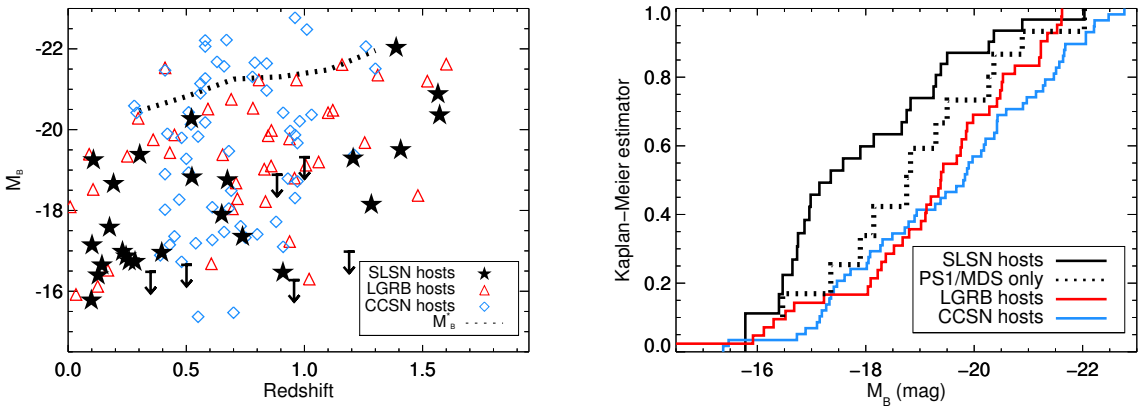

Figure 3.7.—: Left: Absolute B-band magnitudes as a function of redshift for the SLSN host galaxies (black stars and arrows), LGRB host galaxies (red triangles) and GOODS CCSN hosts (blue diamonds). Also shown is the luminosity function parameter M_B^* for blue galaxies as a function of redshift (dotted line; Willmer et al. 2006). Right: The resulting distribution functions of the three populations, as calculated by the Kaplan-Meier estimator to include the information contained in upper limits. The dotted line shows only the hosts from the PS1/MDS subsample, illustrating how the difference between the SLSN hosts and the other populations is driven by the low-redshift end of the sample.

The highest-luminosity (and only $\sim L_*$) host galaxy in this sample is the host of PS1-10afx, which was also an outlier in terms of SN properties (Chornock et al. 2013). It is debated whether this object was a true SLSN, or a normal Type Ia SN lensed by a foreground galaxy (Quimby et al. 2013b). However, we note that given our sample size this one outlier does not drive our results – in fact, excluding it would lead us to find an even lower median luminosity.

As is apparent from Figure 3.7, the SLSN hosts are also significantly less luminous as a population than both LGRB hosts and CCSN hosts in the same redshift range. Applying the generalized Wilcoxon test, we find that the SLSN hosts are not consistent with being drawn from the same underlying distribution as either CCSN hosts or LGRB hosts in terms of their luminosities. The significance levels are listed in Table 3.7. If we consider the PS1/MDS subsample separately, however, the luminosity distribution is consistent with both the LGRB host sample and the CCSN sample ($p = 0.26$ and 0.15 respectively). The change in significance level results from both the PS1/MDS hosts being higher luminosity and the fact that the sample size is smaller.

Table 3.7. Results (p-values) from Statistical Tests

Property	SLSN-LGRB	SLSN-CCSN	SLSN-LGRB (PS1/MDS only)	SLSN-CCSN (PS1/MDS only)	Test used
M_B	0.0013	7×10^{-5}	0.26	0.15	Rank-Sum
Mass	0.007	1.6×10^{-7}	0.17	0.0009	Rank-Sum
SFR	0.067	4×10^{-4}	0.79	0.076	Rank-Sum
sSFR	0.55	0.004	0.53	0.009	Kolmogorov-Smirnov
Hβ EW	0.75	...	...	...	Kolmogorov-Smirnov

3.4.3 Stellar Masses

The FAST SED fitting code provides the stellar mass of the best-fit model, and the 1σ confidence interval. The derived stellar masses and uncertainties are listed in Table 3.6. For host galaxies where we either only have upper limits, or detections in too few filters for an SED fit, we use the galaxy models to calculate a median mass-to-light ratio and use this to convert our single-band measurements into a mass estimate; in these cases the uncertainties quoted reflect the spread in possible mass-to-light ratios.

The resulting stellar masses are shown in Figure 3.8, both as a function of redshift and the cumulative distribution. As with the luminosities, the SLSNe are generally found in low-mass galaxies, with a median stellar mass of $\langle M_* \rangle \approx 2 \times 10^8$ $M_\odot$. There is a range of three orders of magnitude in mass, from 10^7 to 10^{10} $M_\odot$, and the same trend towards smaller galaxies at lower redshift is also seen in the stellar masses. Again, the SLSN hosts are offset from both the CCSN hosts and the LGRB hosts, and the difference between the SLSN and CCSN host galaxies is significant both when comparing the full samples and when considering the full sample and the PS1/MDS subsample only ($p = 1.5 \times 10^{-7}$ and 9×10^{-4}, respectively). The difference between SLSN hosts and LGRB hosts is significant at the 2.7σ level ($p = 0.007$) when comparing to the full sample of SLSN hosts, but not significant when comparing to the PS1/MDS data only ($p = 0.17$).

3.4.4 Star Formation Rates

Star formation rates (SFR) are derived using a variety of methods, depending on the available data for each host galaxy. If available, we calculate the SFR using the Hα emission line flux, according to the relation SFR $= 7.9 \times 10^{-42} L_{\mathrm{H}\alpha}(\mathrm{erg\ s^{-1}})$ (Kennicutt

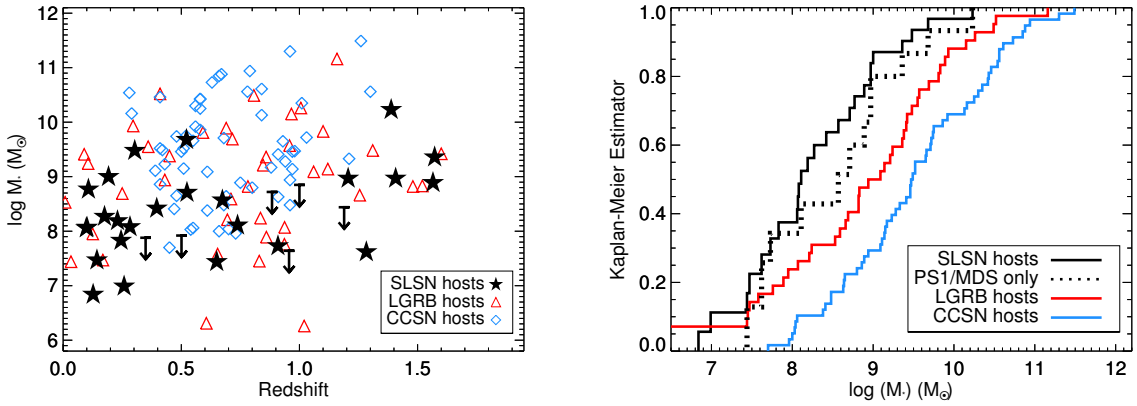

Figure 3.8.—: Left: Stellar mass as a function of redshift for the SLSN host galaxies (black stars and arrows), LGRB host galaxies (red triangles) and CCSN hosts (blue diamonds). Right: The resulting distribution functions of the three populations. The difference between the SLSN and CCSN hosts is statistically significant, both when considering the full SLSN sample and the PS1/MDS subsample only. While having a lower median mass, the SLSN hosts are marginally consistent with being drawn from the same distribution as the LGRB hosts.

1998). If Hα is not available but Hβ and Hγ are both detected, we calculate the expected Hα flux using the measured reddening and Hβ flux, assuming Case B recombination. For some galaxies at higher redshift no Balmer lines are available, but we detect the [O II]λ3727 emission line. For these galaxies, we use SFR $= 1.4 \times 10^{-41} L_{[\rm OII]}$(erg s^{-1}) (Kennicutt 1998).

Finally, for galaxies where we do not have line-based SFR estimates, we calculate a SFR based on the rest-frame UV flux. For galaxies at redshift $z \gtrsim 0.6$, g-band covers rest-frame UV, and we use SFR $= 1.4 \times 10^{-28} L_\nu$(erg s^{-1} Hz^{-1}) (Kennicutt 1998). We use the observed fluxes without correcting for extinction for this calculation, since the extinction is not particularly well constrained by the SED fits and also consistent with zero in most galaxies (Section 3.4.1; Table 3.6). We also use this relation to calculate upper limits for the galaxies with rest-frame UV non-detections. In general, we find that the different diagnostics agree within a factor of $2-3$. For four galaxies (PTF09cwl, PTF09atu, SN 2005ap and SCP06F6) we have neither emission line measurements nor rest-frame UV data, and we therefore lack SFR estimates.

The resulting star formation rate distributions are plotted in Figure 3.9. The median value for the SLSN host sample is $\langle \rm SFR \rangle \approx 1$ M$_\odot$ yr^{-1} and varies from $10^{-2} - 10$ M$_\odot$ yr^{-1}. Consistent with their lower luminosities and stellar masses, the SLSN hosts also have slightly lower absolute SFRs than the LGRB and CCSN hosts. Only the difference between the CCSN and SLSN hosts is statistically significant (Table 3.7).

We also consider the specific star formation rate (sSFR $\equiv$ SFR$/M_*$), which is the inverse of the time required to double the stellar mass of a galaxy given its current SFR. Since we cannot constrain the sSFR if we only have upper limits on both the SFR and

the stellar mass, only detected galaxies are considered for this analysis (23 hosts). The distributions are shown in Figure 3.10. Both at high and low redshifts, the SLSNe show a wide range of sSFRs, with a median of ~ 2 Gyr^{-1}, corresponding to a characteristic doubling time of $\sim$500 Myr. Again their distribution is statistically indistinguishable from that of the LGRB hosts: applying a Kolmogorov-Smirnov test, we find that the LGRB and SLSN distributions are consistent with each other ($p = 0.55$). The SLSN and CCSN distributions are not ($p = 0.004$), mainly due to the tail of high sSFRs that is not observed in the CCSN hosts.

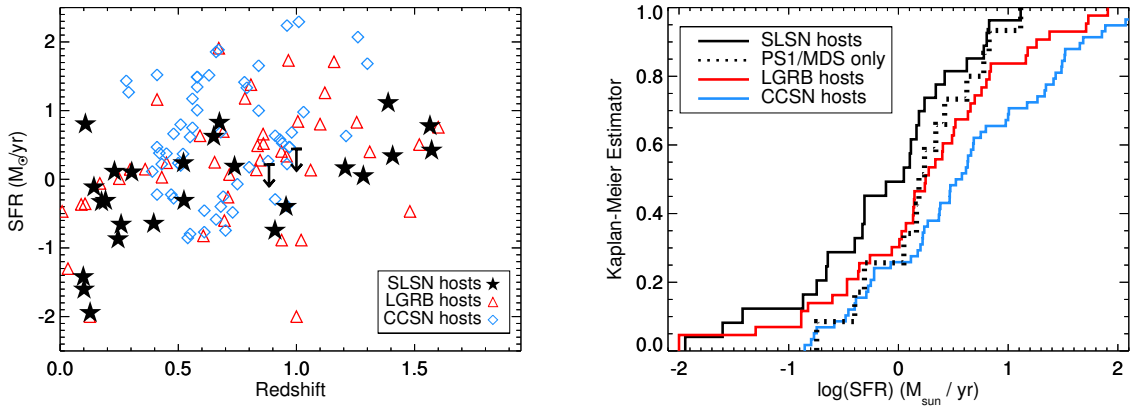

Figure 3.9.—: Left: Star formation rates as a function of redshift for the SLSN host galaxies (black stars and arrows), LGRB host galaxies (red triangles) and GOODS CCSN hosts (blue diamonds). Right: The resulting distribution functions of the three populations. The difference between the SLSN and CCSN hosts is statistically significant, but the difference between LGRB and SLSN hosts is not.

3.4.5 Hβ and [O III] Equivalent Widths

One striking characteristic of our SLSN host spectra (Figure 3.4) is the strong nebular emission lines. The equivalent width of Hβ is of particular interest, as it generally

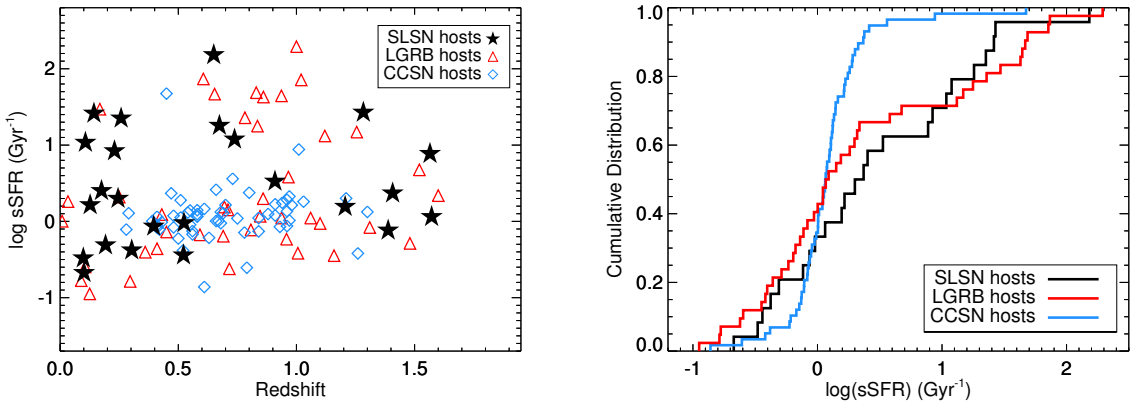

Figure 3.10.—: Left: Specific star formation rates as a function of redshift for the SLSN host galaxies (black stars and arrows), LGRB host galaxies (red triangles) and GOODS CCSN hosts (blue diamonds). Right: The resulting distribution functions of the three populations. As we cannot place limits on the sSFR of undetected objects, only galaxies that are actually detected are plotted here. The three populations have similar medians, but both the LGRB hosts and SLSN hosts show a tail to high specific star formation rates that is not seen in the CCSN host population.

decreases monotonically with the age of the young stellar population (Copetti et al. 1986; Schaerer & Vacca 1998). We show the distribution of Hβ EWs in our sample in Figure 3.11, compared to LGRB hosts (Levesque et al. 2010a,b) and a sample of star-forming field galaxies at $z \approx 0.3 - 1.0$ from the Team Keck Redshift Survey (TKRS; Wirth et al. 2004; Kobulnicky & Kewley 2004). The SLSN and LGRB host distributions are similar (a KS test yields $p = 0.75$), indicating the presence of similar-age young stellar populations in the two groups. The comparison to TKRS shows that the Hβ EWs of the SLSN hosts are also higher than what would be expected if they were drawn from the general field galaxy population, and this remains true also if we weight the field galaxy distribution by star formation rate.

We also note that several of the SLSN hosts exhibit particularly strong [O III]λ5007 emission. While the strength of this line is sensitive to a number of physical parameters, including ionization parameter and metallicity, it serves to illustrate how the SLSN host galaxies are different from the normal star-forming field galaxies. The right panel of Figure 3.11 shows the [O III] equivalent widths measured, compared to the TKRS sample and a sample of Green Pea galaxies from SDSS. The Green Peas are a class of compact, intensely starforming galaxies, originally selected by their unusual colors that is due to extreme [O III] emission (Cardamone et al. 2009). We see that the distribution of [O III] EWs for SLSN hosts galaxies is clearly skewed towards higher values than what would be expected simply drawing from the star-forming population over this redshift range, with about one third of the SLSN sample showing [O III] EWs comparable to what is seen in the lower range of Green Pea galaxies.

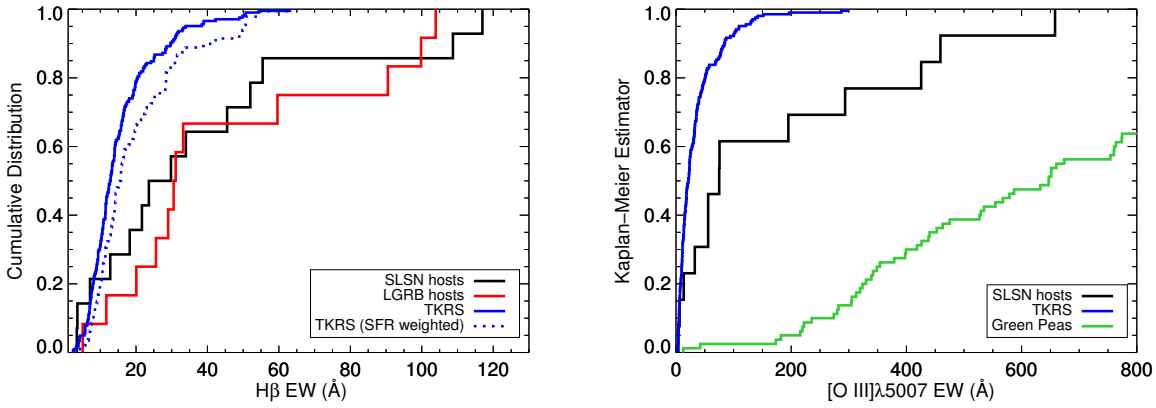

Figure 3.11.—: Left: Hβ equivalent widths for the SLSN host sample (black), a sample of LGRB hosts (red; Levesque et al. 2010a,b), and the Team Keck Redshift Survey (TKRS) sample of field galaxies at $z \approx 0.3 - 1.0$ (blue; Wirth et al. 2004; Kobulnicky & Kewley 2004). The SLSN host sample and LGRB host sample have a similar Hβ EW distribution, suggesting similar young stellar population ages. Right: [O III]λ5007 equivalent widths for our SLSN host sample (black), the TKRS sample, and "Green Pea" galaxies from SDSS, a class of compact, intensely star-forming galaxies characterized by extreme [O III]λ5007 emission (Cardamone et al. 2009). The SLSN hosts generally show much stronger [O III]λ5007 emission than the field star-forming galaxies, with about one third of the sample within the Green Pea regime.

3.4.6 Metallicity

There are a number of metallicity indicators available in the literature, depending on redshift range and the detected emission lines. However, there are known systematic offsets between them (e.g., Kewley & Ellison 2008). We therefore focus on the R_{23} diagnostic, which is available over the entire redshift range of interest, and we use the calibration in Kobulnicky & Kewley (2004). This ensures consistent comparison within the SLSN host sample, and to other galaxy samples using the same diagnostics.

R_{23} is a double-valued diagnostic, and additional information is needed to break the degeneracy between the high-Z and low-Z branches. We accomplish this in either of the following ways. First, if the [O III]λ4363 line is detected, we assume the lower-metallicity branch, as this temperature-sensitive line is not present at high metallicities. Second, when detected, we use the ratio of [N II]λ6584 to [O II]λ3727 (or [N II]λ6584 to Hα, if the reddening is not well constrained) to break the degeneracy. In some cases, [N II]λ6584 is not detected, but the upper limit on this ratio is sufficiently low to allow us to place the host galaxy on the lower metallicity branch. Finally, in some cases the value of R_{23} falls in the turnover region, and either branch gives a value in the range $12 + \log(\mathrm{O/H}) \sim 8.3 - 8.6$. If we cannot formally break the degeneracy, both possible values are listed. However, we note that the low masses of most SLSN host galaxies ($\sim 10^8$ $M_\odot$) suggest that the lower branch solution is more likely over the supersolar metallicity given by the upper-branch solution. Indeed, of the eight galaxies where we can robustly break the degeneracy, only one (MLS121104) is found to lie on the upper branch.

In galaxies were the auroral [O III]λ4363 line is detected we can also calculate a

"direct" metallicity through the electron temperature (T_e) method. We use the `temden` task in the IRAF `nebular` package (Shaw & Dufour 1994) to determine the temperature of O^{++} and the electron density (n_e), from the ratio of the [O III] lines and [S II] lines respectively. The O^+ temperature is then calculated assuming the relation from Stasińska (1982). Finally, we determine O^+/H and O^{++}/H using the relations in Shi et al. (2006). Four galaxies in our sample have detected [O III]λ4363 emission: PS1-10bzj (Lunnan et al. 2013), SN 2010gx (Chen et al. 2013), SN 2011ke and PTF12dam. The host of PTF12dam exhibits both auroral [O III] and [O II] lines; a detailed analysis of this host will be presented in Chen et al. (in preparation).

The distribution of R_{23} metallicities is plotted in Figure 3.12. As we cannot formally break the R_{23} degeneracy in a number of cases, the dotted and dashed lines show what the distribution would be if we assumed all upper-branch or all lower-branch solutions for these galaxies. The solid lines assume the lower branch solution for host galaxies with a stellar mass lower than 10^8 $M_\odot$, and an equal probability of lower/upper branch solutions for the remaining objects. Taking this as the best estimate of the true distribution, we find a median metallicity of 8.35 ($\approx 0.45 Z_\odot$). Also shown in Figure 3.12 are LGRB hosts, and hosts of Type Ib/c and Ic-BL (broad-lined) SNe from untargeted surveys (Sanders et al. 2012a). The SLSN host metallicity distribution is statistically consistent with that of the LGRB hosts and inconsistent with the SN Ib/c hosts, which are generally found at higher metallicities. We note that the SN samples shown here are local (median redshift $\langle z \rangle \approx 0.036$), as the GOODS CCSN sample does not have metallicity measurements.

Figure 3.13 shows the SLSN hosts with metallicity measurements on a mass-metallicity (M-Z) diagram, compared to LGRB host galaxies, the local M-Z relation from SDSS (Tremonti et al. 2004), local core-collapse SN host galaxies from the compilation

of Kelly & Kirshner (2012), and a sample of emission-line selected galaxies at redshift $z \sim 0.6 - 0.7$ (Henry et al. 2013). The SLSN hosts are predominantly found at low masses and metallicities, although there is clearly a wide range – the host of MLS121104, for example, has well detected [N II] lines that place it on the upper branch in the R_{23} diagnostic, at approximately solar metallicity. This shows that any metallicity preference in producing SLSNe does not take the form of an absolute cutoff; the same is true for LGRBs (e.g., Levesque et al. 2010c).

It is also interesting to note that two of the host galaxies with the highest measured metallicities (MLS121104 and PTF11rks) also exhibit some of the largest offsets from the galaxy center to the SN explosion site (Figure 3.1). If there are metallicity gradients present in these hosts (e.g., Zaritsky et al. 1994; Modjaz et al. 2011), it is still possible that the SNe exploded in an environment with a lower metallicity, closer to the median of the SLSN host sample. Indeed, when comparing line ratios along the slit in the host of PTF11rks, we do find indications of a decreasing R_{23} ratio in an extraction region in the outskirts compared to at the center of the galaxy. However, the poor signal-to-noise ratio in the Hβ line prevents us from making a more quantitative statement. We also note that the majority of our galaxies are of such a small angular size (Figure 3.1) that in most cases there is little practical difference between metallicity determined for the galaxy as a whole compared to the explosion site.

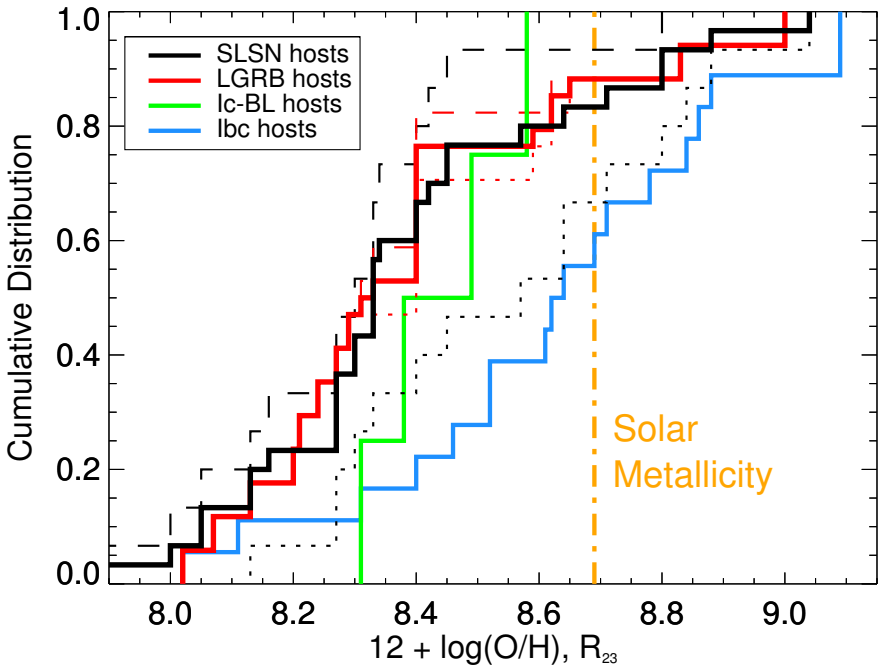

Figure 3.12.—: Metallicity distribution of the SLSN host galaxies (black) and LGRB host galaxies (red). Also shown are hosts of Type Ic-BL (green) and Ib/c (blue) SNe from untargeted surveys (Sanders et al. 2012a). For a number of the SLSN hosts, we cannot formally break the R_{23} degeneracy; the dashed and dotted line shows the resulting distributions if we assume that all of the hosts reside on the lower or upper branches, respectively. The solid line is the resulting distribution when assuming hosts with a stellar mass $\lesssim 10^8$ $M_\odot$ fall on the low-metallicity branch, and assigning equal probability to the upper/lower branch solutions for the rest. This distribution is statistically consistent with the LGRB host galaxies, but not with the Type Ib/c SN hosts.

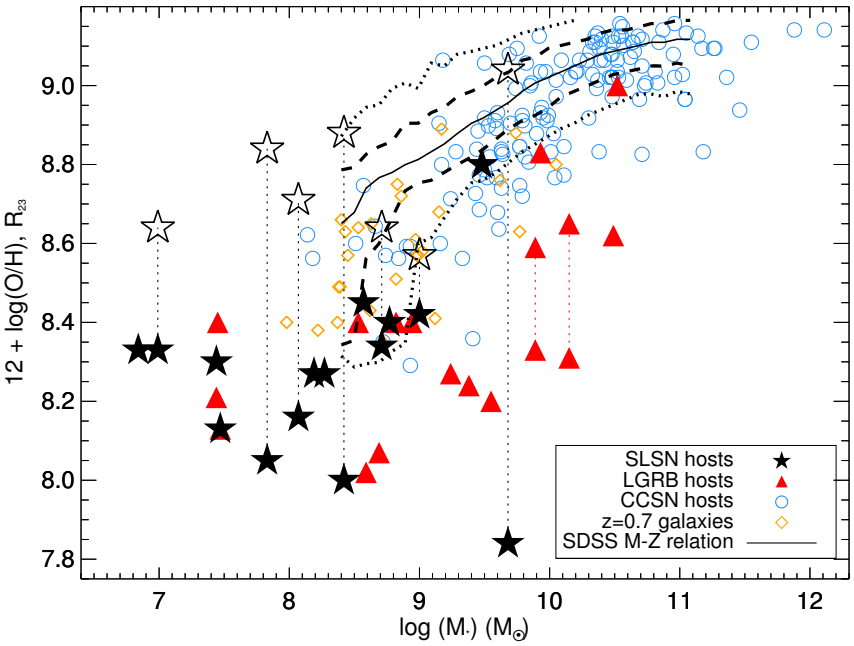

Figure 3.13.—: Mass-metallicity diagram comparing the SLSN hosts (black stars) to LGRB hosts (red triangles), local CCSN hosts (blue circles), the SDSS M-Z relation (black lines), and a galaxy sample at redshift $z \sim 0.7$ (orange diamonds). All metallicities are on the Kobulnicky & Kewley (2004) scale to facilitate comparison. Points joined by lines represent cases where the R_{23} degeneracy could not be formally resolved, and so both the upper- and lower-branch solutions are plotted.

3.5 Implications for SLSN progenitors

We have shown that the H-poor SLSNe are preferentially found in low-luminosity, low-mass, low-metallicity hosts with high sSFR and evidence for very young stellar populations based on line EWs. However, as these properties are found to be correlated in the general galaxy population, it is not clear which is the driving factor in producing SLSNe. This is an on-going debate regarding LGRBs, and many of the same arguments

are relevant to the SLSNe.

A number of factors point towards metallicity being a key ingredient in producing both H-poor SLSNe and LGRBs. They overall show a preference for low-metallicity environments compared to CCSNe as well as a preference for faint, blue irregular galaxies (Fruchter et al. 2006; Stanek et al. 2006; Modjaz et al. 2008). If star formation were the only factor required for producing SLSNe, we would expect them to also occur in star-forming regions of more massive galaxies, and so their galaxy distribution to be more similar to the GOODS CCSN sample. We also note that the potential redshift evolution we see in our SLSN host sample is consistent with a metallicity-based selection: since the mass-metallicity relation evolves with redshift, shifting to lower metallicities for a given stellar mass at higher redshift (e.g., Zahid et al. 2013 and references therein), we expect a trend towards lower-mass galaxies at lower redshift for a given metallicity. This is indeed what we observe for the SLSN hosts (Figures 3.7 and 3.8).

On the other hand, we do observe a range of metallicities in the SLSN host galaxies, and we do not find evidence of a metallicity cutoff; the same is true for LGRB hosts (e.g., Levesque et al. 2010b,c). While there are LGRB hosts at higher metallicities, as a population they tend to fall below the local M-Z relation (Figure 3.13). It has been argued that this could be a result of a proposed anticorrelation between SFR and metallicity at a given stellar mass; the driving factor then would be star formation rather than metallicity (Mannucci et al. 2010, 2011; Kocevski & West 2011). However, even when taking into account the LGRBs in heavily dust-obscured galaxies, the number of LGRBs in massive galaxies still falls short of what would be expected in a purely star formation-selected sample (Perley et al. 2013), suggesting that the LGRB rate is also a function of metallicity. A similar argument can be made for SLSNe: while it is not clear

whether they fall below the M-Z relation (Figure 3.13), they do exclusively populate the low-mass end of this diagram. Regardless of whether they are low-metallicity for their mass, then, they are clearly not simply following the star-forming population.

In terms of progenitor models, a low-metallicity environment preference could be linked to a requirement for high angular momentum in the core. Rotation is thought to be the link between LGRBs and metallicity from the theoretical side, where the GRB is a result of accretion onto a newly formed black hole, following the collapse of a rapidly rotating, massive star (e.g., MacFadyen & Woosley 1999). Higher metallicities are associated with increased mass loss through stellar winds (Vink & de Koter 2005) which strips the core of angular momentum, and so it has been proposed that the observed preference for low-metallicity environments for LGRBs is linked to the need to maintain high rotation (Yoon & Langer 2005; Langer & Norman 2006). A similar argument can be applied to the H-poor SLSNe in the scenario where the energy source is a magnetar: in order to reproduce the observed timescales and luminosities rapid initial neutron star spin is required, as well as a strong magnetic field (Kasen & Bildsten 2010; Chomiuk et al. 2011; Lunnan et al. 2013; Inserra et al. 2013). Alternatively, the central engine could also be a black hole, where large core angular momentum could allow material which remains bound in the explosion to form an accretion disk and inject energy into the supernova (Dexter & Kasen 2013). However, this line of reasoning does not explain how the SLSN progenitors shed their hydrogen envelopes and why that mechanism would not remove angular momentum; this is a puzzle also regarding LGRBs, which are associated with Ic-BL SNe.

We note that while SLSNe and LGRBs seem to be found in similar environments, it does not follow that their progenitors must share common properties, but rather

that the environmental causes for producing massive stars that end their lives as a LGRB or SLSN are likely similar. For example, if the high-mass end of the initial mass function (IMF) varies with environment (e.g., Bastian et al. 2010; Kroupa et al. 2013 and references therein), that could potentially explain the trends we see without needing to invoke a metallicity dependence. Another possibility is dynamical effects: van den Heuvel & Portegies Zwart (2013) speculate that both LGRBs and SLSNe are end products of different dynamical processes in young, dense star clusters, with SLSNe being the result of runaway stellar collisions – our findings at least support their premise that both SLSNe and LGRBs are associated with young star-forming regions.

Due to the expected suppression of stellar winds in low-metallicity progenitors, one might initially expect that an interaction model would be harder to explain in a low-metallicity context. However, the mass loss required to explain the observed light curves of SLSNe is too large to be explained by line-driven stellar winds (Chevalier & Irwin 2011; Chomiuk et al. 2011; Lunnan et al. 2013). A proposed alternative mechanism for ejecting the necessary mass shells is a pulsational pair-instability (e.g., Woosley et al. 2007; Chatzopoulos & Wheeler 2012b), a phenomenon that may be sensitive to both the rotation and metallicity of the progenitor. A binary star channel has also been proposed (Chevalier 2012), where the mass loss is driven by common envelope evolution of a compact object within the envelope of a massive star, and the SN itself is triggered by inspiral of the compact object to the core of the companion star, though it is not clear why such a channel would be environment-dependent as we are finding in this work. We note that whatever the scenario, at the very least our findings suggest that if H-poor SLSNe are powered by strong circumstellar interaction, the mechanism that causes the mass loss is likely to be operating preferentially in low-metallicity environments.

3.5.1 Possible Selection Effects

Extinction

While we have taken care to compare events from untargeted surveys over a similar redshift range, one might worry that selection effects could still be driving the differences we see between the SLSN hosts and the other galaxy populations. One such effect is that the SLSN host sample is likely to be biased against host galaxies with high extinction, since it is selected for hosting a population of blue optical transients. This is consistent with what we find in our SED fits, in that virtually all the host galaxies in our sample are consistent with zero or moderate extinction ($\lesssim 0.5$ mag). This may partially explain the marginally significant difference in galaxy luminosities seen between the SLSN and LGRB hosts, since LGRBs are selected via gamma-rays and therefore much less sensitive to dust extinction. The mid-IR transient SDWFS-MT-1 was proposed to be a dust-enshrouded SLSN (though of unknown type; Kozłowski et al. 2010), suggesting that there may exist a population of these objects in obscured environments that current optical surveys are missing. This would only impact our result if such a population was hosted in significantly different galaxies, however; in this one known case, the host was still a low-metallicity dwarf galaxy.

Extinction is unlikely to explain the difference between the SLSN hosts and the CCSN sample though, as this sample is also selected optically and would suffer from a similar extinction bias. Conversely, if the SLSN hosts were indeed drawn from the same population as CCSN hosts, it would mean that current surveys are only detecting a small fraction of the SLSNe – only $\sim 15\%$ of the GOODS CCSNe were found in galaxies fainter than $M_B = -17.3$ mag, the median of the SLSN host galaxy sample. As explored

in Section 3.5.1, we do not consider this to be a likely scenario.

Incomplete Follow-Up

We also note that while all the samples we are comparing come from untargeted surveys, the spectroscopic follow-up is not complete. In selecting the subsample of objects that will be followed up and confirmed spectroscopically, both light curve and host galaxy properties are typically considered, and this could therefore introduce biases based on host galaxy properties. Here, we can only address how the PS1/MDS sample was selected. The targets included in this paper were primarily chosen for spectroscopic follow-up by some combination of long rise times and/or being significantly brighter than any apparent host. The former effect arises both due to the intrinsically long rise of many SLSNe, as well as due to time dilation since the redshift distribution of the PS1/MDS sample peaks at $z \approx 1$. This selection could bias us towards lower-luminosity galaxies if faster-rising SLSNe were preferentially found in brighter host galaxies; exploring any such correlations is outside the scope of this paper however.

The second effect of preferentially following up faint-host/high-contrast objects is potentially more problematic for the results presented here. We know that our sample is not complete – the question is whether we missed objects systematically due to galaxy properties, and if so, whether the effect is large enough to influence our results. To quantify this, we carried out a number of tests. First, if we assume that the true distribution of SLSN host galaxies was that of the GOODS CCSN host galaxies, we can simulate the effects of a (crude) selection bias by excluding all the CCSN host galaxies brighter than a given magnitude, and ask what fraction of objects we must be missing.

We find that to make the GOODS CCSN host galaxy mass distribution marginally consistent with that of the SLSN host galaxies, we must set the cut at $V = 23.5$ mag, excluding half of the GOODS sample. This implies that if selection effects were the only driver behind our result, we should have systematically missed about half of the SLSNe in PS1/MDS.

To quantify how many such potential bright-host SLSNe we could have missed, we searched the entire PS1/MDS photometric database for transients that had good-quality light curves (bright enough to be considered for spectroscopy) and long observed rise times, but that were not selected for spectroscopic follow-up. We excluded from this sample any object that had a light curve consistent with a Type Ia SN, as determined by PSNID (Sako et al. 2011). We tuned our cuts such that the search would let through all the PS1 SLSNe where the rise is observed, with the exception of the fastest-rising objects such as PS1-10bzj (Lunnan et al. 2013). Applying the same light curve cuts to the spectroscopic subsample, we found that in addition to SLSNe the main group of objects making it through these cuts are Type II SNe at lower redshifts ($z < 0.5$).

For the time period we considered, this left us with 17 long-rising transients without spectroscopic classification. 13 of these have host galaxies that are well-detected in SDSS, and thus have photometric redshifts available (Oyaizu et al. 2008). If we adopt these redshifts, the median implied peak absolute magnitude of these transients is -18 mag, consistent with being the counterparts to the slow-rising Type II SNe seen in the spectroscopic control sample, and in particular unlikely to be missed SLSNe. This leaves us with only four candidates of unknown type/redshift, which already rules out having missed a considerable number of bright-host SLSNe simply due to a bias in the follow-up. Two of these four objects were actually targeted for spectroscopy, but

the spectra were inconclusive, showing a blue and featureless continuum. It is unlikely that these objects belong to the subclass studied in this paper - if they were indeed superluminous, they would be at sufficiently high redshift that we would expect to detect the characteristic broad UV absorption features seen in most H-poor SLSNe (Quimby et al. 2011b; Chomiuk et al. 2011).

In addition, these four remaining objects are all found in host galaxies fainter than 22.0 mag (two have undetected hosts) and so would not be bright-host SLSNe: if we assign them redshifts by assuming the transients were indeed SLSNe (i.e., that the transient light curves peaked at $M = -22.5$ mag), adding them to the sample considered in this paper does not change any of our conclusions. Therefore, we are confident that our results are due to a real effect, rather than a bias towards preferentally following up transients with faint host galaxies.

We note that the preference for low-luminosity hosts is even stronger in the low-redshift non-PS1/MDS sample. This is reassuring, in the sense that the same general trend is found independently by more than one survey, which is certainly a necessary condition for it being a real physical effect. The stronger preference for low-luminosity galaxies at lower redshifts can be interpreted as an evolutionary effect, that may come about if for example metallicity affects the SLSN rate. Without a better understanding of how the different surveys select targets for follow-up, disentangling any selection effects from redshift evolution will be difficult, however.

3.6 Conclusions

We have presented the first comprehensive study of the host galaxy environments of H-poor SLSNe, with 31 objects over the redshift range $z \approx 0.1 - 1.6$. This is the first study to look at the hosts of this subclass of SLSNe specifically, and the largest study of SLSN hosts so far: previous studies (Neill et al. 2011; Stoll et al. 2011) mixed both H-rich and H-poor SLSNe and only detected a few hosts of H-poor SLSNe. Our main findings can be summarized as follows:

- H-poor SLSNe are generally found in low-luminosity galaxies. In our sample, we find the following median properties: B-band luminosity of -17.3 mag, stellar mass of $\sim 2 \times 10^8$ $M_\odot$, star formation rate of ~ 1 $M_\odot$ yr^{-1} and specific star formation rate of ~ 2 Gyr^{-1}.

- Compared to the hosts of core-collapse SNe over the same redshift range, the SLSNe occur systematically in lower-luminosity, lower-mass, lower-metallicity and higher sSFR galaxies. These results are statistically significant at the $> 3\sigma$ level.

- Compared to the hosts of LGRBs over the same redshift range, the SLSNe are consistent with being drawn from the same galaxy population as GRBs in terms of stellar mass, SFR, sSFR, and metallicity; we do however find them in lower-luminosity and lower-mass galaxies particularly at low redshift.

- The SLSNe predominantly occur in low-metallicity galaxies, with a median value of $12 + \log(\mathrm{O/H}) \approx 8.35$ and four galaxies in the sample having a detected [O III]λ4363 emission line. However, we do find a range of metallicities, including a

host galaxy at solar metallicity, and so there is no evidence for a strict metallicity cutoff.

- The preference for low-luminosity galaxies is strongest in the low-redshift ($z \lesssim 0.5$) sample, suggesting that there could be redshift evolution in the host population. A better understanding of how this sample was selected is necessary to disentangle evolution effects and potential selection effects, however.

We have shown that SLSNe select host environments that are similar to those selected by LGRBs over the same redshift range, though seem to prefer even lower-luminosity galaxies. As is the case with LGRBs, the implications in terms of SLSN progenitors are not straightforward. However, if interpreted as a preference for low-metallicity environments as the effect driving the selection, this could lend support to a millisecond magnetar being the energy source powering SLSNe. A key component of this progenitor model is that the magnetar initially must be spinning at close to breakup speeds, and maintaining fast rotation in the core is thought to be more effective at low metallicities since less angular momentum is lost to line-driven stellar winds.

It is less clear how our findings could be interpreted in the context of an interaction model for powering SLSNe, but our results at least indicate that the mechanism responsible for mass loss is likely to be environment-dependent. It would be interesting to compare the results to our study to the host galaxies of hydrogen-rich (Type IIn) SLSNe, since these SLSNe do show clear signs of interaction in their SN spectra. If their host population is found to be similar to the H-poor SLSN hosts, this could point to a similar progenitor population for the two classes.

Acknowledgements

We thank the staffs at PS1, MMT and Magellan for their assistance with performing these observations, and Andy Monson for help with processing the FourStar data. The Pan-STARRS1 Surveys (PS1) have been made possible through contributions of the Institute for Astronomy, the University of Hawaii, the Pan-STARRS Project Office, the Max-Planck Society and its participating institutes, the Max Planck Institute for Astronomy, Heidelberg and the Max Planck Institute for Extraterrestrial Physics, Garching, The Johns Hopkins University, Durham University, the University of Edinburgh, Queen's University Belfast, the Harvard-Smithsonian Center for Astrophysics, the Las Cumbres Observatory Global Telescope Network Incorporated, the National Central University of Taiwan, the Space Telescope Science Institute, the National Aeronautics and Space Administration under Grant No. NNX08AR22G issued through the Planetary Science Division of the NASA Science Mission Directorate, the National Science Foundation under Grant No. AST-1238877, the University of Maryland, and Eotvos Lorand University (ELTE). Support for programs number GO-13022 and GO-13326 was provided by NASA through a grant from the Space Telescope Science Institute, which is operated by the Association of Universities for Research in Astronomy, Inc., under NASA contract NAS5-26555. This paper includes data gathered with the 6.5 m Magellan Telescopes located at Las Campanas Observatory, Chile. Some observations reported here were obtained at the MMT Observatory, a joint facility between the Smithsonian Institution and the University of Arizona. This paper includes data based on observations made with the NASA/ESA *Hubble Space Telescope* and obtained from the Hubble Legacy Archive, which is a collaboration between the Space Telescope

Science Institute (STScI/NASA), the Space Telescope European Coordinating Facility (ST-ECF/ESA) and the Canadian Astronomy Data Centre (CADC/NRC/CSA). This work is based in part on observations made with the *Spitzer Space Telescope*, which is operated by the Jet Propulsion Laboratory, California Institute of Technology under a contract with NASA.This research used the facilities of the Canadian Astronomy Data Centre operated by the National Research Council of Canada with the support of the Canadian Space Agency. Some of the computations in this paper were run on the Odyssey cluster supported by the FAS Science Division Research Computing Group at Harvard University. Partial support for this work was provided by National Science Foundation grants AST-1009749 and AST-1211196.

3.7 Appendix: Notes on Individual Objects

3.7.1 SN 2011ke

Inspection of archival CFHT images shows that SN 2011ke exploded in a compact dwarf galaxy, with a redder and more extended companion.We obtained a spectrum with the slit going through both the SN site and the companion galaxy; while the spectrum was not taken at parallactic angle IMACS has an atmosperic dispersion corrector, so relative line fluxes should not be affected. We find that the two galaxies are at a similar redshift, though with a velocity offset of ~ 100 km s^{-1}. A color image combining g- and r-band from CFHT with our own z-band images from IMACS is shown in Figure 3.14. The blue-green color of the dwarf galaxy is due to strong [O III] emission in r-band, similar to the "Green Pea" galaxies found in SDSS (Cardamone et al. 2009).

The SDSS images of this system do not separate the two galaxies, and the SDSS catalog photometry includes light from both sources. To get host galaxy photometry, we perform photometry in a 1″aperture centered on the compact dwarf on the CFHT (g and r), IMACS (z) and FourStar (J) images and apply an aperture correction in each band calculated from stars in the field. The photometry listed for SN 2011ke in Table 3.3 is for the dwarf galaxy only. Similarly, derived quantities listed are based on the spectroscopy and photometry of the dwarf.

3.7.2 PTF09cnd

We obtained deep imaging of the field of PTF09cnd with MMTCam. As can be seen in Figure 3.1 there are several sources near the reported location of the transient (marked by the green circle). We assume the closest source is the correct host, and use this photometry to construct a model SED. A spectrum confirming the redshift would be necessary, however, to make a definitive association.

To determine a metallicity for PTF09cnd, we download the archival spectra of the transient from Quimby et al. (2011b) from the WISEREP database (Yaron & Gal-Yam 2012). The late-time spectrum exhibits a number of galaxy emission lines, which we use to determine the host properties.

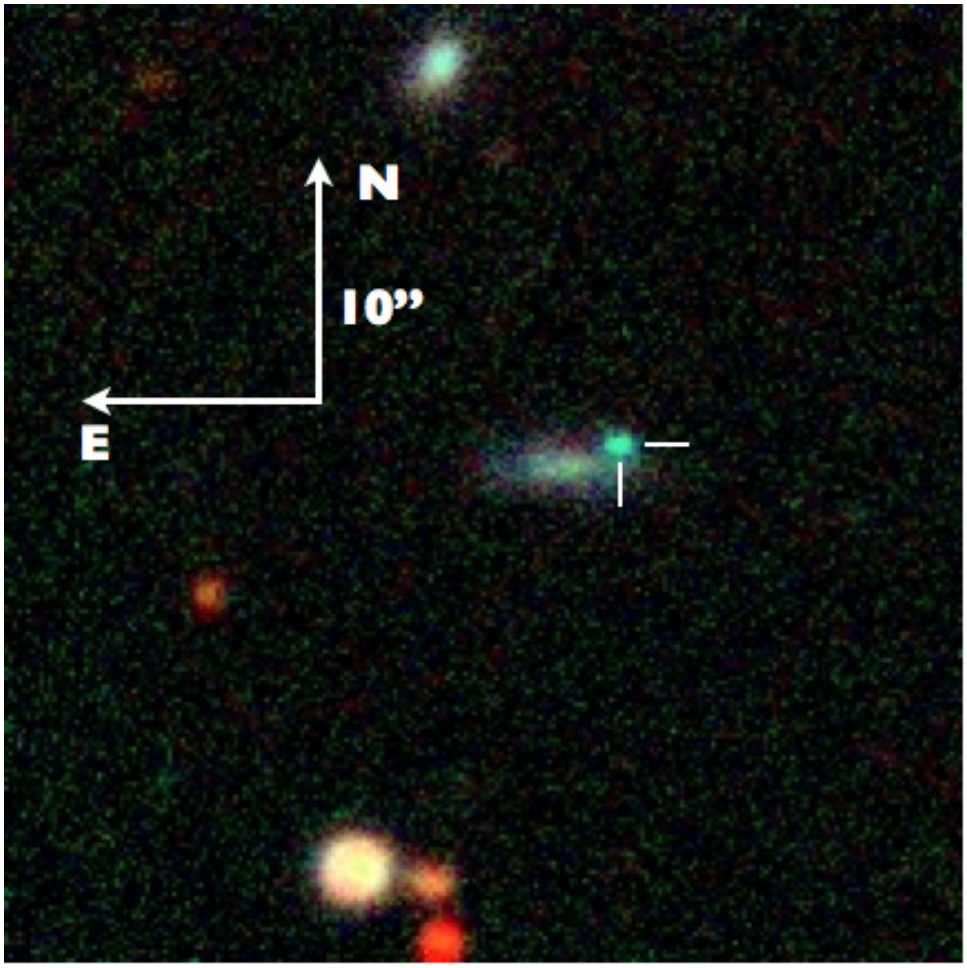

Figure 3.14.—: Combined *grz* image of the host galaxy of SN 2011ke. The location of the SN is marked by the cross-hairs, and show that the SN went off in a compact dwarf galaxy. The redder, more extended galaxy next to it is at the same redshift, with a velocity offset of $\sim$ 100 km s^{-1}. Note the unusual color of the dwarf galaxy, due to the strong [O III] emission that falls in *r*-band.

Chapter 4

Zooming In on the Progenitors of Superluminous Supernovae With the *HST*

R. Lunnan, R. Chornock, E. Berger, A. Rest, W. Fong, D. Scolnic, D. O. Jones, A. M. Soderberg, P. M. Challis, M. R. Drout, R. J. Foley, M. E. Huber, R. P. Kirshner, C. Leibler, G. H. Marion, M. McCrum, D. Milisavljevic, G. Narayan, N. E. Sanders, S. J. Smartt, K. W. Smith, J. L. Tonry, W. S. Burgett, K. C. Chambers, H. Flewelling, R.-P. Kudritzki, R. J. Wainscoat, and C. Waters

The Astrophysical Journal, Vol. 804, No. 90, 2015

Abstract

We present *Hubble Space Telescope* rest-frame ultraviolet imaging of the host galaxies of 16 hydrogen-poor superluminous supernovae (SLSNe), including 11 events from the Pan-STARRS Medium Deep Survey. Taking advantage of the superb angular resolution of *HST*, we characterize the galaxies' morphological properties, sizes and star formation rate densities. We determine the SN locations within the host galaxies through precise astrometric matching, and measure physical and host-normalized offsets, as well as the SN positions within the cumulative distribution of UV light pixel brightness. We find that the host galaxies of H-poor SLSNe are irregular, compact dwarf galaxies, with a median half-light radius of just 0.9 kpc. The UV-derived star formation rate densities are high ($\langle\Sigma_{\rm SFR}\rangle \simeq 0.1 {\rm M}_\odot {\rm yr}^{-1} {\rm kpc}^{-2}$), suggesting that SLSNe form in overdense environments. Their locations trace the UV light of their host galaxies, with a distribution intermediate between that of LGRBs (which are strongly clustered on the brightest regions of their hosts) and a uniform distribution (characteristic of normal core-collapse SNe), though cannot be statistically distinguished from either with the current sample size. Taken together, this strengthens the picture that SLSN progenitors require different conditions than those of ordinary core-collapse SNe to form, and that they explode in broadly similar galaxies as do LGRBs. If the tendency for SLSNe to be less clustered on the brightest regions than are LGRBs is confirmed by a larger sample, this would indicate a different, potentially lower-mass progenitor for SLSNe than LRGBs.

4.1 Introduction

Superluminous supernovae (SLSNe) are a rare class of supernovae (SNe) discovered in wide-field surveys in the past decade. They are characterized by peak luminosities of 10-100 times those of normal core-collapse and Type Ia SNe. At least two clear subclasses have emerged: SLSNe that show narrow hydrogen lines in their spectra (H-rich SLSNe) are thought to represent the extreme end of the Type IIn SN distribution, and are likely powered by interaction with dense circumstellar medium (CSM) (e.g. Ofek et al. 2007; Smith et al. 2007, 2010; Chatzopoulos et al. 2011; Drake et al. 2011a; Rest et al. 2011). For the subclass of SLSNe without hydrogen in their spectra (H-poor SLSNe; e.g. Quimby et al. 2007, 2011b; Barbary et al. 2009; Chomiuk et al. 2011; Pastorello et al. 2010; Leloudas et al. 2012; Lunnan et al. 2013; Inserra et al. 2013), the mechanism powering the extreme luminosities is not known. As in the case of H-rich SLSNe, interaction has also been proposed as the power source, but would require extreme mass loss and should produce narrow lines in the spectra that are not seen (Chevalier & Irwin 2011; Ginzburg & Balberg 2012; Chatzopoulos & Wheeler 2012b; Moriya et al. 2013; Benetti et al. 2014; Nicholl et al. 2014). A central engine model, such as energy injection from a newborn magnetar (e.g. Woosley 2010; Kasen & Bildsten 2010), has also been proposed. Another possibility, applicable to the slowest-evolving H-poor SLSNe, is pair-instability SNe (PISNe; Gal-Yam et al. 2009; Gal-Yam 2012; Kasen et al. 2011; Chatzopoulos & Wheeler 2012a; Kozyreva et al. 2014), although this interpretation is controversial (Young et al. 2010; Moriya et al. 2010; Dessart et al. 2012, 2013; Nicholl et al. 2013).

One way to shed light on the nature of these extreme explosions is to study their

progenitor populations. As all SLSNe discovered to date are far too distant for direct progenitor detections, in practice this means studying their host galaxy environments as a proxy. Early studies (Neill et al. 2011; Stoll et al. 2011) suggested that SLSNe were preferentially found in low-luminosity host galaxies. Detailed studies of two individual hosts (Chen et al. 2013; Lunnan et al. 2013) revealed metal-poor dwarf galaxies with high specific star formation rates. These initial trends were investigated in detail with a much larger sample in Lunnan et al. (2014), who studied properties of 31 SLSN host galaxies, and found that compared to core-collapse SNe, the SLSNe are found in lower-luminosity, lower-mass, higher specific star formation rate (sSFR) and lower metallicity environments. Instead, their properties were found to be broadly consistent with those of long-duration gamma-ray burst (LGRB) host galaxies, though the SLSN host galaxies studied were even lower-luminosity and lower-mass than the LGRB host comparison sample.

A complementary approach is to analyze the sub-galactic environments of SLSNe, i.e. the locations of SLSNe *within* their host galaxies. Studies that compare the locations of Type Ic SNe and LGRBs to the sites of star formation, as traced by UV or Hα emission, show that the supernova locations are strongly correlated with the brightest star-forming regions (Fruchter et al. 2006; Svensson et al. 2010; Kelly et al. 2008; James & Anderson 2006; Anderson et al. 2012). This is used as evidence that the progenitors of these explosions are young and massive. Type II SNe overall trace the UV emission, though not as strongly as Type Ib/c SNe, suggesting a longer-lived and less massive progenitor (Anderson et al. 2012; Kelly et al. 2008). By contrast, the locations of short-duration gamma-ray bursts are unassociated with UV light and show significant offsets from the host galaxy centers, suggesting they do not arise from young, massive

stars, and are consistent instead with the predictions for a compact object merger progenitor (Fong et al. 2010; Fong & Berger 2013). Thus, studying the locations of transients within their (resolved) host light distributions offers a powerful probe of the progenitor properties.

Here, we present the first analysis of the locations of H-poor superluminous supernovae within their host galaxies. We present resolved *Hubble Space Telescope* (*HST*) imaging, allowing us to both study the morphologies of SLSN host galaxies, as well as the host-SN offsets and positions of the SN locations in the overall light distribution. We present our targets, *HST* observations, data processing techniques and astrometric matching to determine the SLSN locations in Section 4.2. Section 4.3 describes the comparison samples and statistical techniques, and we present our results in Sections 4.4 and 4.5. The implications of our findings are discussed in Section 4.6 and summarized in Section 4.7. All calculations in this paper assume a ΛCDM cosmology with $H_0 = 70$ km s^{-1} Mpc^{-1}, $\Omega_{\rm M} = 0.27$ and $\Omega_\Lambda = 0.73$ (Komatsu et al. 2011).

4.2 Observations and Data Analysis

4.2.1 SLSNe Discovered in the Pan-STARRS Medium Deep Survey

The majority of our targets for this study were discovered in the Pan-STARRS Medium Deep Survey (PS1/MDS) transient search, which operated from late 2009 to early 2014. The PS1 telescope on Haleakala is a high-etendue wide-field survey instrument with a 1.8-m diameter primary mirror and a 3.3° diameter field of view imaged by an array of

sixty 4800×4800 pixel detectors, with a pixel scale of $0.258''$ (Kaiser et al. 2010; Tonry & Onaka 2009). Tonry et al. (2012) describes the photometric system and broadband filters in detail.

The PS1/MDS consists of 10 fields (each with a single PS1 imager footprint) observed in $g_{\rm P1}r_{\rm P1}i_{\rm P1}z_{\rm P1}$with a typical cadence of 3 d in each filter, to a 5σ depth of ~ 23.3 mag; $y_{\rm P1}$is used near full moon with a typical depth of ~ 21.7 mag. The standard reduction, astrometric solution, and stacking of the nightly images are done by the Pan-STARRS1 Image Processing Pipeline (IPP) system (Magnier 2006; Magnier et al. 2008) on a computer cluster at the Maui High Performance Computer Center. For the transients search, the nightly MDS stacks were transferred to the Harvard FAS Research Computing cluster, where they were processed through a frame subtraction analysis using the `photpipe` pipeline developed for the SuperMACHO and ESSENCE surveys (Rest et al. 2005; Garg et al. 2007; Miknaitis et al. 2007; Rest et al. 2014).

A subset of targets was selected for spectroscopic follow-up, using the Blue Channel spectrograph on the 6.5-m MMT telescope (Schmidt et al. 1989), the Gemini Multi-Object Spectrograph (GMOS; Hook et al. 2004) on the 8-m Gemini telescopes, and the Low Dispersion Survey Spectrograph (LDSS3) and Inamori-Magellan Areal Camera and Spectrograph (IMACS; Dressler et al. 2006) on the 6.5-m Magellan telescopes. Over the four years of the survey, we have discovered and spectroscopically confirmed more than 15 H-poor SLSNe in the PS1/MDS data (Chomiuk et al. 2011; Berger et al. 2012; Chornock et al. 2013; Lunnan et al. 2013; McCrum et al. 2015, 2014; R. Lunnan et al., in preparation). Due to the modest area and deep detection limit, most of the volume of PS1/MDS is at high redshift. The rare SLSNe in our sample cover $0.5 \lesssim z \lesssim 1.6$.

The spectroscopic follow-up of PS1/MDS was not complete, with follow-up targets selected based on the available light curve and galaxy information. In particular, the SLSNe were generally found by some combination of having long observed rise-times and/or being several magnitudes brighter than any apparent host. Lunnan et al. (2014) examined in detail to what extent the selection could bias the resulting host galaxy population of the PS1/MDS SLSN sample, with the conclusion that the strong environmental preferences seen are real and not caused by selection effects.

4.2.2 Hubble Space Telescope Observations

We obtained *HST* observations of the host galaxies of 11 H-poor SLSNe discovered in the PS1/MDS survey through programs GO-13022 and GO-13326 (PIs: Berger and Lunnan, respectively). The initial program targeted 5 SLSN host galaxies that were undetected in ground-based data, obtaining both rest-frame UV and rest-frame optical imaging, and the follow-up program added rest-frame UV imaging of the remaining SLSN host galaxies in the PS1/MDS sample at the time. In addition the host galaxy of SLSN PS1-10bzj (Lunnan et al. 2013) has archival *HST* imaging from the GEMS survey (Rix et al. 2004). Since the remaining galaxy images by necessity were obtained after the SN explosion, the programs were designed to only include targets where the SNe were expected to have faded well below *HST* detection threshold by the time of the observations, based on the available PS1/MDS light curves. For this reason, the sample only includes events from the first 2.5 years of PS1/MDS. All targets are listed in Table 4.1.

Table 4.1. Target List

Object	Redshift	RA	Dec
PS1-12bqf	0.522	$02^h24^m54.621^s$	$-04°50'22.72''$
PS1-11ap	0.524	$10^h48^m27.752^s$	$+57°09'09.32''$
PS1-10bzj	0.650	$03^h31^m39.826^s$	$-27°47'42.17''$
PS1-11bdn	0.738	$02^h25^m46.292^s$	$-05°03'56.57''$
PS1-10awh	0.909	$22^h14^m29.831^s$	$-00°04'03.62''$
PS1-10ky	0.956	$22^h13^m37.851^s$	$+01°14'23.57''$
PS1-11aib	0.997	$22^h18^m12.217^s$	$+01°33'32.01''$
PS1-10pm	1.206	$12^h12^m42.200^s$	$+46°59'29.48''$
PS1-11tt	1.283	$16^h12^m45.778^s$	$+54°04'16.96''$
PS1-10afx	1.388	$22^h11^m24.160^s$	$+00°09'43.49''$
PS1-11afv	1.407	$12^h15^m37.770^s$	$+48°10'48.62''$
PS1-11bam	1.565	$08^h41^m14.192^s$	$+44°01'56.95''$
PS1-12bmy	1.572	$03^h34^m13.123^s$	$-26°31'17.21''$
SN 2007bi	0.128	$13^h19^m20.19^s$	$+08°55'44.3''$
SN 2011ke	0.143	$13^h50^m57.78^s$	$+26°16'42.40''$
SN 2012il	0.175	$09^h46^m12.91^s$	$+19°50'28.7''$
SN 2010gx	0.230	$11^h25^m46.71^s$	$-08°49'41.4''$
SCP06F6	1.189	$14^h32^m27.395^s$	$+33°32'24.83''$

Each galaxy was imaged with the Advanced Camera for Surveys (ACS/WFC) in a filter corresponding to rest-frame UV emission ($\simeq$ 3000Å; F475W, F606W or F814W were used depending on the redshift). We used a standard four-point dither pattern for optimal pixel subsampling; Table 4.2 lists the details for each observation, including the effective wavelengths for each filter/redshift combination. We processed and combined the calibrated and CTE-corrected individual images using the Astrodrizzle software provided by STScI (Gonzaga et al. 2012), with a final `pixscale` of 0.025″/pixel (i.e. half the native image scale), and a `pixfrac` value of 0.8.

In addition, the H-poor SLSN PS1-11aib was observed in program GO-12529 (PI: Soderberg), capturing both the late-time light curve of the SN and a final epoch for a host galaxy template. The F625W filter corresponds to rest-frame UV at a redshift of $z = 0.997$. In this case, the data are somewhat shallower and we only have two images available per filter, so we do not redrizzle onto a finer grid but keep the original image scale of 0.05″/pixel. We note that what we identify as the host galaxy of PS1-11aib is unresolved in the template image, and does not appear to be offset from the SN centroid (Figure 4.1), so there is a possibility of confusion with lingering SN emission. The fact that the F625W flux remained constant in the two final epochs (220 to 350 rest-frame days past peak), as well as the flat F625W-F775W color in the final epoch argues that we are indeed detecting the galaxy, however.

The peculiar transient PS1-10afx (Chornock et al. 2013) was targeted as part of program GO-13326; however the discovery of a second galaxy along the line of sight combined with the observed SN properties make it likely this object was in fact a lensed SN rather than a SLSN (Quimby et al. 2013b, 2014). Due to the uncertainties in the nature of this object, we do not include it in our analysis here, though we show the *HST*

image and SN location in Appendix 4.8. Additionally, the SLSN PS1-10ky (Chomiuk et al. 2011) was targeted as part of program GO-13022 but its host galaxy was not detected. It is therefore not included in the discussion, except for where the upper limit is relevant.

In addition to the *HST* data from our PS1 sample, a few SLSN host galaxies have *HST* images available in the public archive from proposal GO-13025 (PI: Levan). We included available public images covering rest-frame UV of 5 H-poor SLSNe in our analysis; targets and details of the observations are listed in Tables 4.1 and 4.2. As the public objects are generally at lower redshifts than the PS1 sample, most of these objects were imaged with the Wide Field Camera 3 (WFC3/UVIS). Unlike ACS, WFC3 images are not currently corrected for CTE losses as part of the standard *HST* pipeline, and we used the CTE correction software available from the WFC3 tools webpage[1] before processing and combining the individual images with Astrodrizzle. Again, we used a `pixfrac` of 0.8 and a final `pixscale` of half the native image scale, which corresponds to a final scale of 0.0198″/pixel. All final drizzled images are shown in Figure 4.1.

[1] `http://www.stsci.edu/hst/wfc3/tools/cte\_tools`

Table 4.2. Summary of HST Observations

Object	UT Date (YYYY-MM-DD)	Instrument	Filter	Rest-frame $\lambda_{\rm eff}$ (Å)	Exposure Time (s)
PS1-12bqf	2013-11-18	ACS/WFC	F475W	3118	2200
PS1-11ap	2013-10-09	ACS/WFC	F475W	3113	2464
PS1-10bzj[a]	2002-11-11	ACS/WFC	F606W	3589	2160
PS1-11bdn	2013-11-13	ACS/WFC	F475W	2730	2200
PS1-10awh	2013-09-04	ACS/WFC	F606W	3102	680
PS1-10ky	2012-12-13	ACS/WFC	F606W	3027	680
PS1-11aib	2013-09-12	ACS/WFC	F625W	3160	1000
PS1-10pm	2012-12-10	ACS/WFC	F606W	2684	1960
PS1-11tt	2012-12-02	ACS/WFC	F606W	2593	1960
PS1-10afx	2013-10-08	ACS/WFC	F814W	3373	2200
PS1-11afv	2013-04-09	ACS/WFC	F606W	2460	1960
PS1-11bam	2013-10-11	ACS/WFC	F814W	3141	2304
PS1-12bmy	2013-09-17	ACS/WFC	F814W	3132	2224
SN 2007bi	2012-11-27	WFC3/UVIS	F336W	2974	1808
SN 2011ke	2013-05-16	WFC3/UVIS	F336W	2935	2044
SN 2012il	2013-01-02	WFC3/UVIS	F336W	2855	2036
SN 2010gx	2012-11-22	WFC3/UVIS	F390W	3190	1808
SCP06F6	2013-05-23	ACS/WFC	F606W	2705	8054

[a]Archival data from the GEMS survey (Rix et al. 2004).

4.2.3 Astrometry

PS1-HST Astrometry

To determine the locations of the SNe relative to the *HST* high-resolution images, we take advantage of the astrometry framework in the PS1/MDS `photpipe` pipeline. We use `SExtractor`[2] to create a catalog of suitable astrometric reference sources from the *HST* images, and shift a PS1 template image to this reference frame. Typically, there are 20-60 tie objects available between the ACS images and the PS1 templates, giving resulting tie uncertainties of 10-30 mas. These uncertainties are quoted as $\sigma_{\rm tie}$ in Table 4.3.

In addition to the uncertainty from the astrometric tie between the *HST* images and PS1 templates, there is a contribution based on how well we can determine the SN centroids. To calculate this, we re-run the supernova images through the pipeline, updating the astrometry of the nightly and reference images to the *HST*-defined reference frame, performing image subtractions, and calculate the SN centroids and associated error from the subtracted images. Rest et al. (2014) describe in detail how the astrometry is performed by the pipeline. We then combine all the individual measurements and calculate the weighted, 3σ-clipped average centroid for each SN. We find typical uncertainties in the SN centroids of 10-30 mas, depending on both the number of images available for each SN, and the seeing and signal-to-noise for the individual detections. We note that the scatter in the position measurements are comparable to the astrometric errors calculated by the pipeline (i.e., reduced χ^2-values for the mean centroid close to 1). The uncertainties in SN positions are listed as $\sigma_{\rm SN}$ in Table 4.3. The total uncertainty

[2] `http://sextractor.sourceforge.net`

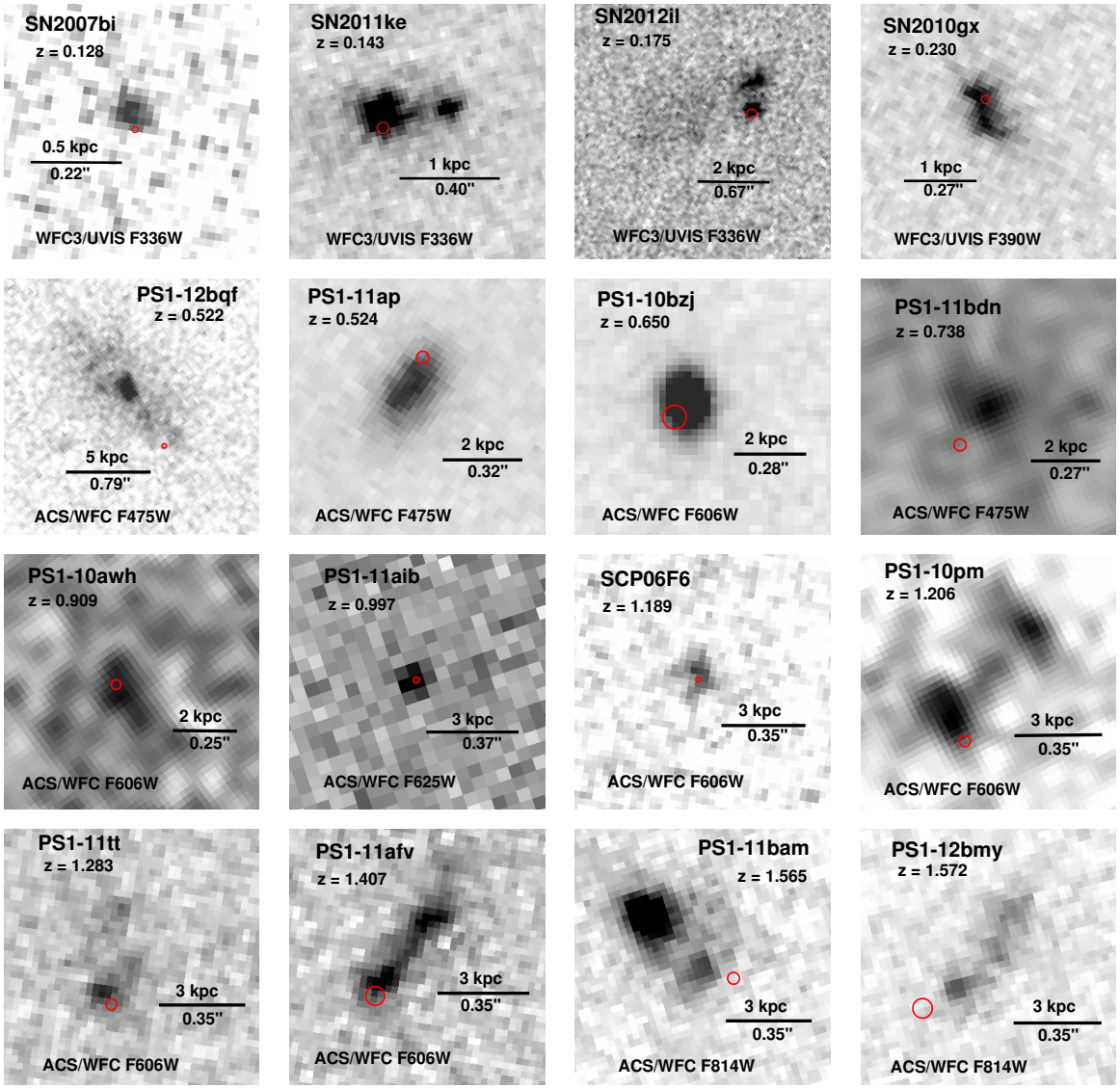

Figure 4.1.—: *HST* rest-frame UV images of 11 host galaxies of PS1/MDS SLSNe, and 5 host galaxies from the literature. All images are oriented with north up and east pointing left. The horizontal bars show the scale of each image. The red circles correspond to the 1σ astrometric uncertainty in the SN position relative to the *HST* image, as described in Section 4.2.3. Some images have been smoothed with a 3-pixel Gaussian filter to make the galaxy more apparent.

of the SN position in the *HST* image is found by combining $\sigma_{\rm tie}$ and $\sigma_{\rm SN}$ in quadrature, and is depicted as red circles in Figure 4.1.

HST-HST Astrometry

Two objects, PS1-11aib and SCP06F6, have *HST* images available for both the SLSNe and their host galaxies: PS1-11aib had both SN and host galaxy imaging done as part of program GO-12529, and SCP06F6 was discovered as part of the *Hubble Space Telescope* Cluster Supernova Survey (program GO-10496; Barbary et al. 2009). In these two cases, we align the *HST* images of the SNe directly to the galaxy images, using the Drizzlepac task `tweakreg`. Since there are not many stars in these fields, we again use catalogs of suitable sources created with `SExtractor` as input (rather than the built-in `imagefind` routine in Drizzlepac). We calculate the weighted SN centroids in the frame of the host galaxy; the $\sigma_{\rm SN}$ values quoted in Table 4.3 is the total final position uncertainty.

Literature Objects

For the remaining literature objects, we use available ground-based imaging of the SNe for astrometry: PS1 3Pi images of SN 2011ke and SN 2012il (Inserra et al. 2013), GMOS imaging of SN 2010gx (Pastorello et al. 2010), and Liverpool Telescope images of SN 2007bi (Gal-Yam et al. 2009; Young et al. 2010). Here, we use `SExtractor` to create catalogs of overlapping sources, and the IRAF task `ccmap` to compute the astrometric tie for each SN image. As with the PS1/MDS images, we then combine the measurements from individual SN images to calculate the weighted SN centroid in the frame of the *HST* images.

Unlike for the PS1-HST astrometry, we do not use host-subtracted images to determine the SN centroid for these literature objects, as we do not have host galaxy images in the same filters available. This could in principle bias the position measured. To minimize such effects, we use SN images as close to maximum light as possible, where the SNe are $\gtrsim 2-4$ mag brighter than their host galaxies, and the contribution of host galaxy flux to the measured centroid should therefore be negligible.

4.3 Comparison Samples

We compare the locations of SLSNe within their host galaxies to different types of astrophysical transients. As our SLSN sample spans a wide range of redshifts ($0.1 \lesssim z \lesssim 1.6$), the comparison samples should ideally cover a similar redshift range (to minimize effects due to galaxy evolution), and also come from an untargeted survey (to avoid biasing towards specific galaxy types). We use the GOODS sample of core-collapse SNe (Fruchter et al. 2006; Svensson et al. 2010) as our main SN comparison sample, as it satisfies both these criteria (see Figure 4.2 for a redshift distribution comparison). Moreover, the SN locations within the host galaxies are very well determined as both the SNe and the host galaxies were observed with *HST*. One drawback of the GOODS sample is that most of the SNe in the core-collapse sample were not spectroscopically confirmed. As the main goal of the GOODS SN search was to find Type Ia SNe, the CCSN sample consists of SNe with colors incompatible with being Type Ia SNe (and therefore not followed up further), or SNe with spectra that were not Type Ia (Strolger et al. 2004). There is therefore no breakdown of sub-types within the GOODS sample. In addition, the papers describing the GOODS sample do not discuss host-SN offsets.

For studies of spectroscopically confirmed CCSNe, as well as studies of host-SN offsets, then, we are limited to low-redshift samples. We utilize the studies of Prieto et al. (2008), Kelly et al. (2008) and Kelly & Kirshner (2012) for host-SN offsets and light distribution statistics for different types of SNe. In addition to the redshift difference to the SLSNe, these comparisons are complicated by the fact that the low-redshift samples contain a larger fraction of high-luminosity galaxies because the supernovae in the samples come from targeted surveys.

LGRBs offer another interesting comparison sample to H-poor SLSNe. The two types of transients share a number of properties; both are rare and energetic explosions, with rates $\lesssim 10^{-3}$ of the CCSN rate (Quimby et al. 2013a; McCrum et al. 2015; Wanderman & Piran 2010). Like H-poor SLSNe, the SNe that accompany LGRBs are stripped of hydrogen. Moreover, Lunnan et al. (2014) found that their environments are similar on a galaxy-scale level, with both samples preferentially found in dwarf galaxy environments with low metallicities and high specific star formation rates. Locations of LGRBs within their host galaxies were studied in Fruchter et al. (2006) and Svensson et al. (2010); we will also refer to Bloom et al. (2002) for offsets of LGRBs. Figure 4.2 also shows the redshift distributions of both these LGRB samples, which are well-matched to the SLSN sample.

To compare the distribution of SLSN properties to the other samples, we use the Kolmogorov-Smirnov (K-S) test. This test calculates the K-S statistic D, defined as $D = \sup_x |F_1(x) - F_2(x)|$, where F_1 and F_2 are the empirical cumulative distribution functions of the two samples. This statistic is then compared to a theoretical distribution to calculate the probability that the two samples were drawn from the same underlying distribution.

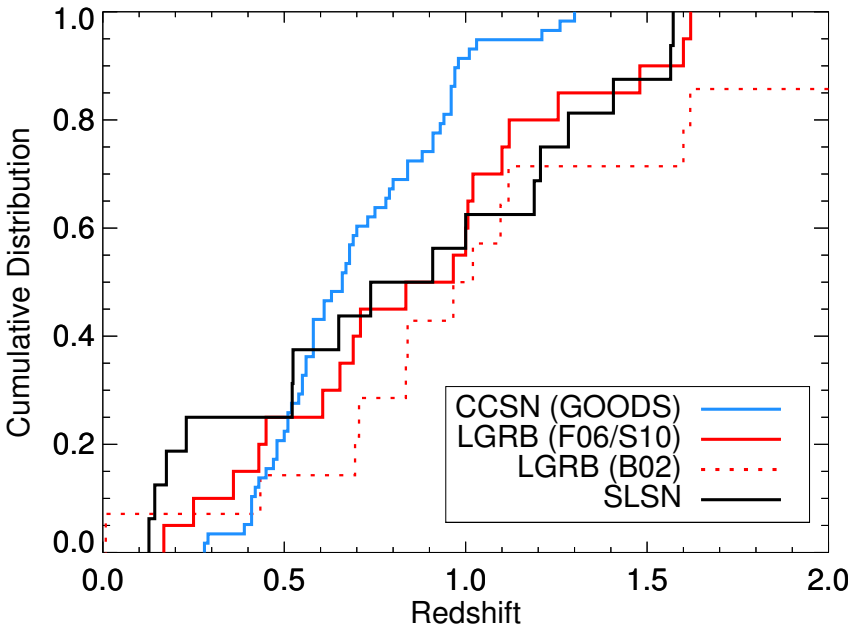

Figure 4.2.—: Redshift distributions of our SLSN sample (black), and of the main comparison samples. The blue and red solid lines show the GOODS CCSN sample and LGRB sample presented in Fruchter et al. (2006) and Svensson et al. (2010). The red dotted line shows the redshift distribution of the LGRB sample from Bloom et al. (2002), which is used in the offset comparison.

4.4 Galaxy Properties from Resolved Imaging

Before we turn to an analysis of the SN locations, discussed in Section 4.5, we investigate the morphologies of the SLSN host galaxies. This is helpful both for understanding the nature of the galaxies, and to normalize the SLSN offset measurements.

4.4.1 Galaxy Morphologies

Visual inspection of Figure 4.1 reveals that most SLSN host galaxies have irregular morphologies. There is a striking lack of grand design spiral galaxies compared to the host galaxies of normal SNe: the GOODS survey found that approximately half of the CCSNe in this redshift range are found in massive spiral galaxies (Fruchter et al. 2006; Svensson et al. 2010). In contrast, none of the SLSN hosts in our sample have visible spiral structure. In addition, the deficit of spiral galaxy hosts agrees with the results from Lunnan et al. (2014) that SLSNe select different environments from normal CCSNe, suggesting that additional factors beyond star formation is necessary to produce a SLSN. Moreover, this is another characteristic that SLSN host galaxies share with LGRB host galaxies, which are also deficient in bright spirals and generally found in galaxies with irregular morphologies (Fruchter et al. 2006; Wainwright et al. 2007).

Another interesting feature of Figure 4.1 is that roughly half of the galaxies exhibit a morphology that is either asymmetric, off-center or consisting of multiple peaks. Such morphologies are common also amongst LGRB host galaxies: Wainwright et al. (2007) classified $\gtrsim 60\%$ of the galaxies in their sample as either showing features consistent with merging system, or asymmetric and irregular structure.

Table 4.3. Results

Object	$\sigma_{\rm tie}$ (mas)	$\sigma_{\rm SN}$ (mas)	$\sigma_{\rm gal}$ (mas)	r_{50} (kpc)	r_{80} (kpc)	$\log(\Sigma_{\rm SFR})$ ($M_\odot {\rm yr}^{-1} {\rm kpc}^{-2}$)	Projected Offset (kpc)	Normalized Offset (r/r_{50})	Light Fraction
PS1-12bqf	13.1	16.1	4.3	2.87	4.69	-1.4	4.34	1.5	0.12
PS1-11ap	23.5	4.9	2.1	0.85	1.45	-1.2	0.98	1.2	0.65
PS1-10bzj	31.4	33.9	1.5	0.58	1.01	-1.0	0.51	0.9	0.51
PS1-11bdn	14.6	18.7	5.9	1.25	2.26	-1.3	1.36	1.1	0.58
PS1-10awh	9.8	16.1	9.7	0.88	2.03	-1.0	0.33	0.4	0.43
PS1-11aib	···	12.3	···	< 0.4	···	···	···	···	1.00
PS1-10pm	8.1	19.9	7.7	2.57	3.92	-1.1	2.22	0.9	0.29
PS1-11tt	13.6	16.3	5.3	1.34	2.04	-1.0	1.21	0.9	0.90
PS1-11afv	11.8	34.8	4.7	1.49	2.25	-0.9	2.15	1.4	0.64
PS1-11bam	8.2	21.8	2.8	1.34	2.36	-0.4	3.04	2.3	0.02
PS1-12bmy	10.5	36.8	4.1	1.55	2.20	-0.6	2.89	1.9	0.02
SN 2007bi	···	19.6	4.8	0.20	0.47	-1.0	0.17	0.8	0.67
SN 2011ke	16.8	14.5	2.4	0.34	0.60	-1.0	0.15	0.4	0.86
SN 2012il	36.5	26.0	3.3	0.53	0.85	-1.1	0.55	1.0	0.95
SN 2010gx	···	16.3	2.7	0.41	0.76	-1.1	0.17	0.4	0.82
SCP06F6	···	9.5	4.4	0.65	1.04	-1.4	0.10	0.2	0.85

Note. — $\sigma_{\rm tie}$ is the uncertainty in the astrometric tie between the *HST* image and a deep template, where applicable. $\sigma_{\rm SN}$ is the uncertainty in the SN centroid. $\sigma_{\rm gal}$ is the uncertainty of the galaxy centroid.

4.4.2 Galaxy Sizes

We use `SExtractor` to measure effective galaxy radii, using a S/N > 1 criterion to determine which pixels are part of the galaxy. In Table 4.3 we list r_{50} and r_{80}, the radii estimated by `SExtractor` to contain 50% and 80% of the total host light, respectively. PS1-11aib is unresolved in the *HST* image, and we take the FWHM of the point-spread function as an upper limit on its size.

As is also evident from the images in Figure 4.1, the SLSN host galaxies are remarkably compact. The half-light radii span 0.2 to 2.9 kpc, with a median of 0.9 kpc. Figure 4.3 shows the distribution of r_{80}, the radius containing 80% of the total light, compared to the LGRB and GOODS CCSN host samples from Svensson et al. (2010). The SLSN host sizes are comparable to the LGRB hosts, if overall slightly smaller, and their distributions are statistically compatible. In contrast, the GOODS CCSN host galaxies are significantly larger, with a median r_{80} of 4.45 kpc. A K-S test rejects the null hypothesis that the two samples are drawn from the same distribution at high significance ($p = 2 \times 10^{-5}$).

Since our observations probe the rest-frame UV, which traces star formation, one might worry that the small sizes measured are a result of only detecting bright knots of star formation rather than the overall distribution of stars; for example in the image of SN 2012il (Figure 4.1), an extended structure at lower surface brightness is visible, and may be more representative of the true size of the galaxy than the two bright knots in the left of the image that dominate the UV light. One way to test this is to compare images that trace rest-frame optical or IR light to our UV images. Such images are available for about half the sample. For SN 2012il, the IR extent of the host galaxy is indeed

similar to the low surface brightness component seen in the UV; the host of SN 2007bi also appears to be more extended in the IR though at a low signal-to-noise level. The remaining 5 galaxies with WFC3/IR imaging in our sample show similar morphologies and sizes as in the UV, suggesting that the UV images are generally representative of the overall host galaxy size. We also note that based on SED modelling (Lunnan et al. 2014), we do not generally expect a significant component of old stars.

4.4.3 Star Formation Rates and SFR Surface Density

Since our images cover rest-frame UV, we can use the galaxy fluxes to estimate UV-derived star formation rates. We use the "isocorr" magnitudes returned by `SExtractor` as the estimate of the total flux from the galaxy, and convert the UV luminosity into star formation rates using the relation from Kennicutt (1998): SFR $(M_\odot/\mathrm{yr}) = 1.4 \times 10^{-28} L_{\nu,\mathrm{UV}}(\mathrm{erg\ s^{-1}Hz^{-1}})$.

Using the galaxy sizes we also calculate the SFR surface density, i.e. the star formation rate per unit area. We use the isophotal area determined by `SExtractor` as our best estimate of the total area of the galaxies. In Figure 4.4 we plot the SFR density as a function of stellar mass, using the masses derived from SED fitting by Lunnan et al. (2014), except for SN 2007bi where we use the updated mass from Chen et al. (2014). Data for the host galaxies of other types of transients are taken from Kelly et al. (2014). We find that, like LGRBs and Type Ic -BL (broad-lined) SNe, the SLSN host galaxies have high SFR densities for their stellar mass, ranging from 0.04 to 0.4 $M_\odot$ yr^{-1} kpc^{-2} with a median value of 0.09 $M_\odot$ yr^{-1} kpc^{-2}.

For the undetected galaxy in our sample, PS1-10ky, we measure the standard

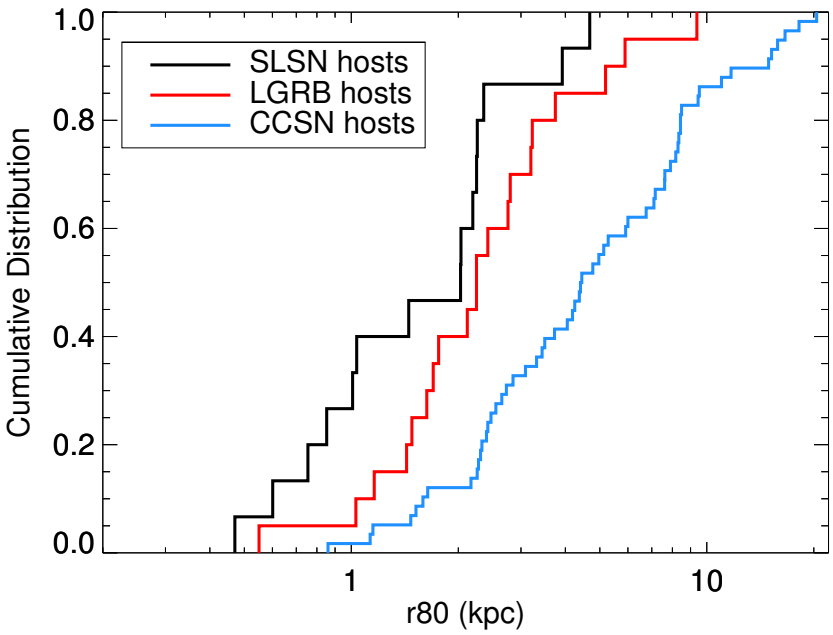

Figure 4.3.—: Distribution of r_{80}, the radius containing 80% of the galaxy flux, for the SLSN host sample (black), LGRB host galaxies (red) and core-collapse SN host galaxies from GOODS (blue).

deviation of the background at the position of the transient, and use this to calculate an upper limit on the galaxy surface brightness. At the redshift of PS1-10ky, the resulting limit on star formation rate density is $0.1 M_{\odot}$ yr^{-1} kpc^{-2} (3σ), similar to the lowest-mass detections. Note that this calculation assumes the galaxy is at least as large as the PSF of the image ($0.075''$, corresponding to ~ 600 pc); if the galaxy is smaller it could in principle have a higher star formation rate density than this limit and remain undetected.

We caution that the samples we are comparing to used sizes derived from rest-frame optical rather than UV images, which could lead to higher derived SFR densities if the UV emission is not representative of the true size of the galaxy. To follow the same relation that is seen in normal core-collapse SN host galaxies, however, the SLSN sizes would have to be underestimated by a factor of ~ 10, which is not supported by the subsample for which we have rest-frame optical or IR imaging (Section 4.4.2).

4.5 Supernova Locations

4.5.1 Offsets

To calculate the offset from the SLSN locations to the host galaxy, we first need to define the center of each galaxy. We use the centers output by `SExtractor`, which correspond to the flux-weighted galaxy centroids. Given the irregular morphology of many of our targets, we note that the center calculated in this way does not necessarily correspond to the brightest region of the galaxy. The uncertainty in the host galaxy centroid is listed as $\sigma_{\rm gal}$ in Table 4.3.

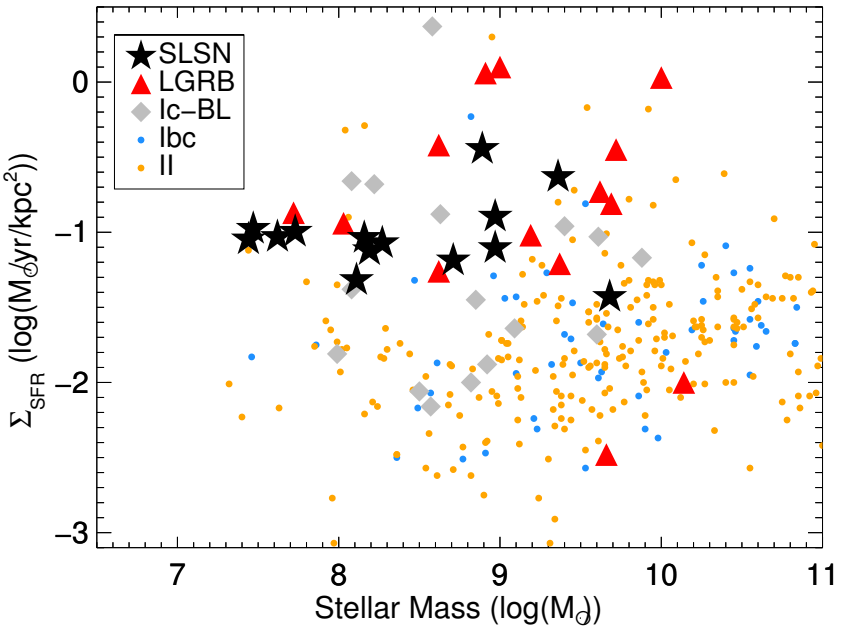

Figure 4.4.—: SFR surface density as a function of stellar mass. The SLSN host galaxies are shown as black stars; data for other types of transients are taken from Kelly et al. (2014). Similar to the host galaxies of Type Ic-BL SNe and LGRBs, the SLSN host galaxies have high SFR surface densities given their stellar masses.

The distribution of resulting offsets is shown in Figure 4.5, both in projected kpc (left) and normalized by the host galaxy size (right). We here use r_{50} rather than r_{80}, since this is what was used to normalize the offsets in the comparison samples. The SLSNe have offsets ranging from 0.1 to 4.3 kpc, with a median of 1.0 kpc, comparable to the LGRBs and significantly smaller than the offsets of the low-redshift CCSNe. However, when normalized by host galaxy size, the SLSNe are statistically compatible to the two other populations, and in particular all three populations have median offsets of about 1 half-light radius. This indicates that the SLSN locations overall track the radial distribution of UV light, similar to other transients with massive star progenitors.

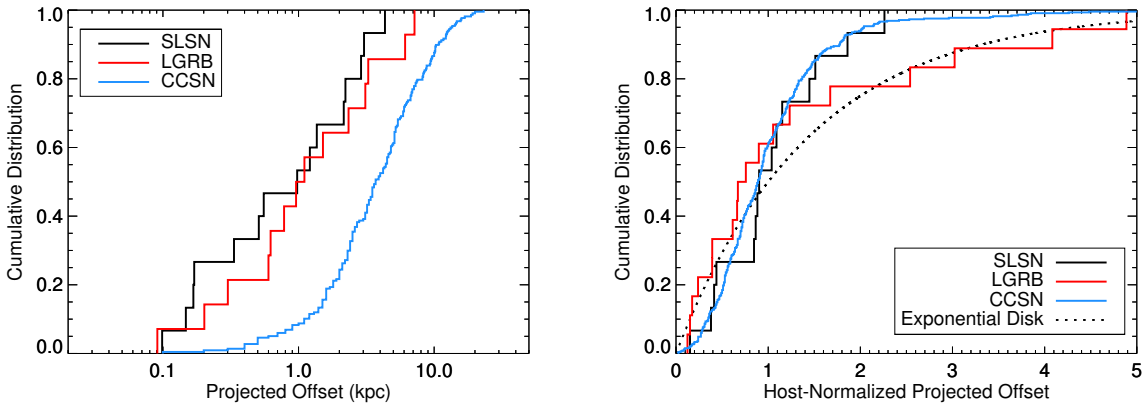

Figure 4.5.—: Distributions of projected offsets from the host center, both in physical units (left) and normalized by the host galaxy's half-light radius (right). The SLSN sample is shown in black, LGRBs from Bloom et al. (2002) in red, and low-z core-collapse SNe from Prieto et al. (2008) and Kelly & Kirshner (2012) in blue. Also shown is the expected distribution for an exponential disk model (dashed line).

4.5.2 Light Distribution Analysis

The offset technique is limited in comparing the locations of transients to the overall light distribution because many of the SLSN host galaxies exhibit irregular, asymmetric structure. The distance from the flux-weighted center of the galaxy is therefore not necessarily a good indicator of the flux level at the SN position. For this reason, Fruchter et al. (2006) developed a morphology-independent technique for quantifying the extent to which SNe trace their host light distribution, by determining the pixel on which the SN occurred, and computing the fraction of light in galaxy pixels of lower surface brightness. A hypothetical population of sources that perfectly tracked the underlying light distribution would follow a uniform distribution: a pixel with twice as much flux would, statistically speaking, be exactly twice as likely to contain a transient.

To calculate this statistic, we first determine which pixels are part of the galaxy. We fit a Gaussian profile to the sky brightness distribution near the galaxy, and determine the 1σ cutoff level (equivalent to taking S/N > 1). Consecutive pixels above this cutoff level are then defined to be part of the galaxy, and we compute the fraction of light in galaxy pixels fainter than the SLSN position. In cases where the SN position is known to a precision worse than the FWHM of the image, we first convolve the image with a Gaussian of the same width as the SN position uncertainty. The results for each galaxy are listed in Table 4.3.

In Figure 4.6 we show the cumulative distribution of the light fractions of SLSN locations, compared to the GOODS CCSNe, LGRBs (Svensson et al. 2010) and local Type Ic SNe (Kelly et al. 2008). The dashed line marks the expectation of a uniform distribution. The SLSN locations overall are slightly skewed towards brighter pixels,

with a median value is 0.65. This suggests that SLSNe are indeed correlated with the UV light of their host galaxies, and are slightly more likely to be found in brighter regions of their host galaxies. They do not appear to be as strongly correlated with the brightest regions as are LGRBs, which have a median value of 0.88. In particular, only one (6%) of the LGRBs in the sample from Svensson et al. (2010) are found in regions of fractional brighness $< 40\%$, whereas about a quarter of the SLSNe are found at such low flux values. The sample sizes are small, however, and statistically we cannot rule out either that the SLSNe come from the same distribution as the LGRBs ($p = 0.25$), or that they are drawn from a uniform distribution ($p = 0.44$).

The comparison is complicated by the fact that the SLSN host galaxies are overall fainter than either of the galaxy populations we are comparing to, and so it is possible the SLSN distribution is shifted to lower relative flux values due to the lower-surface brightness parts of the galaxies not being above the noise threshold. This effect is not likely to be severe, however, since the faintest pixels in the distribution contribute little to the overall *total* flux, which is what matters the most for the relative position. This effect was considered in detail by Fruchter et al. (2006) when comparing the LGRB sample to the GOODS CCSNe, by experimenting with artificially increasing the noise in their images by a magnitude (thus losing a larger fraction of the galaxy edge flux). They found that their results were overall unaffected. It is also worth noting that the galaxies where we find the lowest fractional flux levels at the SN positions are in fact some of the brightest galaxies in the sample: PS1-12bqf, PS1-11bam and PS1-12bmy (Figure 4.1; Table 4.3). Therefore, the result that some SLSNe explode in regions of their galaxy with very little UV flux is unlikely to be caused by a surface brightness bias.

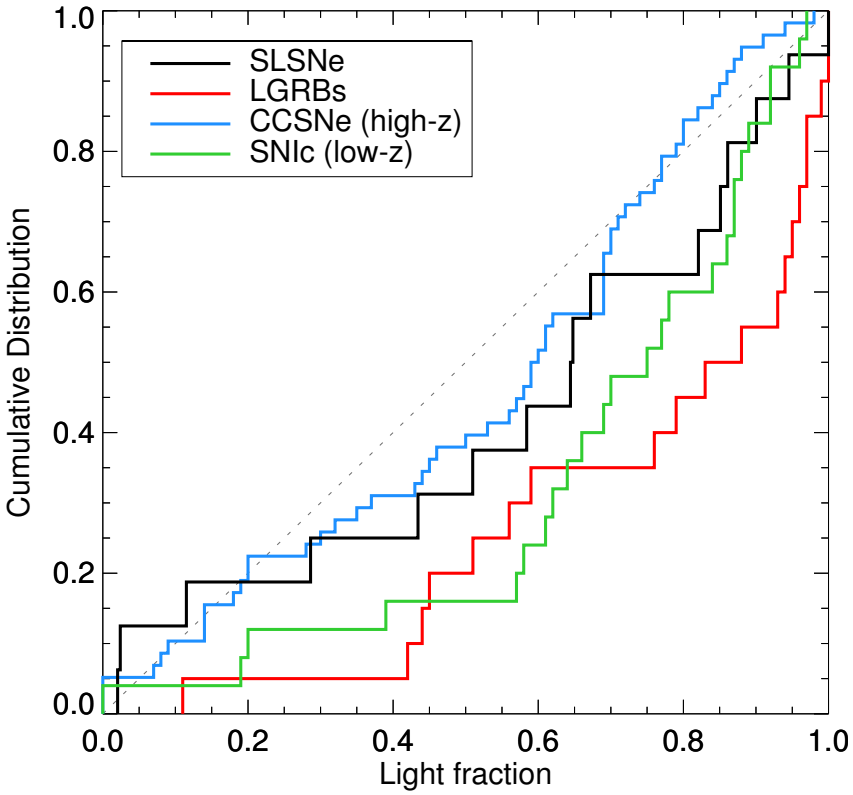

Figure 4.6.—: Cumulative distribution of the fraction of total light found in pixels fainter than the location of the transient. The SLSN sample is shown in black, LGRBs in red, GOODS CCSNe in blue and local Type Ic SNe in green. The dotted line marks a uniform distribution, expected for a theoretical population that perfectly tracked its host light.

Another potential bias arises due to that the contrast between a typical SLSN and its host galaxy is several magnitudes greater than that between a typical CCSN and its host. As a result, the SLSNe are relatively easier to detect in the brightest regions of their host galaxies, whereas the CCSN sample may be missing events in the bright galaxy cores. Fruchter et al. (2006) examined this effect in the GOODS sample, and estimated that the fraction of central SNe missed in the GOODS sample was $< 10\%$. In addition, the low-z Type Ic SN sample (Kelly et al. 2008) appears to trace the brightest

regions of their hosts at least as strongly as the SLSNe do. Thus, SN-host contrast is unlikely to be affecting the comparison on a significant level.

4.6 Discussion

Both the offset distribution and the fractional flux distribution of SLSNe suggest that their locations are correlated with the UV light and hence with recent star formation activity. This is further evidence that SLSNe come from massive stars, as is also seen by their associations with star-forming galaxies in general, and high specific star formation rates in particular (Lunnan et al. 2014). While their locations are statistically consistent with those of LGRBs, the SLSNe appear to not be as strongly correlated with the brightest regions of their host galaxies as the LGRBs are (Figure 4.6). Since a stronger correlation with star formation tracers is generally interpreted as evidence for a younger and more massive progenitor population (Fruchter et al. 2006; Anderson et al. 2012; Kelly et al. 2008), the simplest interpretation is that SLSN progenitors are older/less massive stars than LGRB progenitors. We note that recently, Leloudas et al. (2015) have argued that SLSNe result from more massive stars than LGRBs; our result of SLSN locations is potentially at odds with this interpretation. Instead, as we argued in Lunnan et al. (2014), the host galaxy properties seem to lead to the conclusion that the progenitors require low metallicity, potentially as a requirement for a magnetar remnant.

While the locations of SLSNe may not be more strongly correlated with star formation activity than those of ordinary core-collapse SNe, the fact remains that their overall host environments are strikingly different. Our results can also be interpreted to mean that the most important environmental factor for producing a SLSN is something

different than the progenitor mass alone. One such factor could be metallicity, as H-poor SLSNe are generally found in low-metallicity galaxies (Lunnan et al. 2013, 2014; Chen et al. 2013, 2014; Leloudas et al. 2015). In addition, several proposed models for SLSNe are consistent with a low metallicity preference, either directly in the case of PISN models, or indirectly in the case of models that require a rapidly rotating progenitor, such as the magnetar model (Chatzopoulos & Wheeler 2012a,b; Woosley 2010; Kasen & Bildsten 2010). A low-metallicity requirement could explain why some SLSNe appear to explode in regions away from the most intense star formation, especially in the more massive galaxies in our sample. In particular it is worth noting that in all cases where the SLSN exploded in what looks like an ordinary disk galaxy (PS1-12bqf in the *HST* sample, and the lower-redshift PTF11rks and MLS121104 in Lunnan et al. 2014), the SN location is in the outskirts of the galaxy. The fact that our sample is dominated by irregular dwarf galaxies could explain why a potential metallicity preference is not reflected as a preference for large offsets in the overall distribution.

While metallicity is one possible option (and one that is often invoked also to explain the environmental preferences of LGRBs), it is not the only possibility. Recently, Kelly et al. (2014) showed that the host galaxies of both broad-lined type Ic SNe and LGRBs have high stellar mass and star formation densities, compared to SDSS galaxies of similar masses, and we find that SLSN host galaxies show the same trend (Figure 4.4). Since this trend cannot be explained by a simple metallicity preference, Kelly et al. (2014) instead argue the key factor may be that massive binary progenitor systems can form more efficiently in regions of dense star formation (Goddard et al. 2010; Silva-Villa et al. 2013). van den Heuvel & Portegies Zwart (2013) have proposed a dynamical origin for SLSNe, as the result of runaway collisions in dense star clusters. If this is the dominant

channel for producing SLSNe, however, it would be difficult to explain our result that some fraction of SLSNe explode well away from the brightest regions of star formation.

In the context of the interaction-driven model for SLSNe, the natural comparison sample would be the H-rich SLSNe, since these do show clear signs of interaction in their spectra. No similar study of the locations of this class has yet been carried out, unfortunately, though their overall environments appear to be less extreme than those of H-poor SLSNe (Leloudas et al. 2015). For interaction-driven SNe in general, Habergham et al. (2014) examined the locations of 26 Type IIn SNe, and found that they overall traced the UV light distribution, but was not correlated with ongoing star formation as traced by Hα. This result is perhaps surprising, as Type IIn SNe are thought to have massive progenitors such as Luminous Blue Variable stars (LBVs; e.g. Gal-Yam & Leonard 2009), whereas the Type IIn locations would suggest similar progenitor masses as ordinary Type IIp SNe. Recently, Smith & Tombleson (2015) have argued that both the observed isolated locations of LBVs and the locations of Type IIn SNe are naturally explained in a scenario where LBVs are the product of binary evolution, with a significant fraction being kicked from its birth cluster when the companion goes supernova. This illustrates how other factors than progenitor mass can have a significant impact on the observed locations of SN subtypes, and that the different correlations between SN locations and UV light between different populations need not be due to a simple mass difference if binary progenitor models are considered.

4.7 Conclusions

We have carried out the first study of the sub-galactic environments of H-poor SLSNe, using resolved rest-frame UV imaging from *HST* and precise SN locations. Our conclusions are as follows:

- The host galaxies of H-poor SLSNe are generally irregular dwarf galaxies: about half show asymmetric morphology or multiple peaks, and there is a distinct lack of grand-design spiral galaxies compared to CCSN host galaxies in the same redshift range.

- SLSN host galaxies are compact, with a median half-light radius of 0.9 kpc. The median SFR surface density, as derived from the UV flux, is 0.1 $M_{\odot}\mathrm{yr}^{-1}\mathrm{kpc}^{-2}$. SLSN host galaxies exhibit high SFR surface densities for their stellar masses compared to host galaxies of local CCSNe.

- The median offset between SLSNe and their hosts is $\sim$ 1 kpc. The normalized offset distribution is consistent with those of other types of transients with massive star progenitors, with a median normalized offset of 1 half-light radius.

- The locations of H-poor SLSNe are correlated with the UV light. We find that their distribution is intermediate between those of LGRBs (which trace the brightest regions of their hosts) and a uniform distribution, and cannot be distinguished statistically from either with the current sample size.

The galaxy properties derived from the *HST* images support the overall picture that H-poor SLSNe explode in host galaxies that are overall different from core-collapse

SN hosts, and that share many similarities with LGRB host galaxies. Both samples are primarily found in irregular galaxies, with similar typical sizes. In addition, both are found in galaxies with high star formation surface densities. Thus, the galaxy-scale properties support the results of Lunnan et al. (2014) that similar environmental factors are necessary for stars to end their lives as either a H-poor SLSN or a LGRB.

At the same time, our study of the sub-galactic locations of SLSNe indicates that the *local* environments of SLSNe and LGRBs may be different, with SLSNe being less biased towards the brightest regions of their host galaxies (although a larger sample size is necessary to distinguish them statistically). This can be interpreted as SLSN progenitors being less massive and longer-lived stars than LGRB progenitors, contrary to recent claims that SLSNe are the very first stars to explode in a starburst (Leloudas et al. 2015). Our results are consistent with the recent results of Vreeswijk et al. (2014), however, who find that the ISM column densities along SLSN lines of sight are on the low end of what is seen in LGRBs, also suggesting that they trace different local environments.

Acknowledgements

We thank the anonymous referee for helpful comments that improved the clarity of the paper. Support for programs number GO-12529, GO-13022 and GO-13326 was provided by NASA through a grant from the Space Telescope Science Institute, which is operated by the Association of Universities for Research in Astronomy, Inc., under NASA contract NAS5-26555. The Pan-STARRS1 Surveys (PS1) have been made possible through contributions of the Institute for Astronomy, the University of Hawaii, the

Pan-STARRS Project Office, the Max-Planck Society and its participating institutes, the Max Planck Institute for Astronomy, Heidelberg and the Max Planck Institute for Extraterrestrial Physics, Garching, The Johns Hopkins University, Durham University, the University of Edinburgh, Queen's University Belfast, the Harvard-Smithsonian Center for Astrophysics, the Las Cumbres Observatory Global Telescope Network Incorporated, the National Central University of Taiwan, the Space Telescope Science Institute, the National Aeronautics and Space Administration under Grant No. NNX08AR22G issued through the Planetary Science Division of the NASA Science Mission Directorate, the National Science Foundation under Grant No. AST-1238877, the University of Maryland, and Eotvos Lorand University (ELTE). This paper includes data based on observations made with the NASA/ESA *Hubble Space Telescope* and obtained from the Hubble Legacy Archive, which is a collaboration between the Space Telescope Science Institute (STScI/NASA), the Space Telescope European Coordinating Facility (ST-ECF/ESA) and the Canadian Astronomy Data Centre (CADC/NRC/CSA). SJS acknowledges funding from the European Research Council under the European Union's Seventh Framework Programme (FP7/2007-2013)/ERC grant agreement n^{o} [291222]. RPK acknowledges support from the National Science foundation through AST1211196.

4.8 Appendix: HST Image of the Host Galaxy of PS1-10afx

The unusual transient PS1-10afx was included in our *HST* sample because it was initially considered to be a SLSN at $z = 1.388$ (Chornock et al. 2013). However, Quimby et al.

(2013b) identified it as a strongly gravitationally lensed SN Ia (magnification ∼30). Subsequent spectroscopy by Quimby et al. (2014) identified an emission line from a fainter foreground galaxy at $z = 1.1168$ along the line of sight to the brighter host galaxy. We present the F814W image of the field in Figure 4.7 with the transient location marked by a red circle. No arcs or other strongly distorted images of the background galaxy are clearly identifiable. Deeper images with more color information would be necessary to decompose the observed source into a background host and foreground lens. We leave an analysis of the implied constraints on the lensing geometry to future work.

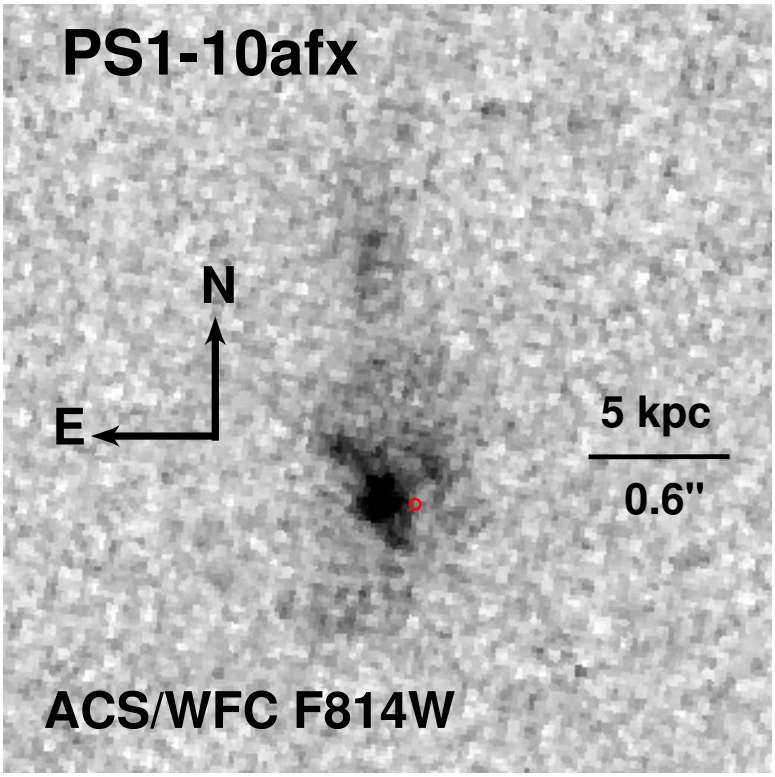

Figure 4.7.—: $4'' \times 4''$ image of the field around PS1-10afx. The SN location is marked with the red circle.

Chapter 5

Hydrogen-Poor SLSNe from the Pan-STARRS Medium Deep Survey

R. Lunnan, R. Chornock, E. Berger, and the Pan-STARRS MDS Transient Group

In Preparation

Abstract

We present light curves and spectra of 15 hydrogen-poor superluminous supernovae (SLSNe) from the Pan-STARRS Medium Deep Survey (PS1/MDS). Our sample contains all objects from the PS1/MDS spectroscopic sample that are similar to either of the prototypes SN 2005ap/SCP06F6 or SN 2007bi, without an explicit cut on luminosity. With a redshift range $0.5 < z < 1.6$, our multi-filter PS1 light curves probe the rest-frame UV emission, sensitive to the peak of the spectral energy distribution. We measure the temperature evolution and construct bolometric light curves, and find peak luminosities ranging from $(0.5 - 5) \times 10^{44}$ erg s^{-1} and total radiated energies of $(0.3 - 2) \times 10^{51}$ erg. When accounting for the flux-limited nature of our survey, we find a lower mean peak luminosity with a larger spread than reported by other studies: $\langle M_{400} \rangle \simeq -21.2 \pm 0.7$ mag. We find that a magnetar spin-down model can reproduce the observed light curves, including the lower-luminosity objects, although we have to include hard emission leakage in order to fit the decline in some cases. Only one object in our sample, PS1-14bj, is spectroscopically similar to SN 2007bi. PS1-14bj shows a broad light curve with a slow rise ($\gtrsim 100$ rest-frame days) and red colors, and while its light curve can be fit with a magnetar model, its properties are also consistent with radioactive Ni as the power source. Thus, it demonstrates that at least some SLSNe could be powered by ^{56}Ni-decay, possibly being examples of pair-instability supernovae in the low-redshift universe.

5.1 Introduction

Superluminous supernovae (SLSNe) are a rare class of supernovae (SNe) discovered in galaxy-untargeted transient surveys in the past decade. They are characterized by peak luminosities of 10-100 times those of normal core-collapse and Type Ia SNe, and are significantly rarer ($\sim 0.01\%$ of the core-collapse SN rate; Quimby et al. 2013a; McCrum et al. 2015). With total radiated energies of order 10^{51} erg, their light curves are difficult to explain with conventional SN energy sources, and as a result this class has garnered significant attention.

SLSNe can be divided into at least two spectroscopic subclasses, based on the presence of hydrogen in the spectrum. The H-rich SLSNe are likely powered by interaction with a dense circumstellar medium (CSM), similar to Type IIn SNe (e.g. Ofek et al. 2007; Smith et al. 2007, 2010; Chatzopoulos et al. 2011; Drake et al. 2011a; Rest et al. 2011). CSM interaction has also been proposed as a mechanism for the H-poor SLSNe, but would require an extreme mass-loss history in order to reproduce the observed light curves: several $M_{\odot}$ of H-poor material lost in the last $\sim$year before explosion (Chevalier & Irwin 2011; Ginzburg & Balberg 2012; Chatzopoulos & Wheeler 2012b; Moriya et al. 2013). The lack of narrow lines seen in the spectra at any epoch is also a puzzle if CSM interaction is the power source. Alternative explanations include a central-engine model, such as the spin-down of a newborn magnetar energizing the ejecta over timescales of weeks (Woosley 2010; Kasen & Bildsten 2010; Dessart et al. 2012). This model is partially supported by that H-poor SLSNe are generally found in dwarf galaxy environments with low metallicities and high specific star formation rates, similar to long gamma-ray burst environments which are also thought to have a rapidly rotating

central engine as the power source (Lunnan et al. 2014, 2015).

It has also been suggested that the slowest-evolving H-poor SLSNe, and in particular SN 2007bi, could be powered by the radioactive decay of several $M_{\odot}$ of ^{56}Ni (Gal-Yam et al. 2009; Gal-Yam 2012). In this scenario, the estimated Ni and ejecta masses would then imply that SN 2007bi was a pair-instability SN (PISN; e.g. Barkat et al. 1967). This interpretation is controversial, however, as the light curve of SN 2007bi can also be explained by magnetar spin-down or interaction models, and similar objects where the entire light curve was observed (SN 2007bi was discovered near peak) have rise times that are too fast for a PISN interpretation (Young et al. 2010; Dessart et al. 2012; Nicholl et al. 2013). Whether slowly-evolving or SN 2007bi-like SLSNe represent a separate subclass or not is still an open question.

Since SLSNe are rare, previous studies have largely focused on individual events. Recently, a few studies compiling low-redshift events have attempted to look at H-poor SLSNe as a class, suggesting that their properties can be explained by a magnetar-powered model (Inserra et al. 2013; Nicholl et al. 2014, 2015), and that their intrinsic spread in luminosities is low, suggesting they may be utilized as standard candles (Inserra & Smartt 2014). These studies are limited in that they combine events from a number of different surveys, making it difficult to account for selection effects. In addition, since SLSNe generally peak in the UV, surveys probing higher redshifts are better suited to address the true luminosities and radiated energies. Here, we present the full sample of H-poor SLSNe discovered in the Pan-STARRS Medium Deep Survey (PS1/MDS) over its four years of operation, comprising of 15 events over a redshift range $0.5 < z < 1.6$. This is the first compilation study of SLSNe from a single survey to date, and also the first study focusing on the high-redshift population.

We describe the survey parameters, our selection criteria for designating something a SLSN, and present the classification spectra and observed light curves in Section 5.2. Inferred physical properties, such as temperature evolution, expansion velocities, bolometric light curves and total radiated energies are presented in Section 5.3. We compare our observed sample to simple models for powering SLSNe in Section 5.4. Implications our our findings are discussed in Section 5.5, and summarized in Section 5.6. Throughout this paper, we assume a flat ΛCDM cosmology with $\Omega_{\rm M} = 0.27$, $\Omega_{\Lambda} = 0.73$ and $H_0 = 70$ km s^{-1} (Komatsu et al. 2011).

5.2 The PS1/MDS SLSN Sample

5.2.1 Pan-STARRS Medium Deep Survey Description

The PS1 telescope on Haleakala is a high-etendue wide-field survey instrument with a 1.8-m diameter primary mirror and a 3.3° diameter field of view imaged by an array of sixty 4800×4800 pixel detectors, with a pixel scale of $0.258''$ (Kaiser et al. 2010; Tonry & Onaka 2009). Tonry et al. (2012) describes the photometric system and broadband filters in detail.

The Pan-STARRS Medium Deep Survey (PS1/MDS) operated from late 2009 to early 2014. PS1/MDS consists of 10 fields (each with a single PS1 imager footprint) observed in $g_{\rm P1}r_{\rm P1}i_{\rm P1}z_{\rm P1}$with a typical cadence of 3 d in each filter, to a typical nightly depth of ~ 23.3 mag (5σ); $y_{\rm P1}$is used near full moon with a typical depth of ~ 21.7 mag. The standard reduction, astrometric solution, and stacking of the nightly images are done by the Pan-STARRS1 Image Processing Pipeline (IPP) system (Magnier 2006;

Magnier et al. 2008) on a computer cluster at the Maui High Performance Computer Center. For the transients search, the nightly MDS stacks were transferred to the Harvard FAS Research Computing cluster, where they were processed through a frame subtraction analysis using the `photpipe` pipeline developed for the SuperMACHO and ESSENCE surveys (Rest et al. 2005; Garg et al. 2007; Miknaitis et al. 2007; Rest et al. 2014).

A subset of targets was selected for spectroscopic follow-up, using the Blue Channel spectrograph on the 6.5-m MMT telescope (Schmidt et al. 1989), the Gemini Multi-Object Spectrograph (GMOS; Hook et al. 2004) on the 8-m Gemini telescopes, and the Low Dispersion Survey Spectrograph (LDSS3) and Inamori-Magellan Areal Camera and Spectrograph (IMACS; Dressler et al. 2006) on the 6.5-m Magellan telescopes. The SLSNe were generally targeted for spectroscopy based on a combination of blue observed color, long observed rise-time, and being several magnitudes brighter than any apparent host in the PS1 deep stacks. We note that the combination of a relatively small survey area and deep photometry provides sensitivity primarily to SLSNe at higher redshifts: the sample spans $0.5 \lesssim z \lesssim 1.6$. Table 5.1 lists the full sample.

Table 5.1. SLSNe from PS1/MDS

Object	Redshift	RA	Dec	Reference
PS1-12bqf	0.522	$02^{h}24^{m}54.621^{s}$	$-04°50'22.72''$	
PS1-11ap	0.524	$10^{h}48^{m}27.752^{s}$	$+57°09'09.32''$	McCrum et al. (2014)
PS1-14bj	0.54	$10^{h}02^{m}08.433^{s}$	$+03°39'19.02''$	
PS1-10bzj	0.650	$03^{h}31^{m}39.826^{s}$	$-27°47'42.17''$	Lunnan et al. (2013)
PS1-11bdn	0.738	$02^{h}25^{m}46.292^{s}$	$-05°03'56.57''$	
PS1-13gt	0.884	$12^{h}18^{m}02.035^{s}$	$+47°34'45.95''$	
PS1-10awh	0.909	$22^{h}14^{m}29.831^{s}$	$-00°04'03.62''$	Chomiuk et al. (2011)
PS1-10ky	0.956	$22^{h}13^{m}37.851^{s}$	$+01°14'23.57''$	Chomiuk et al. (2011)
PS1-11aib	0.997	$22^{h}18^{m}12.217^{s}$	$+01°33'32.01''$	
PS1-10pm	1.206	$12^{h}12^{m}42.200^{s}$	$+46°59'29.48''$	McCrum et al. (2015)
PS1-11tt	1.283	$16^{h}12^{m}45.778^{s}$	$+54°04'16.96''$	
PS1-11afv	1.407	$12^{h}15^{m}37.770^{s}$	$+48°10'48.62''$	
PS1-13or	1.52	$09^{h}54^{m}40.296^{s}$	$+02°11'42.24''$	
PS1-11bam	1.565	$08^{h}41^{m}14.192^{s}$	$+44°01'56.95''$	Berger et al. (2012)
PS1-12bmy	1.572	$03^{h}34^{m}13.123^{s}$	$-26°31'17.21''$	

5.2.2 Classification Spectra

As we are interested in the true luminosity range of SLSNe, we do not include a luminosity cut in our definition, and instead adopt a spectroscopy-based selection. We define our sample of SLSNe as SNe that are spectroscopically similar to either of the prototypes SN 2005ap/SCP06FC (2005ap-like) or to SN 2007bi (2007bi-like). Furthermore, we use the spectrum taken closest to peak light for classification, to make the selection as uniform as possible. With these criteria, we find 14 2005ap-like objects in the PS1/MDS spectroscopic sample, and one 2007bi-like. Their spectra are shown in Figure 5.1, and details of spectroscopic observations (where previously unpublished) are listed in Table 5.2.

Note that PS1-11ap has been classified as 2007bi-like by Nicholl et al. (2013) and McCrum et al. (2014) based on it evolving to show 2007bi-like features in its late-time spectra. The spectrum near peak, however, is dominated by a blue continuum with broad UV features, and so for the purposes of this paper we will consider it as part of the 2005ap-like SLSNe. We return to the question of whether 2005ap-like and 2007bi-like objects should be considered separate physical phenomena or not in Section 5.5.

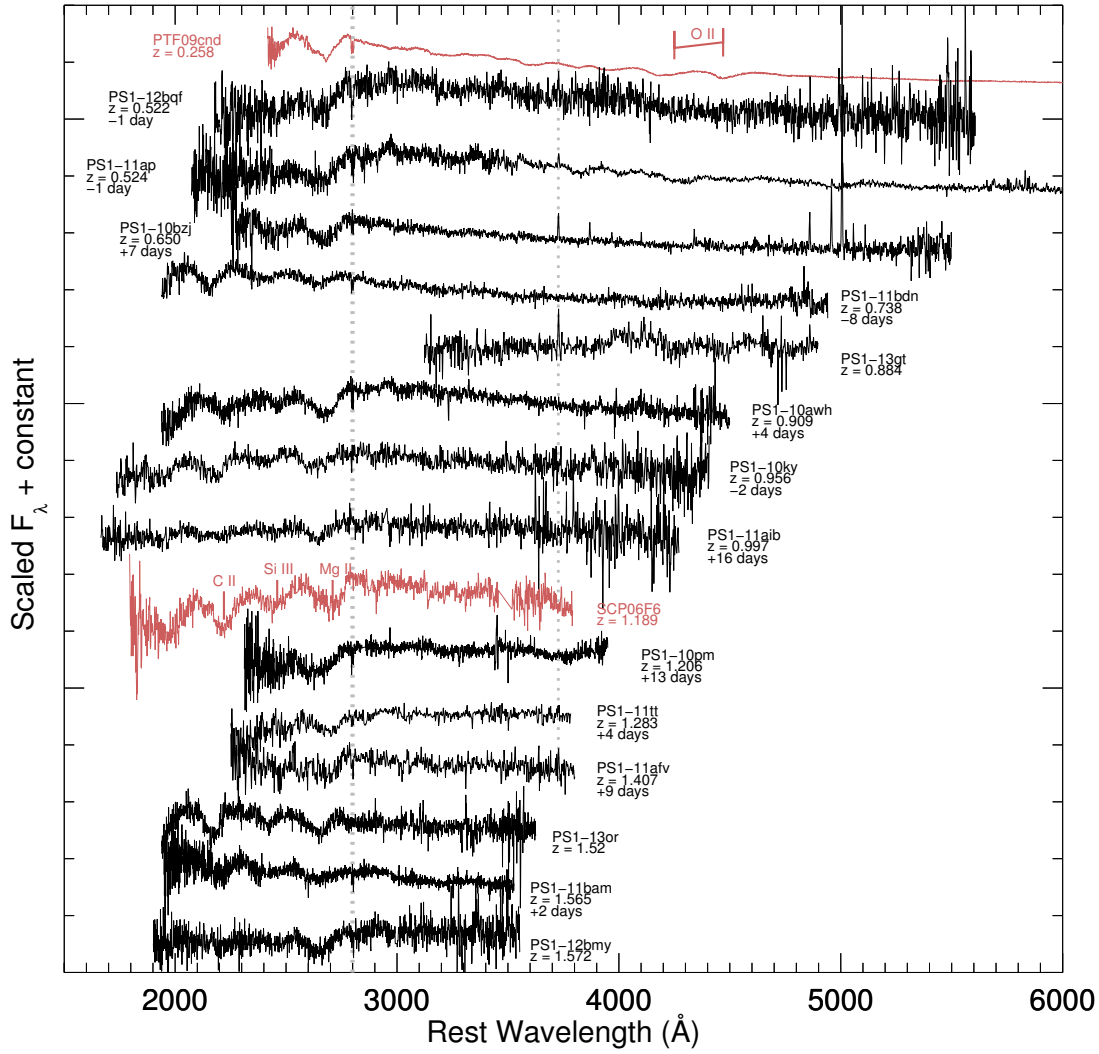

Figure 5.1.—: Classification spectra of the 14 2005ap-like SLSNe in our sample, taken as close to peak light as possible (actual phase indicated for each spectrum, unless time of peak is not constrained). The dotted gray lines show the location of the Mg II $\lambda\lambda$2796,2803 doublet and the [O II]λ3727 emission line, which were used to determine the redshift for most of these objects. SCP06F6 and PTF09cnd are plotted for comparison, with strong spectral features marked (Barbary et al. 2009; Quimby et al. 2011b).

Table 5.2. Log of Spectroscopic Observations

Object	UT Date (YYYY-MM-DD.D)	Phase (days)	Instrument	Wavelength Range (Å)	Slit (″)	Grating	Filter	Exp. time (s)	Airmass
PS1-12bqf	2012-11-14.2	−1	MMT/BlueChannel	3310-8530	1.0	300GPM	none	3000	1.2
PS1-14bj	2014-03-08.3	−63	MMT/BlueChannel	3330-8550	1.0	300GPM	none	3600	1.2
PS1-14bj	2014-03-28.3	−50	GN/GMOS	5640-9910	1.0	R400	OG515	3600	1.0
PS1-11bdn	2012-01-01.1	−8	MMT/BlueChannel	3370-8580	1.0	300GPM	none	3600	1.3
PS1-13gt	2013-03-05.7	···	GN/GMOS	5880-10160	1.0	R400	OG515	3600	1.1
PS1-11aib	2011-11-28.1	+16	MMT/BlueChannel	3330-8540	1.0	300GPM	none	5400	1.3
PS1-11tt	2011-06-07.5	+4	GN/GMOS	4860-8640	1.0	R400	GG455	3000	1.5
PS1-11afv	2011-07-09.3	9	GN/GMOS	4900-9150	1.0	R400	GG455	2400	1.5
PS1-13or	2013-05-04.0	···	GS/GMOS	4890-9140	1.0	R400	GG455	3600	1.2
PS1-12bmy	2012-11-11.1	···	GS/GMOS	4890-9140	1.0	R400	GG455	3600	1.1

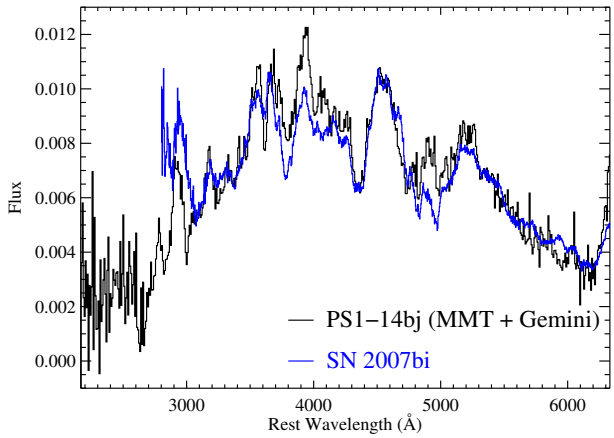

Figure 5.2.—: Classification spectrum of PS1-14bj (black), taken prior to peak light. In contrast to the objects shown in Figure 5.1, PS1-14bj's spectrum is considerably redder and dominated by Mg and Fe features. It is an excellent spectroscopic match to SN 2007bi (blue). We do not detect any narrow lines from a host galaxy in this object, and our redshift of 0.54 is based on the spectral comparison to SN 2007bi.

5.2.3 Light Curves

The multi-band nature of PS1/MDS means we have $g_{\rm P1}r_{\rm P1}i_{\rm P1}z_{\rm P1}$light curves available for all objects. The PS1 photometry, as well as any additional photometry acquired as part of follow-up, are listed in Appendix 5.7. Observed light curves of the 15 objects in our sample are shown in Figure 5.3. Note the long observed timescales in many cases, due both to intrinsically longer timescales of SLSNe, as well as time dilation. The long timescales also mean that depending on when an object was discovered during an observing season, we may not have a complete light curve. We are plausibly catching at least the peak in most cases, at least, with the exceptions of PS1-11bdn, PS1-12bmy, PS1-13gt and PS1-13or.

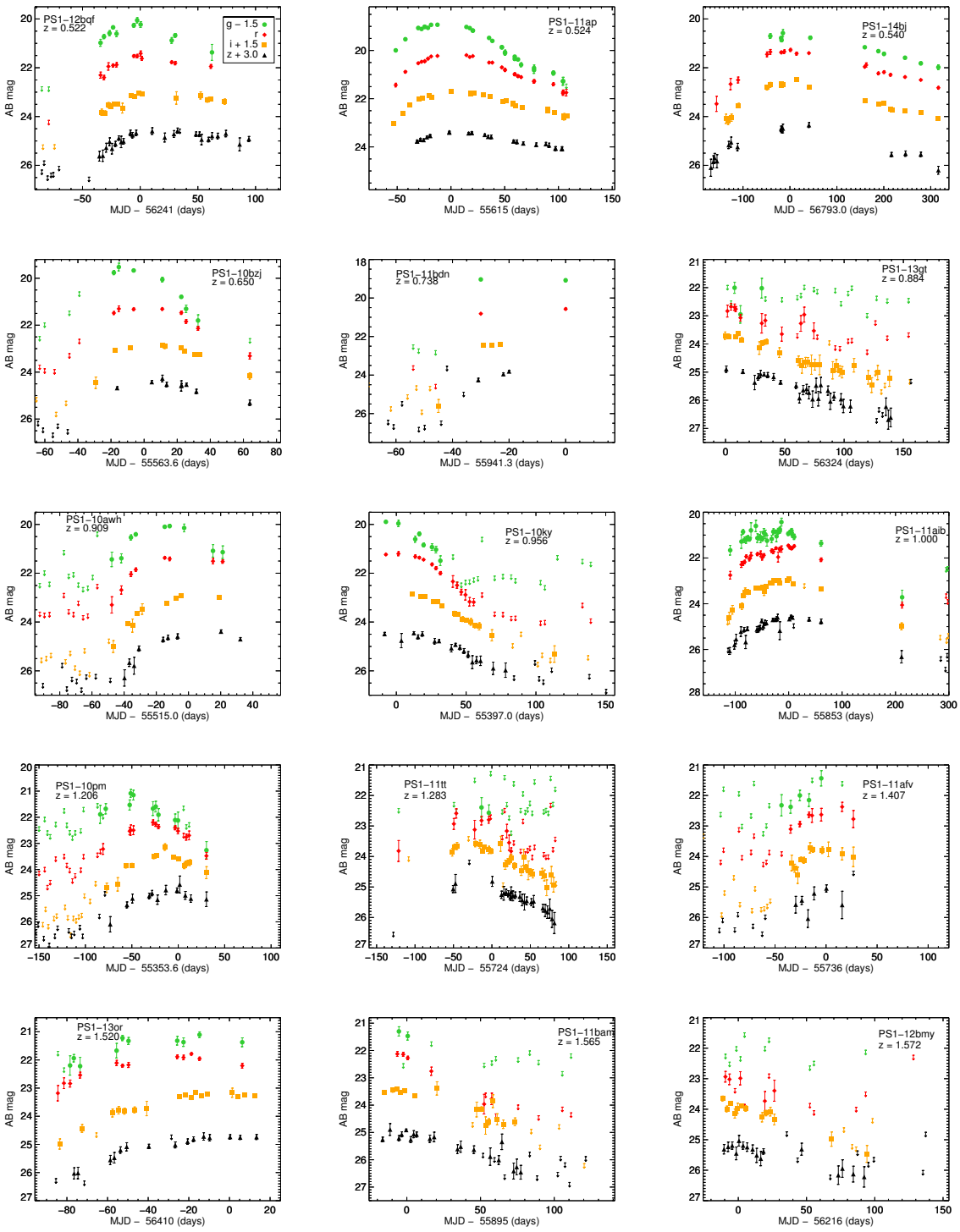

Figure 5.3.—: Light curves of all 15 events in our H-poor SLSN sample, sorted in order of redshift. Filters are offset by 1.5 mag for clarity, as indicated by the legend in the top left panel.

5.3 Derived Physical Parameters

5.3.1 Temperature

We measure temperature as a function of time from the light curves by fitting blackbody curves to the observed photometry. PS1 generally did not observe different filters on the same night, but $g_{\rm P1}$and $r_{\rm P1}$were typically observed the same night, and so we use $r_{\rm P1}$as the baseline. If there is photometry from the other bands from the same night or $\pm$ 1 day, we use those measurements without corrections. If not, we use the polynomial fit to the light curve in that filter and interpolate to the date of the $r_{\rm P1}$observation. We only fit SEDs to epochs where at least 3 filters were observed. Figure 5.4 shows the resulting blackbody temperatures derived from the photometry.

Early measurements in particular are noisy, because the peak of the blackbody can be bluewards of the observed bands, even for the high-redshift PS1/MDS sample. To the extent that we can measure it, we find that the color temperatures prior to peak are either constant or slowly cooling, with temperatures in the range $10,000 - 25,000$ K. This highlights the need for UV follow-up of SLSNe, particularly at early epochs. Post-peak the color temperatures go down as the SNe cool and expand.

Two of the objects in our sample deviate from this trend, essentially having redder colors and cooler temperatures over the entire observed time period: PS1-13gt and PS1-14bj. In PS1-13gt, we only sample the decline and cannot constrain the time of peak, so the red colors could simply be due to the age of the SNe – we cannot rule out that this object had a similar temperature near peak as the other objects. In addition, the spectrum of this object (Figure 5.1) is consistent with this supernova being

reddened by dust, with the main SN features being O II that is normally seen at higher temperatures than the spectral slope would indicate. When dereddened by E($B-V$) $\simeq 0.3$ mag, the spectrum is an excellent match to PTF09cnd.

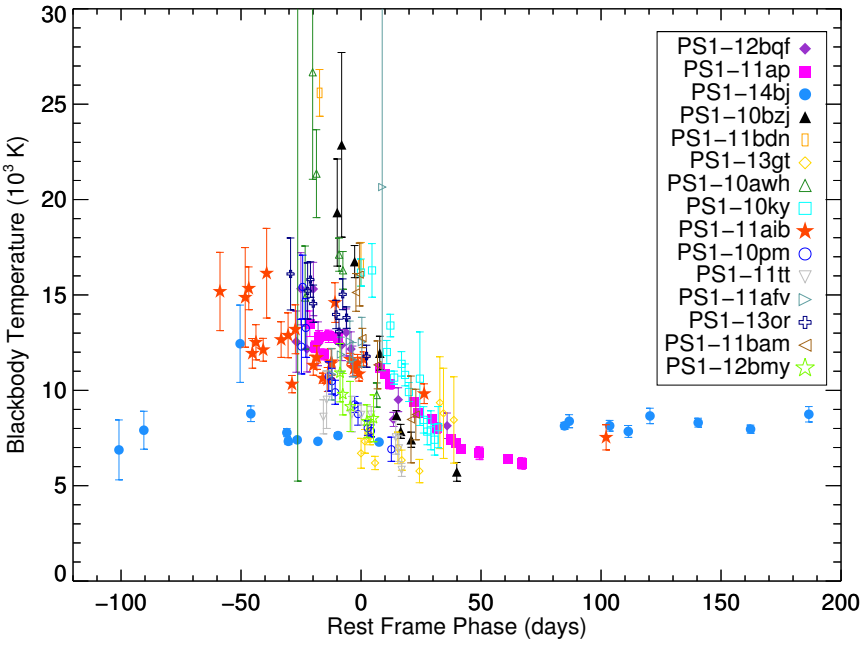

Figure 5.4.—: Color temperature as a function of phase, measured by fitting a blackbody to the photometry at each epoch. Prior to peak, the 2005ap-like SLSNe show hot color temperatures around $15,000-25,000$ K, and cool over a timescale of $20-50$ days after peak light. PS1-14bj, our only 2007bi-like SLSN, shows color temperatures of $6000-8000$ K over its entire evolution.

PS1-14bj was discovered on the rise (so uncertainty in phase cannot explain the colors) and has a near-constant blackbody temperature of $6000-8000$ K during the entire observed period. The red colors of PS1-14bj throughout are interesting in part because one prediction of PISN models is that the photosphere will be much cooler than what is typically observed in SLSNe, due to the large UV opacities of Fe-group elements blanketing the blue flux (e.g., Dessart et al. 2013).

5.3.2 Expansion Velocity

We measure velocities from the spectra by fitting Gaussians to the absorption features and determining the locations of the minima. The ID of the features is debated – Quimby et al. (2011b) identified them with C II, Si III and Mg II, whereas Howell et al. (2013) favors Fe III, C II/III and Mg II. We do not attempt modeling of the spectra given the spread in quality and wavelength coverage for our objects. However, in all but one of our SLSNe that are classified as 2005ap-like our spectra cover the broad Mg II feature, and we use this to get an estimate of the velocity at peak. We fit a Gaussian to this feature to find the minimum, and calculate the associated velocity from the blueshift relative to the narrow Mg II lines from the host galaxy. Table 5.3 lists the expansion velocities derived in this fashion. They range from $10,000$ to $18,000$ km s^{-1}, with typical values of around $15,000$ km s^{-1}. This is similar to what has been seen in other SLSNe around peak light (e.g., Quimby et al. 2011b; Inserra et al. 2013; Nicholl et al. 2014).

5.3.3 Bolometric Light Curves and Total Radiated Energies

To construct bolometric light curves, we start by summing up the flux in the observed bands at each multi-filter epoch via trapezoidal integration, interpolating the flux to the edge of the filter. Since this only takes into account the flux in the observed bands, it is a strict lower limit on the emitted flux. Given the large redshift range of our sample, the rest-frame wavelengths covered in this estimate also varies considerably, between 2660-6050 Å for the lowest redshift objects PS1-11ap and PS1-12bqf, to 1570-3580 Å for the highest redshift objects.

For a better estimate of the bolometric luminosities, we add a correction to the

Table 5.3. Derived Properties

Object	Peak Lum. (10^{44} erg/s)	Rad. Energy (10^{51} erg)	τ_r (days)	τ_d (days)	Velocity at peak (km s^{-1})
PS1-12bqf	0.47	0.28	28.2	70.4	14,000
PS1-11ap	1.62	1.01	34.3	78.1	16,000
PS1-14bj	0.63	0.96	94.0	135.6	···
PS1-10bzj	1.15	0.37	15.3	36.5	14,000
PS1-11bdn	4.39	0.59	20.3	···	16,000
PS1-13gt	1.24	0.41	···	40.4	···
PS1-10awh	2.15	0.59	22.3	···	13,000
PS1-10ky	2.75	0.58	···	28.2	18,000
PS1-11aib	2.22	2.02	56.5	80.9	16,000
PS1-10pm	2.57	0.77	···	···	16,000
PS1-11tt	2.69	1.22	···	47.0	10,000
PS1-11afv	2.49	0.41	···	···	10,000
PS1-13or	5.19	1.12	29.4	···	···
PS1-11bam	4.19	0.94	···	28.0	17,000
PS1-12bmy	3.52	1.05	···	30.5	16,000

observed flux based on the estimated blackbody temperatures. While the spectrum clearly deviates from a blackbody in the UV (bluewards of the observed bands; Figure 5.1), it is reasonably well approximated by a blackbody in the red. We therefore integrate a blackbody curve redwards of the observed bands, with the observed color temperature and scaled to match the flux in the reddest observed filter, and add this to the observed flux. The size of this correction is small (order 10-20%) at early times, but can be substantial at later times as the SNe cool and the blackbody peak shifts to the red. Similarly, the correction gets larger as we move up in redshift, as the observed filters cover bluer rest-frame wavelengths. Again, direct comparison between the different objects is perilous given that the higher-redshift objects will include more of the UV flux and therefore be closer to the true bolometric luminosity.

Figure 5.5 shows the pseudo-bolometric light curves calculated in this fashion. While only a handful of light curves are well sampled both before and after peak, the diversity in light curve shapes is still apparent. We explore this in a more quantitative way below.

Figure 5.6 shows the peak luminosities in erg/s, plotted as a function of redshift. The lack of lower-luminosity redshift objects past redshift $z \simeq 1$ is likely due to the follow-up limit of PS1, and the scatter in peak luminosities is lower as a result of our inabilities to detect fainter objects at these redshifts. Some of the trend towards higher luminosities will also be due to our pseudo-bolometric light curves for these objects capturing more of the UV flux. With the exception of PS1-12bqf and PS1-14bj, all of the PS1 H-poor SLSNe peak at $1 - 5 \times 10^{44}$ ergs^{-1}.

By integrating our estimated bolometric light curves, we get a lower limit on the total radiated energy of each supernova; the results are plotted in Figure 5.7. Filled

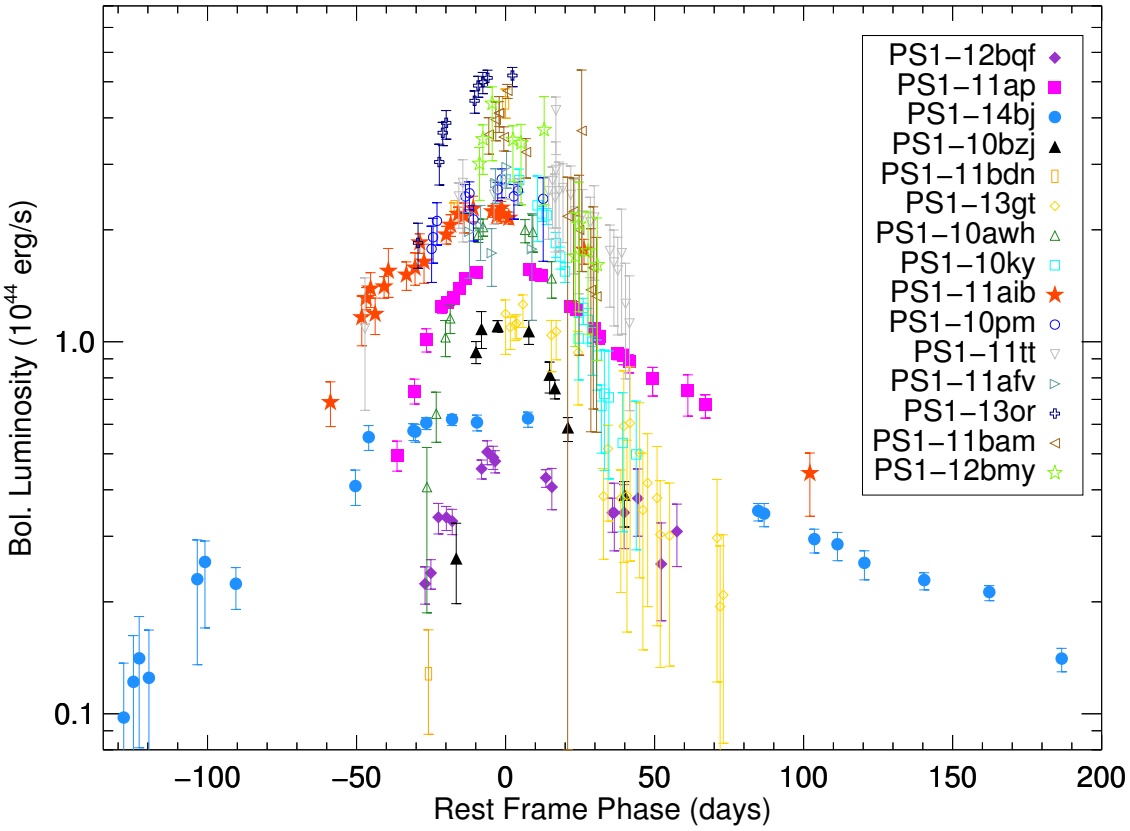

Figure 5.5.—: Pseudo-bolometric light curves, created by summing up the observed flux and adding a blackbody tail in the red. Where there is insufficient color information at the very beginning or end of a light curve, points have been plotted assuming a constant bolometric correction. We use these light curves to measure peak bolometric luminosites, total radiated energies, and rise- and decay timescales.

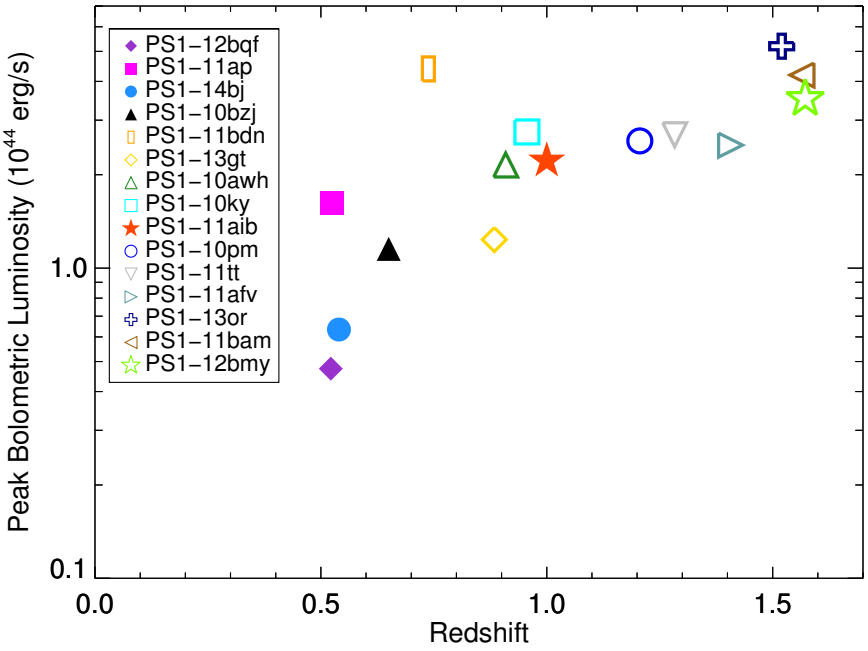

Figure 5.6.—: Luminosities at peak, as measured from our pseudo-bolometric light curves (Figure 5.5). Higher redshift objects have more of the UV flux included in the bolometric estimates, so the numbers at high- and low redshift are not directly comparable; the numbers at low redshift alone show that the peak luminosities of SLSNe can vary by almost an order of magnitude, however. The low scatter at the high redshift end is due to the limitations of spectroscopic follow-up: objects like PS1-12bqf would be too faint to classify at these redshifts.

symbols correspond to objects were we sample both the rise and the decline; the results span close to an order of magnitude. Both light curve shape and overall luminosity obviously contribute here – while PS1-14bj and PS1-12bqf are the lowest-luminosity objects in the sample, the total radiated energy of PS1-14bj is comparable to the higher-luminosity objects, thanks to the exceptionally wide light curve. In contrast, the radiated energy of PS1-12bqf is the lowest of all in the sample, despite many of the other objects having incomplete light curves.

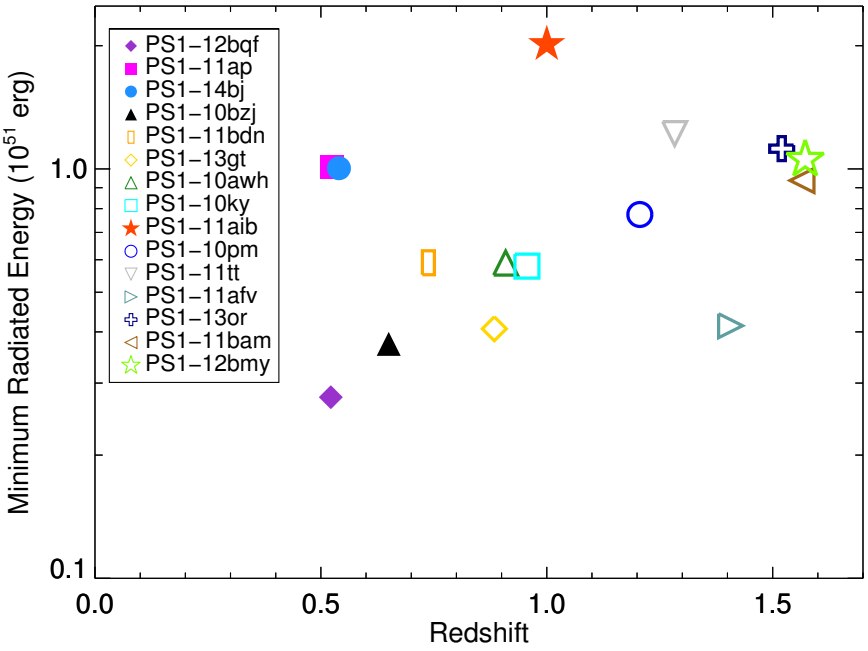

Figure 5.7.—: Total radiated energies, again as a function of redshift, measured by integrating the pseudo-bolometric light curves (Figure 5.5). Filled symbols correspond to objects where both the rise and decline of the light curves are well sampled. Numbers plotted here should be considered lower limits, both because we do not in general cover the entire light curve, and because we are not accounting for the flux bluewards of the observed bandpasses.

5.3.4 Rise- and Decay Timescales

We measure the time of peak, and the rise- and decay times by fitting low-order polynomials to our pseudobolometric light curves. For estimates of the rise- and decay times, we follow Nicholl et al. (2015) and define these timescales as the time between peak and the luminosity being $1/e$ of the value at peak; we will refer to them as τ_r and τ_d, respectively.

The rise- and decline timescales are plotted in Figure 5.8 as a function of redshift, with the data from Nicholl et al. (2015) shown as crosses. Since we have defined our pseudo-bolometric light curves in a different manner, timescales derived may also differ somewhat, since we included more of the bluer flux which fades faster. In the objects overlapping between the two samples, we do find similar numbers to within 10%, however, so this is likely not a large effect. Generally we find similar time scales in the PS1 sample as in the high-redshift sample, with a few interesting exceptions: PS1-14bj is a clear outlier in both plots, with both the rise and decline being significantly slower than the rest of the sample. PS1-11aib also shows a slower rise compared to the rest of the sample, but is not as extreme. Neither PS1-11aib or PS1-14bj fall on the $\tau_d \simeq 2 \times \tau_r$ correlation seen in Nicholl et al. (2014), with the rise being slower and light curves closer to symmetric in both cases. We explore possible models for these two SNe in Section 5.4.

Another interesting feature in Figure 5.8 is the apparent clustering of decay times into two groups: one fast-declining group with a typical time scale of $30 - 40$ days, and a slow-declining group with a typical time scale of about 70 days. This is seen both in the high-redshift PS1 sample and in the low-redshift sample. The earliest example of a "slowly-declining" SLSN was SN 2007bi (Gal-Yam et al. 2009), but none of the three

PS1 objects in this cluster (PS1-11ap, PS1-12bqf and PS1-11aib) would be classified as 2007bi-like based on their spectrum at peak.

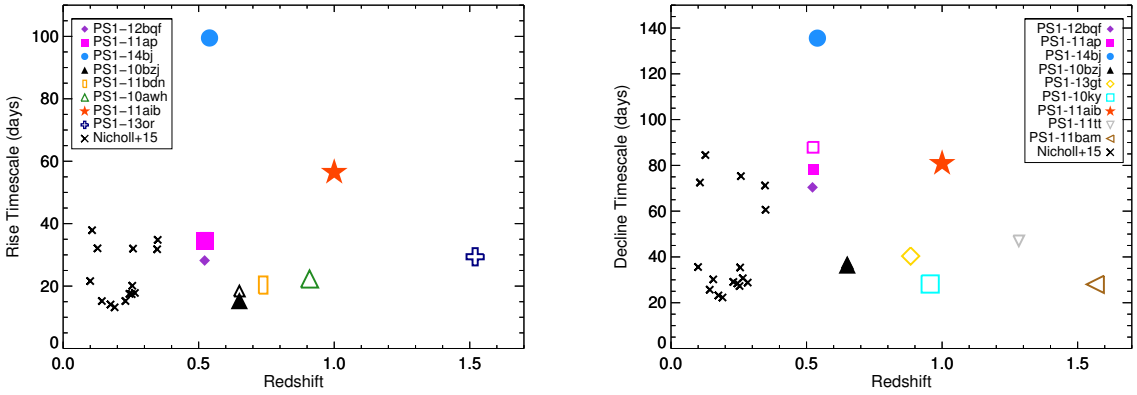

Figure 5.8.—: Rise timescale (left) and decline timescale (right) versus redshift for the PS1 SLSN sample. Black crosses show the low-redshift sample from Nicholl et al. (2015). PS1-10bzj and PS1-11ap were also analyzed by Nicholl et al. (2015), and we plot the values measured from their *griz*-bolometric light curves as open symbols for these two objects. Generally the PS1 sample shows similar timescales as the low-redshift objects, with a few exceptions: PS1-14bj is a clear outlier in both plots, showing significantly longer time scales than the rest of the sample. The rise of PS1-11aib is also slower than any of the low-redshift objects.

5.4 Model Fits to PS1-11aib, PS1-14bj and PS1-12bqf

As a number of our light curves are incomplete, we do not attempt to model the full data set. Here, we instead present model fits for the three objects in our sample that sample both the rise and the decline, and have not been previously published: PS1-11aib, PS1-12bqf and PS1-14bj. These three objects are all interesting in their own right as well. All three fall on the slowly-declining part of Figure 5.8. PS1-12bqf is the

lowest-luminosity object in our sample, and would not be classified as "superluminous" if we were operating by a strict luminosity cut rather than a spectroscopic definition. PS1-14bj is the only object spectroscopically classified as 2007bi-like in our sample, and shows a very distinctive, broad light curve.

5.4.1 Radioactive Decay: PS1-14bj as a PISN

In general, ^{56}Ni decay can be ruled out as the power source for the majority of SLSNe: the combination of high luminosities and reasonably fast evolution near peak leads to an unphysical solution where the Ni mass required to power the light curve peak is comparable to, or larger than, the ejecta mass needed to fit the light curve width (e.g., Quimby et al. 2011b; Chomiuk et al. 2011; Lunnan et al. 2013). Even in SN 2007bi, which was claimed to be ^{56}Ni-powered in Gal-Yam et al. (2009) based on spectroscopic properties as well as a slow decline consistent with ^{56}Co, this interpretation is controversial, in part because SN 2007bi was detected near peak and its rise time was not observed. If SN 2007bi was indeed Ni-powered, the inferred Ni and ejecta masses imply a pair-instability supernova (PISN) explosion, and should be accompanied by a correspondingly long rise time due to the large diffusion time (Kasen et al. 2011; Dessart et al. 2013). A few objects with similar spectroscopic properties as SN 2007bi but with faster rise-times incompatible with PISN models have since been found, casting doubt also on the nature of SN 2007bi (Nicholl et al. 2013).

In this context, PS1-14bj is an extremely interesting comparison object. It is the first SLSN found to show the long ($\sim$ 100 days) rise time predicted by PISN models, thus showing that objects with these kinds of light curves do exist in the local universe, and by

extension that SN 2007bi could plausibly also have had a slow rise. It is spectroscopically similar to SN 2007bi (Figure 5.2), and unlike other SLSNe shows red color temperatures over its entire evolution (Figure 5.4), which is another important prediction of PISN models.

Figure 5.9 shows a simple Ni decay model fit to the light curve of PS1-14bj. Following Arnett (1982), this model has three basic parameters: the nickel mass ($M_{\rm Ni}$) determining the energy input, the kinetic energy ($E_{\rm K}$) and the ejecta mass ($M_{\rm ej}$), which together determine the diffusion time:

$$\tau_m = \left(\frac{10\kappa M_{\rm ej}}{3\beta c v}\right)^{\frac{1}{2}} \propto \kappa^{1/2} M_{\rm ej}^{3/4} E_{\rm K}^{-1/4}. \quad (5.1)$$

$E_{\rm K}$ and $M_{\rm ej}$ are also constrained by measurements of the velocity: $v_{\rm ph} \propto \sqrt{E_{\rm K}/M_{\rm ej}}$, allowing all three parameters to be determined from the data. The light curve of PS1-14bj is well fit by a model with $M_{\rm Ni} = 14$ M$_\odot$ and $M_{\rm ej} = 105$ M$_\odot$, taking the velocity at peak to be 10,000 km s^{-1} and assuming an opacity $\kappa = 0.1$ g^{-1} cm^2. While the Ni mass implied here is more than an order of magnitude higher than what is seen in ordinary Type Ibc SNe (e.g., Drout et al. 2011), the high derived ejecta mass due to the broad light curve gives a reasonable ratio of $M_{\rm Ni}$ to $M_{\rm ej}$. Unlike previous SLSNe, a Ni energy source for PS1-14bj cannot be ruled out from light curve arguments.

An explosion synthesizing $\gtrsim 10$ M$_\odot$ of Ni should produce a luminous light curve tail due to the longer-lived decay of ^{56}Co. The blue line in Figure 5.9 shows the predicted tail phase luminosity produced by 14 M$_\odot$; it fits the observed decline to date very well. Based on the observed luminosity and light curve shape, then, radioactive decay is a plausible energy source for PS1-14bj. The implied ejecta mass in this scenario would put PS1-14bj soundly in the regime of a PISN explosion. We note that the broad light curve

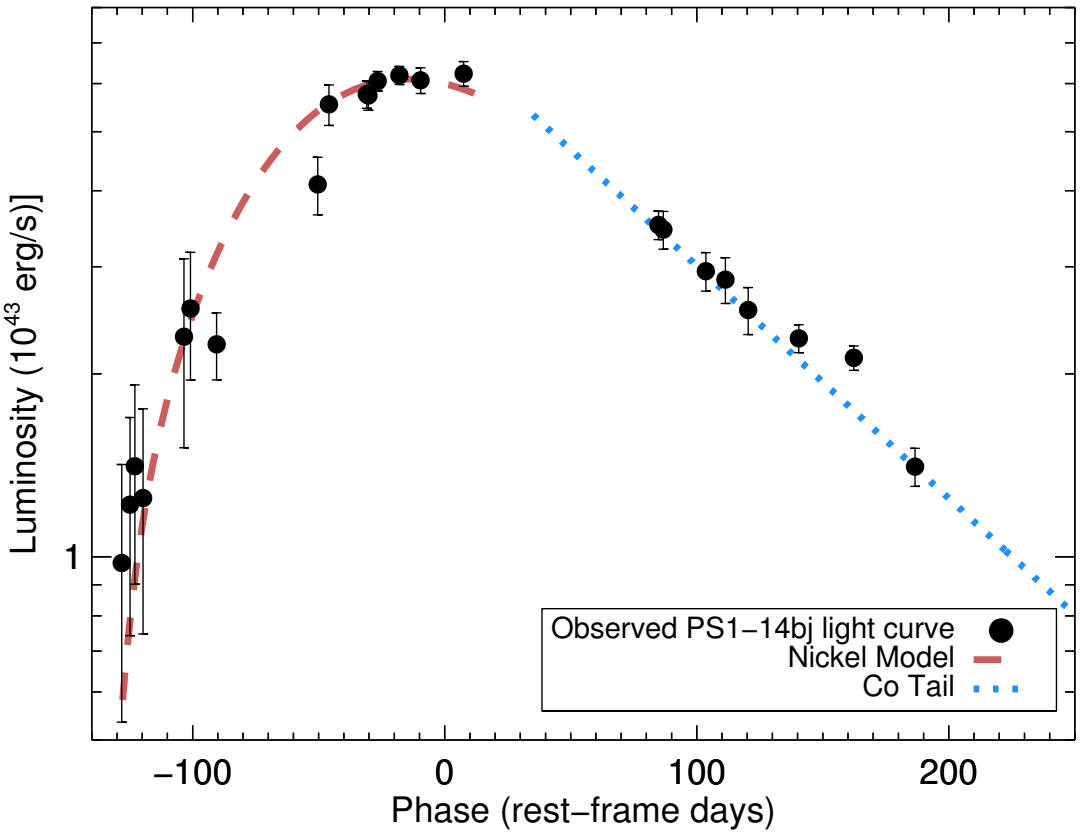

Figure 5.9.—: Radioactive decay model fit to the peak of the light curve of PS1-14bj. The light curve luminosity and width can be reproduced with a model with $M_{\rm Ni} = 14$ M$_\odot$ and a total ejecta mass $M_{\rm ej} = 105$ M$_\odot$. The blue line shows the predicted tail phase luminosity from ^{56}Co decay, assuming an initial Ni mass of 14 M$_\odot$ and full gamma-ray trapping; it matches the observed decline very well.

(in particular the long rise time) and overall red colors of PS1-14bj are consistent with predictions of PISN models (Kasen et al. 2011; Dessart et al. 2013), making it the best candidate for a PISN explosion observed to date.

5.4.2 Magnetar Spin-Down

Kasen & Bildsten (2010) and Woosley (2010) calculated theoretical light curves incorporating energy input from the spin-down of a newborn magnetar, and showed that the evolution of the optical light curve can be significantly affected in the regime with initial magnetar spin $P \sim 1 - 10$ ms and magnetic fields $B \sim 10^{14-15}$ G. A semi-analytic magnetar model with plausible physical parameters has been shown to successfully fit the light curves of a variety of H-poor SLSNe (e.g., Chomiuk et al. 2011; Lunnan et al. 2013; Inserra et al. 2013; McCrum et al. 2014; Nicholl et al. 2013, 2014, 2015). Magnetar models generally tend to overpredict the flux at late times, possibly due to the assumption that all of the magnetar energy being thermalized in the ejecta breaking down. Allowing for late-time hard emission leakage in the models seem to alleviate this problem (Wang et al. 2015); following their derivation the luminosity in a magnetar-powered model can be written as

$$L_{\rm mag}(t) = \frac{2E_p}{\tau_p \tau_m} e^{-(\frac{t}{\tau_m})^2} (1 - e^{-At^{-2}}) \times \int_0^t \frac{1}{(1 + t'/\tau_p)^2} e^{(\frac{t'}{\tau_m})^2} \frac{t'}{\tau_m} dt'. \quad (5.2)$$

Here, $E_p \simeq 2 \times 10^{52}$ erg/s $\times (P/1 \text{ ms})^{-2}$ is the rotational energy of the magnetar, $\tau_p \simeq 4.7$ days $\times (P/1 \text{ ms})^2 \times (B/10^{14} \text{ G})^{-2}$ is the spin-down timescale, τ_m is the diffusion time as before (Equation 5.1), and $A = 9\kappa_\gamma M_{\rm ej}^2 / 40\pi E_{\rm K}$ describes the optical depth of the ejecta to gamma rays as $\tau_\gamma = At^{-2}$. Larger A corresponds to a larger trapping rate and

lower leakage rate; the original magnetar model has $A = \infty$.

PS1-14bj

Figures 5.10 shows the best-fit magnetar model to PS1-14bj. Model shown has a total ejecta mass of 12 $M_\odot$, an initial spin of 2.7 ms and a magnetic field of 4×10^{13} G. The high ejecta mass and low magnetic field drive up the diffusion and spin down timescales respectively, required to reproduce the broad light curve. Unless we use the modified magnetar model that includes hard emission leakage, the late-time luminosity is over-predicted; model shown has $A \simeq 8 \times 10^{14}$ s^2. This is somewhat higher than the values derived in Wang et al. (2015) for five low-z SLSNe, but not unreasonable given the high ejecta mass. Thus, a physically plausible magnetar model can also explain the light curve of PS1-14bj without the need to invoke a PISN explosion. We note that the late-time slope predicted by the magnetar model is shallower than the one predicted by ^{56}Co decay even when accounting for leakage, suggesting that one way to distinguish between the two scenarios would be to obtain late-time ($t \sim 400 - 500$ days) light curve data.

PS1-11aib

Figure 5.11 shows the best-fit magnetar model to the light curve of PS1-11aib. Model shown has $M_{\rm ej} = 9.8\ M_\odot$, $P = 1.85$ ms, and $B = 6 \times 10^{13}$ G. While the model allows some flexibility in the ejecta mass, all of the best-fit models have low values of both B and P, necessary to reproduce the combination of a long rise time and high peak luminosity.

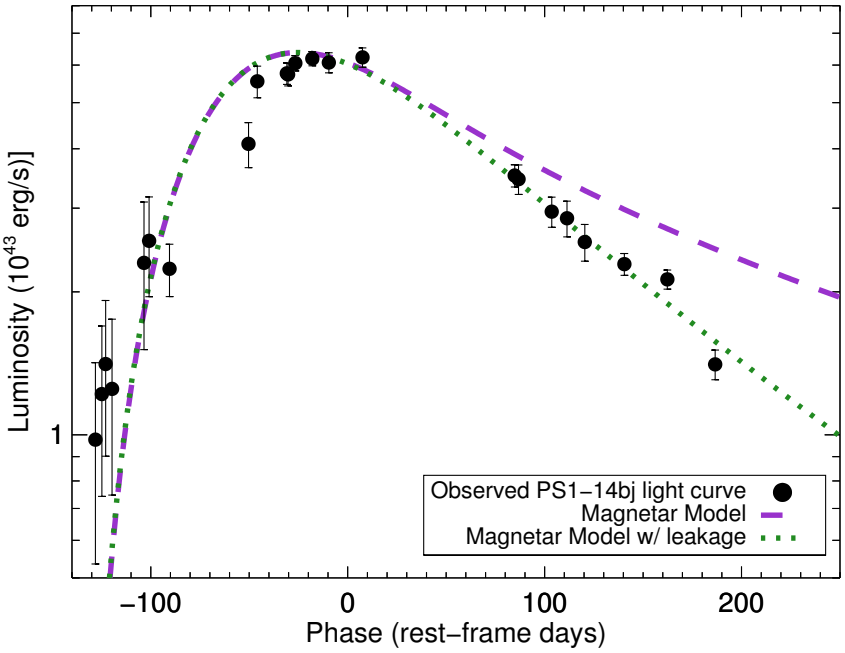

Figure 5.10.—: Magnetar model of PS1-14bj. In order to simultaneously fit the rise and decline phase, it is necessary to use a model that does not assume full gamma-ray trapping at late times; when this hard emission leakage is included the light curve is well fit (green dotted line). Model shown has a total ejecta mass of 12 $M_{\odot}$, an initial spin of 2.7 ms and a magnetic field of 4×10^{13} G.

As with PS1-14bj, the luminosity on the tail phase is over-predicted unless we allow for hard emission leakage; the purple model shown includes a leakage term with $A = 2 \times 10^{14}$ s^2. In general, this comes about because the magnetar models predict light curves where the rise is significantly shorter than the decline, and has problems reproducing light curves with $\tau_r > \tau_d/2$ (Nicholl et al. 2015).

PS1-12bqf

Figure 5.12 shows the best-fit magnetar model to the light curve of PS1-12bqf. Unlike PS1-14bj and PS1-11aib, we do not need to invoke hard emission leakage, and the light curve is well fit with a simple model with $M_{\rm ej} = 3\ M_\odot$, $P = 4.75$ ms, and $B = 1 \times 10^{14}$ G. Given the noise in the light curve, we can find adequate fits with a range of parameters; faster initial spin periods also require higher magnetic fields to reproduce the peak luminosity and rise time. Although PS1-12bqf is lower-luminosity than most H-poor SLSNe, the fact that it can be well fit with a magnetar should not be surprising: magnetar models have a large parameter space, and can naturally produce light curves with a range of luminosities. While the distributions of initial spin and magnetic field for neutron stars are not known, only finding SNe in the highest-luminosity part of parameter space might be more surprising than finding an object like PS1-12bqf.

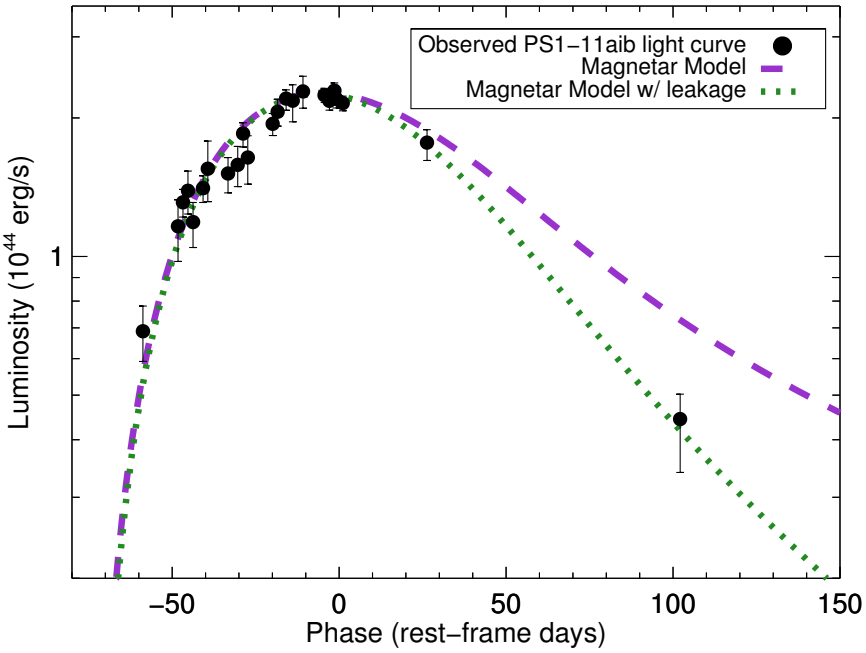

Figure 5.11.—: Magnetar model of PS1-11aib. Model shown has $M_{\rm ej} = 9.8\ M_{\odot}$, $P = 1.85$ ms, and $B = 6 \times 10^{13}$ G. Again, we need to explicitly include hard emission leakage in the model in order to fit the decline.

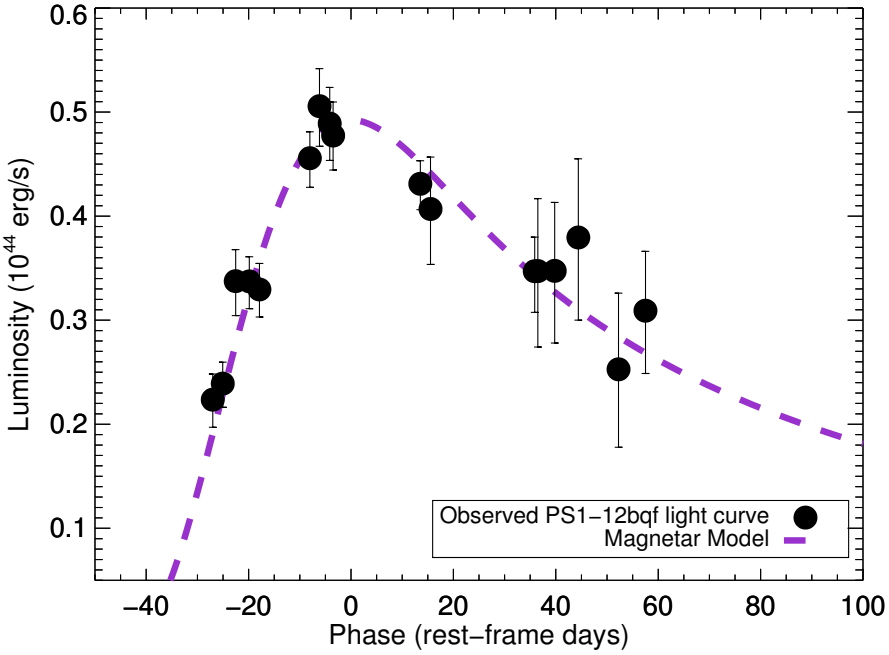

Figure 5.12.—: Magnetar model of PS1-12bqf. Although lower-luminosity than most objects in our sample, the magnetar spin-down model also easily reproduces light curves in this part of parameter space.

5.5 Discussion

5.5.1 Are SLSNe Standard(izable) Candles?

Recently, Inserra & Smartt (2014) looked at a sample of 16 published SLSNe from various literature sources, and found that the peak absolute magnitudes in a bandpass centered at 400 nm had a low intrinsic scatter: $\langle M(400) \rangle = -21.86 \pm 0.35$ mag. They further found that the peak magnitudes were correlated with both the decline rate (brighter events declining more slowly), and with the colors (redder objects being fainter), suggesting that SLSNe may be useful as standard(izable) candles for cosmology. To test the peak-decline rate and peak-color relations with the Pan-STARRS sample would require the ability to calculate k-corrections at late times, as well as coverage in redder bands than we generally have access to given the high redshift of our sample. However, given that all our data is from the same survey and selected based on spectroscopic criteria (rather than employing a luminosity cut), we can at least estimate the mean and scatter of the peak luminosities.

Figure 5.13 shows the absolute magnitudes at peak for 11 of the SLSNe in our sample, in the same 400 nm bandpass used by Inserra & Smartt (2014). We use the observed photometry at peak to calculate k-corrections (assuming a blackbody); comparing to the values quoted in Inserra & Smartt (2014) we find we recover the same values for the Pan-STARRS SLSNe included in their sample. PS1-11bdn, PS1-12bmy, PS1-13or and PS1-13gt are not included on this plot and in these calculations, as the peak is not observed for these objects.

We do indeed see a clustering around $M(400) \simeq -22$ mag, particularly for the

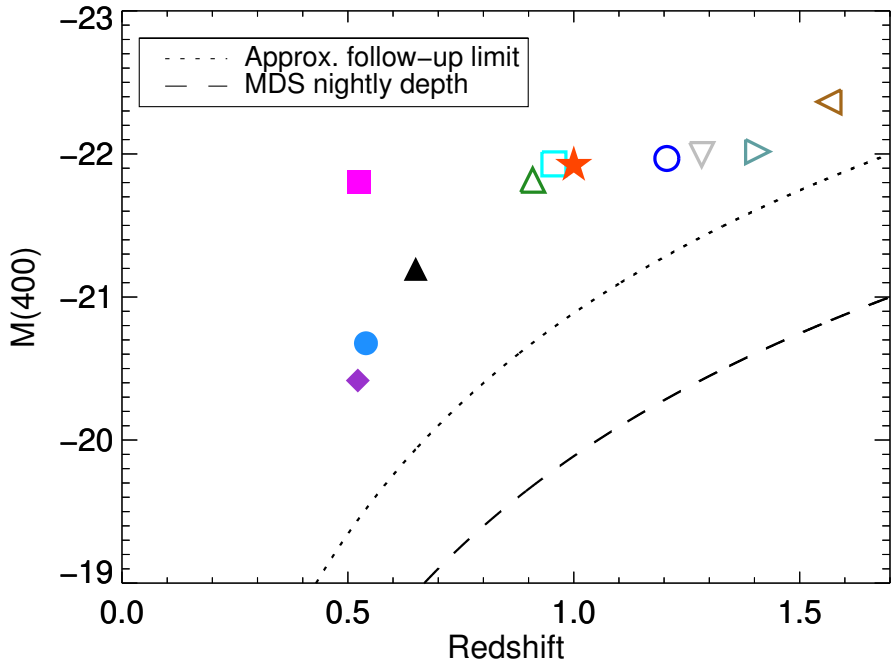

Figure 5.13.—: $M(400)$, absolute magnitude in the 400 nm bandpass used by Inserra & Smartt (2014) versus redshift for the MDS sample. Plot symbols for individual SLSNe as in Figures 5.4-5.8. The dashed line shows the limiting magnitude of MDS nightly images, while the dotted line is our effective survey depth for the spectroscopic sample.

high-redshift objects. Still, just taking the raw measured magnitudes we find a lower mean luminosity and higher scatter in the MDS sample compared to Inserra & Smartt (2014): $\langle M(400)\rangle = -21.6 \pm 0.6$ mag. The difference in both mean and standard deviation is mainly driven by the lower-luminosity objects in our sample at low redshift, PS1-12bqf and PS1-14bj.

This estimate does not account for Malmquist bias: while the depth of nightly exposures in PS1/MDS was ~ 23.5 mag, the limits of our follow-up resources meant we very rarely were able to get spectra of objects fainter than ~ 22.5 mag. These limits are plotted as dashed and dotted lines in Figure 5.13, respectively. We can obtain a better estimate of the true mean magnitude and scatter by finding the maximum redshift to which we could have detected that supernova, and weighting each luminosity by $1/V_{\rm max}$, the volume each SN effectively probes. Using such a correction does make a number of simplifying assumptions, including that the luminosity function of SLSNe does not change with redshift, and that our ability to detect and classify SLSNe only depends on its intrinsic luminosity at 400 nm.

Taking the follow-up limit into account and weighting accordingly, we find $\langle M(400)\rangle = -21.2 \pm 0.7$ mag. This suggests that the low scatter found by Inserra & Smartt (2014) may be driven by the fact that flux-limited surveys are biased towards higher-luminosity events. It is also possible that the scatter in events in the published literature is driven down by "publication bias": given that one suggested definition of a SLSN are objects with $M < -21$ mag (Gal-Yam 2012), otherwise similar events that do not make this luminosity cut may be underreported. As the cutoff at -21 mag is entirely arbitrary, we suggest using a spectroscopic definition will be more helpful in order to uncover the underlying physics.

We do not have the spectroscopic coverage to calculate late-time k-corrections and compare our data to the other relations found in Inserra & Smartt (2014). We note that our two lowest-luminosity objects would appear to be outliers, however: both PS1-12bqf and PS1-14bj have fainter luminosities, but decline slowly; PS1-12bqf also has a color temperature comparable to the rest of the 2005ap-like sample at peak, so may be an outlier in the luminosity-color relation.

5.5.2 Are There Two Classes of H-Poor SLSNe?

Since the discovery of SN 2007bi and the claim of it being a PISN, it has been debated whether the 2007bi-like SLSNe represent a different subclass with a distinct power source (in particular, radioactive decay), or if both 2007bi-like and 2005ap-like SLSNe can be produced by the same mechanism. The question is further complicated by that there is no consensus on how to define a 2007bi-like SLSN (dubbed "SLSN-R" by Gal-Yam 2012, with the "R" standing for radioactivity). For example, while the decay time scales in both our Pan-STARRS sample and the low-redshift Nicholl et al. (2015) sample seem to cluster into one slowly-decaying and one rapidly-decaying group (Figures 5.5, 5.8), several of the slowly-decaying SLSNe would spectroscopically be classified as 2005ap-like. Thus, having a slow decay rate similar to ^{56}Co is clearly not sufficient; as has been pointed out by Inserra et al. (2013), the slope predicted by a magnetar model can look similar to ^{56}Co at certain times. Whether an object is classified as 2007bi-like spectroscopically also depends on the time of the spectrum: PS1-11ap is an example of an object where the spectrum near peak resembled SN 2005ap but the late-time spectra were more similar to SN 2007bi (McCrum et al. 2014). As was argued in Nicholl et al. (2013), there also exists

SLSNe with both similar spectroscopic features and similar decay rates as SN 2007bi, that are still incompatible with radioactivity being the power source. The diversity in observed time scales is thus more likely to reflect the diversity in the parameter space of the explosion mechanism, than to represent two distinct energy sources.

Still, our discovery of PS1-14bj, with its slow rise, decay matching ^{56}Co and red colors also shows that there exists SLSNe where the power source can plausibly be radioactive decay. Our study therefore supports that there can be several mechanisms at play in producing H-poor SLSNe. We note that PS1-14bj stands out in our sample by having a significantly broader light curve than any of the other events considered either in this paper or in the compilation of Nicholl et al. (2015). Even so, it does not require there to be a distinct mechanism: the light curve can also be reproduced by a magnetar model if late-time leakage is included (Figure 5.10; Section 5.4.2). Our modelling suggests that late-time data can be one way to distinguish the models, as the slope predicted in the magnetar case is still shallower than ^{56}Co decay.

5.6 Conclusions

We have presented the light curves and classification spectra of 15 H-poor SLSNe from the Pan-STARRS Medium Deep Survey. Our sample contains all objects from the PS1/MDS spectroscopic sample that are spectroscopically similar to either of the prototypical objects SN 2005ap/SCP06F6 or SN 2007bi, without an explicit cut on luminosity. With a median redshift of ~ 1, this is the largest sample of high-redshift SLSNe presented to date. Our conclusions can be summarized as follows:

- The light curves of H-poor SLSNe are diverse. The estimated peak bolometric luminosities in our sample span $(0.5-5)\times10^{44}$ erg s^{-1}, rise timescales $15-95$ days, and decline timescales $30-135$ days. Similarly, the lower limits on total radiated energy for our sample spans $3\times10^{50}-2\times10^{51}$ erg.

- Prior to peak light, 2005ap-like SLSNe show hot color temperatures $(10,000-25,000$ K) over a timescale of weeks, suggesting there is a sustained source of heating. Post-peak, color temperatures drop to $\sim 6000-8000$ K over a timescale of $20-40$ days. In contrast, the one 2007bi-like SLSN in our sample shows redder color temperatures over its entire evolution.

- Our spectroscopically selected sample contains several objects with peak luminosities fainter than -21 mag, suggesting that such a luminosity cut is arbitrary. We note that several proposed mechanisms for producing SLSNe will naturally produce a range of luminosities, and that excluding the lower end of the luminosity distribution will lead to an artificially narrow spread, particularly when taking into account the effective volumes probed at each luminosity.

- Our sample contains a single 2007bi-like SLSN, PS1-14bj. PS1-14bj shows a rest-frame rise time $\gtrsim$ 100 days, comparatively red colors throughout its evolution, and has a light curve compatible with ^{56}Ni as the power source. Thus, it demonstrates that there exists SLSNe with the broad light curves predicted by PISN models, and that SN 2007bi-like SLSNe can plausibly be radioactively powered.

- We find that magnetar models can also explain the light curve evolution of our sample, including PS1-14bj, though the late-time flux is overpredicted for our slowest-evolving objects unless late-time hard emission leakage is included in the model. Magnetar models can easily reproduce the also the fainter objects in our sample, however.

Our results highlight the need for a better understanding of sample selection when discussing the properties of SLSNe as a class, both in terms of survey biases and in terms of what gets reported as superluminous. We argue that a selection based on spectroscopic properties is more meaningful than a cut on luminosity, in order to compare objects with actual similar physical properties. In addition, the mechanisms proposed to power SLSNe (such as magnetar spindown or circumstellar interaction) naturally produce a range of luminosities. Taking into account the effective volumes probed by PS1/MDS, such lower-luminosity SLSNe should be common.

Acknowledgements

The Pan-STARRS1 Surveys (PS1) have been made possible through contributions by the Institute for Astronomy, the University of Hawaii, the Pan-STARRS Project Office, the Max-Planck Society and its participating institutes, the Max Planck Institute for Astronomy, Heidelberg and the Max Planck Institute for Extraterrestrial Physics, Garching, The Johns Hopkins University, Durham University, the University of Edinburgh, the Queen's University Belfast, the Harvard-Smithsonian Center for Astrophysics, the Las Cumbres Observatory Global Telescope Network Incorporated, the National Central University of Taiwan, the Space Telescope Science Institute, and the National Aeronautics and Space Administration under Grant No. NNX08AR22G issued through the Planetary Science Division of the NASA Science Mission Directorate, the National Science Foundation Grant No. AST-1238877, the University of Maryland, Eotvos Lorand University (ELTE), and the Los Alamos National Laboratory. This work is based on observations obtained at the Gemini Observatory, which is operated by the Association of Universities for Research in Astronomy, Inc., under a cooperative agreement with the NSF on behalf of the Gemini partnership: the National Science Foundation (United States), the National Research Council (Canada), CONICYT (Chile), the Australian Research Council (Australia), Ministério da Ciência, Tecnologia e Inovação (Brazil) and Ministerio de Ciencia, Tecnología e Innovación Productiva (Argentina). This chapter includes data gathered with the 6.5 meter Magellan Telescopes located at Las Campanas Observatory, Chile. Observations reported here were obtained at the MMT Observatory, a joint facility of the Smithsonian Institution and the University of Arizona. This work includes data obtained at the Large Binocular

Telescope (LBT), which is an international collaboration among institutions in the United States, Italy and Germany. LBT Corporation partners are: The University of Arizona on behalf of the Arizona university system; Istituto Nazionale di Astrofisica, Italy; LBT Beteiligungsgesellschaft, Germany, representing the Max-Planck Society, the Astrophysical Institute Potsdam, and Heidelberg University; The Ohio State University, and The Research Corporation, on behalf of The University of Notre Dame, University of Minnesota and University of Virginia.

5.7 Appendix: Photometry

Table 5.4 lists all our photometry for the PS1 SLSNe that have not been previously published. The majority of this photometry is from PS1/MDS; if we obtained photometry from other sources it is also reported. Abbreviations are as follows: GN/GS refer to GMOS with Gemini North/South respectively, LBT refers to the Large Binocular Telescope (LBC), LDSS and IMACS refer to the so-named instruments on Magellan-Clay and Magellan-Baade, and UVOT refers to *Swift's* UltraViolet/Optical Telescope.

Table 5.4. Photometry of PS1 SLSNe

Object	MJD (days)	Rest-frame Phase (days)	Filter	AB Mag	Instrument
PS1-12bqf	56206.6	−26.8	g_{P1}	22.48 ± 0.14	PS1
PS1-12bqf	56209.6	−24.8	g_{P1}	22.22 ± 0.09	PS1
PS1-12bqf	56214.4	−21.7	g_{P1}	22.09 ± 0.11	PS1
PS1-12bqf	56217.5	−19.6	g_{P1}	21.85 ± 0.07	PS1
PS1-12bqf	56220.5	−17.6	g_{P1}	22.11 ± 0.12	PS1
PS1-12bqf	56235.5	−7.8	g_{P1}	21.76 ± 0.08	PS1
PS1-12bqf	56238.3	−5.9	g_{P1}	21.56 ± 0.11	PS1
PS1-12bqf	56241.4	−3.9	g_{P1}	21.73 ± 0.12	PS1
PS1-12bqf	56268.3	13.8	g_{P1}	22.38 ± 0.12	PS1
PS1-12bqf	56271.3	15.8	g_{P1}	22.17 ± 0.08	PS1
PS1-12bqf	56303.2	36.7	g_{P1}	22.87 ± 0.33	PS1
PS1-12bqf	56206.6	−26.8	r_{P1}	22.30 ± 0.12	PS1
PS1-12bqf	56209.6	−24.8	r_{P1}	22.40 ± 0.09	PS1
PS1-12bqf	56213.4	−22.3	r_{P1}	21.95 ± 0.15	PS1
PS1-12bqf	56217.5	−19.6	r_{P1}	21.91 ± 0.07	PS1
PS1-12bqf	56220.5	−17.6	r_{P1}	21.88 ± 0.09	PS1
PS1-12bqf	56235.5	−7.8	r_{P1}	21.52 ± 0.06	PS1
PS1-12bqf	56238.4	−5.9	r_{P1}	21.52 ± 0.07	PS1
PS1-12bqf	56241.4	−3.9	r_{P1}	21.42 ± 0.10	PS1
PS1-12bqf	56242.4	−3.2	r_{P1}	21.62 ± 0.08	PS1
PS1-12bqf	56268.3	13.8	r_{P1}	21.77 ± 0.05	PS1
PS1-12bqf	56271.4	15.8	r_{P1}	21.81 ± 0.07	PS1
PS1-12bqf	56302.3	36.1	r_{P1}	21.95 ± 0.08	PS1
PS1-12bqf	56207.6	−26.1	i_{P1}	22.32 ± 0.13	PS1
PS1-12bqf	56210.5	−24.2	i_{P1}	22.36 ± 0.09	PS1
PS1-12bqf	56213.4	−22.3	i_{P1}	22.03 ± 0.10	PS1
PS1-12bqf	56215.5	−20.9	i_{P1}	22.08 ± 0.09	PS1
PS1-12bqf	56218.5	−18.9	i_{P1}	21.99 ± 0.07	PS1
PS1-12bqf	56221.5	−17.0	i_{P1}	22.00 ± 0.07	PS1

Table 5.4—Continued

Object	MJD (days)	Rest-frame Phase (days)	Filter	AB Mag	Instrument
PS1-12bqf	56225.5	−14.3	i_{P1}	22.16 ± 0.20	PS1
PS1-12bqf	56233.5	−9.1	i_{P1}	21.64 ± 0.06	PS1
PS1-12bqf	56236.4	−7.2	i_{P1}	21.67 ± 0.05	PS1
PS1-12bqf	56239.5	−5.2	i_{P1}	21.55 ± 0.07	PS1
PS1-12bqf	56242.4	−3.3	i_{P1}	21.56 ± 0.08	PS1
PS1-12bqf	56272.4	16.4	i_{P1}	21.74 ± 0.26	PS1
PS1-12bqf	56293.3	30.2	i_{P1}	21.63 ± 0.15	PS1
PS1-12bqf	56299.3	34.2	i_{P1}	21.82 ± 0.09	PS1
PS1-12bqf	56302.3	36.1	i_{P1}	21.79 ± 0.06	PS1
PS1-12bqf	56314.3	44.0	i_{P1}	21.89 ± 0.11	PS1
PS1-12bqf	56205.6	−27.4	z_{P1}	22.63 ± 0.20	PS1
PS1-12bqf	56208.6	−25.5	z_{P1}	22.61 ± 0.23	PS1
PS1-12bqf	56211.5	−23.5	z_{P1}	22.28 ± 0.18	PS1
PS1-12bqf	56214.5	−21.6	z_{P1}	22.03 ± 0.16	PS1
PS1-12bqf	56216.6	−20.2	z_{P1}	22.32 ± 0.22	PS1
PS1-12bqf	56219.5	−18.3	z_{P1}	22.12 ± 0.11	PS1
PS1-12bqf	56222.5	−16.3	z_{P1}	21.88 ± 0.09	PS1
PS1-12bqf	56224.5	−15.0	z_{P1}	22.04 ± 0.23	PS1
PS1-12bqf	56226.5	−13.7	z_{P1}	22.02 ± 0.12	PS1
PS1-12bqf	56232.5	−9.7	z_{P1}	21.67 ± 0.12	PS1
PS1-12bqf	56234.4	−8.5	z_{P1}	21.76 ± 0.11	PS1
PS1-12bqf	56237.5	−6.5	z_{P1}	21.67 ± 0.12	PS1
PS1-12bqf	56251.4	2.7	z_{P1}	21.60 ± 0.14	PS1
PS1-12bqf	56262.3	9.8	z_{P1}	21.86 ± 0.18	PS1
PS1-12bqf	56270.3	15.1	z_{P1}	21.71 ± 0.14	PS1
PS1-12bqf	56273.4	17.1	z_{P1}	21.58 ± 0.11	PS1
PS1-12bqf	56289.3	27.6	z_{P1}	21.72 ± 0.09	PS1
PS1-12bqf	56292.3	29.6	z_{P1}	21.73 ± 0.10	PS1
PS1-12bqf	56294.3	30.8	z_{P1}	21.94 ± 0.21	PS1

Table 5.4—Continued

Object	MJD (days)	Rest-frame Phase (days)	Filter	AB Mag	Instrument
PS1-12bqf	56300.2	34.8	z_{P1}	21.94 ± 0.10	PS1
PS1-12bqf	56303.3	36.7	z_{P1}	21.80 ± 0.14	PS1
PS1-12bqf	56308.3	40.0	z_{P1}	21.79 ± 0.12	PS1
PS1-12bqf	56315.3	44.6	z_{P1}	21.70 ± 0.13	PS1
PS1-12bqf	56327.2	52.5	z_{P1}	22.14 ± 0.26	PS1
PS1-12bqf	56335.2	57.7	z_{P1}	21.92 ± 0.11	PS1
PS1-14bj	56751.2	−50.1	g	22.20 ± 0.10	MMT
PS1-14bj	56774.3	−35.1	g	22.28 ± 0.06	GN
PS1-14bj	56775.3	−34.5	g	22.37 ± 0.06	GN
PS1-14bj	56778.0	−32.7	g	22.08 ± 0.14	GN
PS1-14bj	56836.5	5.3	g	22.27 ± 0.07	LDSS
PS1-14bj	56952.5	80.6	g	22.66 ± 0.04	LBT
PS1-14bj	56981.4	99.4	g	22.82 ± 0.06	MMT
PS1-14bj	56993.5	107.2	g	22.93 ± 0.07	MMT
PS1-14bj	57038.2	136.3	g	23.09 ± 0.05	IMACS
PS1-14bj	57071.9	158.1	g	23.32 ± 0.06	IMACS
PS1-14bj	57109.3	182.4	g	23.48 ± 0.10	GN
PS1-14bj	56636.6	−124.5	r_{P1}	23.48 ± 0.31	PS1
PS1-14bj	56666.6	−105.0	r_{P1}	22.67 ± 0.23	PS1
PS1-14bj	56682.6	−94.7	r_{P1}	22.50 ± 0.12	PS1
PS1-14bj	56744.3	−54.5	r	21.45 ± 0.10	GN
PS1-14bj	56751.2	−50.1	r	21.35 ± 0.10	MMT
PS1-14bj	56774.3	−35.1	r	21.37 ± 0.03	GN
PS1-14bj	56775.3	−34.5	r	21.37 ± 0.03	GN
PS1-14bj	56781.0	−30.8	r	21.34 ± 0.07	GS
PS1-14bj	56794.2	−22.1	r	21.27 ± 0.06	MMT
PS1-14bj	56807.1	−13.8	r	21.42 ± 0.06	MMT
PS1-14bj	56833.5	3.4	r	21.40 ± 0.03	LDSS
PS1-14bj	56952.5	80.6	r	21.96 ± 0.04	LBT

Table 5.4—Continued

Object	MJD (days)	Rest-frame Phase (days)	Filter	AB Mag	Instrument
PS1-14bj	56955.5	82.6	r	21.89 ± 0.09	MDM
PS1-14bj	56981.5	99.4	r	22.23 ± 0.05	MMT
PS1-14bj	56993.4	107.2	r	22.18 ± 0.05	MMT
PS1-14bj	57007.3	116.2	r	22.29 ± 0.05	IMACS
PS1-14bj	57038.2	136.3	r	22.38 ± 0.03	IMACS
PS1-14bj	57071.9	158.1	r	22.50 ± 0.03	IMACS
PS1-14bj	57109.3	182.4	r	22.82 ± 0.05	GN
PS1-14bj	56656.6	−111.5	i_{P1}	22.59 ± 0.19	PS1
PS1-14bj	56661.6	−108.3	i_{P1}	22.69 ± 0.14	PS1
PS1-14bj	56668.5	−103.8	i_{P1}	22.55 ± 0.15	PS1
PS1-14bj	56683.6	−94.0	i_{P1}	22.05 ± 0.09	PS1
PS1-14bj	56744.3	−54.5	i	21.31 ± 0.10	GN
PS1-14bj	56751.2	−50.1	i	21.20 ± 0.10	MMT
PS1-14bj	56774.3	−35.1	i	21.24 ± 0.05	GN
PS1-14bj	56775.3	−34.5	i	21.17 ± 0.03	GN
PS1-14bj	56778.0	−32.7	i	21.20 ± 0.05	GS
PS1-14bj	56807.2	−13.7	i	20.97 ± 0.06	MMT
PS1-14bj	56952.5	80.6	i	21.84 ± 0.03	LBT
PS1-14bj	56833.5	3.4	i	21.28 ± 0.02	LDSS
PS1-14bj	56981.5	99.5	i	21.98 ± 0.05	MMT
PS1-14bj	56993.4	107.2	i	21.95 ± 0.08	MMT
PS1-14bj	57007.3	116.2	i	22.18 ± 0.04	IMACS
PS1-14bj	57010.2	118.1	i	22.22 ± 0.05	IMACS
PS1-14bj	57038.3	136.3	i	22.26 ± 0.05	IMACS
PS1-14bj	57071.9	158.1	i	22.34 ± 0.04	IMACS
PS1-14bj	57109.3	182.4	i	22.57 ± 0.05	GN
PS1-14bj	56624.6	−132.3	z_{P1}	23.10 ± 0.35	PS1
PS1-14bj	56629.6	−129.0	z_{P1}	22.86 ± 0.25	PS1
PS1-14bj	56632.6	−127.1	z_{P1}	22.70 ± 0.19	PS1

Table 5.4—Continued

Object	MJD (days)	Rest-frame Phase (days)	Filter	AB Mag	Instrument
PS1-14bj	56637.6	−123.8	z_{P1}	22.83 ± 0.27	PS1
PS1-14bj	56662.6	−107.6	z_{P1}	22.17 ± 0.15	PS1
PS1-14bj	56667.7	−104.3	z_{P1}	22.05 ± 0.21	PS1
PS1-14bj	56681.5	−95.3	z_{P1}	22.25 ± 0.15	PS1
PS1-14bj	56774.3	−35.1	z	21.49 ± 0.10	GN
PS1-14bj	56775.3	−34.5	z	21.54 ± 0.12	GN
PS1-14bj	56778.0	−32.7	z	21.49 ± 0.18	GS
PS1-14bj	56833.5	3.4	z	21.35 ± 0.10	LDSS
PS1-14bj	57009.3	117.5	z	22.56 ± 0.09	IMACS
PS1-14bj	57039.3	137.0	z	22.52 ± 0.11	IMACS
PS1-14bj	57071.9	158.2	z	22.55 ± 0.09	IMACS
PS1-14bj	57109.3	182.4	z	23.20 ± 0.16	GN
PS11bdn	55941.3	0.	uvm2	21.98 ± 0.32	UVOT
PS1-11bdn	55911.3	−17.3	g_{P1}	20.54 ± 0.02	PS1
PS1-11bdn	55941.3	−0.0	g_{P1}	20.58 ± 0.08	PS1
PS1-11bdn	55911.3	−17.3	r_{P1}	20.81 ± 0.02	PS1
PS1-11bdn	55941.3	0.0	r_{P1}	20.57 ± 0.05	PS1
PS1-11bdn	55896.3	−25.9	i_{P1}	24.10 ± 0.34	PS1
PS1-11bdn	55912.3	−16.7	i_{P1}	20.97 ± 0.03	PS1
PS1-11bdn	55915.3	−15.0	i_{P1}	20.93 ± 0.06	PS1
PS1-11bdn	55918.2	−13.3	i_{P1}	20.90 ± 0.02	PS1
PS1-11bdn	55910.4	−17.8	z_{P1}	21.26 ± 0.09	PS1
PS1-11bdn	55919.3	−12.7	z_{P1}	20.95 ± 0.07	PS1
PS1-11bdn	55921.3	−11.5	z_{P1}	20.81 ± 0.05	PS1
PS1-13gt	56331.6	3.2	g_{P1}	23.50 ± 0.20	PS1
PS1-13gt	56336.6	5.8	g_{P1}	24.45 ± 0.31	PS1
PS1-13gt	56354.6	15.4	g_{P1}	23.52 ± 0.35	PS1
PS1-13gt	56325.6	0.0	r_{P1}	22.83 ± 0.21	PS1
PS1-13gt	56328.6	1.6	r_{P1}	22.68 ± 0.12	PS1

Table 5.4—Continued

Object	MJD (days)	Rest-frame Phase (days)	Filter	AB Mag	Instrument
PS1-13gt	56331.6	3.2	r_{P1}	22.70 ± 0.11	PS1
PS1-13gt	56332.6	3.7	r_{P1}	22.76 ± 0.09	PS1
PS1-13gt	56336.6	5.8	r_{P1}	23.07 ± 0.11	PS1
PS1-13gt	56354.6	15.4	r_{P1}	23.27 ± 0.35	PS1
PS1-13gt	56357.6	17.0	r_{P1}	23.17 ± 0.20	PS1
PS1-13gt	56371.5	24.3	r_{P1}	23.65 ± 0.25	PS1
PS1-13gt	56387.5	32.9	r_{P1}	23.27 ± 0.28	PS1
PS1-13gt	56390.4	34.4	r_{P1}	22.96 ± 0.27	PS1
PS1-13gt	56398.5	38.7	r_{P1}	23.53 ± 0.28	PS1
PS1-13gt	56323.6	−1.1	i_{P1}	22.21 ± 0.13	PS1
PS1-13gt	56326.6	0.5	i_{P1}	22.23 ± 0.08	PS1
PS1-13gt	56332.6	3.7	i_{P1}	22.24 ± 0.06	PS1
PS1-13gt	56334.5	4.7	i_{P1}	22.13 ± 0.08	PS1
PS1-13gt	56337.6	6.4	i_{P1}	22.35 ± 0.08	PS1
PS1-13gt	56352.5	14.3	i_{P1}	22.65 ± 0.22	PS1
PS1-13gt	56355.5	15.9	i_{P1}	22.46 ± 0.09	PS1
PS1-13gt	56358.6	17.5	i_{P1}	22.42 ± 0.09	PS1
PS1-13gt	56369.4	23.2	i_{P1}	22.81 ± 0.17	PS1
PS1-13gt	56385.5	31.8	i_{P1}	23.10 ± 0.16	PS1
PS1-13gt	56388.5	33.4	i_{P1}	23.27 ± 0.26	PS1
PS1-13gt	56391.4	34.9	i_{P1}	23.16 ± 0.18	PS1
PS1-13gt	56393.3	35.9	i_{P1}	23.14 ± 0.15	PS1
PS1-13gt	56396.5	37.6	i_{P1}	23.24 ± 0.34	PS1
PS1-13gt	56399.4	39.2	i_{P1}	23.24 ± 0.19	PS1
PS1-13gt	56403.4	41.3	i_{P1}	23.24 ± 0.35	PS1
PS1-13gt	56414.4	47.1	i_{P1}	23.44 ± 0.31	PS1
PS1-13gt	56417.4	48.7	i_{P1}	23.27 ± 0.22	PS1
PS1-13gt	56420.4	50.3	i_{P1}	23.46 ± 0.18	PS1
PS1-13gt	56422.3	51.3	i_{P1}	23.50 ± 0.20	PS1

Table 5.4—Continued

Object	MJD (days)	Rest-frame Phase (days)	Filter	AB Mag	Instrument
PS1-13gt	56432.3	56.6	i_{P1}	23.26 ± 0.24	PS1
PS1-13gt	56444.3	63.0	i_{P1}	23.68 ± 0.24	PS1
PS1-13gt	56447.3	64.6	i_{P1}	23.96 ± 0.26	PS1
PS1-13gt	56452.3	67.2	i_{P1}	23.52 ± 0.25	PS1
PS1-13gt	56462.3	72.5	i_{P1}	23.72 ± 0.28	PS1
PS1-13gt	56324.6	−0.5	z_{P1}	21.90 ± 0.11	PS1
PS1-13gt	56338.6	6.9	z_{P1}	21.98 ± 0.07	PS1
PS1-13gt	56348.6	12.2	z_{P1}	22.37 ± 0.26	PS1
PS1-13gt	56351.5	13.8	z_{P1}	22.17 ± 0.11	PS1
PS1-13gt	56353.5	14.8	z_{P1}	22.07 ± 0.13	PS1
PS1-13gt	56356.5	16.4	z_{P1}	22.08 ± 0.06	PS1
PS1-13gt	56359.6	18.0	z_{P1}	22.11 ± 0.09	PS1
PS1-13gt	56364.6	20.7	z_{P1}	22.17 ± 0.12	PS1
PS1-13gt	56370.4	23.8	z_{P1}	22.36 ± 0.06	PS1
PS1-13gt	56383.5	30.7	z_{P1}	22.48 ± 0.10	PS1
PS1-13gt	56386.3	32.2	z_{P1}	22.92 ± 0.17	PS1
PS1-13gt	56389.5	33.9	z_{P1}	22.64 ± 0.17	PS1
PS1-13gt	56392.3	35.4	z_{P1}	22.60 ± 0.16	PS1
PS1-13gt	56394.4	36.5	z_{P1}	22.73 ± 0.22	PS1
PS1-13gt	56397.4	38.1	z_{P1}	22.96 ± 0.29	PS1
PS1-13gt	56400.4	39.7	z_{P1}	22.48 ± 0.26	PS1
PS1-13gt	56402.3	40.7	z_{P1}	22.94 ± 0.26	PS1
PS1-13gt	56404.3	41.8	z_{P1}	22.46 ± 0.27	PS1
PS1-13gt	56410.4	45.0	z_{P1}	22.66 ± 0.16	PS1
PS1-13gt	56412.4	46.1	z_{P1}	23.04 ± 0.28	PS1
PS1-13gt	56415.4	47.7	z_{P1}	22.86 ± 0.15	PS1
PS1-13gt	56421.4	50.8	z_{P1}	22.96 ± 0.19	PS1
PS1-13gt	56423.4	51.9	z_{P1}	23.20 ± 0.24	PS1
PS1-13gt	56429.3	55.0	z_{P1}	23.21 ± 0.22	PS1

Table 5.4—Continued

Object	MJD (days)	Rest-frame Phase (days)	Filter	AB Mag	Instrument
PS1-13gt	56459.3	71.0	z_{P1}	23.23 ± 0.31	PS1
PS1-13gt	56461.3	72.0	z_{P1}	23.69 ± 0.34	PS1
PS1-13gt	56463.3	73.1	z_{P1}	23.61 ± 0.33	PS1
PS1-11aib	55743.6	−58.7	g_{P1}	23.16 ± 0.21	PS1
PS1-11aib	55764.6	−48.2	g_{P1}	22.78 ± 0.30	PS1
PS1-11aib	55767.6	−46.7	g_{P1}	22.36 ± 0.10	PS1
PS1-11aib	55770.5	−45.2	g_{P1}	22.71 ± 0.13	PS1
PS1-11aib	55773.6	−43.7	g_{P1}	22.71 ± 0.15	PS1
PS1-11aib	55776.6	−42.2	g_{P1}	22.61 ± 0.08	PS1
PS1-11aib	55779.6	−40.7	g_{P1}	22.68 ± 0.09	PS1
PS1-11aib	55782.4	−39.2	g_{P1}	22.29 ± 0.33	PS1
PS1-11aib	55791.6	−34.7	g_{P1}	22.10 ± 0.25	PS1
PS1-11aib	55794.5	−33.2	g_{P1}	22.63 ± 0.19	PS1
PS1-11aib	55797.5	−31.7	g_{P1}	22.60 ± 0.12	PS1
PS1-11aib	55800.3	−30.3	g_{P1}	22.59 ± 0.24	PS1
PS1-11aib	55803.5	−28.7	g_{P1}	22.67 ± 0.10	PS1
PS1-11aib	55806.4	−27.3	g_{P1}	22.39 ± 0.18	PS1
PS1-11aib	55809.3	−25.8	g_{P1}	22.47 ± 0.18	PS1
PS1-11aib	55812.4	−24.2	g_{P1}	22.75 ± 0.24	PS1
PS1-11aib	55821.3	−19.8	g_{P1}	22.67 ± 0.16	PS1
PS1-11aib	55824.3	−18.3	g_{P1}	22.35 ± 0.13	PS1
PS1-11aib	55828.3	−16.3	g_{P1}	22.35 ± 0.04	PS1
PS1-11aib	55830.3	−15.3	g_{P1}	22.55 ± 0.24	PS1
PS1-11aib	55833.3	−13.8	g_{P1}	22.33 ± 0.12	PS1
PS1-11aib	55836.2	−12.3	g_{P1}	22.32 ± 0.11	PS1
PS1-11aib	55839.4	−10.8	g_{P1}	21.93 ± 0.17	PS1
PS1-11aib	55852.3	−4.3	g_{P1}	22.44 ± 0.08	PS1
PS1-11aib	55855.2	−2.8	g_{P1}	22.38 ± 0.09	PS1
PS1-11aib	55858.2	−1.3	g_{P1}	22.31 ± 0.11	PS1

Table 5.4—Continued

Object	MJD (days)	Rest-frame Phase (days)	Filter	AB Mag	Instrument
PS1-11aib	55860.2	−0.3	g_{P1}	22.50 ± 0.10	PS1
PS1-11aib	55863.3	1.2	g_{P1}	22.58 ± 0.12	PS1
PS1-11aib	55836.5	−12.2	g	22.25 ± 0.10	GS
PS1-11aib	55913.7	26.4	g	22.86 ± 0.13	GS
PS1-11aib	56065.4	102.2	g	25.22 ± 0.31	LDSS
PS1-11aib	55743.6	−58.7	r_{P1}	22.75 ± 0.17	PS1
PS1-11aib	55764.6	−48.2	r_{P1}	22.29 ± 0.13	PS1
PS1-11aib	55767.6	−46.7	r_{P1}	22.24 ± 0.10	PS1
PS1-11aib	55770.6	−45.2	r_{P1}	22.18 ± 0.08	PS1
PS1-11aib	55773.6	−43.7	r_{P1}	21.94 ± 0.07	PS1
PS1-11aib	55779.6	−40.7	r_{P1}	22.04 ± 0.09	PS1
PS1-11aib	55782.4	−39.2	r_{P1}	21.89 ± 0.13	PS1
PS1-11aib	55794.5	−33.2	r_{P1}	21.83 ± 0.07	PS1
PS1-11aib	55800.3	−30.3	r_{P1}	21.82 ± 0.12	PS1
PS1-11aib	55803.5	−28.7	r_{P1}	21.99 ± 0.11	PS1
PS1-11aib	55806.4	−27.3	r_{P1}	21.88 ± 0.07	PS1
PS1-11aib	55821.3	−19.8	r_{P1}	21.68 ± 0.08	PS1
PS1-11aib	55824.3	−18.3	r_{P1}	21.72 ± 0.09	PS1
PS1-11aib	55829.3	−15.8	r_{P1}	21.57 ± 0.05	PS1
PS1-11aib	55833.3	−13.8	r_{P1}	21.96 ± 0.22	PS1
PS1-11aib	55836.2	−12.3	r_{P1}	21.63 ± 0.10	PS1
PS1-11aib	55839.4	−10.8	r_{P1}	21.61 ± 0.14	PS1
PS1-11aib	55852.3	−4.3	r_{P1}	21.46 ± 0.05	PS1
PS1-11aib	55855.2	−2.8	r_{P1}	21.54 ± 0.06	PS1
PS1-11aib	55858.3	−1.3	r_{P1}	21.58 ± 0.05	PS1
PS1-11aib	55859.4	−0.8	r_{P1}	21.57 ± 0.05	PS1
PS1-11aib	55863.3	1.2	r_{P1}	21.48 ± 0.05	PS1
PS1-11aib	55836.5	−12.2	r	21.59 ± 0.04	GS
PS1-11aib	55913.7	26.4	r	22.08 ± 0.08	GS

Table 5.4—Continued

Object	MJD (days)	Rest-frame Phase (days)	Filter	AB Mag	Instrument
PS1-11aib	56065.3	102.2	r	24.06 ± 0.13	LDSS
PS1-11aib	55741.6	−59.7	i_{P1}	23.13 ± 0.25	PS1
PS1-11aib	55747.6	−56.7	i_{P1}	22.76 ± 0.19	PS1
PS1-11aib	55765.6	−47.7	i_{P1}	22.61 ± 0.14	PS1
PS1-11aib	55768.6	−46.2	i_{P1}	22.14 ± 0.07	PS1
PS1-11aib	55771.4	−44.7	i_{P1}	21.99 ± 0.18	PS1
PS1-11aib	55774.6	−43.2	i_{P1}	21.96 ± 0.08	PS1
PS1-11aib	55777.4	−41.8	i_{P1}	22.01 ± 0.09	PS1
PS1-11aib	55792.6	−34.2	i_{P1}	21.82 ± 0.09	PS1
PS1-11aib	55801.3	−29.8	i_{P1}	21.80 ± 0.07	PS1
PS1-11aib	55804.5	−28.2	i_{P1}	21.79 ± 0.07	PS1
PS1-11aib	55807.3	−26.8	i_{P1}	21.95 ± 0.19	PS1
PS1-11aib	55810.3	−25.3	i_{P1}	21.74 ± 0.06	PS1
PS1-11aib	55819.3	−20.8	i_{P1}	21.59 ± 0.06	PS1
PS1-11aib	55822.5	−19.2	i_{P1}	21.60 ± 0.05	PS1
PS1-11aib	55825.3	−17.8	i_{P1}	21.50 ± 0.08	PS1
PS1-11aib	55834.3	−13.3	i_{P1}	21.49 ± 0.06	PS1
PS1-11aib	55850.3	−5.3	i_{P1}	21.46 ± 0.05	PS1
PS1-11aib	55853.4	−3.8	i_{P1}	21.42 ± 0.04	PS1
PS1-11aib	55861.3	0.2	i_{P1}	21.62 ± 0.07	PS1
PS1-11aib	55836.5	−12.2	i	21.58 ± 0.11	GS
PS1-11aib	55913.7	26.4	i	21.86 ± 0.09	GS
PS1-11aib	56064.3	101.7	i	23.49 ± 0.15	LDSS
PS1-11aib	55742.6	−59.2	z_{P1}	23.07 ± 0.15	PS1
PS1-11aib	55751.6	−54.7	z_{P1}	22.80 ± 0.19	PS1
PS1-11aib	55754.6	−53.2	z_{P1}	22.55 ± 0.21	PS1
PS1-11aib	55763.6	−48.7	z_{P1}	22.22 ± 0.21	PS1
PS1-11aib	55769.6	−45.7	z_{P1}	22.13 ± 0.10	PS1
PS1-11aib	55772.5	−44.2	z_{P1}	22.68 ± 0.29	PS1

Table 5.4—Continued

Object	MJD (days)	Rest-frame Phase (days)	Filter	AB Mag	Instrument
PS1-11aib	55775.6	−42.7	z_{P1}	22.10 ± 0.08	PS1
PS1-11aib	55793.6	−33.7	z_{P1}	22.13 ± 0.13	PS1
PS1-11aib	55796.6	−32.2	z_{P1}	22.11 ± 0.13	PS1
PS1-11aib	55799.3	−30.8	z_{P1}	22.04 ± 0.10	PS1
PS1-11aib	55802.5	−29.2	z_{P1}	21.75 ± 0.08	PS1
PS1-11aib	55805.3	−27.8	z_{P1}	21.98 ± 0.15	PS1
PS1-11aib	55808.3	−26.3	z_{P1}	21.83 ± 0.11	PS1
PS1-11aib	55811.3	−24.8	z_{P1}	21.84 ± 0.10	PS1
PS1-11aib	55823.3	−18.8	z_{P1}	21.71 ± 0.06	PS1
PS1-11aib	55827.4	−16.8	z_{P1}	21.70 ± 0.06	PS1
PS1-11aib	55830.3	−15.3	z_{P1}	21.67 ± 0.11	PS1
PS1-11aib	55832.3	−14.3	z_{P1}	21.60 ± 0.14	PS1
PS1-11aib	55854.3	−3.3	z_{P1}	21.67 ± 0.06	PS1
PS1-11aib	55857.2	−1.9	z_{P1}	21.55 ± 0.05	PS1
PS1-11aib	55860.2	−0.4	z_{P1}	21.61 ± 0.06	PS1
PS1-11aib	55891.2	15.2	z_{P1}	21.68 ± 0.08	PS1
PS1-11aib	56155.5	147.3	z_{P1}	23.45 ± 0.31	PS1
PS1-11aib	55836.5	−12.2	z	22.18 ± 0.39	GS
PS1-11aib	55913.7	26.4	z	21.78 ± 0.11	GS
PS1-11aib	56064.4	101.7	z	23.32 ± 0.27	LDSS
PS1-11tt	55710.5	0.1	g_{P1}	23.89 ± 0.32	PS1
PS1-11tt	55720.0	4.2	g	24.07 ± 0.26	GN
PS1-11tt	55602.6	−47.2	r_{P1}	23.82 ± 0.34	PS1
PS1-11tt	55674.5	−15.7	r_{P1}	22.93 ± 0.18	PS1
PS1-11tt	55677.6	−14.3	r_{P1}	22.59 ± 0.15	PS1
PS1-11tt	55701.6	−3.8	r_{P1}	23.12 ± 0.31	PS1
PS1-11tt	55710.5	0.1	r_{P1}	22.82 ± 0.14	PS1
PS1-11tt	55743.3	14.5	r_{P1}	23.17 ± 0.22	PS1
PS1-11tt	55746.3	15.8	r_{P1}	23.55 ± 0.25	PS1

Table 5.4—Continued

Object	MJD (days)	Rest-frame Phase (days)	Filter	AB Mag	Instrument
PS1-11tt	55720.0	4.2	r	22.80 ± 0.11	GN
PS1-11tt	55748.9	16.9	r	23.83 ± 0.11	GN
PS1-11tt	55672.5	−16.6	i_{P1}	22.36 ± 0.12	PS1
PS1-11tt	55675.6	−15.2	i_{P1}	22.18 ± 0.09	PS1
PS1-11tt	55678.6	−13.9	i_{P1}	22.16 ± 0.12	PS1
PS1-11tt	55702.5	−3.4	i_{P1}	22.09 ± 0.09	PS1
PS1-11tt	55708.4	−0.8	i_{P1}	22.10 ± 0.13	PS1
PS1-11tt	55711.5	0.5	i_{P1}	22.32 ± 0.07	PS1
PS1-11tt	55714.4	1.8	i_{P1}	22.19 ± 0.06	PS1
PS1-11tt	55723.4	5.7	i_{P1}	22.33 ± 0.08	PS1
PS1-11tt	55735.5	11.0	i_{P1}	22.08 ± 0.25	PS1
PS1-11tt	55741.5	13.6	i_{P1}	22.78 ± 0.15	PS1
PS1-11tt	55744.3	14.9	i_{P1}	22.69 ± 0.12	PS1
PS1-11tt	55747.3	16.2	i_{P1}	22.63 ± 0.09	PS1
PS1-11tt	55753.3	18.8	i_{P1}	22.81 ± 0.10	PS1
PS1-11tt	55762.3	22.8	i_{P1}	22.97 ± 0.15	PS1
PS1-11tt	55765.3	24.1	i_{P1}	22.53 ± 0.26	PS1
PS1-11tt	55768.3	25.4	i_{P1}	22.87 ± 0.11	PS1
PS1-11tt	55771.3	26.7	i_{P1}	22.95 ± 0.31	PS1
PS1-11tt	55774.3	28.0	i_{P1}	23.02 ± 0.11	PS1
PS1-11tt	55777.3	29.3	i_{P1}	23.07 ± 0.14	PS1
PS1-11tt	55789.3	34.6	i_{P1}	23.06 ± 0.17	PS1
PS1-11tt	55792.3	35.9	i_{P1}	23.12 ± 0.18	PS1
PS1-11tt	55795.3	37.2	i_{P1}	23.53 ± 0.26	PS1
PS1-11tt	55801.3	39.8	i_{P1}	23.11 ± 0.28	PS1
PS1-11tt	55804.3	41.1	i_{P1}	23.43 ± 0.24	PS1
PS1-11tt	55720.0	4.2	i	22.28 ± 0.12	GN
PS1-11tt	55748.9	16.9	i	22.54 ± 0.11	GN
PS1-11tt	55673.6	−16.1	z_{P1}	22.07 ± 0.12	PS1

Table 5.4—Continued

Object	MJD (days)	Rest-frame Phase (days)	Filter	AB Mag	Instrument
PS1-11tt	55676.6	−14.8	z_{P1}	21.89 ± 0.30	PS1
PS1-11tt	55724.4	6.2	z_{P1}	21.82 ± 0.16	PS1
PS1-11tt	55736.5	11.5	z_{P1}	22.25 ± 0.12	PS1
PS1-11tt	55739.5	12.8	z_{P1}	22.21 ± 0.23	PS1
PS1-11tt	55742.3	14.0	z_{P1}	22.18 ± 0.10	PS1
PS1-11tt	55745.3	15.3	z_{P1}	22.22 ± 0.10	PS1
PS1-11tt	55748.3	16.6	z_{P1}	22.34 ± 0.10	PS1
PS1-11tt	55751.3	18.0	z_{P1}	22.29 ± 0.16	PS1
PS1-11tt	55754.3	19.3	z_{P1}	22.27 ± 0.11	PS1
PS1-11tt	55760.3	21.9	z_{P1}	22.32 ± 0.16	PS1
PS1-11tt	55763.3	23.2	z_{P1}	22.43 ± 0.19	PS1
PS1-11tt	55766.3	24.5	z_{P1}	22.49 ± 0.26	PS1
PS1-11tt	55769.3	25.8	z_{P1}	22.45 ± 0.13	PS1
PS1-11tt	55775.3	28.4	z_{P1}	22.50 ± 0.12	PS1
PS1-11tt	55778.3	29.8	z_{P1}	22.47 ± 0.19	PS1
PS1-11tt	55790.3	35.0	z_{P1}	22.69 ± 0.13	PS1
PS1-11tt	55793.3	36.4	z_{P1}	22.77 ± 0.20	PS1
PS1-11tt	55796.3	37.6	z_{P1}	22.82 ± 0.20	PS1
PS1-11tt	55799.2	38.9	z_{P1}	22.71 ± 0.31	PS1
PS1-11tt	55802.2	40.3	z_{P1}	23.05 ± 0.28	PS1
PS1-11tt	55805.2	41.6	z_{P1}	23.18 ± 0.35	PS1
PS1-11tt	55748.9	16.9	z	22.15 ± 0.15	GN
PS1-11afv	55692.4	−15.8	g_{P1}	23.82 ± 0.35	PS1
PS1-11afv	55701.3	−12.1	g_{P1}	23.87 ± 0.21	PS1
PS1-11afv	55710.3	−8.3	g_{P1}	23.50 ± 0.17	PS1
PS1-11afv	55719.3	−4.6	g_{P1}	23.65 ± 0.21	PS1
PS1-11afv	55731.3	0.4	g_{P1}	22.94 ± 0.25	PS1
PS1-11afv	55701.3	−12.1	r_{P1}	23.10 ± 0.13	PS1
PS1-11afv	55710.3	−8.3	r_{P1}	22.94 ± 0.09	PS1

Table 5.4—Continued

Object	MJD (days)	Rest-frame Phase (days)	Filter	AB Mag	Instrument
PS1-11afv	55719.3	−4.6	r_{P1}	22.63 ± 0.09	PS1
PS1-11afv	55722.3	−3.3	r_{P1}	22.66 ± 0.22	PS1
PS1-11afv	55731.3	0.4	r_{P1}	22.63 ± 0.21	PS1
PS1-11afv	55751.8	8.9	r	22.37 ± 0.15	GN
PS1-11afv	55762.7	13.5	r	22.77 ± 0.28	GN
PS1-11afv	55702.3	−11.6	i_{P1}	22.71 ± 0.26	PS1
PS1-11afv	55705.3	−10.4	i_{P1}	22.88 ± 0.13	PS1
PS1-11afv	55708.3	−9.1	i_{P1}	23.12 ± 0.27	PS1
PS1-11afv	55711.3	−7.9	i_{P1}	22.60 ± 0.08	PS1
PS1-11afv	55714.3	−6.7	i_{P1}	22.62 ± 0.10	PS1
PS1-11afv	55720.3	−4.2	i_{P1}	22.22 ± 0.17	PS1
PS1-11afv	55723.3	−2.9	i_{P1}	22.28 ± 0.08	PS1
PS1-11afv	55732.3	0.8	i_{P1}	22.30 ± 0.11	PS1
PS1-11afv	55738.3	3.3	i_{P1}	22.27 ± 0.24	PS1
PS1-11afv	55751.8	8.9	i	22.41 ± 0.20	GN
PS1-11afv	55762.8	13.5	i	22.51 ± 0.32	GN
PS1-11afv	55706.3	−10.0	z_{P1}	22.58 ± 0.27	PS1
PS1-11afv	55712.3	−7.5	z_{P1}	22.44 ± 0.13	PS1
PS1-11afv	55718.3	−5.0	z_{P1}	23.04 ± 0.29	PS1
PS1-11afv	55724.3	−2.5	z_{P1}	22.21 ± 0.21	PS1
PS1-11afv	55736.3	2.5	z_{P1}	22.05 ± 0.12	PS1
PS1-11afv	55751.8	8.9	z	22.59 ± 0.45	GN
PS1-13or	56331.6	−31.4	g_{P1}	23.70 ± 0.35	PS1
PS1-13or	56333.4	−30.7	g_{P1}	23.44 ± 0.13	PS1
PS1-13or	56336.5	−29.5	g_{P1}	23.72 ± 0.32	PS1
PS1-13or	56354.4	−22.4	g_{P1}	23.17 ± 0.26	PS1
PS1-13or	56357.4	−21.2	g_{P1}	22.72 ± 0.10	PS1
PS1-13or	56360.3	−20.0	g_{P1}	22.82 ± 0.12	PS1
PS1-13or	56384.3	−10.5	g_{P1}	22.82 ± 0.15	PS1

Table 5.4—Continued

Object	MJD (days)	Rest-frame Phase (days)	Filter	AB Mag	Instrument
PS1-13or	56387.4	−9.3	g_{P1}	22.87 ± 0.15	PS1
PS1-13or	56395.3	−6.2	g_{P1}	22.61 ± 0.10	PS1
PS1-13or	56416.3	2.2	g_{P1}	22.87 ± 0.16	PS1
PS1-13or	56325.6	−33.8	r_{P1}	23.18 ± 0.27	PS1
PS1-13or	56328.5	−32.6	r_{P1}	22.83 ± 0.19	PS1
PS1-13or	56331.6	−31.4	r_{P1}	22.84 ± 0.12	PS1
PS1-13or	56336.5	−29.5	r_{P1}	22.54 ± 0.10	PS1
PS1-13or	56354.5	−22.4	r_{P1}	22.11 ± 0.09	PS1
PS1-13or	56357.4	−21.2	r_{P1}	22.20 ± 0.05	PS1
PS1-13or	56360.3	−20.0	r_{P1}	22.18 ± 0.09	PS1
PS1-13or	56384.3	−10.5	r_{P1}	21.89 ± 0.06	PS1
PS1-13or	56387.4	−9.3	r_{P1}	21.91 ± 0.08	PS1
PS1-13or	56391.3	−7.7	r_{P1}	21.79 ± 0.04	PS1
PS1-13or	56395.3	−6.2	r_{P1}	21.96 ± 0.06	PS1
PS1-13or	56416.3	2.2	r_{P1}	22.20 ± 0.09	PS1
PS1-13or	56326.5	−33.4	i_{P1}	23.49 ± 0.18	PS1
PS1-13or	56337.5	−29.1	i_{P1}	22.93 ± 0.14	PS1
PS1-13or	56352.5	−23.2	i_{P1}	22.39 ± 0.14	PS1
PS1-13or	56355.5	−22.0	i_{P1}	22.29 ± 0.13	PS1
PS1-13or	56358.3	−20.8	i_{P1}	22.32 ± 0.11	PS1
PS1-13or	56363.3	−18.9	i_{P1}	22.27 ± 0.10	PS1
PS1-13or	56369.3	−16.5	i_{P1}	22.22 ± 0.26	PS1
PS1-13or	56385.4	−10.1	i_{P1}	21.81 ± 0.05	PS1
PS1-13or	56388.3	−8.9	i_{P1}	21.75 ± 0.07	PS1
PS1-13or	56391.3	−7.7	i_{P1}	21.84 ± 0.07	PS1
PS1-13or	56393.4	−6.9	i_{P1}	21.65 ± 0.04	PS1
PS1-13or	56396.4	−5.7	i_{P1}	21.77 ± 0.07	PS1
PS1-13or	56399.3	−4.6	i_{P1}	21.72 ± 0.06	PS1
PS1-13or	56411.4	0.2	i_{P1}	21.66 ± 0.16	PS1

Table 5.4—Continued

Object	MJD (days)	Rest-frame Phase (days)	Filter	AB Mag	Instrument
PS1-13or	56414.3	1.4	i_{P1}	21.82 ± 0.05	PS1
PS1-13or	56417.3	2.6	i_{P1}	21.75 ± 0.04	PS1
PS1-13or	56422.3	4.6	i_{P1}	21.78 ± 0.04	PS1
PS1-13or	56333.5	−30.7	z_{P1}	23.03 ± 0.20	PS1
PS1-13or	56335.5	−29.9	z_{P1}	23.02 ± 0.21	PS1
PS1-13or	56351.4	−23.6	z_{P1}	22.55 ± 0.16	PS1
PS1-13or	56353.3	−22.8	z_{P1}	22.47 ± 0.19	PS1
PS1-13or	56356.4	−21.6	z_{P1}	22.20 ± 0.11	PS1
PS1-13or	56359.4	−20.4	z_{P1}	22.08 ± 0.15	PS1
PS1-13or	56370.3	−16.1	z_{P1}	22.07 ± 0.08	PS1
PS1-13or	56383.3	−10.9	z_{P1}	22.02 ± 0.11	PS1
PS1-13or	56389.4	−8.5	z_{P1}	21.90 ± 0.10	PS1
PS1-13or	56392.3	−7.3	z_{P1}	21.81 ± 0.08	PS1
PS1-13or	56397.3	−5.3	z_{P1}	21.72 ± 0.13	PS1
PS1-13or	56400.3	−4.2	z_{P1}	21.76 ± 0.11	PS1
PS1-13or	56410.3	−0.2	z_{P1}	21.73 ± 0.08	PS1
PS1-13or	56415.3	1.8	z_{P1}	21.75 ± 0.08	PS1
PS1-13or	56423.3	5.0	z_{P1}	21.74 ± 0.09	PS1
PS1-11bam	55889.6	−2.6	g_{P1}	22.80 ± 0.17	PS1
PS1-11bam	55895.6	−0.3	g_{P1}	22.97 ± 0.15	PS1
PS1-11bam	55888.5	−3.1	r_{P1}	22.13 ± 0.09	PS1
PS1-11bam	55892.5	−1.5	r_{P1}	22.14 ± 0.07	PS1
PS1-11bam	55895.6	−0.3	r_{P1}	22.27 ± 0.07	PS1
PS1-11bam	55911.6	5.9	r_{P1}	22.76 ± 0.15	PS1
PS1-11bam	55947.4	19.9	r_{P1}	23.96 ± 0.36	PS1
PS1-11bam	55952.6	21.9	r_{P1}	23.77 ± 0.21	PS1
PS1-11bam	55879.6	−6.5	i_{P1}	22.05 ± 0.06	PS1
PS1-11bam	55885.6	−4.2	i_{P1}	21.95 ± 0.08	PS1
PS1-11bam	55888.5	−3.1	i_{P1}	21.90 ± 0.06	PS1

Table 5.4—Continued

Object	MJD (days)	Rest-frame Phase (days)	Filter	AB Mag	Instrument
PS1-11bam	55890.6	−2.3	i_{P1}	22.02 ± 0.05	PS1
PS1-11bam	55893.6	−1.1	i_{P1}	21.97 ± 0.05	PS1
PS1-11bam	55900.6	1.6	i_{P1}	22.15 ± 0.06	PS1
PS1-11bam	55915.4	7.4	i_{P1}	21.89 ± 0.24	PS1
PS1-11bam	55942.4	17.9	i_{P1}	22.66 ± 0.27	PS1
PS1-11bam	55945.6	19.2	i_{P1}	22.65 ± 0.08	PS1
PS1-11bam	55948.4	20.3	i_{P1}	23.25 ± 0.32	PS1
PS1-11bam	55950.6	21.1	i_{P1}	23.11 ± 0.12	PS1
PS1-11bam	55953.5	22.2	i_{P1}	22.36 ± 0.23	PS1
PS1-11bam	55956.3	23.4	i_{P1}	23.02 ± 0.20	PS1
PS1-11bam	55960.4	25.0	i_{P1}	23.20 ± 0.15	PS1
PS1-11bam	55968.3	28.0	i_{P1}	23.11 ± 0.14	PS1
PS1-11bam	55878.6	−7.0	z_{P1}	22.26 ± 0.09	PS1
PS1-11bam	55883.6	−5.0	z_{P1}	21.89 ± 0.22	PS1
PS1-11bam	55889.6	−2.6	z_{P1}	22.21 ± 0.10	PS1
PS1-11bam	55891.5	−1.9	z_{P1}	22.07 ± 0.09	PS1
PS1-11bam	55894.5	−0.7	z_{P1}	21.91 ± 0.03	PS1
PS1-11bam	55897.6	0.5	z_{P1}	22.26 ± 0.11	PS1
PS1-11bam	55899.6	1.3	z_{P1}	22.07 ± 0.13	PS1
PS1-11bam	55901.6	2.0	z_{P1}	22.08 ± 0.09	PS1
PS1-11bam	55910.6	5.5	z_{P1}	22.23 ± 0.13	PS1
PS1-11bam	55913.5	6.7	z_{P1}	22.17 ± 0.18	PS1
PS1-11bam	55929.4	12.9	z_{P1}	22.61 ± 0.16	PS1
PS1-11bam	55931.6	13.7	z_{P1}	22.52 ± 0.21	PS1
PS1-11bam	55940.5	17.2	z_{P1}	22.63 ± 0.14	PS1
PS1-11bam	55951.6	21.5	z_{P1}	22.89 ± 0.32	PS1
PS1-11bam	55957.4	23.8	z_{P1}	23.01 ± 0.16	PS1
PS1-11bam	55959.5	24.6	z_{P1}	22.34 ± 0.28	PS1
PS1-11bam	55967.5	27.7	z_{P1}	23.41 ± 0.29	PS1

Table 5.4—Continued

Object	MJD (days)	Rest-frame Phase (days)	Filter	AB Mag	Instrument
PS1-11bam	55969.5	28.5	z_{P1}	23.27 ± 0.29	PS1
PS1-11bam	55972.3	29.6	z_{P1}	23.46 ± 0.25	PS1
PS1-12bmy	56206.6	−9.1	r_{P1}	22.94 ± 0.18	PS1
PS1-12bmy	56209.5	−7.9	r_{P1}	23.02 ± 0.17	PS1
PS1-12bmy	56217.5	−4.8	r_{P1}	22.99 ± 0.22	PS1
PS1-12bmy	56235.5	2.2	r_{P1}	23.73 ± 0.31	PS1
PS1-12bmy	56242.4	4.9	r_{P1}	23.39 ± 0.34	PS1
PS1-12bmy	56204.5	−9.8	i_{P1}	22.15 ± 0.08	PS1
PS1-12bmy	56207.6	−8.7	i_{P1}	22.49 ± 0.09	PS1
PS1-12bmy	56210.5	−7.5	i_{P1}	22.32 ± 0.05	PS1
PS1-12bmy	56213.5	−6.4	i_{P1}	22.64 ± 0.15	PS1
PS1-12bmy	56215.5	−5.6	i_{P1}	22.47 ± 0.17	PS1
PS1-12bmy	56218.5	−4.4	i_{P1}	22.40 ± 0.06	PS1
PS1-12bmy	56221.5	−3.3	i_{P1}	22.48 ± 0.09	PS1
PS1-12bmy	56233.5	1.4	i_{P1}	22.76 ± 0.15	PS1
PS1-12bmy	56236.4	2.5	i_{P1}	22.63 ± 0.09	PS1
PS1-12bmy	56239.5	3.7	i_{P1}	22.58 ± 0.14	PS1
PS1-12bmy	56242.4	4.9	i_{P1}	22.84 ± 0.18	PS1
PS1-12bmy	56284.3	21.2	i_{P1}	23.48 ± 0.23	PS1
PS1-12bmy	56310.3	31.3	i_{P1}	23.97 ± 0.28	PS1
PS1-12bmy	56205.5	−9.5	z_{P1}	22.31 ± 0.15	PS1
PS1-12bmy	56208.6	−8.3	z_{P1}	22.23 ± 0.15	PS1
PS1-12bmy	56211.5	−7.1	z_{P1}	22.19 ± 0.12	PS1
PS1-12bmy	56214.5	−6.0	z_{P1}	22.45 ± 0.21	PS1
PS1-12bmy	56216.5	−5.2	z_{P1}	22.03 ± 0.17	PS1
PS1-12bmy	56219.5	−4.0	z_{P1}	22.19 ± 0.12	PS1
PS1-12bmy	56222.5	−2.9	z_{P1}	22.24 ± 0.14	PS1
PS1-12bmy	56226.5	−1.3	z_{P1}	22.31 ± 0.14	PS1
PS1-12bmy	56229.5	−0.2	z_{P1}	22.51 ± 0.23	PS1

Table 5.4—Continued

Object	MJD (days)	Rest-frame Phase (days)	Filter	AB Mag	Instrument
PS1-12bmy	56232.5	1.0	z_{P1}	22.62 ± 0.23	PS1
PS1-12bmy	56234.4	1.8	z_{P1}	22.38 ± 0.09	PS1
PS1-12bmy	56262.4	12.6	z_{P1}	22.31 ± 0.20	PS1
PS1-12bmy	56289.3	23.1	z_{P1}	23.16 ± 0.30	PS1
PS1-12bmy	56292.3	24.3	z_{P1}	22.95 ± 0.29	PS1
PS1-12bmy	56300.3	27.4	z_{P1}	23.13 ± 0.26	PS1
PS1-12bmy	56308.2	30.5	z_{P1}	23.22 ± 0.33	PS1

Chapter 6

Conclusions and Future Directions

6.1 Conclusions

This thesis has explored the properties and environments of the new class of hydrogen-poor superluminous supernovae, through analyzing the sample of such objects found in PS1/MDS, and by carrying out the first comprehensive survey of SLSN host galaxies. Here, I summarize my conclusions.

First, the sample of SLSNe from PS1/MDS demonstrates the diversity within the class of H-poor SLSNe. PS1-10bzj, discussed in Chapter 2, was an early example of an object that was fainter and faster-evolving than previously-known members of this class but clearly a part of the same phenomenon. The compilation study presented in Chapter 5 demonstrates that the peak luminosities, radiated energies and timescales seen in SLSNe can all vary by factors of $5 - 10$.

This diversity also highlights the need for a better definition of the SLSN

phenomenon than an arbitrary luminosity cut at $M = -21$ mag, as demonstrated by the existence of objects in the PS1/MDS sample with similar spectroscopic properties that do not meet this cut. This is particularly important for understanding the relationship between SLSNe and "normal" core-collapse SNe, as well as for evaluating the usefulness of SLSNe as standard(izable) candles. When accounting for the flux-limited nature of the PS1/MDS survey and including objects with similar spectroscopic properties without a luminosity cut, we find a mean absolute magnitude of -21.2 ± 0.7 mag; this scatter is twice as large as what was reported by Inserra & Smartt (2014) using a similar-size sample comprised of objects from the literature.

The diversity in light curve shapes indicates that the underlying mechanism must be able to reproduce a wide variety of peak luminosities and timescales. I find that a magnetar spin-down model can reproduce the light curves of the SLSNe from PS1/MDS, though it is necessary to explicitly include hard emission leakage in the model to simultaneously fit the rise and decline phase of our widest light curves, which tend to be more symmetric. In contrast, the magnetar model can easily reproduce the lower-luminosity objects in our sample.

During the PS1/MDS survey we found a single object, PS1-14bj, which has a significantly wider light curve than the rest of the SLSN sample. PS1-14bj shows a slow rise to maximum over $\gtrsim 100$ days, a decay rate matching ^{56}Co, comparatively red colors throughout its evolution, and similar spectroscopic properties to SN 2007bi. The light curve is consistent with radioactive decay being the power source, though requires a total ^{56}Ni mass $\sim 14\ M_{\odot}$ and a total ejecta mass $\sim 105\ M_{\odot}$, making PS1-14bj the best candidate for a PISN explosion found in Pan-STARRS. While we can also fit the light curve with a magnetar model, PS1-14bj demonstrates that Ni decay is a plausible energy

source for some SLSNe.

A separate probe on the origin of SLSNe comes from studying their host environments. I have carried out the first systematic survey of SLSN host environments, demonstrating that SLSNe show a strong environmental preference for low-luminosity, low-mass galaxies, with many also having high specific star formation rates. They are statistically incompatible with coming from the same galaxies as core-collapse SNe in the same redshift range, suggesting that an additional ingredient beyond star formation is necessary for a massive star to end its life as a SLSN.

I further find that the host galaxies of SLSNe tend to be metal-poor, with a median metallicity of $0.45Z_{\odot}$. However, at least one host galaxy in my sample has solar metallicity, suggesting that there cannot be a strict metallicity threshold for producing SLSNe. About a third of the galaxies with spectroscopy are extreme emission-line galaxies, showing [OIII]λ5007 equivalent widths > 100 Å, indicating that some SLSN host galaxies are undergoing an intense starburst. Using resolved host galaxy imaging from the *Hubble Space Telescope*, I find that SLSN host galaxies are irregular, compact dwarf galaxies, with a median half-light radius of just 0.9 kpc.

The galaxy-scale properties of SLSN hosts are similar to those found in the galaxies that host LGRBs, suggesting that the environmental factors necessary to produce the two types of transients are similar. Studying the locations of SLSNe relative to their host UV light distribution, I find that SLSNe are not as strong tracers of the brightest UV regions as are LGRBs, however. This indicates that their actual progenitor populations may be separate, with SLSN progenitors being lower-mass stars than GRB progenitors, although a larger sample is necessary to definitely distinguish the populations statistically.

A preference for low-metallicity environments at first glance seems to argue against a CSM interaction power source for H-poor SLSNe, but may be reconciled by that a different mechanism than stellar winds is needed to produce the massive CSM required to power the light curve. If e.g. pulsational pair-instability was the mass-loss mechanism, this could also explain the preference for low-metallicity environments (Woosley et al. 2007; Chatzopoulos & Wheeler 2012b). However, this mechanism would require the SLSN progenitors to be very massive stars, which may be hard to reconcile with our finding that some SLSNe explode in regions with very little underlying UV flux. Combined with the fact that narrow emission lines are not seen in SLSN (both the sample studied here, as well as others, e.g. Nicholl et al. 2015), CSM interaction is unlikely to be the dominant mechanism producing H-poor SLSNe.

Both the overall galaxy scale properties, the similarities to LGRB host galaxies, and the possibility of a lower-mass progenitor are consistent with a picture where both SLSNe and LGRBs require high core angular momentum to form, with LGRB progenitors collapsing to a black hole and launching a relativistic jet, and SLSN progenitors collapsing to a neutron star creating a rapidly spinning magnetar. In both cases, the preference for low metallicity environments is explained by that at higher metallicities, line-driven winds will remove angular momentum. Thus, both the properties of the SLSNe themselves, and their host environments, are consistent with the energy source being a long-lived central engine driven by rotation, such as a magnetar.

6.2 Future Directions

With the upcoming Large Synoptic Survey Telescope (LSST), the future of studying rare transients like SLSNe is bright. In the meantime, ongoing surveys like PTF and its successor Zwicky Transient Factory (ZTF), CRTS, the La Silla Quest (LSQ) survey and the Dark Energy Survey (DES) are contributing to the growing sample of known SLSNe. Here, I outline some promising directions for making progress in the immediate future.

6.2.1 Going Beyond the Optical

While both the properties of the observed SLSNe and their host environments are consistent with a magnetar origin, they constitute circumstantial evidence, lacking a definite test that can distinguish it from alternatives. One proposed signature of the magnetar central engine is luminous X-ray emission at late times, following the breakout of the ionization front created by the wind from the magnetar (Metzger et al. 2014). If the X-rays manage to break out, the resulting luminosity is predicted to be of order $L_{\rm X} \sim 10^{43-45}$ erg s^{-1} (Fig. 6.1). X-ray emission can also be produced in interaction models, though generally at lower luminosity, although Pan et al. (2013) has shown that under certain conditions they can reach similar luminosities as predicted in the magnetar model. Still, the interaction case predicts a steeper spectrum and shallower time evolution than is predicted in the central engine scenario. Detecting and characterizing X-ray emission thus offers a promising test to distinguish the two scenarios.

To date, only a single H-poor SLSN has detected X-ray emission: SCP06F6 was detected in a single epoch of XMM-Newton observations at a time corresponding to

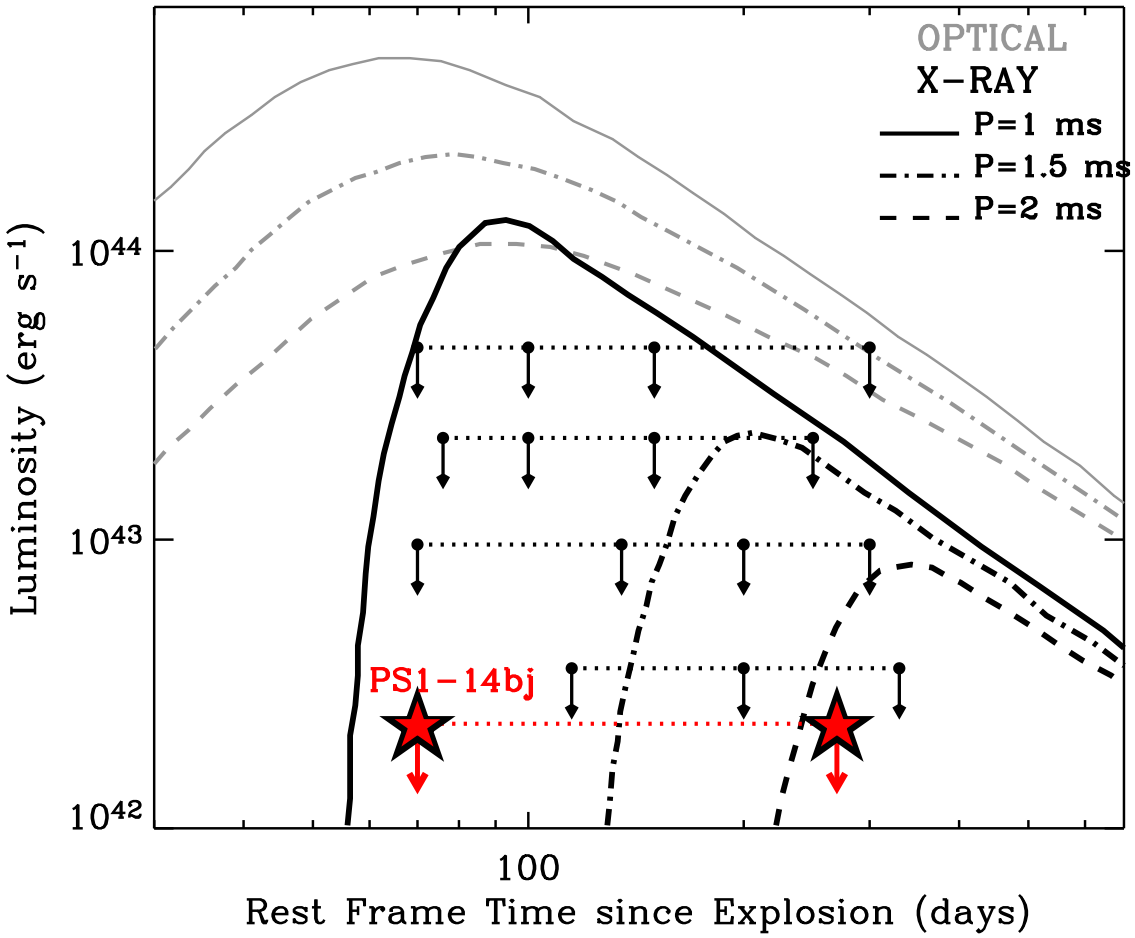

Figure 6.1.—: Predicted optical (gray) and X-ray (black) light curves for magnetars with different initial spin periods (adapted from Metzger et al. 2014). The arrows show upper limits from our *Swift* and XMM-Newton campaigns for searching for late-time X-rays from SLSNe, ruling out the fastest spinning magnetar models for these objects. From Margutti et al., in preparation.

$\sim$ 70 days after optical peak, with a spectacular X-ray luminosity of $\sim 10^{45}$ erg s^{-1}. A follow-up observation with *Chandra* about 40 rest-frame days later yielded a non-detection suggesting that the source was transient (Levan et al. 2013). Other SLSNe have been followed with *Swift* XRT yielding nondetections to date; these observations have generally been at earlier time periods than when the X-ray emission is predicted to peak, however (Levan et al. 2013; Metzger et al. 2014).

To remedy this, we are currently carrying out a search campaign for *late-time* X-ray emission from SLSNe using XMM-Newton and *Swift* (PI: Margutti). Figure 6.1 shows early results from this campaign, with the black arrows showing upper limits from *Swift* from four low-redshift SLSNe, and the red stars showing deep XMM-Newton limits for PS1-14bj. These non-detections demonstrate that the X-ray luminosity observed in SCP06F6 cannot be common in SLSNe, and argue against a central engine with very rapid initial spin periods for these particular events.

6.2.2 Detailed Studies of Low-Redshift SLSNe

While SLSNe are intrinsically very luminous, at the typical redshift $z \sim 1$ of the PS1/MDS sample, they are still not very bright. This limited the amount of late-time follow up we were able to do, both in terms of photometry and spectroscopy. However, late-time spectroscopic data also has the potential to discriminate between models. Another prediction of the magnetar model is that the ejecta should be swept into a dense shell, resulting in a period of nearly constant photospheric velocity at late times ($\sim 100-300$ days past peak; Kasen & Bildsten 2010). In contrast, if SLSNe were powered by the conversion of KE to radiation through CSM interaction, this conversion should

manifest itself as a decrease in the expansion velocity over time. These predictions are testable with spectroscopic monitoring at late times constraining the velocity evolution at these epochs, which is possible for the lower-redshift SLSNe that are currently being discovered by shallower, wide-area surveys like PTF, LSQ and CRTS.

A disadvantage of low-redshift surveys is that standard optical follow-up will not be able to capture the copious UV flux that dominates the early emission in H-poor SLSNe. In order to tie well-studied low redshift events to their higher-redshift counterparts, it is necessary to include UV follow up, as can be done with *Swift* and *HST*, to accurately measure the temperature evolution and total radiated energies.

6.2.3 Preparing for the LSST Era

The SLSN sample from PS1/MDS discussed in this thesis was discovered by virtue of humans visually inspecting light curves of transient candidates, and selecting a subsample for spectroscopic follow-up. With the expected rates of alerts from LSST, this old-fashioned approach for searching for needles in haystacks is no longer feasible, and we will have to rely on computer-based techniques such as machine learning and automated classification. With its multi-filter strategy and similar cadence to the proposed LSST observations, the PS1/MDS data set, including the SLSN sample presented here, has the potential to serve as an important training set for photometry-based searches for SLSNe. The results of this thesis demonstrating a preference for low-luminosity host galaxy environments can also be utilized in future searches, by focusing on events that are several magnitudes brighter than any observed host galaxy.

References

Ahn, C. P., Alexandroff, R., Allende Prieto, C., et al. 2012, ApJS, 203, 21

Akerlof, C. W., Kehoe, R. L., McKay, T. A., et al. 2003, PASP, 115, 132

Alard, C., & Lupton, R. H. 1998, ApJ, 503, 325

Amorín, R., Pérez-Montero, E., Vílchez, J. M., & Papaderos, P. 2012, ApJ, 749, 185

Anderson, J. P., Habergham, S. M., James, P. A., & Hamuy, M. 2012, MNRAS, 424, 1372

Andrews, B. H., & Martini, P. 2013, ApJ, 765, 140

Arnett, W. D. 1982, ApJ, 253, 785

Ashby, M. L. N., Willner, S. P., Fazio, G. G., et al. 2013, ApJ, 769, 80

Asplund, M., Grevesse, N., Sauval, A. J., & Scott, P. 2009, ARA&A, 47, 481

Baade, W., & Zwicky, F. 1934, Proceedings of the National Academy of Science, 20, 254

Balberg, S., & Loeb, A. 2011, MNRAS, 414, 1715

Barbary, K., Dawson, K. S., Tokita, K., et al. 2009, ApJ, 690, 1358

Barkat, Z., Rakavy, G., & Sack, N. 1967, Physical Review Letters, 18, 379

Bastian, N., Covey, K. R., & Meyer, M. R. 2010, ARA&A, 48, 339

Benetti, S., Nicholl, M., Cappellaro, E., et al. 2014, MNRAS, 441, 289

Berger, E., Chornock, R., Lunnan, R., et al. 2012, ApJ, 755, L29

Bloom, J. S., Kulkarni, S. R., & Djorgovski, S. G. 2002, AJ, 123, 1111

Bohlin, R. C., Dickinson, M. E., & Calzetti, D. 2001, AJ, 122, 2118

Brammer, G. B., van Dokkum, P. G., & Coppi, P. 2008, ApJ, 686, 1503

Branch, D., Benetti, S., Kasen, D., et al. 2002, ApJ, 566, 1005

Bresolin, F., Gieren, W., Kudritzki, R.-P., et al. 2009, ApJ, 700, 309

Cardamone, C., Schawinski, K., Sarzi, M., et al. 2009, MNRAS, 399, 1191

Cardamone, C. N., van Dokkum, P. G., Urry, C. M., et al. 2010, ApJS, 189, 270

Cardelli, J. A., Clayton, G. C., & Mathis, J. S. 1989, ApJ, 345, 245

Chatzopoulos, E., & Wheeler, J. C. 2012a, ApJ, 748, 42

—. 2012b, ApJ, 760, 154

Chatzopoulos, E., Wheeler, J. C., & Vinko, J. 2012, ApJ, 746, 121

Chatzopoulos, E., Wheeler, J. C., Vinko, J., Horvath, Z. L., & Nagy, A. 2013, ApJ, 773, 76

Chatzopoulos, E., Wheeler, J. C., Vinko, J., et al. 2011, ApJ, 729, 143

Chen, T.-W., Smartt, S. J., Bresolin, F., et al. 2013, ApJ, 763, L28

Chen, T.-W., Smartt, S. J., Jerkstrand, A., et al. 2014, ArXiv e-prints, arXiv:1409.7728

Chevalier, R. A. 2012, ApJ, 752, L2

Chevalier, R. A., & Irwin, C. M. 2011, ApJ, 729, L6

Chomiuk, L., Chornock, R., Soderberg, A. M., et al. 2011, ApJ, 743, 114

Chornock, R., Berger, E., Rest, A., et al. 2013, ApJ, 767, 162

Copetti, M. V. F., Pastoriza, M. G., & Dottori, H. A. 1986, A&A, 156, 111

Damen, M., Labbé, I., van Dokkum, P. G., et al. 2011, ApJ, 727, 1

Dessart, L., Hillier, D. J., Waldman, R., Livne, E., & Blondin, S. 2012, MNRAS, 426, L76

Dessart, L., Waldman, R., Livne, E., Hillier, D. J., & Blondin, S. 2013, MNRAS, 428, 3227

Dexter, J., & Kasen, D. 2013, ApJ, 772, 30

Drake, A. J., Djorgovski, S. G., Mahabal, A., et al. 2009, ApJ, 696, 870

Drake, A. J., Djorgovski, S. G., Prieto, J. L., et al. 2010, ApJ, 718, L127

Drake, A. J., Djorgovski, S. G., Mahabal, A., et al. 2011a, ApJ, 735, 106

Drake, A. J., Djorgovski, S. G., Mahabal, A. A., et al. 2011b, The Astronomer's Telegram, 3343, 1

—. 2012a, The Astronomer's Telegram, 3873, 1

—. 2012b, The Astronomer's Telegram, 4595, 1

Dressler, A., Hare, T., Bigelow, B. C., & Osip, D. J. 2006, in Society of Photo-Optical Instrumentation Engineers (SPIE) Conference Series, Vol. 6269, Society of Photo-Optical Instrumentation Engineers (SPIE) Conference Series

Drout, M. R., Soderberg, A. M., Gal-Yam, A., et al. 2011, ApJ, 741, 97

Fatkhullin, T., & Gabdeev, M. 2012, The Astronomer's Telegram, 4599, 1

Filippenko, A. V. 1982, PASP, 94, 715

—. 1997, ARA&A, 35, 309

Fong, W., & Berger, E. 2013, ApJ, 776, 18

Fong, W., Berger, E., & Fox, D. B. 2010, ApJ, 708, 9

Fruchter, A. S., & Hook, R. N. 2002, PASP, 114, 144

Fruchter, A. S., Levan, A. J., Strolger, L., et al. 2006, Nature, 441, 463

Gal-Yam, A. 2012, Science, 337, 927

Gal-Yam, A., & Leonard, D. C. 2009, Nature, 458, 865

Gal-Yam, A., Mazzali, P., Ofek, E. O., et al. 2009, Nature, 462, 624

Garg, A., Stubbs, C. W., Challis, P., et al. 2007, AJ, 133, 403

Gezari, S., Halpern, J. P., Grupe, D., et al. 2009, ApJ, 690, 1313

Ginzburg, S., & Balberg, S. 2012, ApJ, 757, 178

Glazebrook, K., & Bland-Hawthorn, J. 2001, PASP, 113, 197

Goddard, Q. E., Bastian, N., & Kennicutt, R. C. 2010, MNRAS, 405, 857

Gonzaga, S., Hack, W., Fruchter, A., & Mack, J. 2012, The DrizzlePac Handbook (Baltimore, STScI)

Graham, J. F., & Fruchter, A. S. 2013, ApJ, 774, 119

Green, D. A. 2015, Historical Supernova Explosions in Our Galaxy and Their Remnants, ed. W. Orchiston, D. A. Green, & R. Strom, 91

Guseva, N. G., Papaderos, P., Meyer, H. T., Izotov, Y. I., & Fricke, K. J. 2009, A&A, 505, 63

Habergham, S. M., Anderson, J. P., James, P. A., & Lyman, J. D. 2014, MNRAS, 441, 2230

Heger, A., & Woosley, S. E. 2002, ApJ, 567, 532

Henry, A., Martin, C. L., Finlator, K., & Dressler, A. 2013, ApJ, 769, 148

Hook, I. M., Jørgensen, I., Allington-Smith, J. R., et al. 2004, PASP, 116, 425

Howell, D. A., Kasen, D., Lidman, C., et al. 2013, ApJ, 779, 98

Hoyos, C., Koo, D. C., Phillips, A. C., Willmer, C. N. A., & Guhathakurta, P. 2005, ApJ, 635, L21

Ilbert, O., Tresse, L., Zucca, E., et al. 2005, A&A, 439, 863

Inserra, C., & Smartt, S. J. 2014, ApJ, 796, 87

Inserra, C., Smartt, S. J., Jerkstrand, A., et al. 2013, ApJ, 770, 128

James, P. A., & Anderson, J. P. 2006, A&A, 453, 57

Kaiser, N., Burgett, W., Chambers, K., et al. 2010, in Society of Photo-Optical Instrumentation Engineers (SPIE) Conference Series, Vol. 7733, Society of Photo-Optical Instrumentation Engineers (SPIE) Conference Series

Kasen, D., & Bildsten, L. 2010, ApJ, 717, 245

Kasen, D., Woosley, S. E., & Heger, A. 2011, ApJ, 734, 102

Kelly, P. L., Filippenko, A. V., Modjaz, M., & Kocevski, D. 2014, ApJ, 789, 23

Kelly, P. L., & Kirshner, R. P. 2012, ApJ, 759, 107

Kelly, P. L., Kirshner, R. P., & Pahre, M. 2008, ApJ, 687, 1201

Kennicutt, Jr., R. C. 1998, ARA&A, 36, 189

Kewley, L. J., Brown, W. R., Geller, M. J., Kenyon, S. J., & Kurtz, M. J. 2007, AJ, 133, 882

Kewley, L. J., & Ellison, S. L. 2008, ApJ, 681, 1183

Kewley, L. J., Geller, M. J., & Jansen, R. A. 2004, AJ, 127, 2002

Kobulnicky, H. A., & Kewley, L. J. 2004, ApJ, 617, 240

Kocevski, D., & West, A. A. 2011, ApJ, 735, L8

Komatsu, E., Smith, K. M., Dunkley, J., et al. 2011, ApJS, 192, 18

Kozłowski, S., Kochanek, C. S., Stern, D., et al. 2010, ApJ, 722, 1624

Kozyreva, A., Blinnikov, S., Langer, N., & Yoon, S.-C. 2014, A&A, 565, A70

Kriek, M., van Dokkum, P. G., Labbé, I., et al. 2009, ApJ, 700, 221

Kroupa, P., Weidner, C., Pflamm-Altenburg, J., et al. 2013, The Stellar and Sub-Stellar Initial Mass Function of Simple and Composite Populations, ed. T. D. Oswalt & G. Gilmore, 115

Langer, N., & Norman, C. A. 2006, ApJ, 638, L63

Laskar, T., Berger, E., & Chary, R.-R. 2011, ApJ, 739, 1

Lavalley, M. P., Isobe, T., & Feigelson, E. D. 1992, in Bulletin of the American Astronomical Society, Vol. 24, Bulletin of the American Astronomical Society, 839–840

Law, N. M., Kulkarni, S. R., Dekany, R. G., et al. 2009, PASP, 121, 1395

Leibler, C. N., & Berger, E. 2010, ApJ, 725, 1202

Leloudas, G., Chatzopoulos, E., Dilday, B., et al. 2012, A&A, 541, A129

Leloudas, G., Schulze, S., Krühler, T., et al. 2015, MNRAS, 449, 917

Levan, A. J., Read, A. M., Metzger, B. D., Wheatley, P. J., & Tanvir, N. R. 2013, ApJ, 771, 136

Levesque, E. M., Berger, E., Kewley, L. J., & Bagley, M. M. 2010a, AJ, 139, 694

Levesque, E. M., Kewley, L. J., Berger, E., & Zahid, H. J. 2010b, AJ, 140, 1557

Levesque, E. M., Kewley, L. J., Graham, J. F., & Fruchter, A. S. 2010c, ApJ, 712, L26

Lunnan, R., Chornock, R., Berger, E., et al. 2013, ApJ, 771, 97

—. 2014, ApJ, 787, 138

—. 2015, ApJ, 804, 90

MacFadyen, A. I., & Woosley, S. E. 1999, ApJ, 524, 262

Magnier, E. 2006, in The Advanced Maui Optical and Space Surveillance Technologies Conference

Magnier, E. A., Liu, M., Monet, D. G., & Chambers, K. C. 2008, in IAU Symposium, Vol. 248, IAU Symposium, ed. W. J. Jin, I. Platais, & M. A. C. Perryman, 553–559

Mannucci, F., Cresci, G., Maiolino, R., Marconi, A., & Gnerucci, A. 2010, MNRAS, 408, 2115

Mannucci, F., Salvaterra, R., & Campisi, M. A. 2011, MNRAS, 414, 1263

Maraston, C. 2005, MNRAS, 362, 799

Mauduit, J.-C., Lacy, M., Farrah, D., et al. 2012, PASP, 124, 714

McCrum, M., Smartt, S. J., Kotak, R., et al. 2014, MNRAS, 437, 656

McCrum, M., Smartt, S. J., Rest, A., et al. 2015, MNRAS, 448, 1206

Metzger, B. D., Vurm, I., Hascoët, R., & Beloborodov, A. M. 2014, MNRAS, 437, 703

Miknaitis, G., Pignata, G., Rest, A., et al. 2007, ApJ, 666, 674

Milisavljevic, D., Soderberg, A. M., Margutti, R., et al. 2013, ApJ, 770, L38

Miller, A. A., Chornock, R., Perley, D. A., et al. 2009, ApJ, 690, 1303

Minkowski, R. 1941, PASP, 53, 224

Modjaz, M., Kewley, L., Bloom, J. S., et al. 2011, ApJ, 731, L4

Modjaz, M., Kewley, L., Kirshner, R. P., et al. 2008, AJ, 135, 1136

Modjaz, M., Li, W., Butler, N., et al. 2009, ApJ, 702, 226

Moriya, T., Tominaga, N., Tanaka, M., Maeda, K., & Nomoto, K. 2010, ApJ, 717, L83

Moriya, T. J., Blinnikov, S. I., Tominaga, N., et al. 2013, MNRAS, 428, 1020

Moriya, T. J., & Maeda, K. 2012, ApJ, 756, L22

Neill, J. D., Sullivan, M., Gal-Yam, A., et al. 2011, ApJ, 727, 15

Nicholl, M., Smartt, S. J., Jerkstrand, A., et al. 2013, Nature, 502, 346

—. 2014, MNRAS, 444, 2096

—. 2015, ArXiv e-prints, arXiv:1503.03310

Nugis, T., & Lamers, H. J. G. L. M. 2000, A&A, 360, 227

Ofek, E. O., Cameron, P. B., Kasliwal, M. M., et al. 2007, ApJ, 659, L13

Osterbrock, D. 1989, Astrophysics of gaseous nebulae and active galactic nuclei, A series of books in astronomy (University Science Books)

Oyaizu, H., Lima, M., Cunha, C. E., et al. 2008, ApJ, 674, 768

Pan, T., Patnaude, D., & Loeb, A. 2013, MNRAS, 433, 838

Pastorello, A., Smartt, S. J., Botticella, M. T., et al. 2010, ApJ, 724, L16

Peng, C. Y., Ho, L. C., Impey, C. D., & Rix, H.-W. 2002, AJ, 124, 266

Perley, D. A., Levan, A. J., Tanvir, N. R., et al. 2013, ApJ, 778, 128

Persson, S. E., Barkhouser, R., Birk, C., et al. 2008, in Society of Photo-Optical Instrumentation Engineers (SPIE) Conference Series, Vol. 7014, Society of Photo-Optical Instrumentation Engineers (SPIE) Conference Series

Persson, S. E., Murphy, D. C., Smee, S., et al. 2013, PASP, 125, 654

Prieto, J. L., Stanek, K. Z., & Beacom, J. F. 2008, ApJ, 673, 999

Prieto, J. L., Drake, A. J., Mahabal, A. A., et al. 2012, The Astronomer's Telegram, 3883, 1

Quataert, E., & Shiode, J. 2012, MNRAS, 423, L92

Quimby, R. M., Aldering, G., Wheeler, J. C., et al. 2007, ApJ, 668, L99

Quimby, R. M., Gal-Yam, A., Arcavi, I., et al. 2011a, The Astronomer's Telegram, 3841, 1

Quimby, R. M., Yuan, F., Akerlof, C., & Wheeler, J. C. 2013a, MNRAS, 431, 912

Quimby, R. M., Kulkarni, S., Ofek, E., et al. 2010, The Astronomer's Telegram, 2740, 1

Quimby, R. M., Kulkarni, S. R., Kasliwal, M. M., et al. 2011b, Nature, 474, 487

Quimby, R. M., Arcavi, I., Sternberg, A., et al. 2012, The Astronomer's Telegram, 4121, 1

Quimby, R. M., Werner, M. C., Oguri, M., et al. 2013b, ApJ, 768, L20

Quimby, R. M., Oguri, M., More, A., et al. 2014, Science, 344, 396

Rakavy, G., & Shaviv, G. 1967, ApJ, 148, 803

Rest, A., Stubbs, C., Becker, A. C., et al. 2005, ApJ, 634, 1103

Rest, A., Foley, R. J., Gezari, S., et al. 2011, ApJ, 729, 88

Rest, A., Scolnic, D., Foley, R. J., et al. 2014, ApJ, 795, 44

Rix, H.-W., Barden, M., Beckwith, S. V. W., et al. 2004, ApJS, 152, 163

Sako, M., Bassett, B., Connolly, B., et al. 2011, ApJ, 738, 162

Sanders, D. B., Salvato, M., Aussel, H., et al. 2007, ApJS, 172, 86

Sanders, N. E., Soderberg, A. M., Levesque, E. M., et al. 2012a, ApJ, 758, 132

Sanders, N. E., Soderberg, A. M., Valenti, S., et al. 2012b, ApJ, 756, 184

Savaglio, S., Glazebrook, K., & Le Borgne, D. 2009, ApJ, 691, 182

Schaerer, D., & Vacca, W. D. 1998, ApJ, 497, 618

Schlafly, E. F., & Finkbeiner, D. P. 2011, ApJ, 737, 103

Schlegel, D. J., Finkbeiner, D. P., & Davis, M. 1998, ApJ, 500, 525

Schmidt, G. D., Weymann, R. J., & Foltz, C. B. 1989, PASP, 101, 713

Shaw, R. A., & Dufour, R. J. 1994, in Astronomical Society of the Pacific Conference Series, Vol. 61, Astronomical Data Analysis Software and Systems III, ed. D. R. Crabtree, R. J. Hanisch, & J. Barnes, 327

Shi, F., Kong, X., & Cheng, F. Z. 2006, A&A, 453, 487

Silva-Villa, E., Adamo, A., & Bastian, N. 2013, MNRAS, 436, L69

Smith, N., Chornock, R., Li, W., et al. 2008, ApJ, 686, 467

Smith, N., Chornock, R., Silverman, J. M., Filippenko, A. V., & Foley, R. J. 2010, ApJ, 709, 856

Smith, N., & McCray, R. 2007, ApJ, 671, L17

Smith, N., & Tombleson, R. 2015, MNRAS, 447, 598

Smith, N., Li, W., Foley, R. J., et al. 2007, ApJ, 666, 1116

Stanek, K. Z., Gnedin, O. Y., Beacom, J. F., et al. 2006, Acta Astron., 56, 333

Stasińska, G. 1982, A&AS, 48, 299

Stoll, R., Prieto, J. L., Stanek, K. Z., et al. 2011, ApJ, 730, 34

Strolger, L.-G., Riess, A. G., Dahlen, T., et al. 2004, ApJ, 613, 200

Svensson, K. M., Levan, A. J., Tanvir, N. R., Fruchter, A. S., & Strolger, L.-G. 2010, MNRAS, 405, 57

Taylor, E. N., Franx, M., van Dokkum, P. G., et al. 2009, ApJS, 183, 295

Thomas, R. C., Nugent, P. E., & Meza, J. C. 2011, PASP, 123, 237

Tonry, J., & Onaka, P. 2009, in Advanced Maui Optical and Space Surveillance Technologies Conference,

Tonry, J. L., Stubbs, C. W., Lykke, K. R., et al. 2012, ApJ, 750, 99

Tremonti, C. A., Heckman, T. M., Kauffmann, G., et al. 2004, ApJ, 613, 898

Valenti, S., Benetti, S., Cappellaro, E., et al. 2008, MNRAS, 383, 1485

van den Heuvel, E. P. J., & Portegies Zwart, S. F. 2013, ApJ, 779, 114

Vink, J. S., & de Koter, A. 2005, A&A, 442, 587

Vinko, J., Zheng, W., Romadan, A., et al. 2010, Central Bureau Electronic Telegrams, 2556, 1

Vreeswijk, P. M., Savaglio, S., Gal-Yam, A., et al. 2014, ApJ, 797, 24

Wainwright, C., Berger, E., & Penprase, B. E. 2007, ApJ, 657, 367

Wanderman, D., & Piran, T. 2010, MNRAS, 406, 1944

Wang, S. Q., Wang, L. J., Dai, Z. G., & Wu, X. F. 2015, ApJ, 799, 107

Willmer, C. N. A., Faber, S. M., Koo, D. C., et al. 2006, ApJ, 647, 853

Wirth, G. D., Willmer, C. N. A., Amico, P., et al. 2004, AJ, 127, 3121

Woosley, S. E. 2010, ApJ, 719, L204

Woosley, S. E., Blinnikov, S., & Heger, A. 2007, Nature, 450, 390

Yaron, O., & Gal-Yam, A. 2012, PASP, 124, 668

Yoon, S.-C., & Langer, N. 2005, A&A, 443, 643

Young, D. R., Smartt, S. J., Valenti, S., et al. 2010, A&A, 512, A70

Zahid, H. J., Geller, M. J., Kewley, L. J., et al. 2013, ApJ, 771, L19

Zaritsky, D., Kennicutt, Jr., R. C., & Huchra, J. P. 1994, ApJ, 420, 87